Predicting the Ultimate Axial Load Capacity of Joints formed using V-Band Retainers

Matthias Müller

A thesis submitted to the University of Huddersfield in partial fulfilment of the requirement for the degree of Doctor of Philosophy

August 2011

Abstract

V-band retainers are widely used in the automotive, aircraft and aerospace industries to connect a pair of circular flanges to provide a joint with good axial strength and torsional rigidity. V-band retainers are manufactured using a cold roll forming process. Despite their wide application, once assembled to a pair of flanges little is known about the interaction between flange and band. Moreover the failure mode of V-band retainers when applying an axial load is not fully understood.

In this thesis the ultimate axial load capacity of V-band retainers is predicted using finite element and theoretical models and validated using experimental testing. It was shown that the ultimate axial load capacity was strongly dependent on the joint diameter, increasing between 114mm and 235mm, and decreasing beyond that. Moreover, the peak in ultimate axial load capacity was dependent on parameters such as the axial clamping load and coefficient of friction, and its position lay between 235mm and 450mm, as predicted by the finite element models. Other geometrical parameters such as flange and band thickness showed large impacts on the ultimate axial load capacity as well.

A theoretical model was developed that allowed the ultimate axial load capacity to be calculated from a single formula for larger bands and using a simple algorithm for smaller bands. This model supported the findings that, depending on the band diameter, the ultimate axial load capacity had a peak, but predicted its position at approximately 181mm. This position at 181mm was validated by the experimental data. However, when compared to the tests, the finite element and theoretical models both over-predicted the ultimate axial load capacity. Both the finite element models and practical tests showed that for small V-bands axial failure is due to a combination of section deformation and ring expansion, whereas large V-bands fail due to ring expansion only. These two distinct types of behaviour were incorporated into the theoretical model.

The hardness development throughout the cold roll forming process was predicted using finite element models. This was validated by hardness measurements, for which a new technique was generated, that directly linked plastic strain and hardness values.

Acknowledgement

First of all I would like to thank my supervisor Dr Simon Barrans for giving me the opportunity to undertake this PhD course and for his constant advice, help, guidance, and encouragement over the last few years.

Second of all, I would like to thank Dr Kiumars Shoghi from Borg Warner in Bradford, and Ian Brown from Teconnex Ltd. in Keighley, who have supported me throughout my project with test flanges and V-band retainers. The discussions with them and their detailed knowledge about V-band retainers were a big inspiration and help for me.

Many thanks go also to Prof Liam Blunt for being my second supervisor, and for providing the facilities to carry out my experiments.

Finally I would like to thank all my friends and my family but especially my parents for giving lots of inspiration and for their patience, understanding and support whilst I was dealing with this project.

Table of Contents

Table of Figures

Table of Tables

Notations

a	the flange length of strip [mm]
A	current area of the cross section [mm^2]
A_0	initial area of the cross section [mm^2]
A_B	area of the V-band section [mm^2]
b	breadth [mm]
c	restriction in a contact due to a rigid body
C_T	temperature conversion factor
CP_i	initial contact point between band and flange
CP_{ib}	initial contact point on band
CP_{if}	initial contact point on flange
CP_s	subsequent contact point
D_{bo}	outside diameter of the band [mm]
D_b	inner diameter of the band [mm]
d_c	contact distance [mm]
D_s	seal diameter [mm]
D_f	flange diameter [mm]
D_{fo}	flange outer diameter [mm]
d_p	pitch diameter of the bolt [mm]
d_1	inside diameter of the nut bearing surface [mm]
d_2	outside diameter of the nut bearing surface [mm]
E	Elastic modulus [N/mm^2]
$\mathrm{E_p}$	potential Energy [J]
Δf_{ex}	load increments [N]
f	the function of the hardening parameter
F	homogeneous function of stress components of symmetric tensor
f_a	axial force per unit length [N/mm]
F_A	axial load [N]
F_{ACL}	axial clamping load [N]

f_{ex}	external nodal force vector
F_f	frictional force [N]
f_n	natural frequency[Hz]
F_N	normal force [N]
f_r	radial force per unit length [N/mm]
F_R	radial force [N]
F_s	safety factor
F_t	tangential force on surface [N]
F_{UALC}	ultimate axial load capacity [N]
F_x	tensile or compressive force in x-direction of tensile test [N]
F_θ	circumferential force in the V-band at $d\theta$ [N]
F_β	clamping load in the T-bolt [N]
g	acceleration due to gravity [mm/s²]
h	height [mm]
H	lever of axial force F_A [mm]
h^*	hardening function
H_b	depth of V-band section [mm]
h_c	clearance between the clamp and the flange [mm]
HV	Vickers Hardness values [HMV]
I	second moment of the area through a section of the V-band [mm^4]
$I_{\varepsilon p}$	Odqvist hardening parameter
k	spring stiffness [N/mm]
K	lever of radial force F_R [mm]
K^*	current stiffness [N/mm]
K_h	hardening multiplier
K^i	isotropic hardening parameter
k_p	penalty spring stiffness [N/mm]
l	current length [mm]

L	length of assumed cantilever for V-band section in combined theory [mm]
Δl	change in length [mm]
l_b	V-band length (circumference) [mm]
L_b	length between end of cantilever and centre of r_b (used in combined theory) [mm]
Δl_b	change in band length [mm]
l_c	length band where plastic strain value are from cross section [mm]
L_d	deformation length [mm]
l_s	radial sliding length of flat part on V-band leg [mm]
l_{sv}	axial sliding length of flat part on V-band leg [mm]
l_0	initial length [mm]
m	mass [kg]
M	bending moment [Nmm]
M_L	actual bending moment applied [Nmm]
M_U	bending moment for unit load method [Nmm]
M_{ult}	ultimate bending moment [Nmm]
N_A	factor due to axial tension [mm²]
N_B	factor due to bending moment [mm]
n_d	normal direction
n_h	hardening plastic strain index
N_P	factor due to pressure load [N/mm]
N_T	factor due to total load
p	radial force per unit length [N/mm]
P	radial force per unit length [N/mm]
P_e	equivalent pressure [N/mm]
R	Radius of curvature [mm]
r_b	cold formed inner bending radius of V-section between band leg and foot [mm]
R_b	V-band radius [mm]

R_{bi}	initial/open inner radius of the band [mm]
Δr_b	portion of δ_r described by band parameters [mm]
r_c	corner radius of flange [mm]
R_c	radius of contact point between band and flange [mm]
Δr_c	portion of δ_r described by flange parameters [mm]
R_f	radius of the flange [mm]
R_m	mean radius of the fastener under-head bearing surface [mm]
R_t	fictive tool radius [mm]
t	thickness of work material [mm]
T_a	axial tensile load [N]
t_b	thickness of the band (strip) [mm]
t_f	flange thickness [mm]
t_n	corresponding time for f_n [s]
T_t	torque applied to the T-bolt [Nmm]
t_{10}	time period for explicit solver, 10 times slower than t_n [s]
u	displacement [mm]
Δu	incremental displacement solution [mm]
u_A	position vector at node A [mm]
$u_{closure}$	specific distance in contact analyses [mm]
u_t	relative tangential displacement [mm]
w	load per unit length of circumference [N/mm]
W_D	strain energy of volume change [J]
w_s	strip width [mm]
W_S	elastic distortion energy [J]
W_{SY}	distortion energy at yield point [J]
W^p	accumulated plastic work [J]
W_0	elastic strain energy [J]
x_I	deformed position vector [mm]

y	distance from the neutral axis (used to determine the initial stage bending stress) [mm]
z	distance from the neutral axis (used for determining the bending stress in the axial direction) [mm]
α	angular position around the band [rad]
α_{ij}	translational tensor
α_h	helix angle [rad]
β	subtended angle of half the V-section band [rad]
γ	angle associated with L_b [rad]
Δ	displacement for unit load method
δ_H	horizontal displacement during assembling process
δ_r	radial expansion of V-band due to ring deformation [mm]
δ_s	radial expansion of V-band due to section deformation [mm]
ε	strain
ε_e	elastic strain
ε_{eng}	engineering strain
ε_{ij}^p	the components of the plastic strain tensor
ε_{true}	true/ logarithmic strain
ε_p	plastic strain
ε_{peak}	peak longitudinal strain
ε_{ps}	plastic strain on contacting surface at inside of V-band
ε_{pr}	plastic strain in at root of bending radius
ε_θ	hoop strain at $d\theta$
ζ	angle for half the open gap in the band [rad]
θ	angular position around the band [rad]
$\Delta\theta$	bend angle increment [rad]
θ_a	deformation angle due to bending at free end of cantilever for combined theory [rad]
$\Delta\theta_a$	increment size of angle θ_a for combined theory [rad]
θ_p	prescribed fold angle in one particular stage [rad]

θ_r	angle between axial and radial force when contact between band and flange is established along radius r_b for combined theory [rad]
λ	total load [N]
Λ	Lagrange multiplier
λ_n	load level at increment n
λ_{n-1}	load level at increment $n-1$
μ	coefficient of friction between the V- band and rigid flanges
μ_h	underhead coefficient of friction
μ_{th}	coefficient of friction of threads
ν	poisson's ratio
Π	potential energy [J]
σ	stress [N/mm²]
σ_α	hoop stress [N/mm²]
σ_θ	hoop stress at $d\theta$ [N/mm²]
σ_b	bending stress [N/mm²]
σ_B	maximum bending stress [N/mm²]
σ_{eng}	nominal/ engineering stress [N/mm²]
σ_L	longitudinal stress [N/mm²]
σ_M	von Mises equivalent stress [N/mm²]
$\sigma_{t\ UTS}$	true ultimate tensile strength [N/mm²]
σ_{true}	true stress [N/mm²]
σ_{ult}	ultimate stress [N/mm²]
σ_{xb}	fibre stress due to bending [N/mm²]
σ_Y	yield stress [N/mm²]
$\sigma_1, \sigma_2, \sigma_3$	stress components in three directions [N/mm²]
τ_{max}	maximum shear stress of the material [N/mm²]
τ_Y	yield shear stress [N/mm²]
ϕ	half angle of the V-band section [rad]
ϕ^*	angle between axial and radial force components for ring theory [rad]

1 Introduction

1.1 Background

V-band retainers as shown in Figure 1-1 are an easy way of forming a joint between a pair of circular flanges for hoses, pipes, ducts, pipelines, turbocharger housings, and many more applications.

As stated by Shoghi (2003) V-band retainers were invented during the Second World War by the Marmon Corporation and are presently used in a wide range of applications in the aerospace and automotive industries as the joints they form offer good axial and torsional rigidity. As one of the first attempts in literature Mountford (1980) has mathematically described the V-band retainers used to connect together housings of diesel engine turbochargers, secure the lid of a metal drum, which contains a lead pot used for the safe transport of the radioactive isotope Iridium 197 and to retain the metal covers of an Rotork valve actuator motor. Another major field of application is described by NASA (2000) and Stavrindis *et al.* (1996), where Marman-type clamps are used to assemble satellites to their delivery vehicle during launch and ascent. Wilkey (1966) discusses the use of a V-band type clamp to secure the adaptor of a velocity package to the sustainer-stage of a launch vehicle. In aerospace applications, Marman clamp systems are not only used to fasten components together, but also to be separated once the spacecraft has reached its designated destination. This is done by releasing the clamp using a pyrotechnic device. They are also used to connect the stages of large rockets used for space missions which are arranged on top of each other as stated by Meyer (1999).

When compared to traditional re-assembling joints using bolts and screws offering the same strength, V-band retainers have many benefits. As only one T-bolt nut needs to be tightened they are faster and easier to assemble and re-assemble. Since the flange load is more evenly distributed and the flanges contain fewer stress raisers, they can be manufactured with less material, leading to a much lighter joint. As smaller flange thicknesses and no movement of the fastener in the axial direction are required, V-band joints need less space, which makes them very effective where a compact joint is needed. Especially in automotive and aerospace applications these latter two benefits are crucial as weight and space reductions will reduce costs. Due to their axisymmetric form, the flanges can have an infinitely variable circumferential orientation. The orientation of the band is similarly variable. This enables easier and faster access to the T-bolt nut for assembly and maintenance purposes.

The V-band itself (as shown in Figure 1-1) is manufactured in a cold roll forming process, consisting of two major stages. In the first stage using 6 roller pairs an initially flat strip is formed into a V-shaped section with an angle of 35°, still remaining straight in the longitudinal direction. In the second stage the straight strip is then roll bent into a circular ring shape, also changing the V-angle in the section from 35° to 40°. The plastic deformation induced by the roll forming results in substantial work hardening of the V-band section in the bending zone. After this, the trunnion loops, which hold the T-bolt and the end cap, are welded to the V-band.

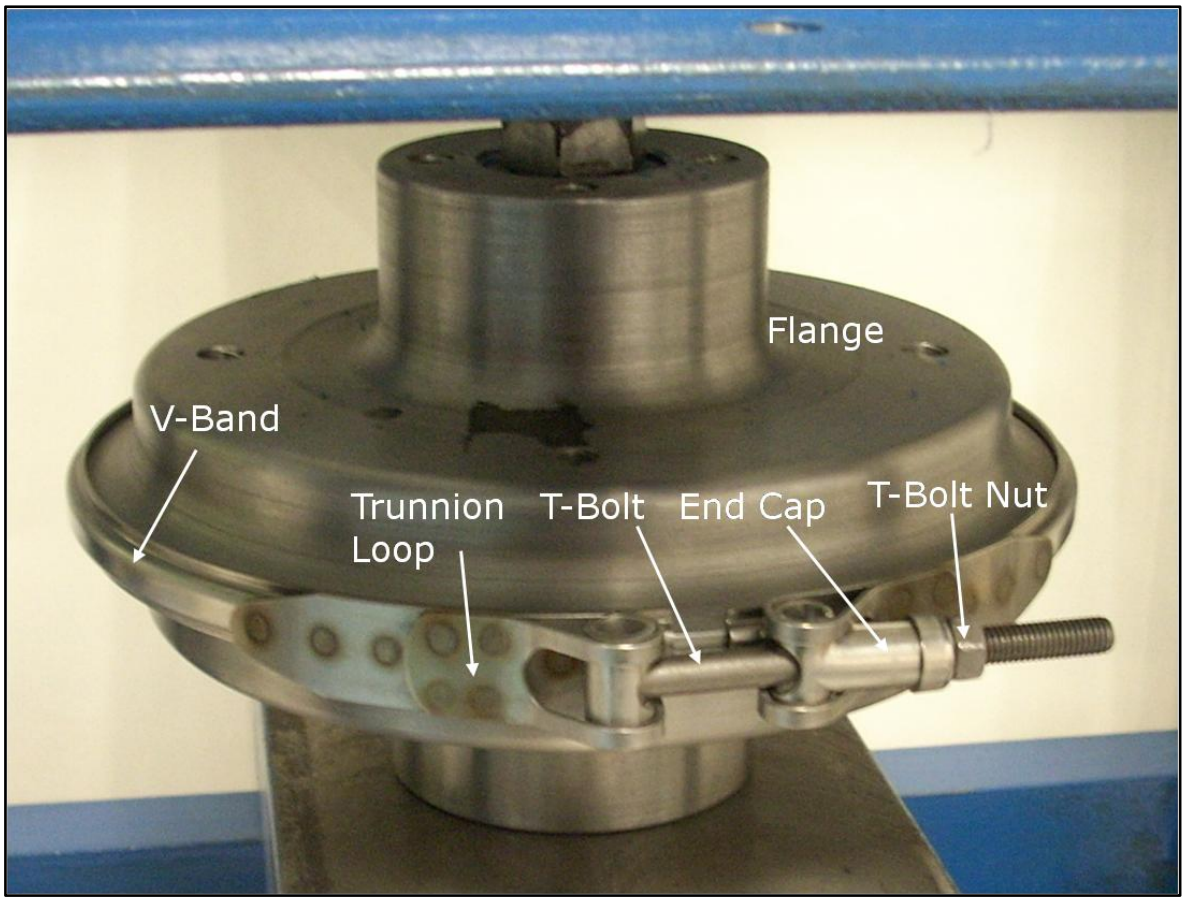

Figure 1-1: V-band retainer assembled to a pair of test flanges

The mechanism by which a V-band retainer creates a joint is easily understood. Placing the retainers around a pair of flanges the T-bolt nut is tightened which results in reducing the circumference and thereby creating a radial force, as can be seen in Figure 1-2. The wedging action created by the radial force then generates an axial force, pressing both flanges together, which is regarded as the axial clamping force or load F_{ACL}.

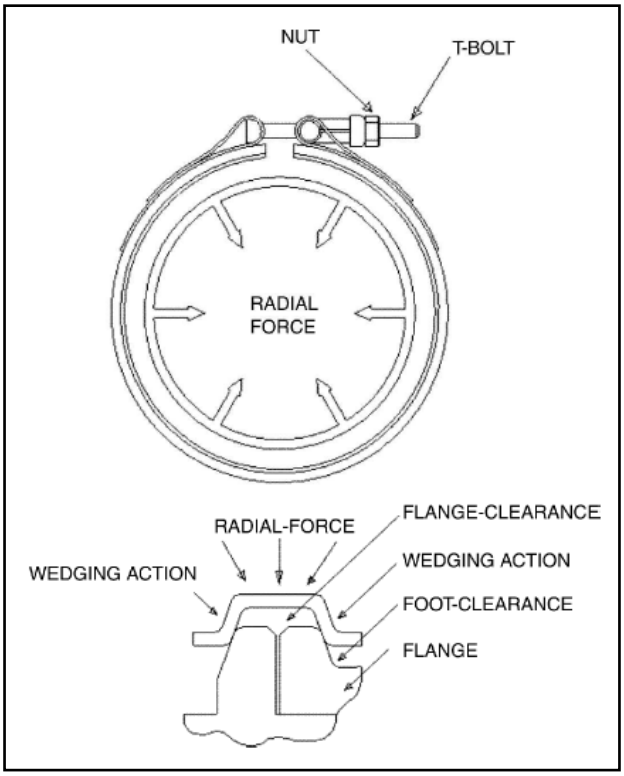

Figure 1-2: Working principle of V-band clamp assembled to a pair of flanges, taken from *(*Shoghi *et al.*2004)

Despite their wide application, once assembled to a pair of flanges, only little is known about the interaction between the flanges and the retainer itself. Failure of a V-band joint mainly occurs due to an external load, which may be a bending load, axial load, rotational load, or any combination of all three load types. To start understanding these failure mechanisms it is worth investigating a pure axial load applied to the joint, which this thesis focuses on. Axial loading of the joint can be split into two major failure modes. Firstly small separation of the flanges with elastic deformation of the V-band retainer, where the flanges reconnect again after the axial load is taken off. Although no physical damage takes place, this failure is undesirable, as especially in turbocharger applications, fluid leakage may occur or components may clash (Shoghi 2003), and in aerospace applications failure of the whole system due to chatter may occur (Stavrindis *et al*. 1996). Secondly irrecoverable separation of the flanges, which occurs when the V-band retainer moves over one or both flanges, and hence total failure of the mechanical V-band joint occurs. This thesis is mainly concerned with the latter mode, in which the maximum axial load that leads to total failure of the V-band joint is regarded as the Ultimate Axial Load Capacity F_{UALC}.

Turbocharger manufacturers carry out burst containment tests in which the rotor of a turbocharger undergoes an over speed until it bursts. The V-band joint must be able to withstand the load from rotor fragments, keeping all mechanical parts inside the housing, exhaust, and inductions components, and by this, avoiding damage to other engine parts

in the surrounding area. Unfortunately, these tests do not allow the F_{UALC} to be measured directly, but only report the maximum turbine-/ compressor-speed in rpm (revolutions per minute). An example of the second failure mode during experimental testing is given in Figure 1-3, where an axial load F_A was applied and the retainer has moved over one flange, as indicated by the red arrow.

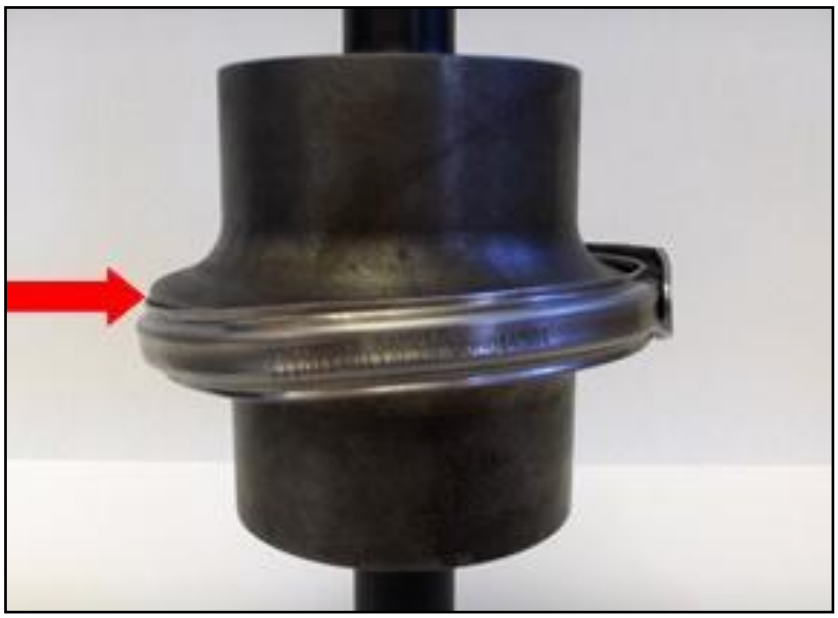

Figure 1-3: V-band retainer fully failed during experimental testing

Current methods of predicting the F_{UALC} are empirical with very little theoretical basis. This approach is expensive and may be unreliable across a wide range of V-band retainers. Therefore, the work in this thesis aims to provide a robust method of predicting the F_{UALC} of joints formed using V-band retainers.

This aim was achieved by addressing the following objectives:

1. To generate a finite element modelling technique able to predict the work hardening development during the manufacture of V-section band clamps.
2. To produce finite element models, validated by experimental data that allow V-band joint ultimate axial load capacity to be accurately predicted and also allow the internal stresses within the band to be studied.
3. To extend the existing theory of V-band behaviour to predict the effect of various joint parameters on the ultimate axial load capacity, taking into account plastic deformation effects.
4. To generate an empirical understanding of the relationship between V-band tightening force, V-band internal stresses and V-band joint ultimate axial load capacity by conducting experimental tests on samples from different sizes of V-band.

Within this work the variation in ultimate axial load capacity due to small changes in joint parameters was judged to be more important than the absolute load capacity.

1.2 V-Band Nomenclature

In this section the most important notations used in this thesis to describe V-band retainers are presented. Figure 1-4 shows a V-band (not including T-bolt and trunnion loops) when the T-bolt is tightened, generating a circumferential load F_β acting on both ends, as discussed by Shoghi (2003), and Shoghi *et al.* (2004). The two ends and the gap shown in this figure do not represent the actual ends of the V-band, but indicate where the trunnion loops are welded to the band and F_β is acting. Therefore, β describes the subtended angle of half the V-band retainer. D_b indicates the full diameter once the band is fully assembled to a pair of flanges.

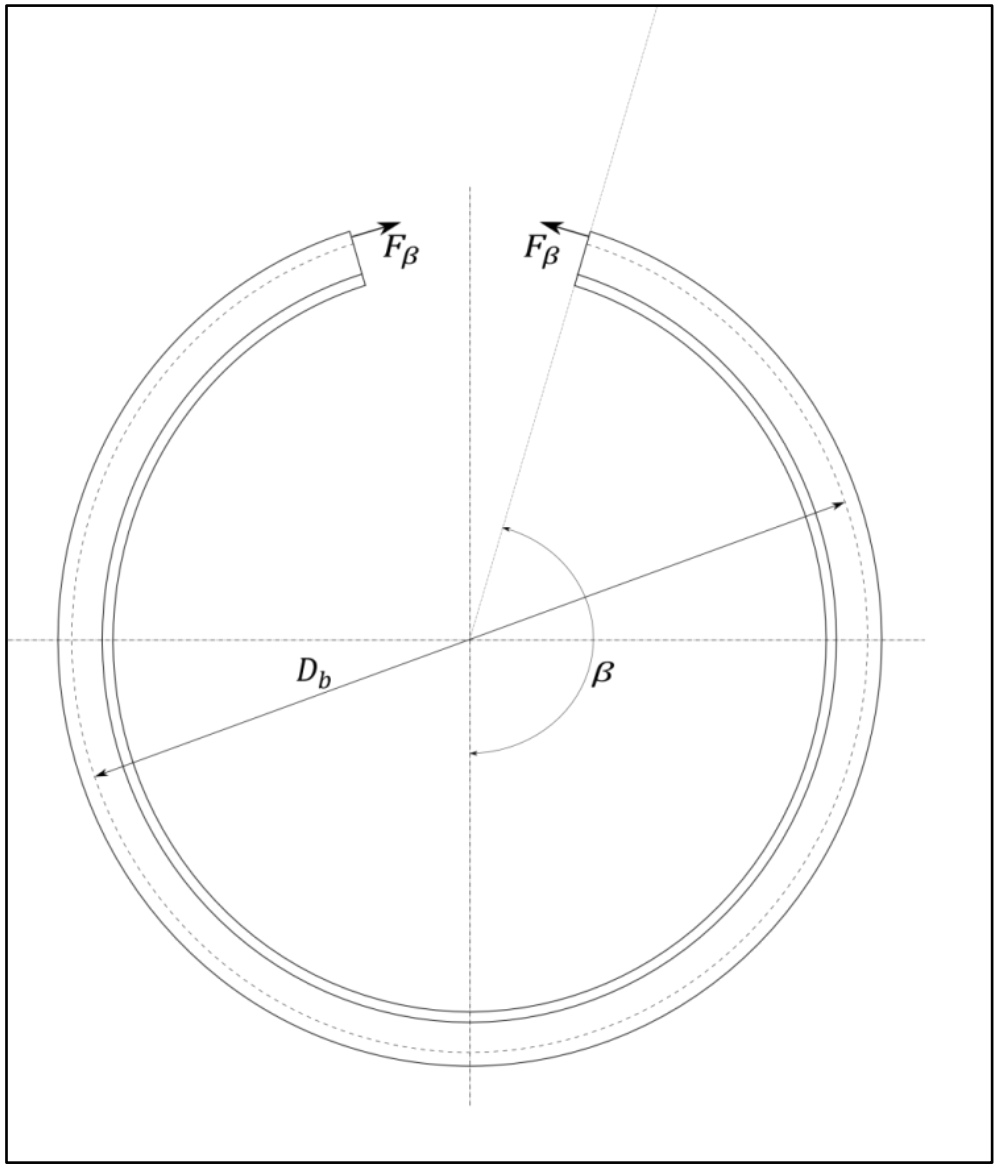

Figure 1-4: V-band with circumferential load applied

Figure 1-6 shows half the cross section of a joint where a V-band is fully assembled onto a pair of flanges. The V-band cross section can be split in approximately three parts, the foot, the leg and the back. This sectioning was chosen in order to simplify the discussion throughout this thesis.

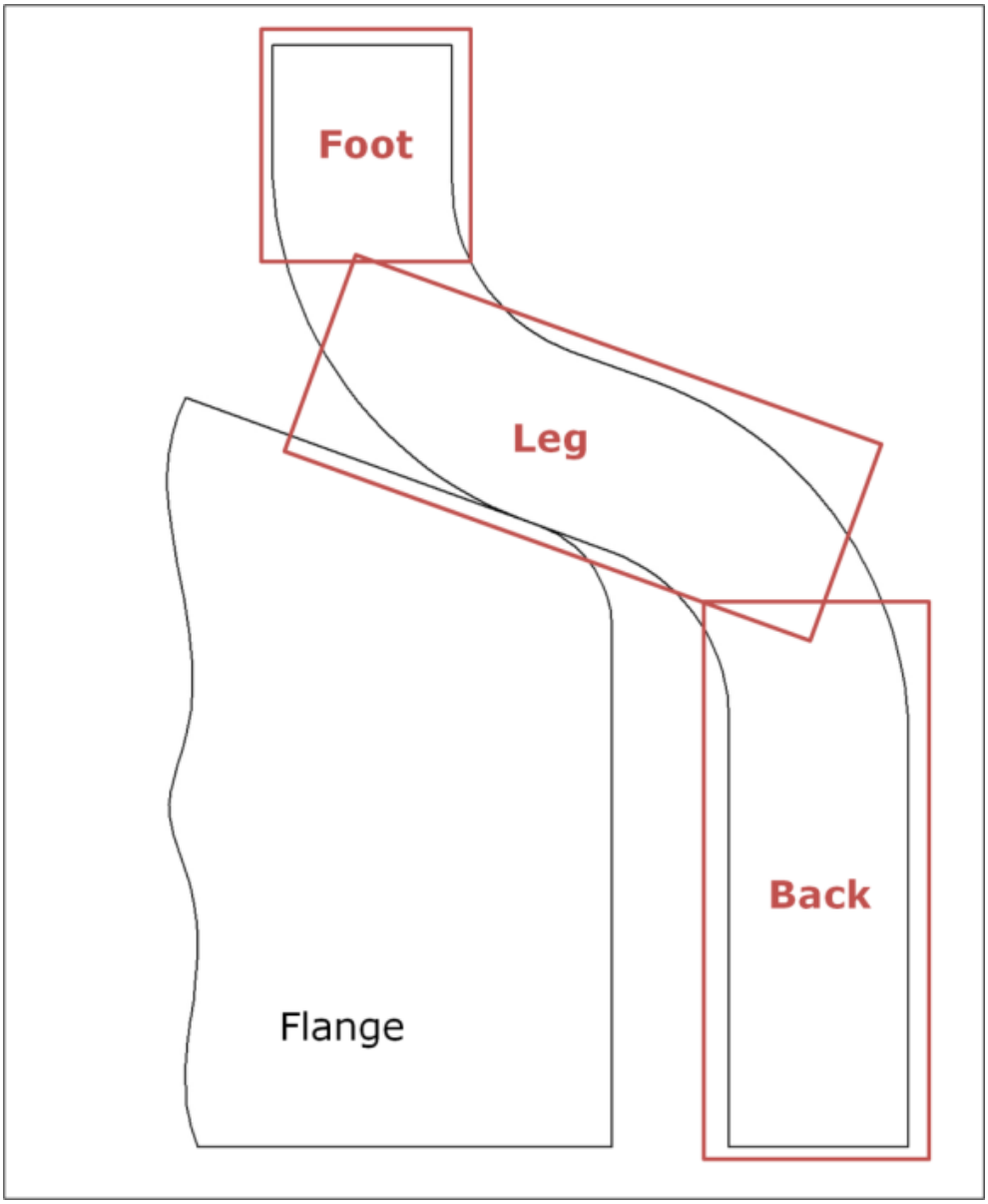

Figure 1-5: Section of V-band cross section

The most important notations defining a V-band cross section are given in Figure 1-6, where R_b is the radius of the V-band and equals $\frac{D_b}{2}$. R_c then describes the contact between V-band and flanges where the axial F_A and radial forces F_R are acting. Half the V-band angle is defined by ϕ, the radius generated by the roll forming process by r_b, and the band thickness by t_b.

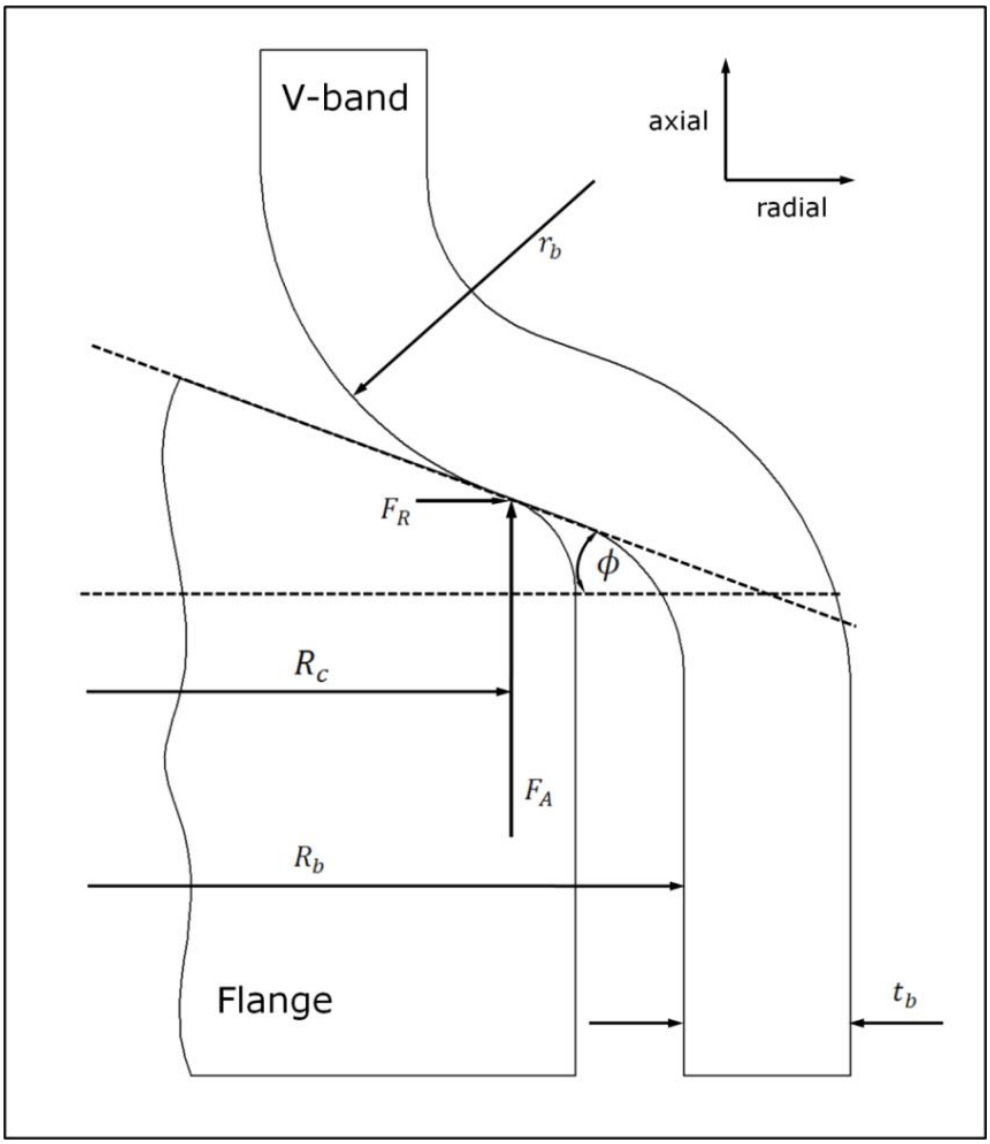

Figure 1-6: Half the cross section of a V-band retainer fully assembled onto a pair of flanges

1.3 Research Methodology

1. The properties of the band material during plastic deformation when in flat form were determined experimentally. Of particular use were the stress/strain relationship beyond yield and the relationship between plastic deformation and hardness.
2. Non-linear contact, elastic-plastic, 2 dimensional and 3 dimensional finite element models were used to simulate the 2 stages of V-band manufacture: formation of the V-section from the flat strip supplied and bending of the strip to form the hoop. These models were used to investigate the plastic deformation and change in yield stress for a variety of band diameters.
3. Samples of the strip were extracted from the rolling mill such that all stages of the rolling process could be examined. The strip samples were sectioned and the micro-hardness through the section measured. This data was used together with data gathered in (1) to determine the plastic deformation of the material. Hence, validation data for the finite element model in (2) was generated.
4. Non-linear contact, elastic-plastic axisymmetric finite element models were used to simulate total failure of the V-band joint by applying an external axial load, and to predict the Ultimate Axial Load Capacity, which represents the maximum load the joint can stand. These models did not take into account residual stresses and strains induced by the preceding cold roll forming process.
5. The finite element models generated in (4) were used to investigate the impact of various band diameters, band and flange section geometries, coefficients of friction, and clamping loads on the Ultimate Axial Load Capacity.
6. Non-linear contact, elastic-plastic 3 dimensional finite element models were generated to investigate the Ultimate Axial Load Capacity of V-band joints, by mounting the formed band from the 3 dimensional simulation in (2) onto circular flanges and applying an external axial load. The results for various band diameters were compared to simulations from (4) and (5), and the influence of residual stresses and strains from the cold roll forming process on the Ultimate Axial Load Capacity was determined.
7. Sample V-bands with a range of diameters were mounted on matching flanges and tested to failure in the axial direction. This determination of the Ultimate Axial Load Capacity was used to validate the finite element models in (4), (5), and (6).
8. Sample V-bands with a range of diameters were mounted on matching flanges and tightened to levels matching those simulated in (5). The inner surface of the bands was then measured to determine the degree of permanent indentation and hence the

distribution of contact pressure around the band. This was used to validate the models generated in (5).

9. With the aid of the results obtained in (4), (5) and (6), an analytical analysis was generated describing the failure mode, leading to total failure of the V-band joint.

1.4 Thesis structure

In chapter 2 existing research and background knowledge is discussed. The existing theory on V-band retainers is critiqued, and the sources of non-linearity in the finite element method and non-linear contact problems are included. The nature of plastic deformation and subsequent yielding of metals along with its link to the cold roll forming processes is discussed, which is vital to understand much of the numerical and experimental work described in this thesis. Moreover, approaches to analytically and numerically investigating the cold roll forming processes are discussed. Finally a brief overview of techniques used to determine contact pressure in general and their limitations in the V-band application is given, leading to the technique used in this thesis to determine the indentation in the contact area.

In chapter 3 finite element simulations of the cold roll forming process of V-band retainers are described and the limitations and assumptions of these models discussed. Both 2 dimensional and 3 dimensional models are included here.

Finite element models used to predict the Ultimate Axial Load Capacity of V-band Joints are specified in chapter 4 with both 2 dimensional and 3 dimensional approaches being used. The modes of failure are also investigated in this chapter.

In chapter 5 a classical theory has been developed to predict the deformation of the V-band retainer during failure, due to an external force, after being fully assembled to a pair of circular flanges.

The experimental validation of the finite element analyses and classical theory is presented in chapter 6. The roll forming simulation is validated using induced material hardness tests. Destructive tensile testing is used to validate the Ultimate Axial Load Capacity models. Final conclusions are presented in chapter 7.

This is followed by a discussion of topics not covered in this thesis but being in great need of further investigation, numerically, experimentally, and using classical approaches in chapter 8.

2 Literature Survey

2.1 V-Band Retainers

As one of the first approaches to theoretically describe V-band retainers, Mountford (1980) presented equations to enable selection of the appropriate clamp for a certain application. Estimating the loads due to bending moments, tensile load and internal pressure, these equations can be given as:

$$w(Bending) = \frac{4M}{\pi D_{bo}^2} \tag{2.1}$$

$$w(Tensile) = \frac{F_A}{\pi D_{bo}} \tag{2.2}$$

$$w(Pressure) = \frac{D_{bo} P}{4} \tag{2.3}$$

Where:

w load per unit length of circumference,

M bending moment applied,

F_A axial tensile load,

P internal pressure

D_{bo} outside diameter of the band.

The equations given convert tensile forces and bending moments acting on a clamped joint into a line load on the flange circumference, and not a pressure as stated by Mountford (1980). This can easily be proven by the units as all equations above have results with a unit of N/mm. The line loads are then summed and can be compared to experimental results on a design chart. Adding an appropriate factor of safety, a selection can then be made. As stated by Shoghi (2003), the equations presented by Mountford (1980) should be regarded as design guidelines rather than accurate calculations. In his work the equations do not take into account the effect of the angle of the V-section or the effect of friction between flanges and retainer.

More recently a detailed investigation of the process of assembling V-band joints has been undertaken by Shoghi (2003), with classical analysis in Shoghi *et al*. (2004), finite element analysis in Shoghi *et al*. (2003) and experimental validation in Shoghi *et al.* (2006).

In Shoghi *et al*. (2004) a classical theory predicting the assembly process is presented. The initial stage of the assembly process is a bending procedure to open the band so it can be loosely fitted around the flanges. When the band undergoes this manual bending it must be ensured that the band is not over-bent, as this may lead to plastic

deformation and hence change the strength behaviour of the V-band retainer. Therefore, based on their theory on flat bands presented in Shoghi *et al.* (2003), Shoghi *et al.* (2004) have developed a formula which predicts the maximum bending stress σ_B, as shown in equation 2.4. This bending stress can then be compared to the material yield stress.

$$\sigma_B = \frac{yE\,\delta_H(cos\zeta + cos\theta)}{R_{bi}^2\,I\left\{\beta\left(\frac{1}{2}+cos2\beta\right)-\frac{3}{4}sin2\beta\right\}} \tag{2.4}$$

E Elastic modulus

R_{bi} initial/open inner radius of the band

y distance from the neutral axis (used to determine the initial stage bending stress)

β subtended angle of half the V-section band

θ angular position around the band

δ_H horizontal displacement

ζ angle for half the open gap in the band

After loosely placing the V-band retainer around the flanges, the T-bolt nut can be tightened generating the force F_β (see Figure 2-1) which leads to the band establishing contact with the flanges. Taking into account that the mechanism of V-band retainers is similar to V-belt drives presented by Redford *et al*. (1969), a description of the axial clamping load has first been presented by Shoghi *et al.* (2004). More recently it has been improved by Shoghi *et al.* (2006), in which the authors have included both circumferential and transverse friction. The improved equation derived for the axial clamping load, F_{ACL}, occurring in the V-band retainer when tightening the T-bolt nut is given as:

$$F_{ACL} = \frac{(1-\mu tan\phi)F_\beta(\mu cos\Phi + sin\phi)}{\mu(\mu + tan\phi)}\left\{1 - e^{\frac{-\mu\beta}{\mu cos\phi + sin\phi}}\right\} \tag{2.5}$$

μ coefficient of friction

ϕ half angle of the V-section

Shoghi *et al*. (2004) assume that a sliding friction force only acts in the hoop direction. Taking this into account along with half of the included angle of the V-section Φ, and considering the improved equation 2.5 from Shoghi *et al*. (2006), the relationship between the applied load and the hoop stress σ_α at a certain angle α, can be expressed as

$$\sigma_\alpha = \left(\frac{F_\beta}{A_B}\right)\left(e^{\frac{-\mu(\beta-\alpha)}{\mu cos\,\phi + sin\,\phi}}\right) \tag{2.6}$$

A_B area of the V-band section

The formula is based on the assumption that a small segment $d\alpha$, is subjected to a radial force, p, per unit length as shown in Figure 2-1.

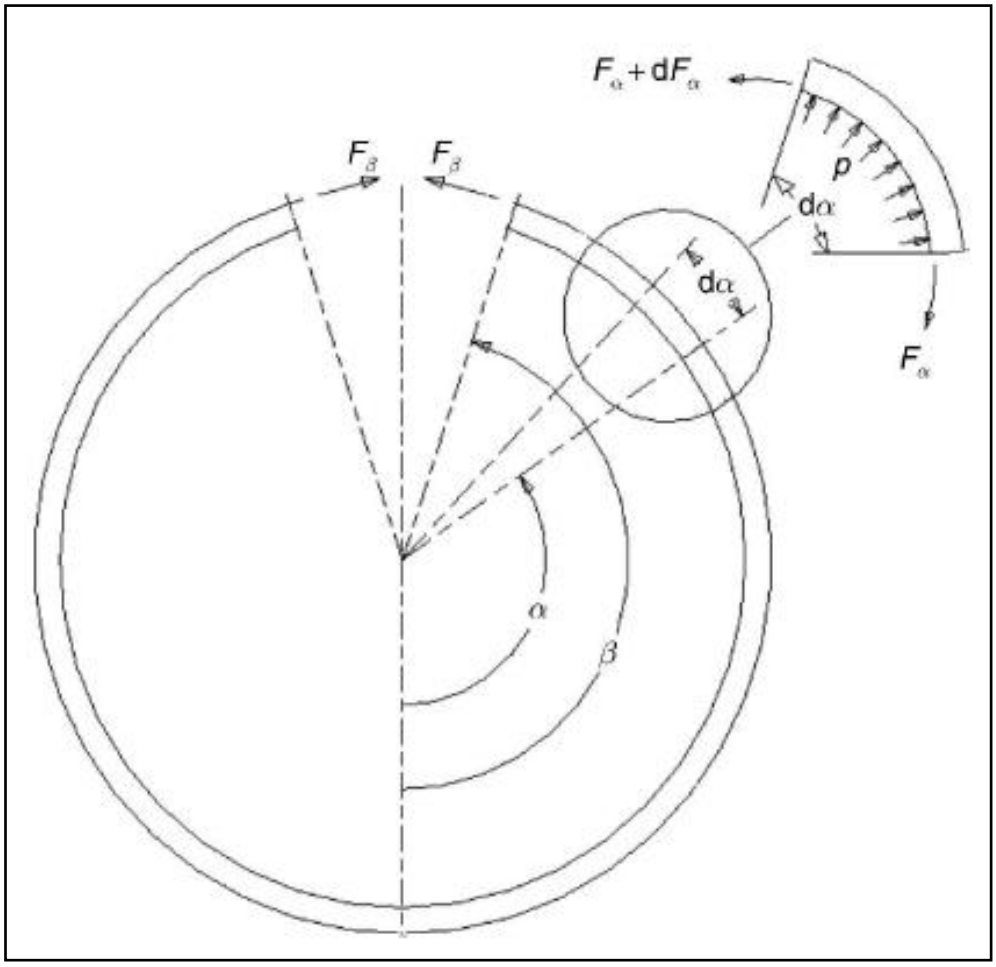

Figure 2-1: Small segment of V-band retainer model subjected to a radial force per length (taken from Shoghi *et al*. (2004))

The wedging action of the band clamp creates a bending of the cross section, leading to a bending stress σ_b in the top of the band clamp above the contact point. The equation for the bending stress presented by Shoghi *et al*. (2004) is based on engineering bending and along with the assumption of Shoghi *et al*. (2006), that takes into account transverse and circumferential friction, the bending stress can be expressed as:

$$\sigma_b = \frac{Mz}{I} = \frac{3F_\beta (h_c cos\phi + t_f sin\phi)}{{t_b}^2(\mu cos\phi + sin\phi)(R_f + h_c)} e^{\frac{-\mu(\beta-\alpha)}{\mu cos\phi + sin\phi}} \quad (2.7)$$

f flange edge thickness

h_c clearance between the clamp and the flange

I second moment of the area through a section of the band

M bending moment

R_f radius of the flange

t_b thickness of the band

z distance from the neutral axis (used for determining the bending stress in the axial direction)

α angular position around the band

The equation for the longitudinal stress σ_L derived by Shoghi *et al*. (2004), along with the updated assumptions from Shoghi *et al*. (2006), the stress is given as:

$$\sigma_L = \frac{F_\beta(\cos\phi - \mu\sin\phi)}{2t_b R_f(\mu\cos\phi + \sin\phi)} e^{\frac{-\mu(\beta-\alpha)}{\mu\cos\phi + \sin\phi}} \tag{2.8}$$

According to Shoghi *et al.* (2004) the above stresses have a combined effect and it is possible to quantify them by the von Mises equivalent stress σ_M:

$$\sigma_M = \sqrt{(\sigma_b + \sigma_L)^2 + (\sigma_\alpha + \sigma_B)^2 - (\sigma_b + \sigma_L)(\sigma_\alpha + \sigma_B)} \tag{2.9}$$

About at the same time as Shoghi, Fritskey (2003) has published a guide on how to choose the right V-band retainer for certain applications. In his work the author states that friction reduces the bolt load needed to prevent the flanges from separating. This will be of particular interest for this work, when discussing the Ultimate Axial Load Capacity of V-band retainers, both using experimental and numerical analysis, presented in later chapters. The equations presented in this article, seem to be very similar to Mountford's (1980) work and equations 2.1 to 2.3, although no clear reference is given. Fritskey's (2003) equations can be given as:

$$N_P = \frac{pD_s^2}{4D_{fo}} \tag{2.10}$$

$$N_B = \frac{4M}{pD_{fo}^2} \tag{2.11}$$

$$N_A = \frac{T_a}{pD_{fo}} \tag{2.12}$$

The total load can then be written as:

$$N_T = \{(N_P + N_B + N_A)C_T\}F_s \tag{2.13}$$

Converting the total load into an equivalent pressure (line load), P_e as also described by Mountford (1980). P_e, can be written as:

$$P_e = \frac{4N_T D_{fo}}{D_s^2} \tag{2.14}$$

Where:

D_S seal diameter

M bending moment

T_a axial tensile load

D_{fo} flange OD

F_s safety factor

p internal pressure (radial force per unit length)

P_e equivalent pressure

C_T temperature conversion factor

N_P factor due to pressure load

N_B factor due to bending moment

N_A factor due to axial tension

N_T factor due to total load

Again, the pressures described here are actually line loads acting on the circumference, as stated earlier in the case of Mountford's work. An approach employing similar equations as Mountford (1980), and Fritskey (2003) was undertaken in a patent for a spacecraft clamp connection published by Wittman (1987).

Fritskey (2003) then moves on mentioning that single –segment retainers are only suitable in larger diameters (greater than 127mm) and applications with only infrequent removal, due to the stiffness of the continuous ring.

V-band retainers are also widely employed in the aerospace industry to fasten satellites to their delivery vehicle during launch and ascent and rockets to the launch pad. In this application in particular they are very often referred to as Marman clamps and consist of small V-shaped segments held together by a flat band. In this field Stavrindis *et al.* (1996) have undertaken work concerning the dynamical testing and verification of satellite mechanical systems. Around the same time, Di Tolla and Ernst (1994) demonstrated that the gap capability (when the flanges separate) of a Marman Clamp joint is independent of the application of load circles by performing experimental tests and further investigated the joint using axisymmetric finite element simulations. Another dynamic analysis was carried out by Lin and Cole (1997), who showed that in this analysis, the axial and bending stiffness of the retainer are key variables, and claimed that the stiffness values given by the manufacturers were inaccurate. Also NASA (2000) acknowledge the complexity of V-band retainer behaviour and explicitly point out the poor documentation of Marman clamp system failures in the public domain, and base their installation procedure on this poor knowledge. Therefore, they suggest loading the retainers incrementally when installing them, and to tap them around the periphery to help produce a uniform internal circumferential force. The use of strain gauges helps monitoring this force. As this is a very time consuming, expensive, and highly complicated procedure, Lancho *et al*. (2000) have proposed a new so called Clamp Ring Separation System (CRSS) using a much stiffer band increasing the load capability and simplifying the installation procedure, but still have not managed to create a theory for the failure mode. Marmon Clamp Systems (MCS) are often used not only to connect but

also to form separation joints in aerospace applications. In order to estimate separation shock during inter stage separation, Takeuchi and Onoda (2002) have proposed a simple band-mass model, using Finite Element Analysis (FEA). Comparing the numerical results for axial, tangential, and radial directions to experimental results their investigation showed significant peak responses in the radial direction. Knowing this, they presented a simpler analytical method based on an axisymmetric shell, only predicting these radial effects. Dowen *et al.* (2001) have published work describing the design, performance, and initial test results for a low-shock clamp band release system, in which they have undertaken static and dynamic tension tests. In the static tests, they applied 21.36 kN in the three orthogonal axes (including the axial direction), using strain gauges to detect permanent deflections in the joint, and to determine the clamp band-adaptor stiffness. More recently Iwasa and Shi (2008) have presented a simplified method to estimate the shock response spectrum envelope during separation of a space satellite system from a launcher in space. As with most pyrotechnic devices, V-band clamp separation systems generate high magnitude and high frequency shock accelerations which may damage equipment. Based on their work, Iwasa and Shi (2010) have predicted a limit value of the separation shock load. At the same time Qin *et al*. (2010a) presented a dynamic model predicting the forced response of a band clamp joint under axial excitation, which was validated by experimental tests. Based on this, Qin *et al*. (2010b) went on to investigate the dynamic responses of LV/SC system to the vibration and impact excitations, taking into account the effect of the band clamp joint.

2.2 Nonlinearity in Finite Element Analysis

In this section a brief introduction on the sources of nonlinearities that can occur in solid mechanics finite element analyses, along with a more detailed description on nonlinear contact problems is given.

2.2.1 Sources of Nonlinearity

According to Fagan (1992), Konter (2000), Cook *et al*. (2002), and Dassault Systems (2007b) there are three types of nonlinearity in solid mechanics:

- *Material nonlinearity* which occurs when plasticity or creep is present.
- *Contact (boundary) nonlinearity* which arises where an initial gap between two or more surfaces or parts may open or close, and/or where sliding contact or friction in the contact may take place and
- *Geometric nonlinearity* which appears where large displacement, snap through, initial stresses or load stiffening take place.

2.2.2 Introduction to Contact Analysis

The characteristics of linear problems are the displacements being proportional to the load and the stiffness of the structure being independent of the structure of the load level value. However, this statement is not valid for contact problems, as the stiffness of an assembly of at least two separate bodies is entirely different. If contact between two bodies is established, the total stiffness depends on the individual stiffness of the parts and the degree of contact between them. In addition, other sources of non-linearity in contact analysis can be friction as well as large displacement before or during the contact. (Konter 2000)

An ***incremental solution procedure,*** in combination with iterations is used to solve non-linear problems, as discussed by Konter (2000). This procedure subdivides the total loading into a number of load increments Δf_{ex} and then determines the incremental displacement solution Δu for each increment. A specific load increment can be represented by:

$$K^* \times \Delta u = \lambda_n \times f_{ex} - \lambda_{n-1} \times f_{ex} \tag{2.15}$$

Where K^* describes the current stiffness matrix of the structure, f_{ex} the external nodal force vector, λ describes the total load and the total loading is applied in N increments. λ_n, specifies a load level at increment n, $n = 1, N$.

As Konter (2000) observes that, when undertaking a contact analysis, it is highly possible that non-linearity can occur within an increment, which necessitates an iterative procedure to find the incremental solution. This is important especially when new contact or local tensile forces on the contact surface appear half-way through an increment. A converged solution for each increment is reached if no changes occur in the assumed and obtained contact status and the residual forces are small compared to the maximum reaction force. Relative changes in incremental displacement or changes in internal energy can be other measures for deciding convergence. During the iterative process the applied load increment is normally held constant, but in some cases can change. All these sources of non-linearity lead to an increase in computer time, as the matrix needs to be solved for each increment and often also for each iteration.

2.2.3 Contact Problem Definition

Before carrying out a contact analysis, several aspects of the contact such as the direction of the nodal displacement have to be defined. The nodal displacement is then used to describe body deformation, and the contact interaction consists of a normal and tangential component, as discussed by Konter (2000).

Konter (2000) then moves on, that in general contact problems it is necessary that there is a specific distance $u_{closure}$, which must be larger than the nodal displacement $u_A$of node A in the normal direction n_d of the body to be contacted. This can be expressed as

$$u_A \circ n_d - u_{closure} \leq 0 \tag{2.16}$$

Contact can be established between two nodes or a node and a segment, where the segment can either be part of a deformable or rigid body. The contact distance d_c can be written as

$$d_c = (x_I - x_A) \circ n \leq 0 \quad \text{for no contact, and} \tag{2.17a}$$

$$d_c > 0 \quad \text{for contact} \tag{2.17b}$$

in which x_I represents the deformed position vector, and x_A the position vector of node A. (Konter 2000)

Where nodes or segments are displaced along the surface of another contacting body, caused by deformation, large displacements of bodies, or rigid body motion, contact must be described not only in the normal but also tangential direction. If no friction exists, the nodes are not restricted by any constraints and can freely slide over the surface. Tangential frictionless contact problems are therefore fairly easy to analyse. If, during contact, one body slides over the other, a simple node to node contact (discussed in next sub-section) can not be applied. The procedure of detecting which nodes interact with specific segments is extensive, and the location of where contact appears is not known initially. Therefore, contacts in which sliding occurs need an algorithm for the normal part and a contact detection mechanism, as stated by Konter (2000)

For tangential contact problems, friction is another even more complex parameter, especially since the mechanisms involved in friction are not yet fully understood. The most common models describing friction in contact interactions are the Coulomb friction, shear friction or a combination of both. As discussed by Wriggers (2006), the first model differentiates between a stick and sliding state, where stick refers to no tangential movement, and in sliding the contacting bodies move by a relative tangential displacement u_t. Moreover, the author points out that stick occurs where the force F_t acting in the tangential direction is smaller than the frictional force F_f, and slip occurs where it is larger. Considering that F_t can either be positive or negative, the load-displacement relationship for frictional contact can be presented as in Figure 2-2.

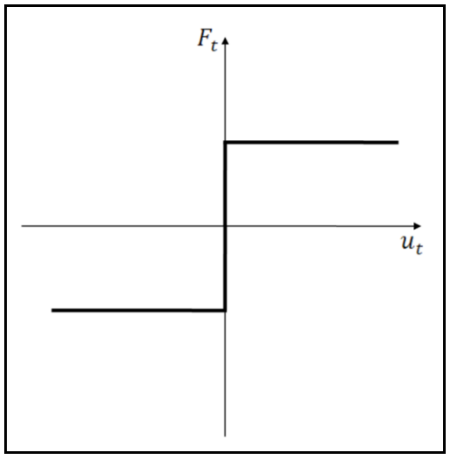

Figure 2-2: Load-displacement diagram for frictional contact, taken from Wriggers (2006)

A shear friction model can be useful where high contact pressures are present and therefore stresses resulting from maximum tangential forces can be larger than the maximum shear stress of the material $\tau_{max} = {}^{\sigma_Y}/_{\sqrt{3}}$, such as in metal forming, in which σ_Y is the yield stress. In cases where no relative tangential movement between two contacting bodies exists and the deformable body can be moved by a rigid body, the contact algorithm can be used to apply necessary boundary conditions.

2.2.4 Elements used in Contact

Also worth mentioning is the importance of selecting the right type of elements when modelling contact bodies. Quadratic elements are usually the best choice for stress analysis as they give very accurate solutions, especially when analysing curved boundaries, such as holes. This is valid for most linear elastic and even for some non-linear analyses. However, when boundary non-linearity in the form of contact is present this general statement is not valid anymore. For this case, linear 4-noded planar elements for 2 dimensional analyses, and linear 8-noded brick elements for 3 dimensional analyses are typically the best choice. The problem associated with quadratic elements when using them in contact analysis is the non-uniform distribution of reaction forces on their nodes. The mid-side nodes generally transfer larger forces than the corner nodes, which has been discussed by Konter (2000), Becker (2004) as well as by Dassault-Systems (2007b).

While all three agree that linear elements distribute reaction forces equally, so that this problem can easily be overcome, Dassault-Systems (2007b) and Dassault-Systems (2007a) present a more detailed and broader view. The authors suggest using reduced integration for linear elements, so that in each direction one integration point is used

rather than two. This is particularly useful where significant bending in the model is expected as fully integrated linear elements suffer from shear locking.

2.2.5 Contact Analysis Interactions

Unlike most general finite element analyses, contact analyses are not specifically describable by finite element equations; therefore it is necessary to specify certain contact procedures to treat the constraints.

As contact can be established between at least two deformable bodies or deformable and rigid bodies, several methods for handling contact are required, which are widely discussed in the literature. Good discussions of these models can be found in the work of Konter (2000) and Zienkiewicz and Taylor (2005). ***Node to Node Contact*** is applicable where only small sliding is present, as both bodies should have a similar mesh and each node on a contact surfaces should always have a direct opposing node on the other contact surface. Also the contact area method requires a node on each side of a potential contact zone. ***Node to Segment Contact*** is a much more widely applied method, because opposing surfaces do not need to have the same number of elements at exactly the same position. However, convergence problems can occur next to corners, as it is not always clear which normal should be used for the contact direction. ***Segment to Segment Contact*** is the probably the most stable method and can be used especially where large sliding is predominant.

In order to avoid the *impenetrability condition,* which means preventing nodes from penetrating the opposing contact surface, it is necessary to enforce *kinematic constraints* (Zienkiewicz and Taylor 2005). The two most commonly used enforcement methods are the ***Lagrange multiplier*** and ***penalty function***, as discussed in the work of several authors such as Hinton and Hellen (1992), Belytschko *et al*. (2000), Konter (2000), Cook *et al*. (2002), Laursen (2002) and Zienkiewicz and Taylor (2005).

However, possibly the most demonstrative description of these two methods is given by Wriggers (2006). Assuming a simple spring-mass system under gravitational load with the mass m, acceleration due to gravity g, displacement u, and the spring stiffness k, a term containing the constraint due to a rigid support $c(u)$, is added to the potential energy, $\Pi(u,\Lambda)$, of the system by the ***Lagrange multiplier method***. This can be written as

$$\Pi(u,\Lambda) = \frac{1}{2}k\,u^2 - m\,g\,u + \Lambda\,c(u) \tag{2.18}$$

with Λ being the *Lagrange multiplier* and the equivalent to the reaction force normal to the contacting surface.

In a tangential frictional contact, the Lagrange multiplier Λ becomes equal to the frictional force F_f , with μ being the coefficient of friction. This frictional force acts between the moving masses that they slide past each other. The frictional force F_{fl} can be written as

$$|F_f| = \mu\, m\, g \tag{2.19}$$

The ***Penalty method*** on the other hand assumes that an additional penalty spring with the stiffness k_p is added to the spring-mass energy system, yielding as

$$\Pi(u) = \tfrac{1}{2}ku^2 - mgu + \tfrac{1}{2}k_p[c(u)]^2 \qquad \text{with } k_p > 0 \tag{2.20}$$

In tangential frictional contact, a spring is added at the interface between the moving masses sliding over the rigid surfaces and the rigid surface itself, with the penalty spring representing the frictional force F_f, and the displacement in the tangential direction u_t. The frictional force can then be given as

$$F_f = k_p\, u_t \tag{2.21}$$

The disadvantage of the Lagrange multiplier technique is discussed by Konter (2000), in which the author refers to it as being more accurate than the Penalty method, but also increasing the number of degrees of freedom, as the Lagrange multiplier Λ is treated as an additional variable. Wriggers (2006) moves on pointing out the ability of the Penalty method to be more robust and to lead to a converged solution more easily, as the energy system is made up of the single displacement variable.

Apart from all these factors, also a possible time dependency of the results should be taken into account, which introduces the discussion of the ***Implicit*** and ***Explicit solver method***. Again a variety of authors such as Hinton and Hellen (1992), Laursen (2002), Konter (2000) and Wriggers (2006) have discussed differences between both methods and their field of application in contact analyses. From their work it can be claimed in general, that Implicit methods are preferably used where the analysis is static or quasi-static, and hence not time dependent. The Explicit Solver method is also able to analyse quasi-static problems but is mainly used in dynamic contact analyses such as high velocity impact. As specifically identified by Wriggers (2006), implicit time integration methods must be combined with an iterative algorithm such as Newton-Raphson or Quasi-Newton, in order to solve non-linear equations at each time step, which makes them quite expensive. In contrast, Explicit Solvers use a much easier time integration, where the solution at time point t_{n+1} is only dependent on known variables at t_n, and no iterative procedure is needed. Therefore, the latter method is much more stable and more efficient, especially when a lumped mass matrix is used to approximate the mass

matrix. Konter (2006) explains the efficiency of the Explicit Solver method as small time steps being used, enabling a simple contact algorithm to be applied. On the other hand, both Wriggers (2006) and Wriggers (2008) acknowledge that the use of Implicit Solvers can be advantageous, because they can be constructed so that they become more stable, and the time step size is then unlimited. In contrast, explicit methods will always suffer from a limitation in the time step size in order for the solution to remain stable.

Concluding it can be said, that contact analysis in general is highly non-linear and not straight forward, requiring a certain amount of experience from the operator.

2.3 Cold Roll Forming and Subsequent Yielding

V-band retainers are manufactured using a cold roll forming process. Therefore, in this section the working principle of "cold roll forming" and what happens to the material as it undergoes such a process is explored.

2.3.1 An Introduction to Cold Roll Forming

As stated in Schuler (1998) who cites DIN 8582, forming is a manufacturing process which uses a three dimensional, plastic modification of a shape while retaining material cohesion and mass of the manufactured product. It is a modification of a shape with a controlled geometry and can be categorised as a chip-less or non-material removal process. The classification of processes used in forming is shown in Figure 2-3.

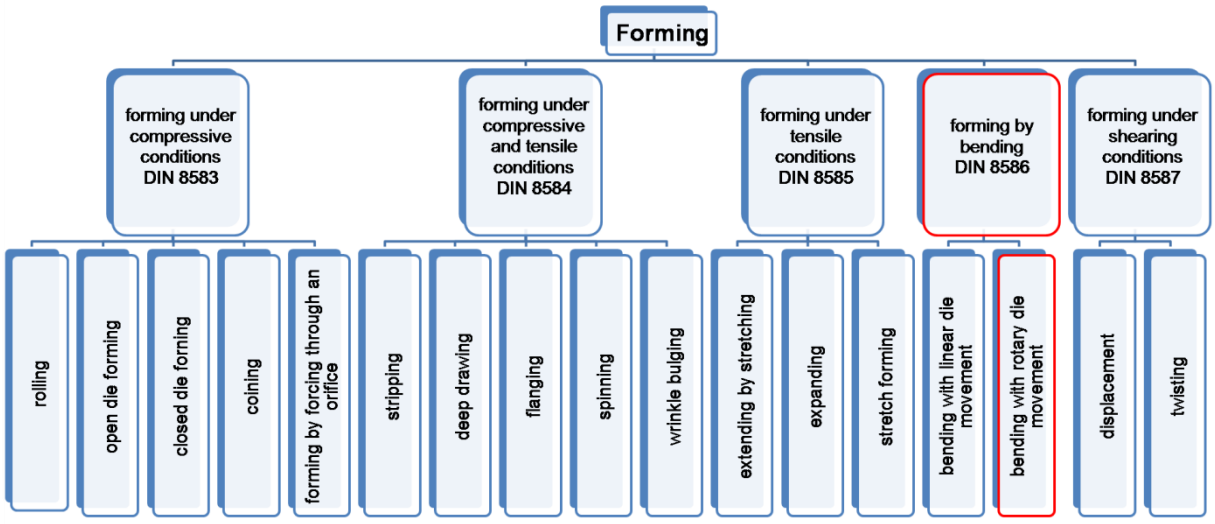

Figure 2-3: Classification of production processes used in forming in accordance with DIN 8582, taken from Schuler (1998)

Dixit and Dixit (2008) also point out that metal forming changes the shape of a product permanently by plastic deformation, the mass and the volume remain unchanged, and the advantages are no wastage of the raw material, better mechanical properties of the

product and a much faster production rate. Using Schuler's (1998) terminology, the forming process discussed and analysed throughout this thesis is categorised as "bending with rotary die movement" as highlighted in Figure 2-3.

A more widely known expression of this process used by most authors such as Bui and Ponthot (2008), Farzin *et al.* (2002) and Zeng *et al*. (2009) is "roll forming". As the manufactured product undergoes no heat treatment the process can be called "cold roll forming", which is the preferred expression continuously used throughout this thesis. Another categorisation of forming can be found in Black and Kohser (2008) and Dixit and Dixit (2008) who divide metal forming into two fields, bulk forming processes and sheet forming processes. Black and Kohser (2008) and Marciniak (2002) place roll forming in the sheet forming field. A more specific definition of cold roll forming is given in Bui and Ponthot (2008), Farzin *et al.* (2002), Zeng *et al*. (2009) and Tehrani *et al.* (2006), stating that it is a widely used industrial process to progressively deform a long sheet metal strip with a constant section into a desired profile. The process includes a continuous bending operation and is carried out using several roll stations in which the sheet metal strip is plastically deformed.

2.3.2 One Dimensional Description of Plasticity Problems

As discussed by Dixit and Dixit (2008), cold roll forming is based on plastic deformation caused by external forces. Hence, typically only ductile metals able to withstand large plastic deformations are used as work-pieces. In many cases only some of the material is plastically deformed. Since most metals have completely different material behaviours in loading and unloading within the plastic region, plastic deformation will generate residual stresses in the structure.

All together six different criteria are needed to analyse plastic deformation (Dixit and Dixit 2008):

- measures of plastic deformation
- plastic stress-strain relations
- yield criterion
- criterion for subsequent yielding (hardening)
- unloading criterion
- objective stress rate and objective incremental stress measures

As presented by Skrzypek (2000) Chapter 3, the measures of plastic deformation can be explained by considering a rod with a uniform cross-section subjected to an axial tensile load, as being the most common test in plasticity.

A_0 is the initial area of the cross section, l_0 the initial length and Δl the change in length. The engineering (nominal) stress σ_{eng} and engineering strain ε_{eng} are given by Dixit and Dixit (2008) as:

$$\sigma_{eng} = \frac{F_x}{A_0} \tag{2.22}$$

$$\varepsilon_{eng} = \frac{\Delta l}{l_0} \tag{2.23}$$

At a certain deformation the force F_x and engineering stress σ_{eng} start to decrease, because equation 2.22 does not take into account the decrease of cross-sectional area, as the rod deforms axially. The true stress on the other hand still increases.

The measure of deformation able to correctly represent large deformations is the logarithmic (also called true or natural) strain. In the one dimensional case the logarithmic strain, indicated by ε_{true}, is given by Dixit and Dixit (2008) as:

$$\varepsilon_{true} = \ln\frac{l}{l_0} \tag{2.24}$$

in which l is the current length, shown in equation 2.25

$$l = l_o + \Delta l \tag{2.25}$$

Using equations 2.23, 2.24 and 2.25, the relationship between ε_{true} and ε_{eng} as stated by Dixit and Dixit (2008), Skrzypek (2000), Johnson and Mellor (1983) and Dassault Systems (2007d) can be established:

$$\varepsilon_{true} = \ln(1 + \varepsilon_{eng}) \tag{2.26}$$

For small deformations (ε_{eng} < 0.05) ε_{true} is approximately equal to ε_{eng}.

The benefit of using logarithmic over engineering strain for large strain values is described by Durelli *et al*. (1958). In their work they assume a rubber thread of length l_o being stretched to twice its initial length. Using equation 2.16 the resulting engineering strain value would be

$$\varepsilon_{eng} = \frac{\Delta l}{l_0} = \frac{2l_0 - l_0}{l_0} = 1 \tag{2.27}$$

whereas equation 2.17 for the true strain value would give

$$\varepsilon_{true} = \ln\frac{l}{l_0} = \ln\frac{2l_0}{l_0} = \ln 2 = 0.693. \tag{2.28}$$

Taking the example of Durelli *et al*. (1958) for compression rather than tension, and assuming a constant volume of the test sample during deformation, the same values for engineering and logarithmic strain values as above should be gathered, but with negative magnitudes. As can be seen below, this is only the case for true but not engineering values.

$$\varepsilon_{eng} = \frac{\Delta l}{l_0} = \frac{\frac{1}{2}l_0 - l_0}{l_0} = -\frac{1}{2} \tag{2.29}$$

$$\varepsilon_{true} = \ln\frac{l}{l_0} = \ln\frac{\frac{1}{2}l_0}{l_0} = \ln\frac{1}{2} = -0.693 \tag{2.30}$$

According to Dixit and Dixit (2008) and Dassault-Systems (2007d), the true stress σ_{true} can be given as:

$$\sigma_{true} = \frac{F_x}{A}, \tag{2.31}$$

in which A is the current cross section. Taking into account that the volume remains constant during a plastic deformation, the relationship between A_0 and A can be described as

$$A = \frac{l_0}{l} A_0. \tag{2.32}$$

Substituting equations 2.21, 2.15 and 2.19 into 2.20, σ_{true} and σ_{eng} are related by the equation:

$$\sigma_{true} = (1 + \varepsilon_{eng})\sigma_{eng}\,. \tag{2.33}$$

With the equations above it is now possible to describe a true stress strain curve as shown in Figure 2-4. From this point on stress σ and strain ε, will be taken as true stress σ_{true} and logarithmic strain ε_{true}, and are also used throughout this project to describe the material properties in the finite element analysis models and to interpret results taken from experimental testing.

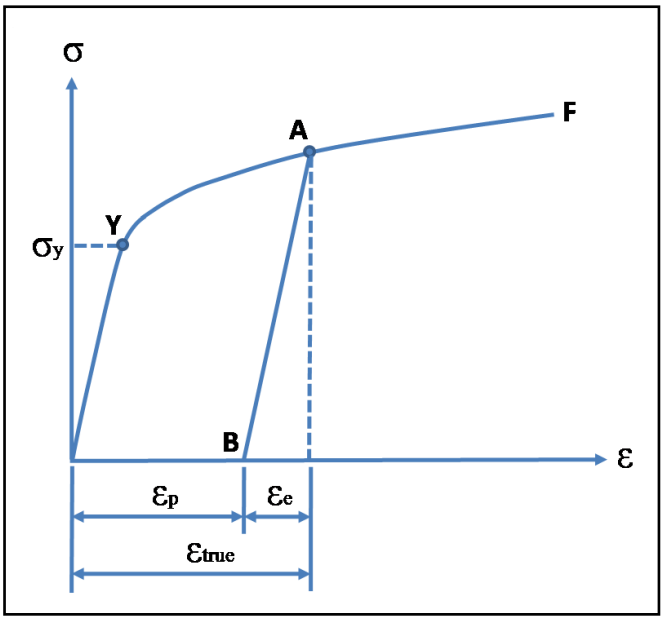

Figure 2-4: True stress-strain curve with logarithmic strain in tension test (Dixit and Dixit 2008)

In Figure 2-4 point Y at the end of the straight line describes the yielding point, which is the change from elastic to plastic material behaviour. If the work piece is stressed up to

a level below point Y, it will be deformed only elastically, meaning that the original shape is reached after unloading. Therefore, σ_Y is defined as the yield stress, and it is observed that it increases with the strain rate and decreases with temperature. In the one-dimensional state of stress *initial yielding* occurs, once condition (Dixit and Dixit 2008)

$$\sigma - \sigma_Y = 0 \tag{2.34}$$

is fully satisfied. The generalisation of this criterion for the three-dimensional state of stress is discussed in further detail in sub-section 2.3.3.

In Figure 2-4 the curved part above point Y is called the plastic region. If the work piece is continually loaded beyond Y up to point F then the stress-strain curve will follow the path YF and will lead to fracture at point F. YF is called the loading path. If the work piece is unloaded at point A to a zero stress level, the stress-strain curve will follow the path AB leaving a permanent strain $\varepsilon_{p,}$ also called the plastic part of the true strain ε_{true}, wherein ε_e represents the elastic part. If the work piece is loaded again at point B, the material first behaves elastically and follows the straight line from B to A. After yielding starts at point A the stress-strain curve follows the path from A towards F. From this behaviour it can be seen that the yielding stress σ_Y increases to a higher level as plastic deformation takes place, which is called *subsequent* or *continued yielding*. In the literature a few simplifications of the plastic stress-strain relation can be found. They are based on approximating or idealizing the real stress-strain behaviour and can be summarised in the following most commonly used combinations:(Dixit and Dixit 2008)

- Rigid perfectly plastic material
- Rigid-plastic material with linear hardening
- Elastic perfectly plastic material
- Elastic-plastic material with linear hardening

These schematizations of the stress-strain behaviour can also be found in the diagrams, shown in Figure 2-5.

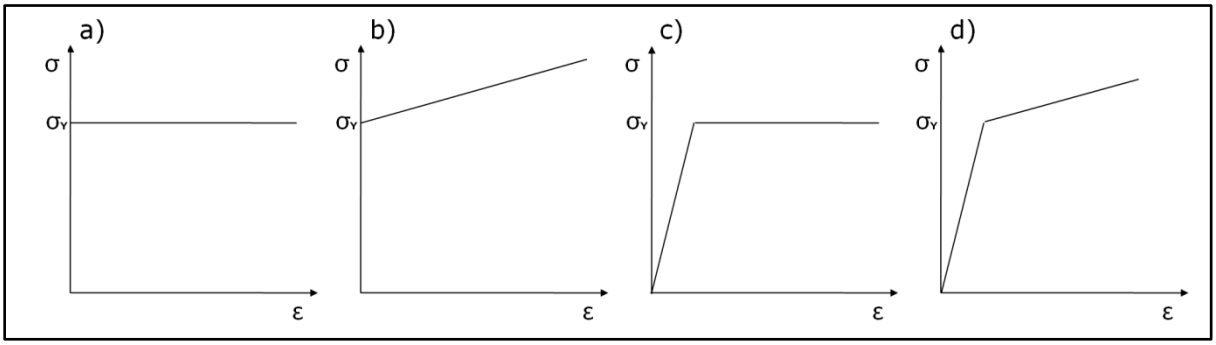

Figure 2-5: Linear schematisation of stress-strain diagrams: a) Rigid perfectly plastic, b) Rigid plastic with linear hardening, c) Elastic perfectly plastic, d) Elastic-plastic with linear hardening (Skrzypek 2000)

The term *rigid-plastic* refers to the fact that the elastic strain is very small compared to the plastic one and hence can be neglected. If the elastic behaviour is taken into account in the model, then it will be referred to as *elastic-plastic*. The next simplification is to assume a straight line between Y and F, which defines the material as being *linearly hardening*. Assuming a constant stress value of σ_Y between Y and F makes the material *ideal or perfectly plastic*. (Dixit and Dixit 2008)

The plastic part of the curve between points Y and F in Figure 2-4 can also be described by the equation:

$$\sigma - h^*(\varepsilon_p) = 0, \tag{2.35}$$

in which h^* is the hardening function. This equation represents *subsequent* or *continued yielding* for the one-dimensional state of stress. (Dixit and Dixit 2008) The generalisation of this term to the three-dimensional case is discussed in further detail in sub-section 2.3.4.

The experimental stress-strain curve can be represented by several forms of h. The most common ones are listed below (Dixit and Dixit 2008):

1. Ludwik: $\sigma = \sigma_Y + K_h(\varepsilon_p)^{n_h}$ (2.36)

2. Swift: $\sigma = \sigma_Y + (\sigma_Y \varepsilon_p)^{n_h}$ (2.37)

3. Voce: $\sigma = \sigma_Y + K_h(1 - \varepsilon_{eng}{}^{-(n_h \varepsilon_p)})$ (2.38)

In all the expressions above, K represents the hardening multiplier and n the hardening plastic strain index, in which both are also known as the *hardening parameters*, and can be gained by fitting the equations shown above with experimental curves of the true stress vs. the plastic part of logarithmic strain. For Ludwik's and Swift's expressions, linear hardening can easily be represented by setting n_h to 1. (Dixit and Dixit 2008)

2.3.3 Criteria for Initial Yielding of Isotropic Materials

The *Yield Condition* or *Yield Criterion* is a law that defines the limit of the elastic behaviour. For the one-dimensional state of stress initial yielding is given by equation 2.23, where only one stress component is non-zero. In a three dimensional state of stress normally all stress components are non-zero.(Dixit and Dixit 2008)

Amongst several others, the two most commonly used yield criteria, are the *Distortion Energy Criterion* (also known as the von-Mises Criterion), and the *Maximum Shear Stress Criterion* (also called Tresca Criterion) and are discussed in further detail in this sub-section. The following information has mainly been taken from Polakowski and Ripling (1966), Wempner (1995), and Dixit and Dixit (2008), unless indicated differently.

Distortion Energy Criterion (Mises)

This criterion assumes plastic deformation to arise once the elastic distortion energy W_S is equal to the elastic distortion or shear strain energy W_{SY}, stored in the material when it is uniaxially loaded up to its yield point. W_S is gathered from the difference between the elastic strain energy W_0 and the strain energy of volume change W_D, and can be written as:

$$W_S = W_0 - W_D = \frac{1+\nu}{6E}[(\sigma_1 - \sigma_2)^2 + (\sigma_2 - \sigma_3)^2 + (\sigma_3 - \sigma_1)^2] \quad (2.39)$$

In the three dimensional state of stress, assuming a simple tensile test, setting $\sigma_1 = \sigma_Y$, $\sigma_2 = 0$, and $\sigma_3 = 0$, W_{SY} can be written as:

$$W_{SY} = \frac{1+\nu}{3E}\sigma_Y^2 \quad (2.40)$$

Setting W_S equal to W_{SY}, to indicate when plastic deformation begins, it can be said that

$$(\sigma_1 - \sigma_2)^2 + (\sigma_2 - \sigma_3)^2 + (\sigma_3 - \sigma_1)^2 = 2\sigma_Y^2 \quad (2.41)$$

According to Roylance (1996), by rearranging equation 2.41, the general expression of the *von-Mises stress* σ_M (also known as *equivalent* or *effective stress*) can be defined as

$$\sigma_M = \sqrt{\frac{1}{2}(\sigma_1 - \sigma_2)^2 + (\sigma_2 - \sigma_3)^2 + (\sigma_3 - \sigma_1)^2} \quad (2.42)$$

This is the criterion that all work in this thesis will be based on.

Maximum Shear Stress Criterion (Tresca)

In this criterion, plastic deformation is defined to begin once the shear stress on any plane reaches the value that it has when it starts to yield in simple tension or compression.

Considering that the yield stress σ_Y in tension and compression has the same magnitude with inversed signs, the corresponding shear stress, τ_Y, at a point is the difference between the maximum and minimum principal stresses. The Tresca criterion can then be expressed by equations 2.43:

$$\frac{1}{2}(\sigma_1 - \sigma_3) = \pm\tau_Y \quad (2.43a,b)$$

$$\frac{1}{2}(\sigma_1 - \sigma_2) = \pm\tau_Y \quad (2.43c,d)$$

$$\frac{1}{2}(\sigma_2 - \sigma_3) = \pm\tau_Y \quad (2.43e,f)$$

As for the von-Mises criteria, setting $\sigma_1 = \sigma_Y$, $\sigma_2 = 0$, and $\sigma_3 = 0$, the yield stress in shear is given as:

$$\tau_Y = {}^{\sigma_Y}/_{2} \tag{2.44}$$

Comparison and Graphical Representation of Mises and Tresca Criteria

Comparing the Mises to the Tresca criteria, the latter comprises some difficulties, as the general expression requires six equations. These six equations in 2.43 describe six planes, parallel to the line $\sigma_1 = \sigma_2 = \sigma_3$, forming a hexagonal prism. Only when the relative magnitudes of the principal stresses are known, this theory becomes more practical and more convenient to use, because only one out of six equations is needed. This also means that only one plane of the yield surface is required.

The Mises criterion on the other hand avoids this problem, as it can be described by one single equation 2.31. Following from this, the hexagonal prism is replaced by a cylindrical surface, also along the axis $\sigma_1 = \sigma_2 = \sigma_3$, where all the stresses are equal. Thus, as the state of stress at this line is hydrostatic, it is called the *hydrostatic line*. This line is perpendicular to the *deviatoric plane*, in which $\sigma_1 + \sigma_2 + \sigma_3 = 0$.

The Tresca hexagonal prism only intersects the Mises cylinder at its six edges, whereas anywhere else the hexagonal prism lies inside the cylinder. If a point defining the material stress state reaches one of these six edges, yielding will occur according to both the Tresca and the Mises criteria. Anywhere else in between the six edges, the point would reach the hexagonal prism first, and yield according to the Tresca criterion.

As shown in Figure 2-6, the geometrical representation of both criteria is reduced to curves, once the part of the stress in the hydrostatic direction reduces to zero. The curves represent the yield surfaces intersecting with the deviatoric plane, and are therefore called *yield loci on the deviatoric plane*. In there, the Mises yield surface is described by a circle with the radius $(\sqrt{2/3})\sigma_Y$, and the Tresca criteria by a regular hexagon. The greatest radial separation is about 15% of the Mises circle. As a result, the Mises criterion predicts a higher yielding stress than the Tresca.

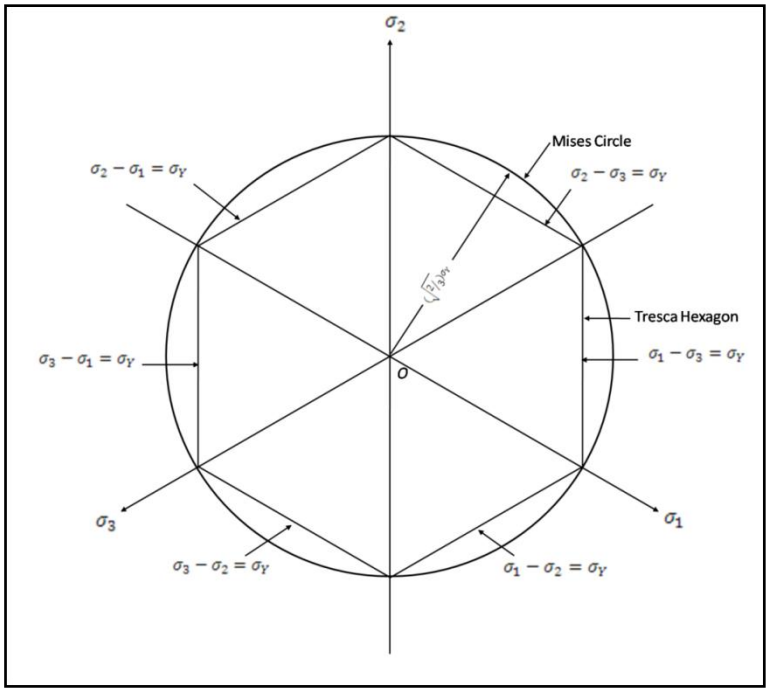

Figure 2-6: Loci of the Mises and Tresca yield surfaces on the deviatoric plane. The axes $(\sigma_1, \sigma_2, \sigma_3)$ are not in the deviatoric plane (Dixit and Dixit 2008)

Another important fact pointed out by Shanley (1957) is that any combined loading condition which reduces the intensity of the shear stresses, also reduces internal slippage and hence leads to brittle behaviour.

2.3.4 Hardening Laws for Multi-Dimensional Case

Figure 2-4 represents the experimental results for a one-dimensional axial tensile test, taking into account subsequent yielding. The variation of yield stress with the level of plastic deformation can be described by equation 2.24, with an appropriate hardening function, h^*.

As Bicanic (1992) states, before an elastic-plastic analysis can be performed, it is important to define the initial yield surface mathematically and describe how it changes as a result of plastic strain or dissipated energy. In a similar way to equation 2.35 for uni-axial plasticity, the initial yield surface can be expressed here as:

$$F(\sigma_{ij}) - \sigma_Y = 0 \qquad (2.45)$$

In which F being the function of the stress components of the symmetric stress tensor σ_{ij}.

A *surface evolution law* or *hardening law* is then used to describe the change of the initial yield surface and can be split in three main areas, depending on the nature of change. According to Bicanic (1992) and Skrzypek (2000) they are:

- Isotropic hardening (initial yield surface expands or shrinks),

  - Strain hardening
  - Work hardening
- Kinematic hardening (initial yield surface moves in principal stress space or remains fixed), or
- Mixed hardening (initial yield surface changes shape in an affine or in a non-uniform manner).

Isotropic hardening implies that the subsequent yield surface can be obtained by the initial yield surface expanding (or shrinking) in a uniform matter, in which the increase (or decrease) of dimensions can be described by a common hardening parameter. Using the Odqvist hardening parameter $I_{\varepsilon p}$, representing a unique dependency of effective stress σ_M (2.42) to the effective plastic strain path, the hardening law can be specified as the *isotropic strain hardening* where for a simple process (Skrzypek 2000):

$$I_{\varepsilon p} = \sqrt{\frac{3}{2}}. \tag{2.46}$$

In which ε_{ij}^p are the components of the plastic strain tensor, leading to the relationship:

$$\sigma_M = f(I_{\varepsilon p}) \tag{2.47}$$

In which $f(I_{\varepsilon p})$ is the function of the hardening parameter.

Isotropic work hardening assumes a unique dependency of the effective stress σ_M and the accumulated plastic work W^p (Skrzypek 2000), where:

$$W^p = \int_0^{\varepsilon^p} \sigma_{ij}\, d\varepsilon_{ij}^p. \tag{2.48}$$

Writing these two hardening rules in a more general form of the isotropic evolution law, which assumes that the subsequent yield surfaces can be described using an arbitrary isotropic hardening parameter K^i as presented by Skrzypek (2000):

$$F\left(\sigma_{ij}\right) - K^i(\varepsilon_{ij}^p) = 0. \tag{2.49}$$

As kinematic hardening describes the translation of the initial yield surface into a new position, without the change of shape or size, it is very important in modelling cyclic behaviour, as described by Bicanic (1992). For this case a translational tensor α_{ij}, describing the position of the centre of the subsequent yield surface is introduced (Skrzypek 2000). This is important as the well known Bauschinger effect requires a hardening law as following

$$F\left(\sigma_{ij} - \alpha_{ij}\right) = 0. \tag{2.50}$$

The general *mixed hardening* law is described by combining isotropic and kinematic hardening, (Skrzypek 2000)., and includes both an expansion and translation of the initial yield surface, as a result of plastic flow (Bicanic 1992).

2.3.5 Hardening of Austenitic Stainless Steels

In the case of austenitic stainless steel as used for the V-band retainers, Budinski and Budinski (2010) describe the hardening process as a result of strain induced martensite generation. Austenitic stainless steels are metastable, but at normal-use-temperatures the structure remains austenitic. These steels have a very strong tendency to work harden or cold work, with the energy of deformation promoting the transformation of metastable austenite to martensite.

This phenomenon has been observed and confirmed in the literature by many authors, as for example Milad *et al.* (2008) and Kain *et al*. (2004).

In their work Milad *et al*. (2008) have analysed the influence of a variety of plastic deformation degrees introduced by cold rolling on the tensile properties of AISI 304 stainless steel. As they found out, the tensile strength, yield strength, and hardness increase as the cold rolling percentage (%CR) increases. Moreover, they have shown that in austenitic stainless steels, the formation of strain induced martensite causes the material to harden.

Kain *et al*. (2004) have investigated how cold work influences the low-temperature sensitization (LTS) of AISI 304 austenitic stainless steel. Sensitization in this case is the process whereby chromium carbides form at grain boundaries with adjacent depletion of chromium and is the main reason for inter-granular corrosion (IGC) and inter-granular stress corrosion cracking (IGSCC). Sensitization normally happens at a temperature range of 550-800°C but LTS occurs at temperatures below 500°C. They have shown that after 15% cold work AISI 304 starts to develop martensite, which, in agreement with Milad et al. (2008) in stainless steels increases the hardness. They found that this martensite became heavily sensitized at 500°C. This is an important consideration in applications where the metal reaches this temperature.

2.3.6 Plastic Bending

In order to better understand the roll forming process used to manufacture V-bands, it is useful to consider the example of plastic bending of a beam. The following sub-section has mainly been taken from the work of Polakowski and Ripling (1966) p. 368-370.

Due to the nature of plasticity once the stress on the outer side of a beam reaches the yield stress the stress is no longer proportional to the strain. Small load increments will result in the plastic deformation rapidly propagating towards the neutral surface. On the

convex and concave surfaces, plastic tension T and compression C will result in a permanently deformed beam. The fibre stress, σ_{xb}, as shown in Figure 2-7, can be determined from the stress-strain curve, shown in Figure 6.

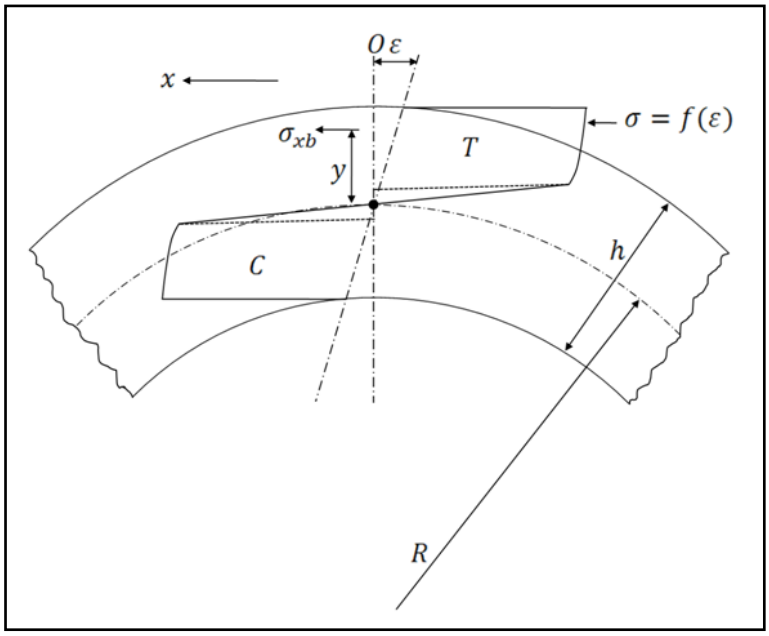

Figure 2-7: Stress-strain distribution across the cross-section of a bent beam, taken from Polakowski and Ripling (1966)

As long as the beam has a symmetrical cross-section, and the curvature is not excessive, the neutral surface will remain at the centre of the beam. The equilibrium can be written as the bending moment M with b as the breadth:

$$M = b \int_{-h/2}^{+h/2} \sigma_{xb}\, y\, dy \tag{2.51}$$

The distance of the fibre from the neutral surface, y, can be related to the radius of curvature R using:

$$y = \varepsilon\, R \tag{2.52}$$

Substituting this into equation 2.51:

$$M = bR^2 \int_{-h/(2R)}^{+h/(2R)} \sigma_{xb}\, \varepsilon\, d\varepsilon. \tag{2.53}$$

If the stress-strain characteristics are known, using equation 2.53, it is now possible to calculate the bending moment M.

2.3.7 Residual Stresses due to Plastic Deformation

The following sub-section has mainly been taken from the work of Polakowski and Ripling (1966) p. 368-370, Timoshenko and Gere (1973) p. 358-360, and Shanley (1975) p. 305-307.

After bending a beam beyond its elastic limit and following unloading, the beam does not return to its original shape, as discussed in the previous sub-section. The plastic strain induced creates a permanent set, as the plastic fibres in the beam prevent the elastic fibres from recovering their configuration. The stresses that remain in the beam after unloading are therefore called *residual stresses*. In order to calculate residual stresses it is only necessary to find the elastic stress distribution that is gathered from exactly the same bending moment as its plastic counterpart, and subtract it from it. For example, consider an in-elastically bent beam with rigid perfectly plastic material behaviour and a yield stress σ_Y. Figure 2-8a shows the plastic stress distribution during bending.

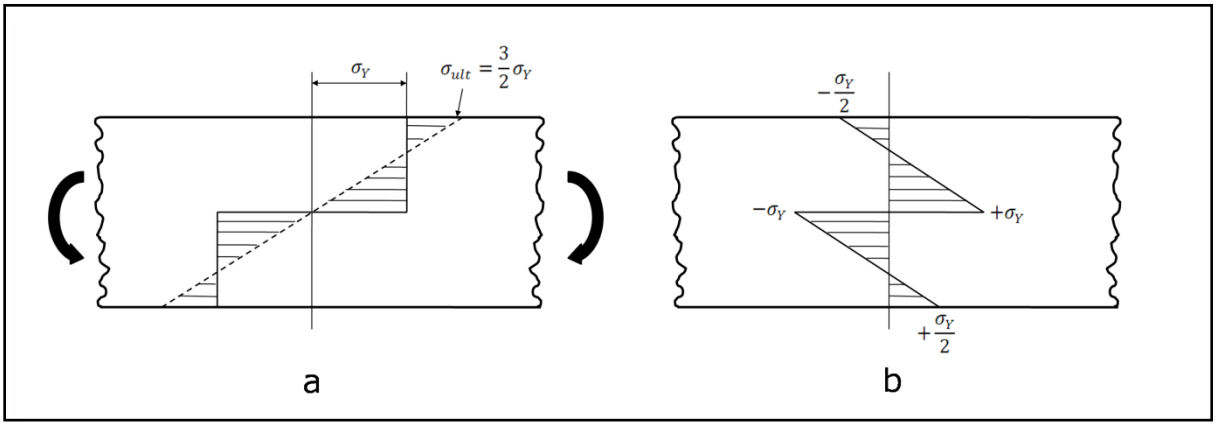

Figure 2-8: Residual stresses in a rectangular member, with ideal plasticity assumed, taken from Shanley (1975)

The ultimate stress that needs to be subtracted on the outer fibre of a beam with rectangular cross section can be found from equation 2.55

$$\sigma_{ult} = \frac{4M_{ult}}{bh^2} \tag{2.54}$$

and in this case discussed gives $^3/_2\ \sigma_Y$, as shown in Figure 12a. Resulting from this after unloading, the residual stress at the outer fibre equals half of the yielding stress, as presented in Figure 2-8 b).

2.4 Investigations on Metal Forming Processes and Residual Stresses

Metal roll forming processes have been analysed and investigated by many authors using different methods such as analytical approaches using deriving mathematical equations and numerical approaches using the finite element method, all attempting to describe the stress and strain distributions in formed metal strips. The results of each method were mainly validated by comparing them to experimental results that were gathered from strain gauges reporting the surface membrane strains.

Over the last decades the finite element method has widely been used to describe a roll forming process. However, most publications mainly focus on the longitudinal strain distribution in the metal strip, as they have a large impact on wave edges, longitudinal curvature and end flare, hence reducing the quality of the metal strip. One of the first computer aided simulations of a roll forming process allowed, Kiuchi and Koudabashi (1984) to optimise the production of circular tubes. The simulation enabled them to prevent the occurrence of edge waves, and it ensured that the energy dissipated in each roll pass was equal. McClure and Li (1995) analysed a roll forming process with three passes using a three dimensional finite element model, and validated their investigation by measuring the strain with strain gauges, bonded to the upper and lower surface of the strip. Another three dimensional finite element prediction of a U-shaped cold roll forming process consisting of three passes was undertaken by Heislitz *et al.* (1996). They found a continuous rise of longitudinal strain in the strip just ahead of each roll stand and comparison of their numerical work to previous experiments showed an approximate deviation of 10%. Around the same time Panton *et al*. (1996) also predicted the strain distribution in a cold roll forming process. Experiments using strain gauge rosettes showed an increase of longitudinal strain on the strip surface before each roll stand, and a drop after each roll stand, and a continuous increase in shear strain throughout the forming process. From their finite element work, Hong *et al.* (2001) conclude that the work-hardening exponent has a significant effect on the forming length. The authors claim that a highly work-hardened strip has a shorter forming length, and an annealed strip has a longer. Numerical data for the longitudinal stress was compared to experiments, in which there was good correlation only for the first out of three roll stands. Lindgren (2005) predicted the longitudinal membrane strain in the flange of a metal strip roll formed in a process consisting of six roll stands, and based on this work, Lindgren (2007a) have undertaken a more detailed finite element analysis predicting the influence of the yield strength on the longitudinal peak strain and deformation length. The results of Lindgren (2005) correlated very well with those of Heislitz *et al*. (1996). In their numerical investigation on edge buckling of a roll forming process producing a symmetric channel section, Tehrani *et al*. (2006) validated their numerical results with

strain gauge analysis and agreed with McClure and Li (1995) that the strain is positive/ tensile in the flange, and negative/ compressive in the web. From the three dimensional finite element simulation of Bui and Ponthot (2008) it can be observed that the product quality of the rolled strip significantly depends on the yield limit and work-hardening exponent, this latter conclusion being close to the findings of Hong *et al*. (2001). For the first time, Zeng *et al.* (2009) introduced the response surface method to optimise the design of cold roll formed profiles. Employing a finite element model to predict the maximum edge longitudinal membrane strain, the method enabled the authors to reduce the roll passes from six to four, which, as they concluded, saves money and time. Paralikas *et al.* (2009) developed a model to predict the effect of major process parameters on the quality characteristics of a V-section profile. The characteristics that they mainly focussed on were elastic and longitudinal residual strains. This work is particularly interesting, as it discusses the possibility of using a simulation of the whole manufacturing chain of the roll forming process to predict the development and transmission of residual strains. Based on their work, Paralikas *et al*. (2010) introduced an optimisation procedure to improve the quality of the product and reduce costs. Selecting the optimum major process parameters, they managed to reduce longitudinal strains by up to 20-35%, and shear strains by up to 30-50%. Han *et al.* (2002) also investigated a multi-stand cold roll forming process, but by using the finite strip rather than the finite element method. They, too, mainly analysed the development of longitudinal strains throughout the process. This model was employed by Han *et al* (2005) to investigate the effect of forming parameters on the peak longitudinal edge membrane strain development. Zhang *et al.* (2010) introduced a finite strip model in which the stiffness and transition matrix have been improved. Proving the accuracy of the method by predicting the longitudinal strain, the authors claim that their results are more applicable. One phenomenon that has been found by all authors mentioned so far is that the peak longitudinal strain occurs just ahead of the roll stand. Also Han *et al.* (2002), Han *et al.* (2005), and Zhang *et al.* (2010) have observed the same results, but instead of using the finite element method, they have used the spline finite strip method. This method has been introduced to specifically investigate the effects of several roll forming parameters on the longitudinal edge membrane strain development.

McClure and Li (1995) showed that the maximum longitudinal strain is a function of fold angle, whereas Han *et al.* (2005) proved that increasing the bend angle increment, the strip thickness, the flange length, the distance between roll stands, and the web width increase the peak longitudinal edge membrane strain. Zhu et al (1996) claim that the peak longitudinal strain increases with a larger material thickness and bend angle, and that increasing the female radius decreases the peak longitudinal strain due to longer contact length with the tool. Han *et al.* (2005) and Lindgren (2007a) agree that

increasing the material yield limit decreases the longitudinal membrane strain. Paralikas *et al.* (2009) identified several other parameters as being influential to the peak longitudinal strain such as the line velocity, friction coefficient, roller diameter, roller gap, and the roller inter-distance, with the latter two having the major impact as increasing them reduces the longitudinal strains.

Measuring the longitudinal membrane strains to calibrate their finite element simulations and as a reference factor, Farzin *et al.* (2002) and Tehrani *et al.* (2006) analysed buckling of the metal strip while being cold roll formed. Farzin *et al.* (2002) based their work on the experiments of Kiuchi and Koudabashi (1984) and for the first time defined a buckling limit of strain, for channel and circular sections. Tehrani *et al*. (2006) on the other hand focussed more on localised edge buckling and demonstrated that the conditions involving the folding of the flat strip into the initial channel form had the largest influence.

It is worth pointing out at this point that all of the work mentioned so far has used either the finite element method or some other numerical method to predict cold roll forming and have experimentally validated the results, whereas the work presented in the following tried to analytically describe it.

Bhattacharyya *et al.* (1984) and based on their work Lindgren (2007b) have mathematically analysed a cold roll forming process. Bhattacharyya *et al.* (1984) predicted the deformation length of trapezoidal cross-sectional strips, that are formed with several passes, as presented in Figure 13.

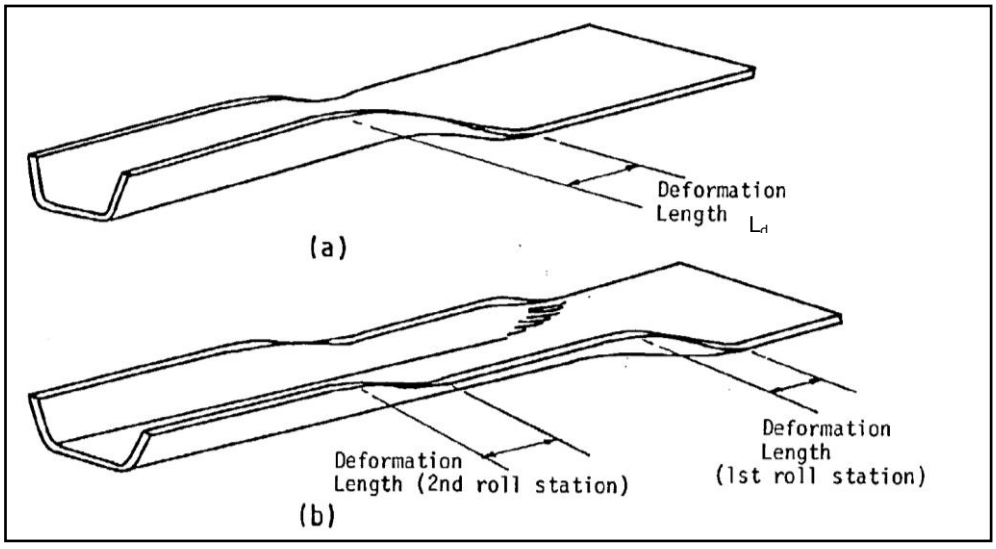

Figure 2-9: Deformed specimen using: a) one roll pass, b) two roll passes, taken from Bhattacharyya et al. (1984)

The derived equation for this can be written as

$$L_d = a\sqrt{\frac{8a\theta_p}{3t}} \tag{2.55}$$

In which L_d is the deformation length, a is the flange length, t the thickness of the work-material and θ_p the prescribed fold angle in one particular stage, as shown in Figure 14.

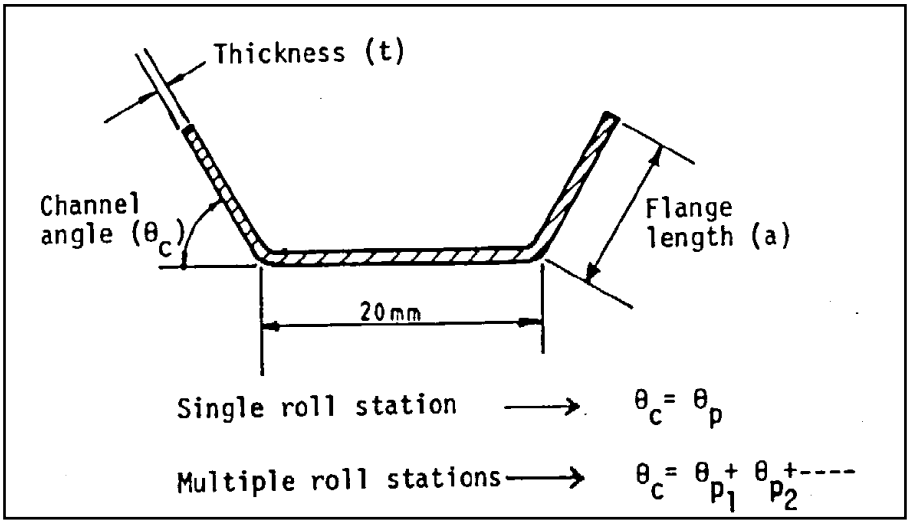

Figure 2-10: A typical cross section of the formed product, taken from Bhattacharyya et al. (1984)

The theory was validated by experimental testing using linear variable differential transformers (LVDT) measuring the position of the flange, and the errors between their experimental and theoretical investigations lay within ±6%. Moreover the research showed that the deformation length depended highly on the prescribed fold angle, flange length and material thickness, but was independent of the mechanical properties of the material. It should be noted that the study did not predict stress and strain distributions through the thickness of the sheet. Lindgren (2007b) points out that the theory of Bhattacharyya *et al.* (1984) does not include material properties and tool geometry, but that these do affect longitudinal strain. According to Lindgren's theory the deformation length can be written as

$$L_d = 12\frac{a^{0.8}\Delta\theta^{0.41}\sigma_Y{}^{0.07}}{t^{0.25}} \tag{2.56}$$

with a being the flange length, $\Delta\theta$ the bend angle increment, σ_Y the yield strength, and t the strip thickness. Comparing this to the experimental results of Lindgren (2007a) gave a good correlation.

The longitudinal peak strain is given as

$$\varepsilon_{peak} = 0.67\frac{t^{0.85}\Delta\theta^{1.9}}{a^{0.28}\sigma_Y{}^{0.28}R_t{}^{0.15}} \tag{2.57}$$

with R_t being the effective tool radius of the roller, also gives good correlations when compared to experiments of Lindgren (2005) and Lindgren (2007a).

Both, Bhattacharyya *et al*. (1984) and Lindgren (2007b) have only predicted either the deformation length or longitudinal strains. As discussed in chapter 3, this project is not concerned with longitudinal strains but with stress and strain distributions through the thickness of a cold roll formed metal strip, hence it is necessary to highlight more work concerning these distributions.

One of the earliest analytical attempts focusing not only on longitudinal strains, but also on strain distributions through the thickness of circular formed cross sections was undertaken by Kiuchi (1973). This mathematical description is based highly on the experimental investigations of cold roll forming processes of different cross-sections, such as tube, V-, and trapezoidal shapes, carried out by Suzuki *et al*. (1972). Their results were obtained from strain gauges attached to the surfaces of the sheet metal. For reasons of simplifying the theoretical model, Kiuchi (1973) divided the strip into two sub-problems of the region, one in the roll gap, and the other region between roll stands. The stress and strain distributions through the thickness of the sheet were only estimated by interpolation and not measured. These estimations were verified by experimentally determined transitions from longitudinal and transversal surface strains, taken from sheet metal with the strip width and thickness $w_s = 180mm$ and $t = 3mm$.

More recently Quach *et al*. (2004) and Moen *et al*. (2008) predicted residual stresses and plastic strains through the thickness of cold formed steel members. Quach *et al*. (2004) focused on the first manufacturing process of sheet coiling, uncoiling and flattening comparing analytical and finite element results. Moen *et al.* (2008) also took into account longitudinal strains, assuming an elastic perfectly plastic material behaviour for their analytical model. Moen's quite detailed model predicts a steel member to have transverse and longitudinal residual stress distributions which are non-linear through the thickness. This is in agreement with Quach *et al* (2004) for at least the first manufacturing process. Moreover, the finding of Moen et al. (2008) that stress and strain magnitudes increase when the yield stress decreases, agrees with Han et al (2005) and Lindgren (2007a). The predicted increase in stress and strain as sheet thickness increases was also pointed out by Han *et al* (2005). Moen *et al*. (2008) admit that their predictions were only partially evaluated by comparing them to specimens where the surface strains were measured. At the same time they claim their predictions to be very consistent with the through-thickness findings of Quach *et al.* (2006), which predicted the residual stresses in press-braked thin-walled steel sections. Quach *et al*'s numerical results correlate very well with the experimental work of Weng and White (1990a and 1990b), and Weng and Pekoz (1990). In their work Weng and Pekoz (1990) studied residual stresses in cold formed products for channel sections, Weng and White (1990a and 1990b) for thick steel plates,

and Kleiner and Homburg (2004) for sheet metal forming. Kleiner and Homburg (2004) have also investigated residual stresses in sheet metal forming and in common with Weng and Pekoz (1990) have applied either the hole-drilling or sectioning technique using strain gauges to measure residual strains. The latter technique was also used by Cruise and Gardner (2008) who stated that this is the better method when testing stainless steel. In contrast to other finite element work mentioned using shell elements, Quach *et al.* (2004) and Quach *et al.* (2006) have both used a rather large number of linear continuum elements with reduced integration through the sheet thickness.

More detailed experimental work on measuring residual stresses through a cold roll formed sheet metal has been carried out by Li *et al*. (2009). Surface and through thickness stresses were gathered from X-ray diffraction, stating that the through thickness residual stresses were bi-linear as opposed to most measurements reported in the literature. As the measurements were carried out on a hollow square section welded together on one side, they hold this welding process after the last stand responsible for these differences, as it anticipates springback.

As discussed in sub-section 2.3.5, it is very well understood that stainless steel is an excellent working material for cold formed product, because it can be work hardened as demonstrated by Hong *et al*. (2001) and Kain *et al.* (2004). Kumar *et al*. (2004) and Milad *et al.* (2008) state that for austenitic stainless steel unstable austenite partially transforms into martensite and greatly increases the mechanical strength and hardness. Kim *et al.* (2007) have studied exactly this relation and their results showed good agreement between numerically predicted plastic strain and experimentally obtained hardness values.

In the work reported in this section the authors have either used analytical or finite element methods to predict roll forming processes and experimental data to validate their findings. They have mainly focused on longitudinal strains, and only occasionally on through thickness stress and strain distributions. Moreover, apart from Li *et al.* (2009) even the latter cases were only evaluated by measurements of surface strains. None of the publications mentioned earlier give a direct link between predicted and measured strains.

2.5 Measuring Contact Pressure

In a V-band joint, it is not only important to analyse the V-band retainer itself, but also the contact interaction between flanges and retainer. In previous theories describing the stress distribution in V-band retainers, the contact pressure between retainer and flange around the circumference is assumed to be uniformly distributed. In real applications on the other hand it must be taken into account that the pressure distribution is non-uniformly distributed, and only recently Shoghi *et al.* (2006) have extended their

theoretical work to account for that. Also NASA (2000) acknowledge this problem as during the assembling procedure they attach strain gauges to the outer surface of the band to ensure uniform tension, and load the band incrementally, tapping the strap around the periphery. It is therefore worth revising existing knowledge on contact pressure measurement.

Pressure sensitive sensors are widely used especially in biomechanics to measure pressure in human joints such as hips and knees. Atkinson *et al.* (1998) have undertaken a study on how the sensitive range of pressure sensitive films can be increased. They found that it is possible to increase the accuracy of the measurement by several layers of Fuji films under a pure normal load. More recently Bachus *et al.* (2006) have compared three methods employing film sensors. In their analysis it was shown that the *erase* and *threshold* method, both using Fuji films, are less accurate than TekScan, when comparing values for pressure and area. On the other hand they point out that TekScan is relatively unstudied, whereas methods employing Fuji films have been evaluated numerous times in the literature. Komi *et al.* (2007) have undertaken work in which they too compared three different types of film sensors, namely two commercially available TekScan 9811 and Flexiforce, and a new invention called quantum tunneling composite (QTC). The thickness of the first two sensors was up to 0.1mm, which in this work is highly disadvantageous, as in V-band joints this would increase the virtual thickness of the flanges, leading to a change in contact zone. The authors point out the lack of existing knowledge about the film sensors when being subjected to shear force. In their study they have only applied minor shear forces up to 3.2N for static and dynamic loads and found that all three types of sensor had errors. In some cases these errors were only acceptable because of the benefits offered by obtaining them. In another publication, Hoffman and Decker (2007) have investigated measurement inaccuracies of the TekScan system by comparing results to Fuji film measurements and finite element simulations. They point out that, depending on the application, the finite thickness and structure of the sensor can affect the accuracy of the measured results.

Because of the difficulties arising with sensor films, it was decided that for this project, the contact pressure between flanges and retainer could be measured by the change in surface roughness before and after assembly, provided that the contact pressure is large enough to plastically deform the surface. It is therefore useful to gather further knowledge about contact interaction of rough surfaces. Moore (1948) experimentally investigated the deformation of steel and copper in static and sliding contacts. In static contact asperities were little deformed although considerable bulk deformation had occurred. For a sliding contact, a similar surface was so severely damaged that irregularities vanished completely. Moreover, he found junctions formed by sliding on the softer material that may be strong enough to rupture the harder surface. Even

considerable work hardening may occur below the actual points of contact, due to shearing of the junctions. All surfaces were measured prior to and after contact was established by using a talysurf (stylus instrument). Moore points out that in accordance with Hertz's classical equations describing elastic deformation (Hertz 1896), and Timoshenko (1934), plastic deformation occurs below the centre of contact in the softer material once the maximum shear strain exceeds its elastic limit. Pullen and Williamson (1972) have derived a theory relating the load, separation, and degree of contact in terms of the height distribution of the surface. This approach also accounts for the persistence of the asperities, which agrees with Moore (1948). This has led to the idea in this thesis, to detect changes in contact pressure around the inside of the V-band by surface metrology. However, using a stylus the measurements did not show a significant deformation at the surface. As an excessive amount of noise appeared in the results due to the setting up of the sample, they were not included.

2.6 Conclusion

The literature review in this chapter revealed significant gaps in the knowledge about the manufacturing, application, working behaviour, and failure modes of V-band retainers. Attempts made by several authors to predict the F_{UALC} taking into account the joint diameter turned out to be rather rough approximations mainly based on experiments, and experience in this field. Moreover, these attempts did not include environmental influences such as the coefficient of friction, or any other geometrical joint parameters. Other researchers carried out work concerned with internal stresses in V-band retainers and successfully managed to include the angle of the V-section and friction in the circumferential and axial directions, giving a much more detailed insight in V-band joints. Their theory predicted the axial load generated by tightening the T-bolt nut and did not include the V-band joint diameter, as they stated that the there was no relationship between these two parameters during V-band assembly. So far, the literature does not include any robust information, or guidelines on predicting the F_{UALC} of V-band joints.

In the literature a large amount of work and publications on metal forming and especially cold roll forming could be found. Those focussing on the latter subject were mainly concerned with predicting and measuring stress and strain in the longitudinal direction of thin sheet metal strips, and did not present any direct link of residual stresses and strains on the working behaviour of the formed products. Work investigating through thickness residual stresses and strains and gave approximate results rather than detailed distributions.

It is basic engineering knowledge and very well understood that austenitic stainless steels work hardens due to plastic deformation. However, during this literature survey no

work could be found directly linking plastic strain and hardness. Moreover, all finite element work analysing plastic strains being inducing during forming processes was validated by measuring surface strains using strain gauges applied to the formed product.

With the exception of Shoghi *et al*. (2004), the theoretical analyses of V-band retainers always assumed a uniformly distributed contact pressure around the circumference between band and flanges. The nature of the contact problem, taking into account friction in several directions usually prevents this from appearing and instead suggests a non-uniformly distribution of the contact pressure.

This survey demonstrated the existence of a significant knowledge gap in the field of V-band retainer applications and led to the work presented in the following chapters.

3 Finite Element Models Predicting the Cold Roll Forming Process

3.1 Introduction

The V-band of the retainers discussed in this thesis are produced in a cold roll forming (CRF) process, with cross sectional forming, and then in a second stage with a roll bending process giving the band its ring shape. A schematic representation of this two stage CRF process can be seen in Figure 3-1 and the actual roll forming machine can be seen in Figure 3-2.

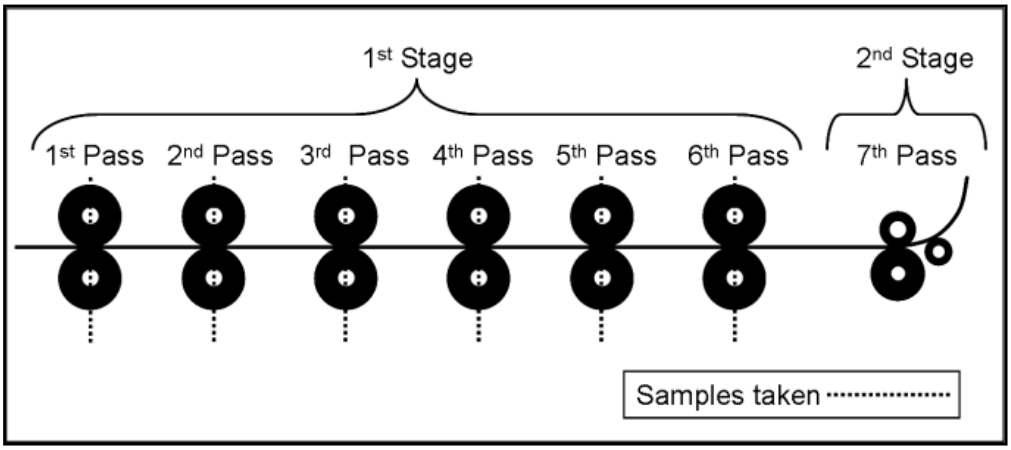

Figure 3-1: Two dimensional schematic of roll forming process including 1st stage of forming the V-section and 2nd stage of forming circular shape

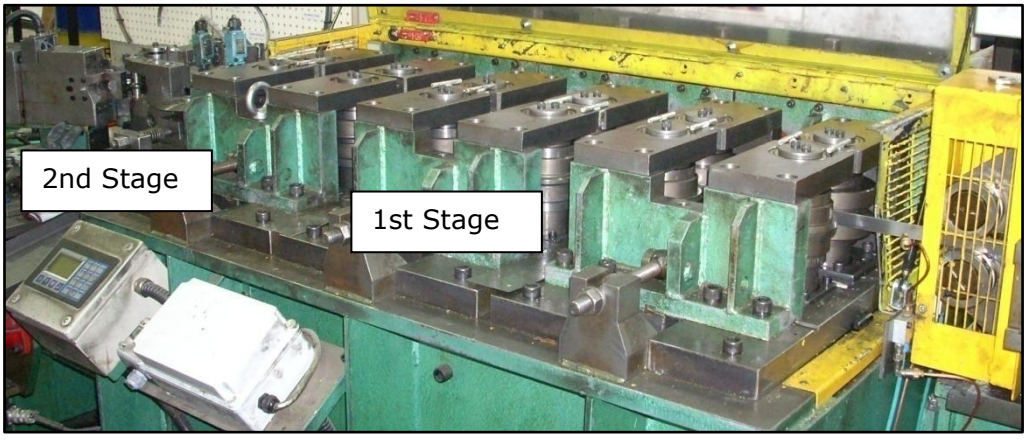

Figure 3-2: CRF of V-band retainers

In this section finite element models simulating this cold roll forming process are described and the limitations and assumptions of these models are discussed. These analyses are necessary to investigate the stress and strain distributions in the cold formed metal strip, to gain more information about the impact of the manufacturing

process on the strength of the final V-band product. A two dimensional plane strain simulation with a relatively fine mesh was created to investigate the cross section of the formed band in detail, reporting the plastic strain distribution in each pass. Due to the two dimensions used, only the section forming (first stage) could be analysed, excluding the ring forming (second stage). Therefore, a three dimensional model was generated, being able to simulate both forming stages, but containing less detailed information of the cross section, as it consisted of a coarser mesh. Moreover, this latter model, still containing the plastic strain (PEEQ) changes due to the cold forming, could then be used to investigate the ultimate axial load capacity, F_{UALC}, of V-band joints, as presented in the subsequent chapter 4.

Both, two dimensional and three dimensional models are presented here in sections 3.3 and 3.5. The finite element software package ABAQUS versions 6.7 and 6.8 were used to carry out all numerical work.

Sections 3.2 to 3.4 are taken from the author's own publication Muller et al. (2011).

3.2 Material Properties for FE Models

The material properties are the same for every finite element simulation discussed in this thesis. The metal strip used in the CRF process was initially 18mm wide and 1.2mm thick, and made of AISI 304 quarter hardened austenitic stainless steel with experimentally determined values for Young's Modulus of 227 GPa, Poisson's Ratio of 0.29, yield stress of 648 MPa and an ultimate tensile strength of 857 MPa, taken from Shoghi et al. (2004). For the FE-Analyses the material was defined to be elastic-plastic with linear hardening, as also used in the study of Kiuchi (1973) and with a von-Mises yield function as mentioned in Dixit and Dixit (2008). Using equations (2.26), (2.33), and (3.1) all engineering values were transformed into true values for the yield stress σ_Y and ultimate tensile strength σ_{tUTS}, and the plastic behaviour could be calculated as described by Tehrani et al. (2006) and Meyers and Chawla (1999).

$$\varepsilon_{true} = \ln(1 + \varepsilon_{eng}) \tag{2.26}$$

$$\sigma_{true} = (1 + \varepsilon_{eng})\sigma_{eng}\,. \tag{2.33}$$

$$\varepsilon_p = \varepsilon - \varepsilon_e \tag{3.1}$$

The complete true strain hardening curve and all engineering stress and strain values are shown in Figure 3-3.

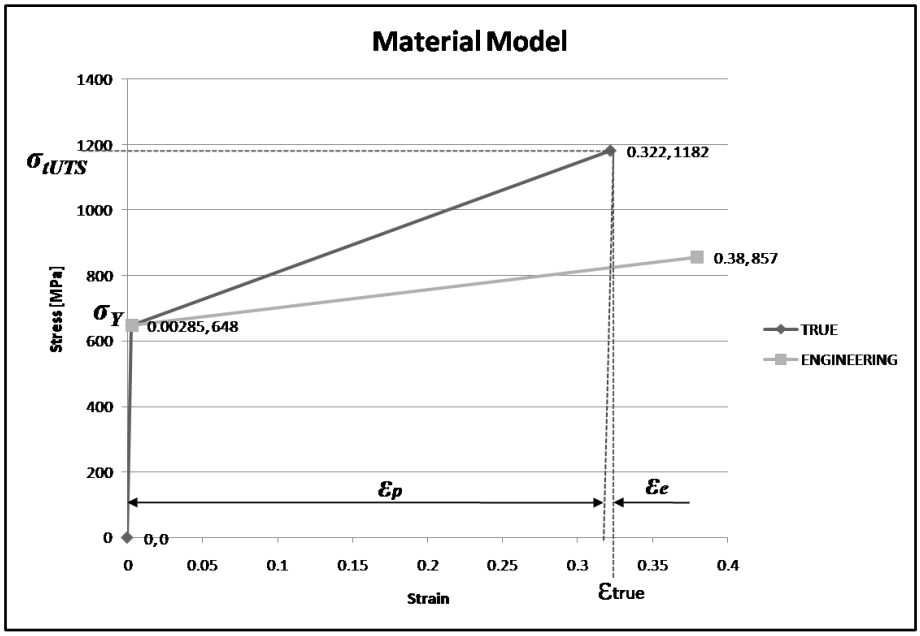

Figure 3-3: Material model used for finite element simulation

3.3 Definition of Plane Strain FE-Model Predicting First Stage of Cold Roll Forming Process

To make the analysis independent of the clamp diameter only the first stage incorporating six passes was set up, analysing only one half as the process is symmetrical, as shown in Figure 3-4.

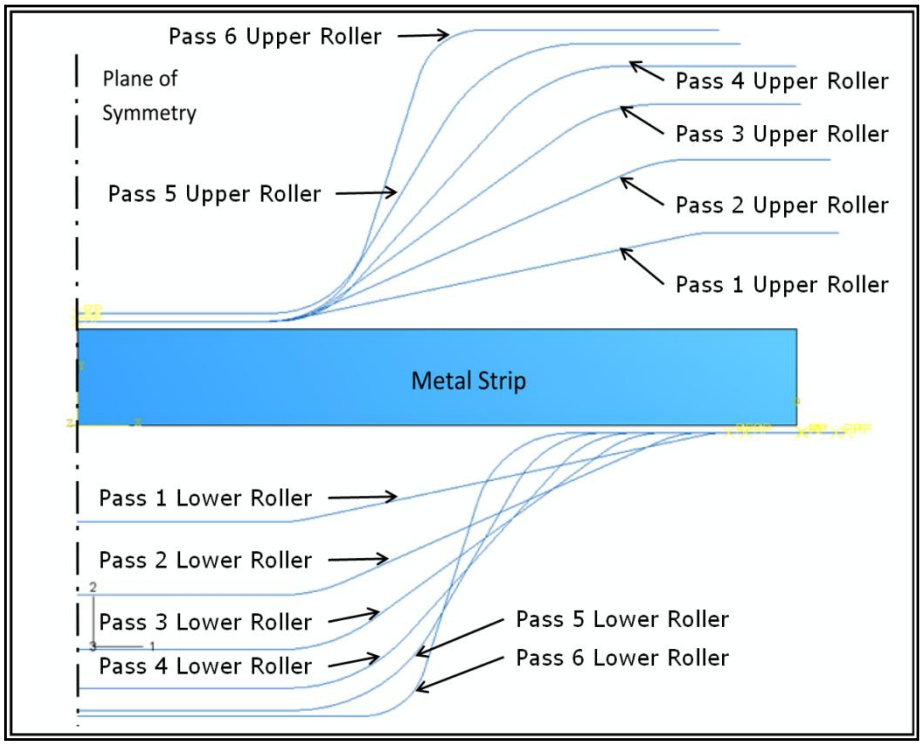

Figure 3-4: Two dimensional FE model of roll formed cross section

The strip was modelled using three different mesh densities with 12x90, 24x180, and 48x360 equally spaced 2 dimensional reduced integration linear plane strain elements (CPE4R). The analysis was carried out in an implicit static environment and, as undertaken by Papeleux and Ponthot (2002) for a similar 2 dimensional forming process, a penalty algorithm was used to enforce contact. All tools and contact interactions were removed after every pass to include the effect of springback. Papeleux and Ponthot (2002) state that the results obtained for explicit and implicit solvers were only slightly different but CPU costs for the explicit solver were almost 60 times higher than for its implicit counterpart. This analysis was generated in two dimensions because although the rolling process is 3 dimensional, the final state of each rolling pass is achieved on a plane. Linear Elements had to be used since as described by Konter (2000), in ABAQUS second-order quadrilateral elements at the contact surface will transfer the contact-force/pressure non-uniformly, sharing 1/6 on each corner node and 2/3 for each middle node. Moreover, Bui et al. (2004) found linear elements with reduced integration to be very suitable for metal forming processes including large bending and large plastic strains, and compared to their fully integrated counterparts, do not suffer from shear locking. A more general discussion of this type of elements can be found in sub-section 2.2.4.

Within the finite element simulation each pass consisting of a pair of rollers was modelled using analytical rigid bodies representing a surface. The rollers were therefore not meshed. The contact between the rollers and the band was simulated using surface-to-surface interactions. No friction was assumed because this would add extra surface stress and strains as the rigid rollers slide over the surface, whereas in the real process the rollers do not slide over the band surface in the vertical direction. All upper rollers were prevented from moving in any direction by applying a boundary condition at their reference points, whereas the lower rollers where moved upwards pushing the band against their upper counterpart until the distance between the rollers in the simulation matched the clearance in the real rolling process. The clearance between the rollers is the same as the thickness of the initial flat strip.

3.4 Results of Plane Strain Finite Element Analyses

3.4.1 Mesh Convergence Study

The predicted equivalent plastic strain (PEEQ) in each of the six roll passes for a finite element model with a mesh density of 12x90 elements can be seen in Figure 3-5. The simulation clearly shows a large increase in plastic strain in the bent areas, and first noticeable in the 4^{th} pass, plastic deformation along the neutral line in the straight part of

the clamp leg. As the mesh deformation shows, this latter deformation is due to shear stresses acting in this area.

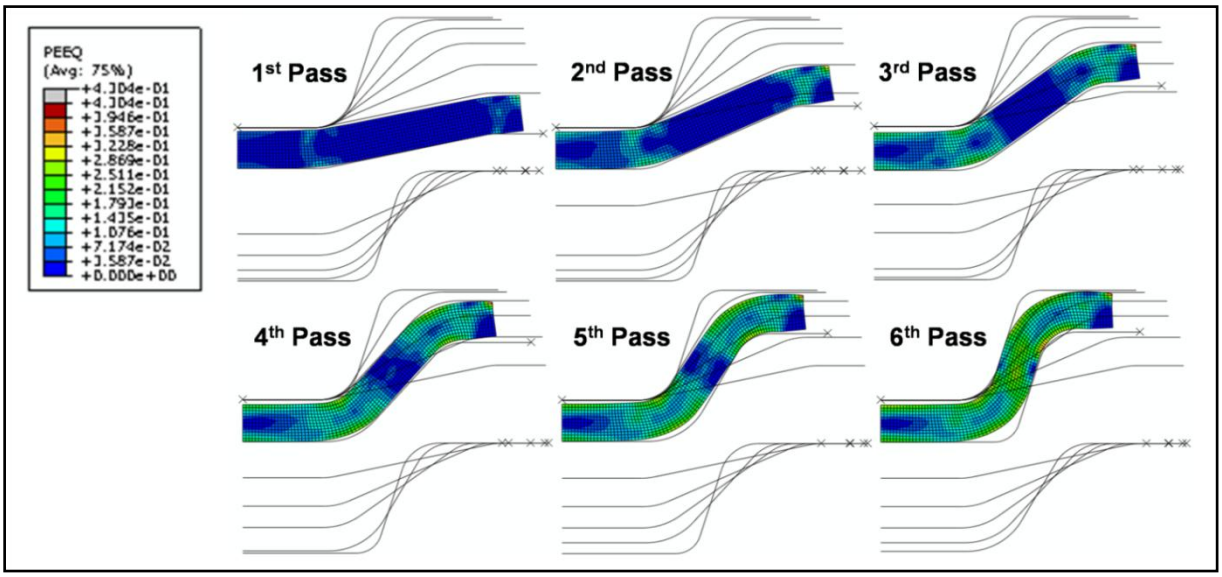

Figure 3-5: Equivalent plastic strain (PEEQ) in each roll pass for a 12x90element mesh

In order to demonstrate the accuracy and correctness of the initial mesh density with 12x90 elements, a convergence study with two more mesh densities of 24x180 and 48x360 elements was carried out. Three areas in the cross section after the 6th pass were chosen to be compared to each other. These areas lay where predicted plastic strain values were compared to measured hardness values to validate the finite element model, as discussed in further detail in chapter 6. The areas compared in the convergence study are indicated in Figure 3-6 by red lines through the corner nodes of the elements from which the strain values were extracted. In all three meshes nodes existed along the indicated lines making it possible to make a direct comparison between models. This part of the cross section was chosen because experience showed that in certain turbocharger applications cracks occurred in this particular area, as stated by Brown 2009.

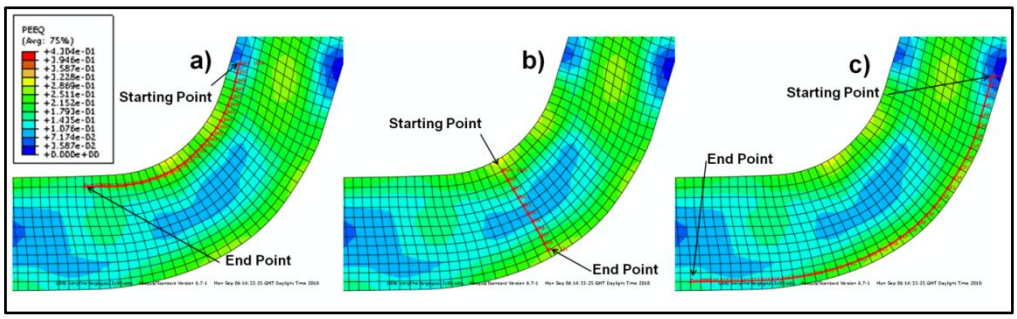

Figure 3-6: Line of element corner nodes, where plastic strain was reported after 6th pass, a) close to inner surface, b) through the thickness and c) close to outer surface

Figure 3-7 shows the plastic strain values taken from line (a) (Figure 3-6). These results show very good agreement, and only differ slightly between 0.5mm and 1.2mm. As expected, the plastic strain significantly drops at both ends of the red line, as these nodes lie further away from the bent area and either no or very little plastic deformation has taken place. The peaks and valleys visible in the bent area between 0.5mm and 2mm along the line are discussed further in sub-section 3.4.2.

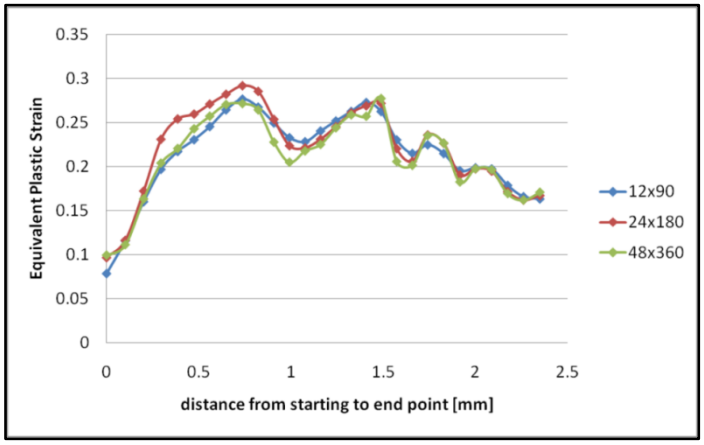

Figure 3-7: Equivalent plastic strain distribution close to inner surface of the cross section after the 6th pass

The next area of interest was at the outside corner (line (c) in Figure 3-6), where mainly tension rather than compression took place. Again reading the plastic strain values taken from the element corner nodes the predicted values are shown in Figure 3-8. Very good correlation between the results for all mesh densities can be seen, and as in the results for the inner side, the plastic strain drops further away from the bent area, at 0mm and 3.8mm. The two peaks are due to the bending area being slightly shifted to the right of the section (i.e. the left of the graph) as the cold roll forming process progresses, with the peak at 1.1mm being introduced in the 6th pass.

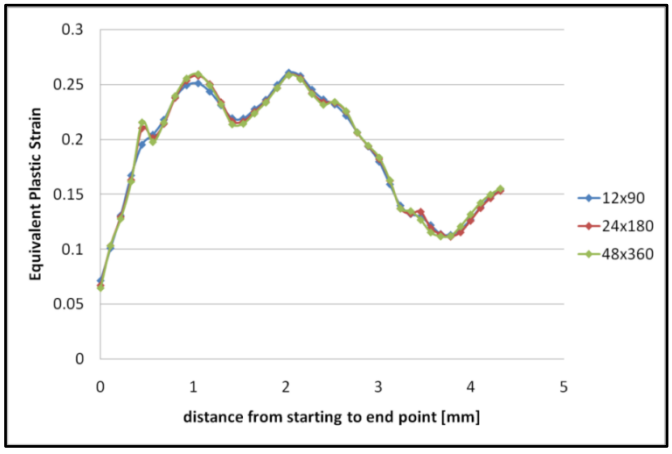

Figure 3-8: Equivalent plastic strain distribution close to outer surface of the cross section after the 6th pass

The increase in plastic strain between 3.8mm and 4.5mm lies in the nature of the cold roll forming process, as the band is initially subjected to three point bending with contact on the symmetry line as shown in Figure 3-9 shortly before the band gets fully deformed during this first pass. This phenomenon appears throughout all six passes, leading to the plastic strain increasing as well.

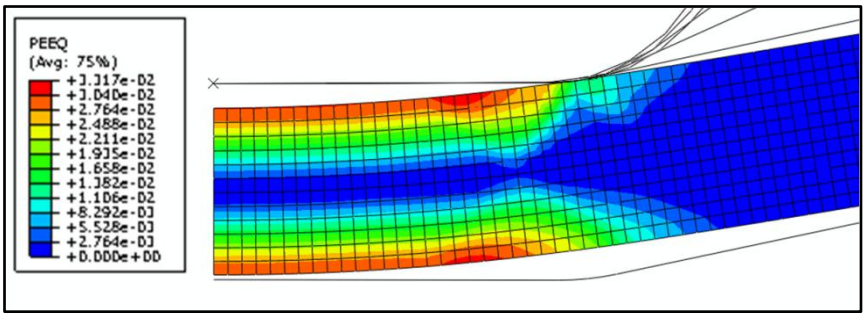

Figure 3-9: Plastic strain close to the symmetry plane shortly before entering the first pass

The plastic strain distribution through the thickness of the band in the third area investigated in the convergence study , indicated by the red line in Figure 3-6b, can be seen in Figure 3-10. The graphs show very good correlation for all mesh densities, and distributions as expected, with very little plastic deformation towards the neutral line halfway through the thickness.

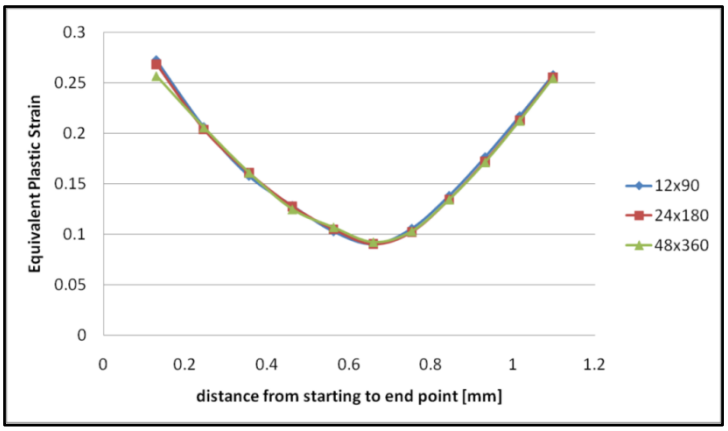

Figure 3-10: Equivalent plastic strain distribution through the thickness of the cross section after the 6th pass

In all three areas the results shown here demonstrate good convergence after the 6th pass.

3.4.2 Influence of Hydrostatic Stress on Plastic Strain Distribution

As described in the previous sub-section, the non-uniform distribution of the equivalent plastic strain (PEEQ) in Figure 3-7 is worth further investigation. This is of particular

interest as Muller and Barrans (2009) have discussed the problem of cracks occurring in this particular area of the inner surface of V-band clamps assembled to turbochargers for diesel engines.

In the zone of band strip where it is in contact with the upper rollers, the stress distribution consists of three compressive stress components. The first one σ_1 acting in the plane of the section and parallel to the surface of the strip is largest at the inner surface due to the bending. The second component σ_2 acts out of the plane. This stress is generated as the material is compressed in plane due to bending and contact but is restrained from expanding out of plane by the material in the remainder of the cross section. The third compressive stress σ_3 is due to the contact force between upper roller and band strip. Considering the yield surface geometrically representing the von Mises yield criterion (also see Dixit and Dixit 2008) the first two components σ_1 and σ_2 on their own would pass the yield surface leading to material yielding in this zone and significantly increasing the plastic strain. The stress component σ_3 due to the contact pressure however, acts in the perpendicular direction to the plane represented by σ_1 and σ_2, and brings the material closer to the yield surface, significantly reducing plastic strain. This phenomenon can be seen several times in this cold roll forming process such as in Figure 3-11a. Here two large peaks in plastic strain appear on both sides of the contact zone with the upper roller during pass 1. Figure 3-11b shows a peak in the hydrostatic stress (termed "pressure" in ABAQUS), at the contact zone due to the large contact force. For the first pass, this larger hydrostatic stress indicates the correctness of the theory, in which the stress due to contact leads to less plastic deformation.

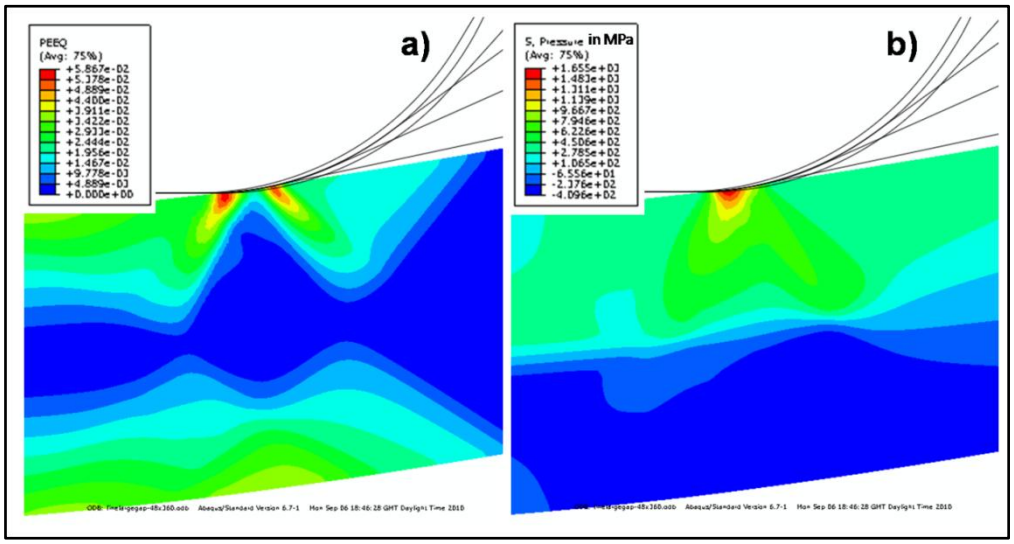

Figure 3-11: Band strip in contact with upper roll 1 before being fully deformed, a) equivalent plastic strain (PEEQ), b) stress component due to contact force of roller

For the second roll pass, the same tendency can be observed as Figure 3-12a shows not only two peaks in plastic strain next to the contact zone, but also another third peak left from pass one. Again the two peaks in plastic strain are next to the high hydrostatic stress zone, shown in Figure 3-12b.

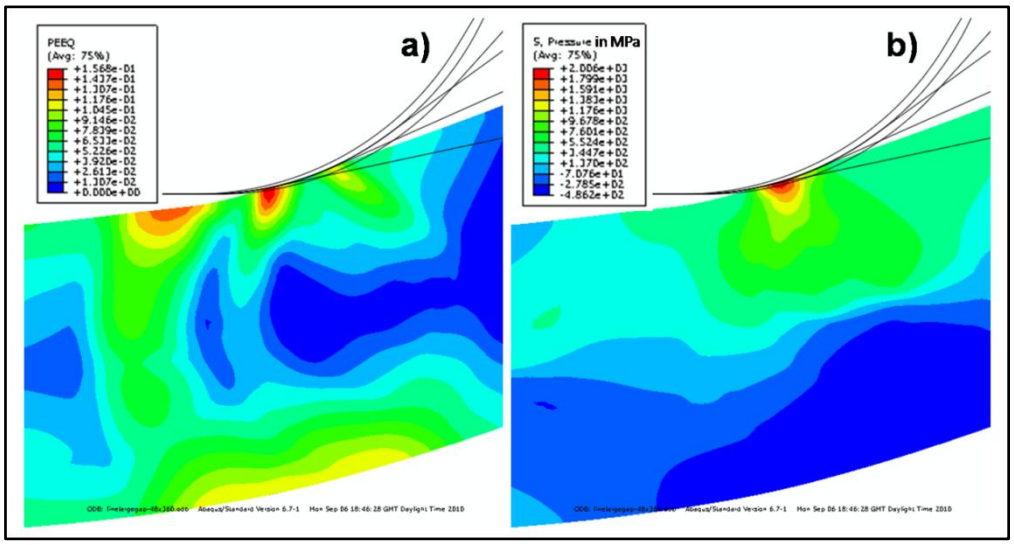

Figure 3-12: Band strip in contact with upper roller 2 before being fully deformed, a) equivalent plastic strain (PEEQ), b) stress component due to contact force of roller

In Figure 3-13a, several peaks in plastic strain (PEEQ) can be observed at the inner surface of band cross section. The largest peak in plastic strain of 0.29 is generated from the contact in the first and second passes, and the next slightly smaller peak of 0.1995 is generated from the contact interaction in the second, third and fourth passes. The final strain peak of 0.1711 is the second part due to the contact in pass 4, which is clearer when taking into account the large hydrostatic stress in Figure 3-13b.

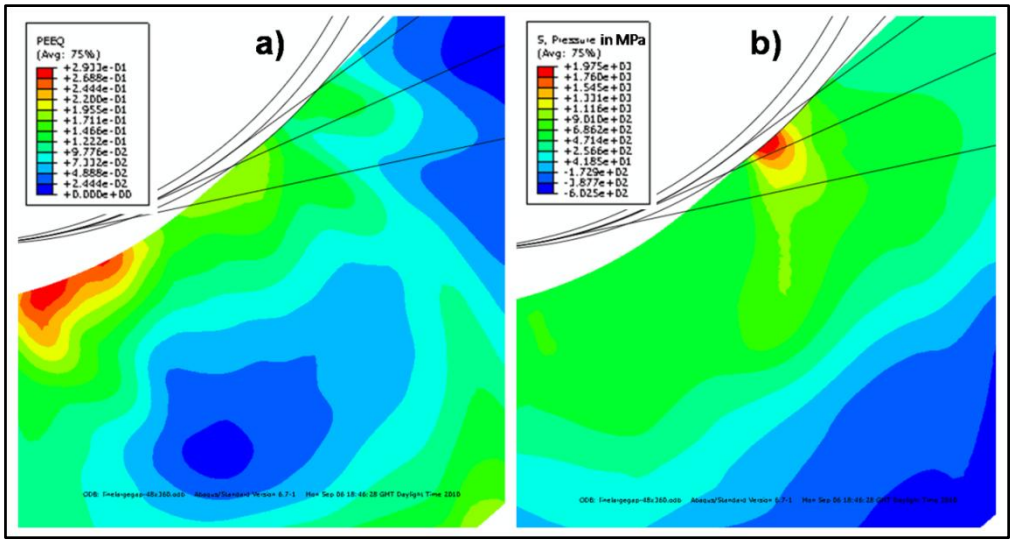

Figure 3-13: Band strip in contact with upper roller 4 before being fully deformed, a) equivalent plastic strain (PEEQ), b) stress component due to contact force of roller

The two dimensional finite element model clearly showed that in a plane strain case with bending acting, stresses due to the contact force can significantly reduce the plastic deformation in this local area.

Cracks are very likely to occur in the region of these peaks, especially in the root of the bending radius, next to the left hand side of the largest peak indicated by the graph in Figure 3-7.

3.5 Definition of Three Dimensional FE Simulation of First and Second Stage of Cold Roll Forming Process

The 3 dimensional finite element models take into account both stages of the CRF process simulating strain distributions through the thickness and in the longitudinal direction.

The contact problem was modelled with a master-slave contact interaction, and a penalty algorithm. For the analyses a coefficient of friction, μ, of 0.2 between the rollers and the band strip was assumed, as suggested by Bui and Ponthop (2008). The strip itself was modelled with a deformable solid body, and 8-node linear brick elements with reduced integration and hourglass control, as recommended by Bui and Ponthop (2008) for a similar simulation, and as discussed in section 3.3. As in the case of the plane strain simulation, also here the rollers were modelled as rigid analytical bodies, which required no meshing. In the same way, only one half of the process was simulated due to symmetry. Since the strip in this 3 dimensional model underwent longitudinal movement making it a quasi-static problem, unlike its 2 dimensional counterpart in section 3.3, it was solved using ABAQUS Explicit v6.7 which was able to simulate dynamic effects and greatly reduced problems associated with very complex contact interactions. The Explicit solver requires a density to be added to the material properties. The density for austenitic stainless steel normally is at approximately $8x10^{-9}\ {}^{t}/_{mm^3}$, but in this case was set to $8x10^{-6}\ {}^{t}/_{mm^3}$. This reduction by the factor of 1000 was necessary as otherwise the model suffered from buckling, and had only very little effect on the stress and strain distribution. Another option to overcome this problem was to reduce the roller speed, but which proved to be unpractical as it increased CPU time by a factor of 10 (up to 80hours) for each simulation. Highly dependent on the mesh density, the simulations took between 6 and 15 hours to be solved. In the real machine, buckling is avoided because firstly the roller speed increases gradually throughout the roll forming process, as two pairs of rollers are always linked together, and secondly each roller is mounted by springs so that it can adjust in the longitudinal feeding direction, as pointed out by Brown (2009).

During the first six passes of the process, each pair of rollers was positioned to have a 1.2mm gap between them, the exact width of the initial band strip. At the first pass, the strip was fed in using a displacement BC to establish contact between band and rollers. Once the band strip was in contact it was moved through by rotating rollers, all running with exactly the same speed, as shown in Figure 3-14. This procedure was the same for all diameters, only varying the length of the band strip.

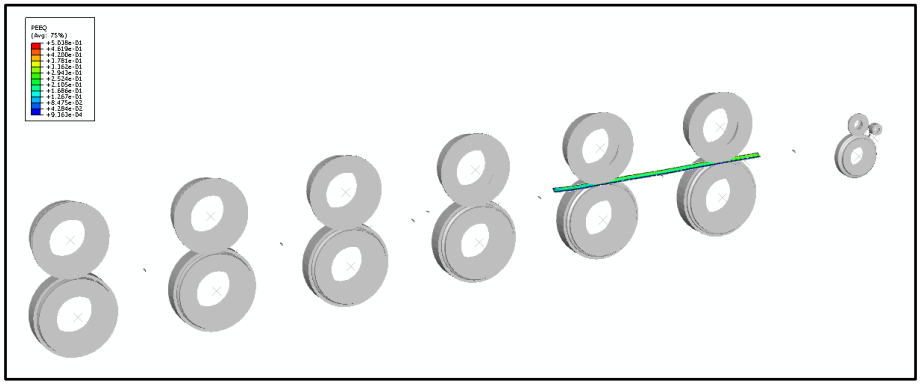

Figure 3-14: Three dimensional finite element model of CRF process of both stages, with a band strip for a $D_b = 114mm$ band

After the band strip had left the 6th pass, it was fed into the second stage where it was bent in a circular ring form, as indicated by Figure 3-15 for a 114mm band. The rollers in this stage were set up and moved to individual positions, so that all diameters could be produced.

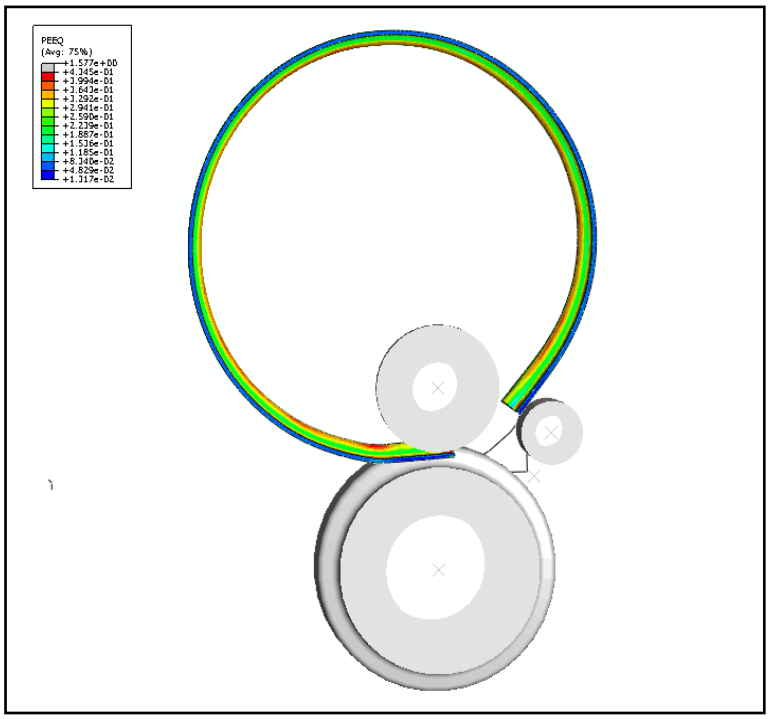

Figure 3-15: V-band ($D_b = 114mm$) at end of ring forming stage

In the real manufacturing process the metal strip is very long and wound up on an external roll and after section and ring are formed the strip is cut to the right size. In this simulation the band strip had already had the correct lengths $l_b = 356mm$, and $l_b = 567mm$ when fed into the process for the two modelled band diameters of $D_b = 114mm$, and $D_b = 181mm$.

In the 3 dimensional finite element model fewer elements were used through the thickness and across the width of the section than for the 2 dimensional plane strain model, as trying to include the same number of elements would have resulted in a much longer, impractical CPU time. All mesh densities with the associated amount of elements and band diameters are listed in Table 3-1.

Band diameter	No. of elements			mesh
	length	width	thickness	
114	150	20	4	coarse
114	300	20	4	medium
114	300	20	8	fine
181	233	20	4	coarse

Table 3-1: Mesh densities for 3 dimensional FEA models

3.6 Results of Three Dimensional Finite Element Analyses

In this section the results of the three dimensional finite element analyses of both stages of the cold roll forming process are discussed and evaluated. The first stage is compared to the plane strain model discussed previously in sections 3.3 and 3.4, and then the change in strain distribution between section and ring forming is discussed.

3.6.1 Section Forming

This sub-section discusses the formed cross section of the band strip after leaving the sixth pass.

The 3D cross section discussed in this section was taken from the cold roll forming process after passing through the sixth roller pair. The exact cross section was defined by l_c=125.787mm, as can be seen in Figure 3-16 to avoid end effects.

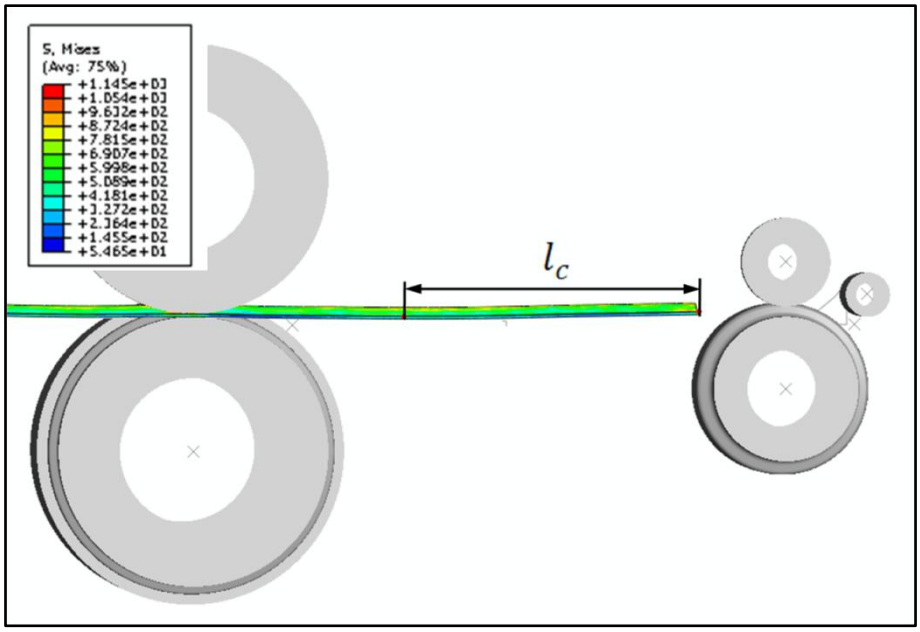

Figure 3-16: Definition of 3D cross section in cold roll forming process

The coarser meshes influenced the final geometry of the cold rolled strip to a certain extent as can be seen when comparing the 3D to the 2D plane strain model in Figure 3-17, especially noticeable on the right hand side of the three dimensional model. A coarser mesh impacts not only on the geometry but also on the strain distribution. Although the maximum strain results are lower, the overall distribution is similar to that of the plane strain model in Figure 3-17a, with the maximum on the right hand side top where the top rollers pushed on the band and in the bent areas due to the bending process. Also noticeable are the minimum strains close to the symmetry plane on the left hand side of the band and on the bottom of the right hand side.

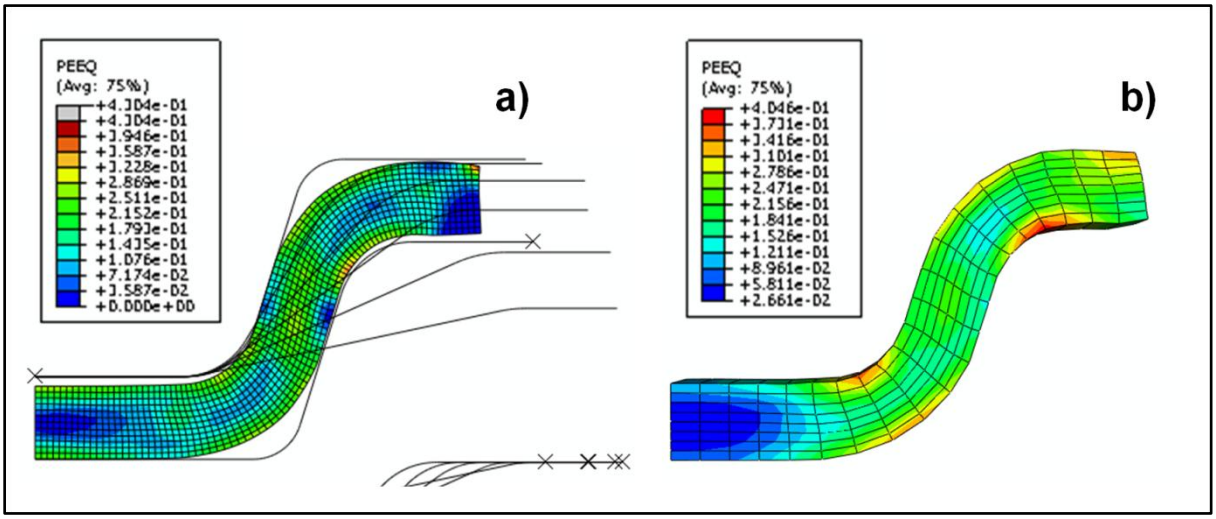

Figure 3-17: Predicted plastic strain (PEEQ) in V-band cross section after 6th pass, a) plane strain model, b) three dimensional model ($D_b = 114mm$, Mesh 300x20x8)

As with the 2 dimensional model, the 3 dimensional model is analysed in greater detail in the bent area, starting with the inside. However, the latter model had a coarser mesh density and, hence fewer elements in the cross section. To enable comparison with the 2D model, results for the plastic equivalent strain were extracted from nodes beneath the surface and along the surface, as indicated by red lines in Figure 3-18, of which each line contained 7 nodes. The strain results for these two lines were then linearly interpolated (linear elements) to match the position of the nodes in the 2D cross section. The interpolation was undertaken for the fine mesh, and for the inner side of the bent area only, since this is the area where cracks usually develop.

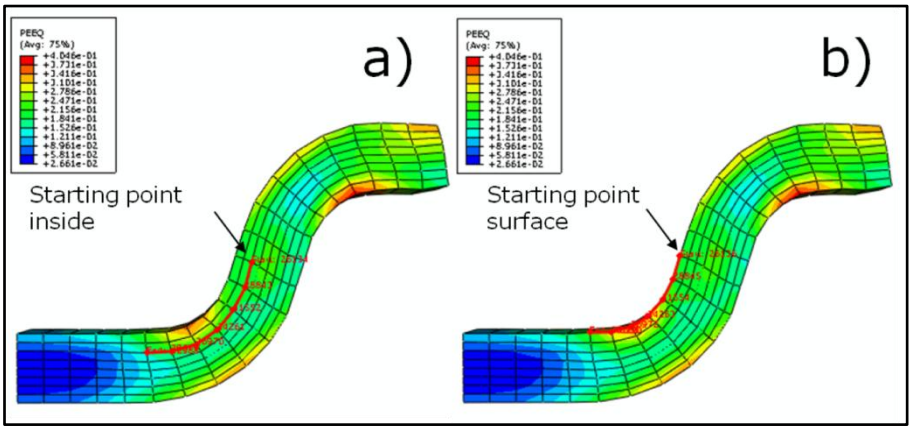

Figure 3-18: Nodes in 3D finite element model from where plastic strain values are taken from at inside bending radius, a) inside node line, and b) surface node line

In Figure 3-19 it can be observed that the 2D strain results lie in-between the 3D results for the inside and surface. Only on the left hand side at the beginning of the graphs up to approximately 0.4mm is a significant deviation between 2 and 3D results. The interpolated strain results do partially over-predict the strain. Since these results are for the fine mesh (300x20x8, $D_b = 114mm$) with 8 elements through the thickness, the additional line represented by the orange graph lies half way between the surface and inside red lines and exists only in this mesh. It is included in the diagram simply for orientation and to validate the interpolated values. All 3D-values predict the overall distribution accurately enough, but lack the detailed information such as the smaller peaks due to contact as described in section 1.4.2. The differences between these two analyses are mainly due to fewer elements being used in the 3D version, hence making the model stiffer.

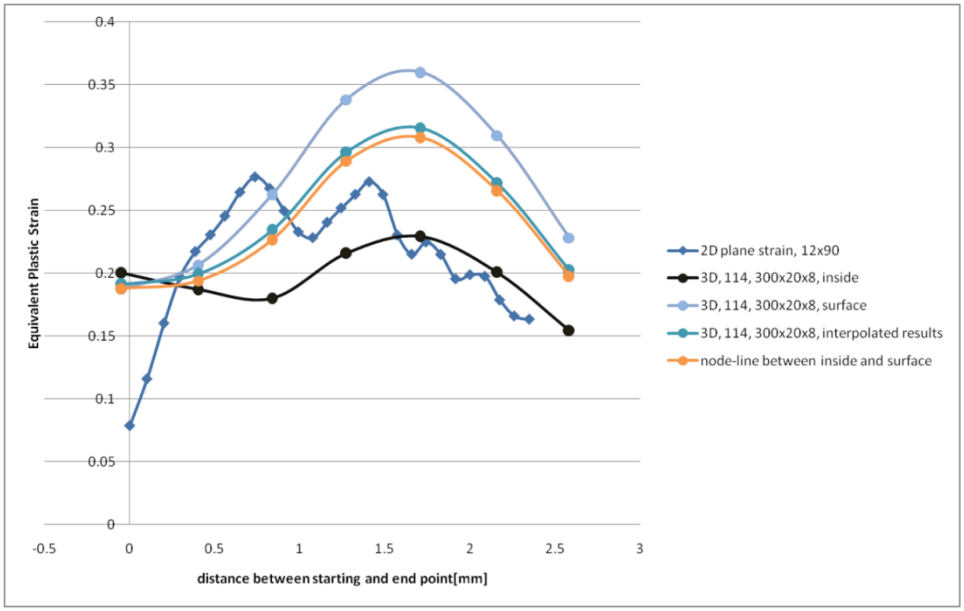

Figure 3-19: Plastic strain for 2D and 3D models after section forming at the inside

Figure 3-20 and Figure 3-21 illustrates the influence of the mesh for 3D models only. For all mesh densities, the strain values beneath the surface (*inside* the mesh, Figure 3-20) are very similar and differences can be neglected. For the surface values, in Figure 3-21, on the other hand a significant difference can be seen between meshes with 4 and 8 elements through the thickness of the strip, those for the latter being notably larger. Changing the number of elements along the length for the same length ($l_b = 356mm$), as well as changing the length of the strip from 356mm to 567mm but keeping the element length the same, has a negligible influence on the strain distribution.

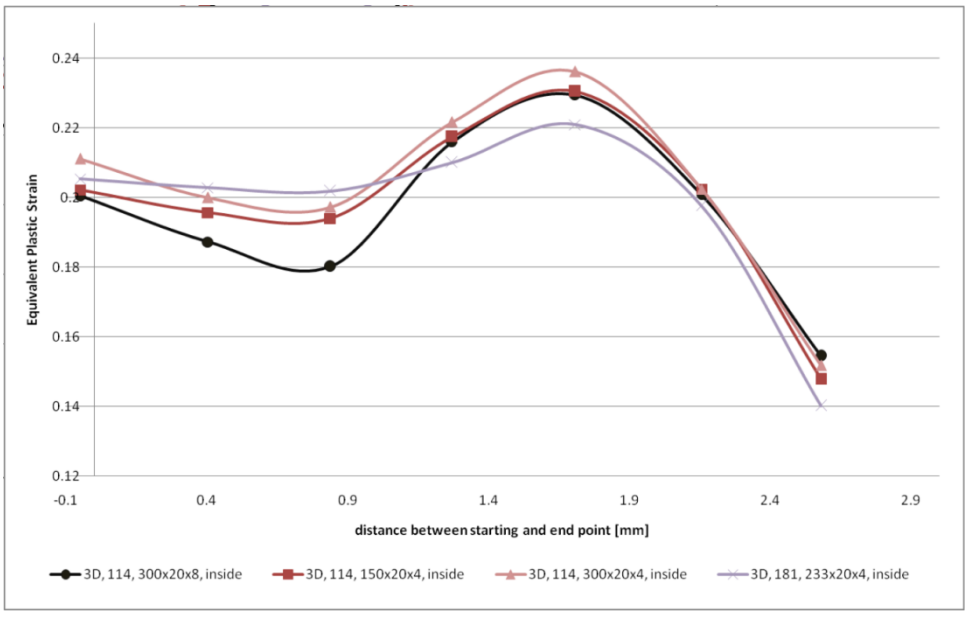

Figure 3-20: Mesh convergence study of plastic strain at the inside for inside node-line

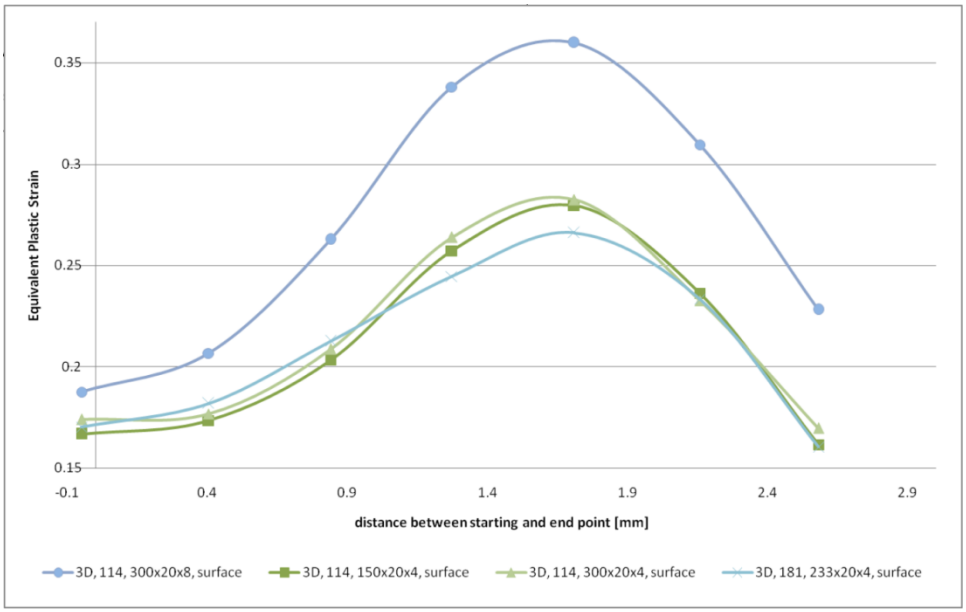

Figure 3-21: Mesh convergence study of plastic strain at the inside for surface node-line

Following from this, the outer surface of the bend was investigated in the same way, again with strain values being recorded from corner nodes along lines beneath the surface (inside the mesh) and on the surface, as demonstrated by the red lines in Figure 3-22.

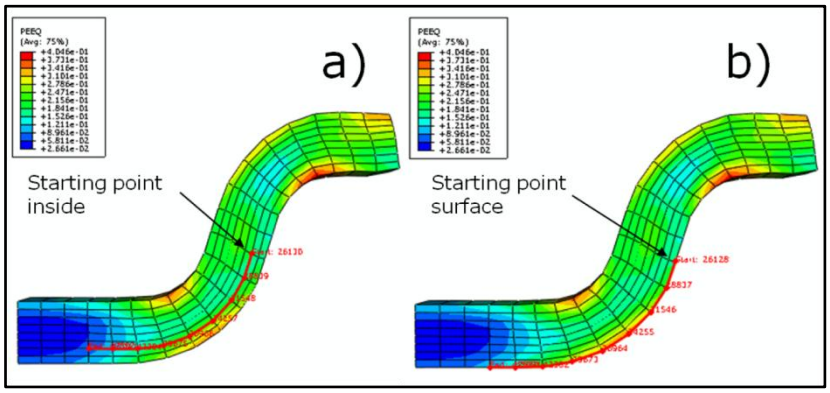

Figure 3-22: Nodes in 3D finite element model from where plastic strain values are taken from at outside bending radius, a) inside node line, and b) surface node line

In Figure 3-23 the strain results for the inside and surface of the fine mesh (300x20x8) are compared to the 2D results, along with an additional node line half way between the inside and surface ones. Again, this additional line only exists in the fine mesh. When compared to Figure 3-19, the results presented here are much more accurate both for the overall distribution, and also for the individual strain values of each node. However, the 3D analyses cannot predict the two peaks at 1 and 2.1mm, but simulates these as one single peak. The 3D values are closer to those of the 2D analysis on the right hand of the peak between 2.1 and 4.2mm. Finally it can be said that the fine mesh for the small

band diameter $D_b = 114mm$ can accurately predict the strain distribution on the outer side of the bent area.

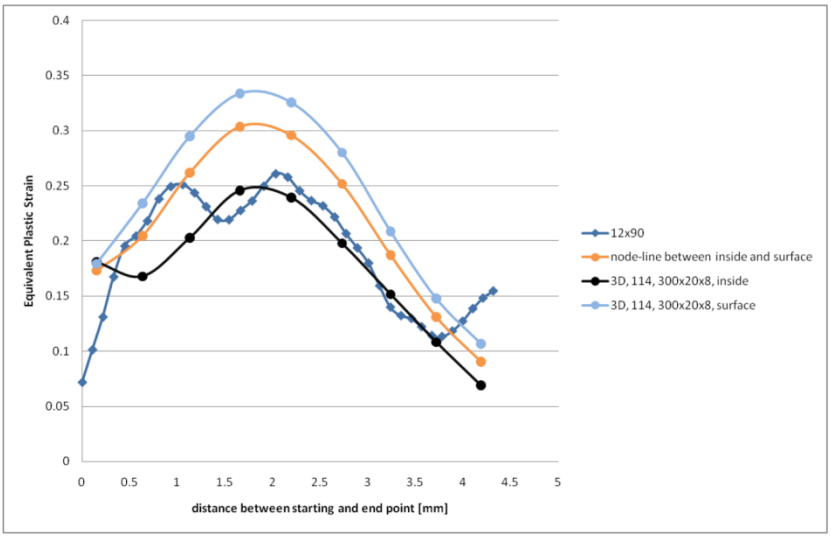

Figure 3-23 Plastic strain for 2D and 3D models after section forming at the outside

A mesh convergence study for this area was undertaken for the inside and surface lines too, and is pictured in Figure 3-24 and Figure 3-25. It can clearly be seen that the band strip length, as well as the number of elements along the strip length have no influence on inside and surface strain results. The only major difference can be spotted on the surface for the fine mesh with 8 elements through the thickness, as these values are larger than those for 4. The overall tendency and distribution is well predicted by all 3D mesh densities.

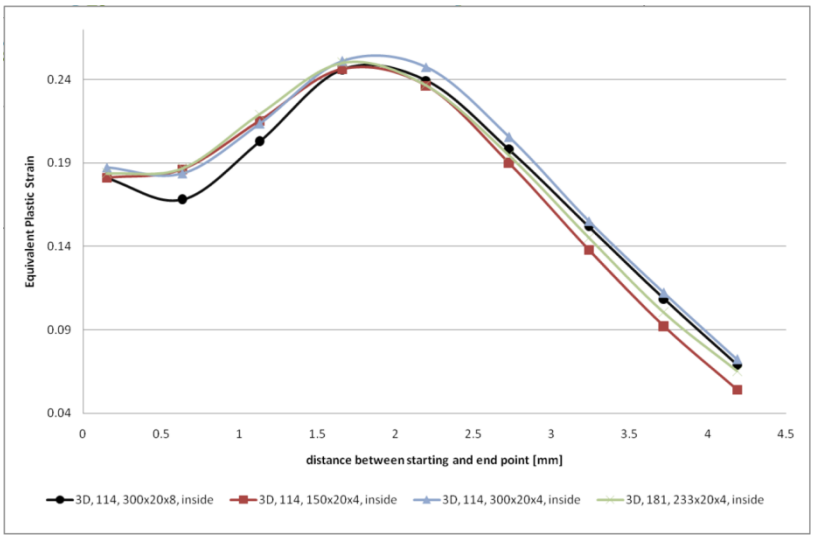

Figure 3-24: Mesh convergence study of plastic strain at the outside for inside node-line

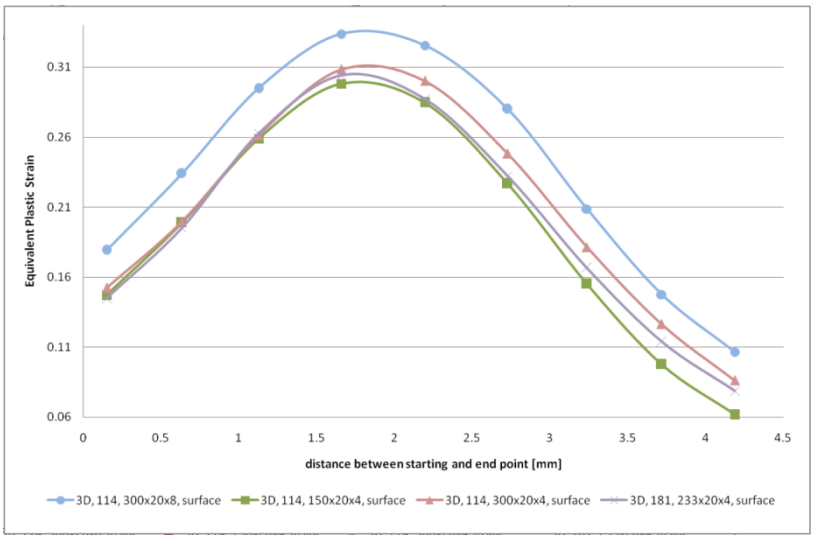

Figure 3-25: Mesh convergence study of plastic strain at the outside for surface node-line

Finally the plastic strain (PEEQ) was reported along a line through the thickness of the cross section, as shown in Figure 3-26, very close to the position of the line in the 2 dimensional counterpart in Figure 3-6b.

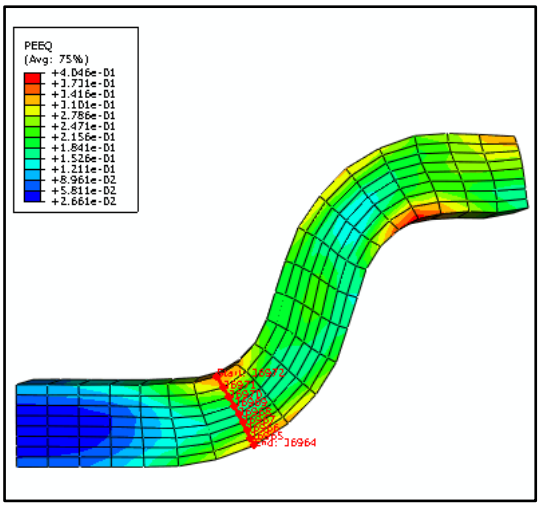

Figure 3-26: Nodes in 3D finite element model from where plastic strain values are taken from through the thickness

The results obtained from this line are shown in Figure 3-27, taking into account that here the red line started and ended at the inside and outside surface of the bent area, unlike in the 2 dimensional simulation. Again, the length of the strip and the number of elements along the length of the strip do not influence the results. Increasing the number of elements through the thickness on the other hand highly impacted on the results, increasing the overall strain values for each node and changing the distribution, thus making it more accurate. The differences when compared to the 2 dimensional case can be ascribed to the coarser mesh not being able to predict and pick up details, as well as

increasing the strip's stiffness. The overall results are predicted with sufficient accuracy by all meshes to proceed with the ring forming.

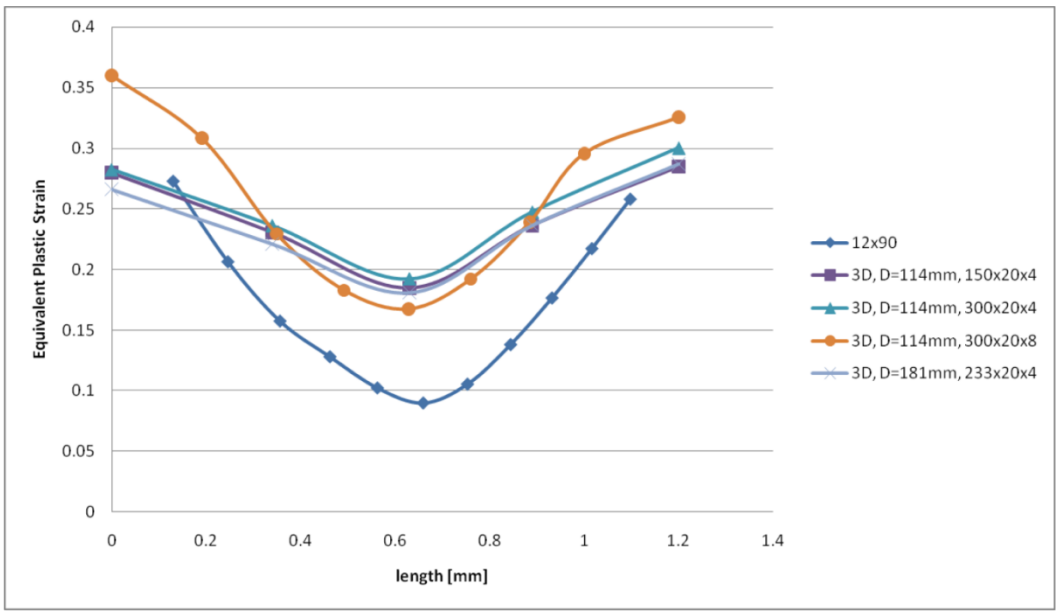

Figure 3-27: Plastic strain for 2D and 3D models after section forming through the thickness

3.6.2 Ring Forming

After establishing that the section deformation and plastic strain (PEEQ) distribution could be predicted well by the 3D model, it is now possible to analyse the cross section while undergoing the ring formation. In Figure 3-28 the cross section for the 3D model (300x20x8 elements), $D_b = 114mm$ is shown at the end of section forming, a), and during ring forming, b). The nodes are taken from the same cross section with l_c=125.787mm as shown in Figure 3-16. Comparing these two images for a first overview, only minor changes in plastic strain can be found.

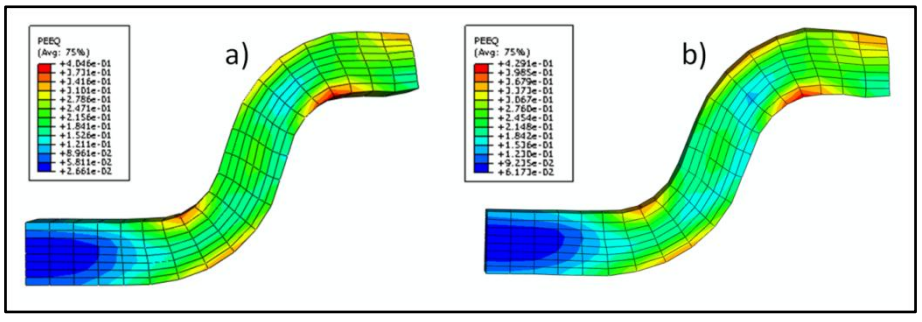

Figure 3-28: PEEQ distribution in 3D model (300x20x8 elements), $D_b = 114mm$, a) at the end of section forming, and b)during ring forming

For a more detailed investigation of the inside, outside, and through thickness strains in the bent area, only the sub-surface node lines of the previous analyses (as identified in

Figure 3-18a and Figure 3-22a) were compared to the ring formation. Figure 3-29 shows the inside area for all 3D meshes, for section and ring formation, and it can clearly be seen that the distribution remains similar but the ring forming increases the absolute values for plastic strain.

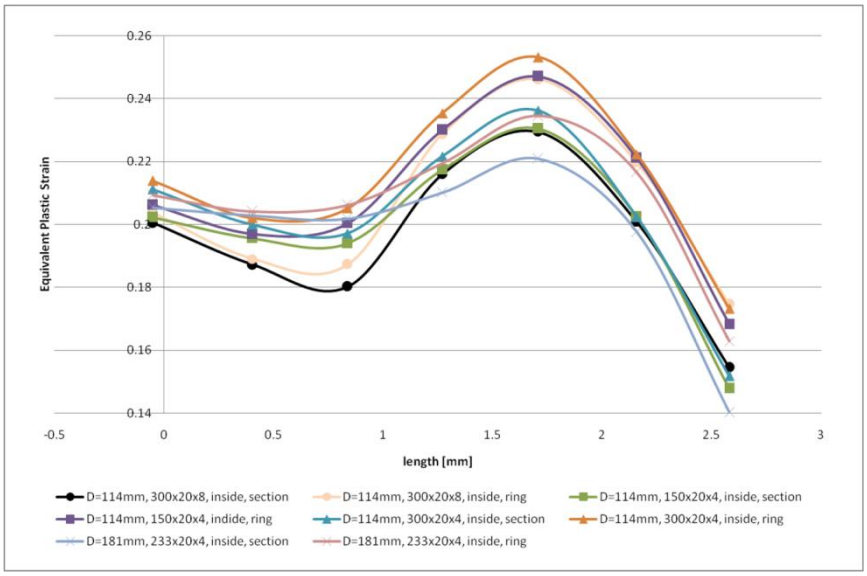

Figure 3-29: Plastic strain in section and ring forming stage at inside

In order to show the plastic strain increase for each node, the differences between section and ring forming are shown in Figure 3-30. For all three meshes of the small band diameter (114mm) the change is minor along the node from 0mm to approximately 0.4mm. However, the differences increase steadily further along the line, but from 1.7mm seem to converge to a constant value. When formed into a ring, the strip is bent around its neutral axis, as pointed out by Brown (2009). Since the first part of the graph (0 to 0.4mm) lies very close to the neutral line very little plastic deformation takes place here, whereas the second part (from 0.4mm on) is situated further away from the neutral axis, where more deformation takes place. The part where the graphs converge is where the node line reaches into the flat part of the V-band cross section. All nodes in the flat part have the same distance to the neutral axis which is why the same amount of plastic strain is induced in the strip during ring formation.

For the larger clamp size (181mm) the change in plastic strain is the same as for the three previous meshes between 0 and 0.4mm. From that point on the change in plastic strain increases linearly along the node line, and, unlike for the smaller band sizes, seems not to converge to a constant value. The changes for larger clamps (181mm) are also smaller than those for their smaller counterparts (114mm), and become larger only from 2mm onwards. These two effects are mainly due to the larger ring diameter, as less plastic strain was induced into the strip during ring formation.

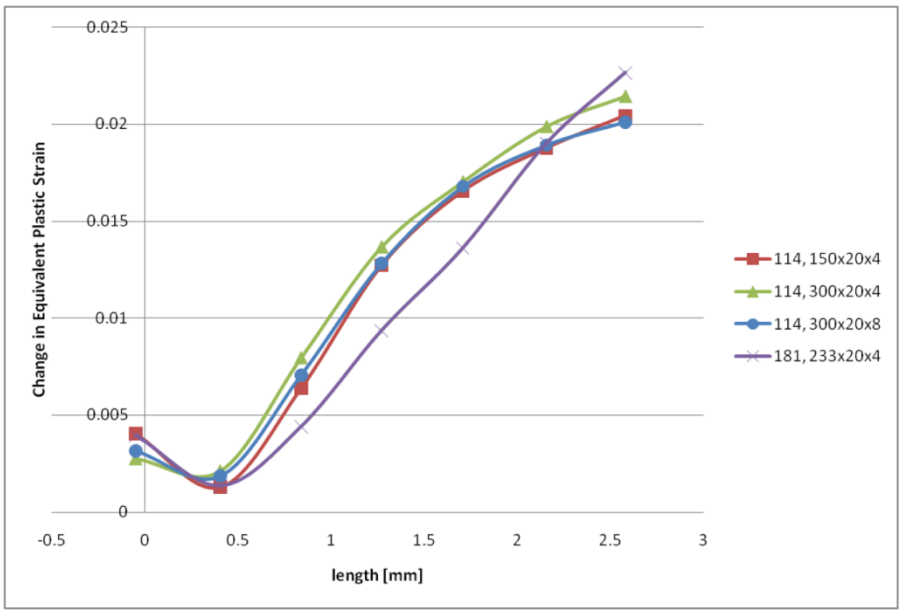

Figure 3-30: Change in equivalent plastic strain between section and ring forming at inside

For the outside of the bent area, Figure 3-31 shows the plastic strain distribution for the same nodes of the cross section after section formation and during ring formation. Only minor differences can be seen between the 3 meshes for the small V-band (114mm), and also for the larger band clamp (181mm).

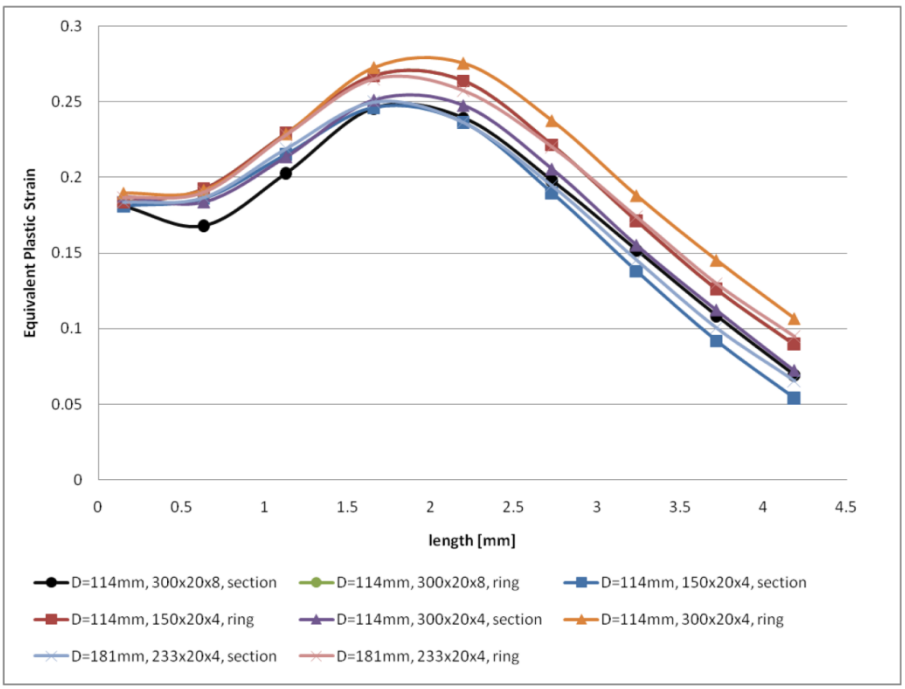

Figure 3-31: Plastic strain in section and ring forming stage at outside

In order to get a much more detailed view, Figure 3-32 shows the plastic strain increase, induced into the strip during ring formation. For small sized band clamp (114mm), the

three graphs start off at approximately the same values as in Figure 3-30, because the nodes reported at the inside and outside bending zone have a similar distance from the neutral axis. The plastic strain then linearly increases until the graphs reach a constant strain value from 2.8mm on. This convergence could also be seen previously for the inside area, where the nodes are situated along the flat part of the cross section and have all the same distance to the neutral axis. However, the nodes of the node line reaching into the flat part on the outside bent area have a much larger distance to the neutral axis than those of the inside bent area, which is also why the graphs in Figure 3-32 tend to converge to a much larger value.

The same can be observed for the larger band (181mm), whereas now all plastic strain values are smaller than those of the smaller band, which is, again, due to the larger ring diameter (181mm), as less deformation takes place, and hence, inducing less plastic strain.

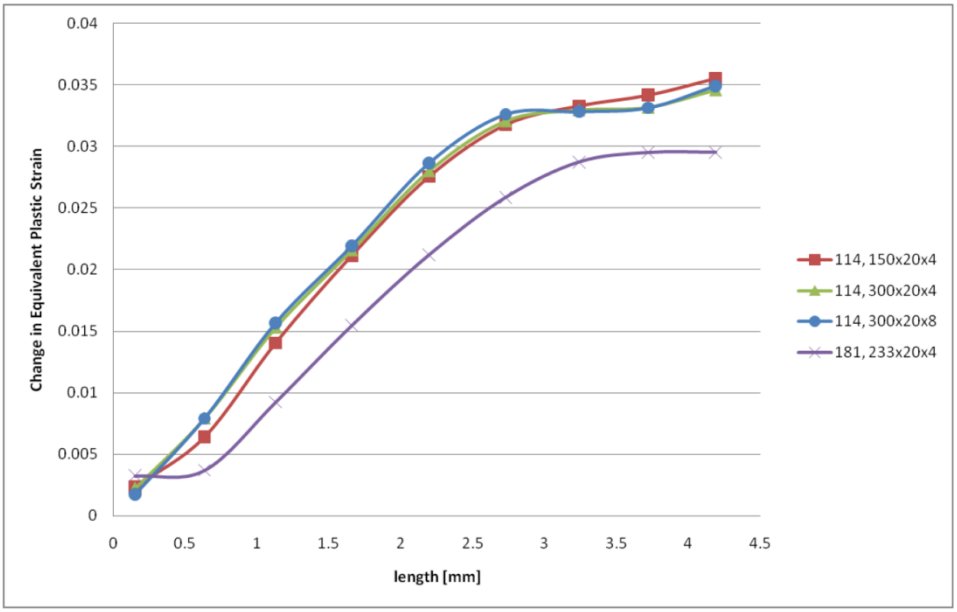

Figure 3-32: Change in equivalent plastic strain between section and ring forming at outside

For the previous two cases, the mesh density is shown not to influence the plastic strain distribution significantly. For the through thickness strain on the other hand an increase of elements does significantly influence the strain, especially further towards the surface, as shown in Figure 3-33.

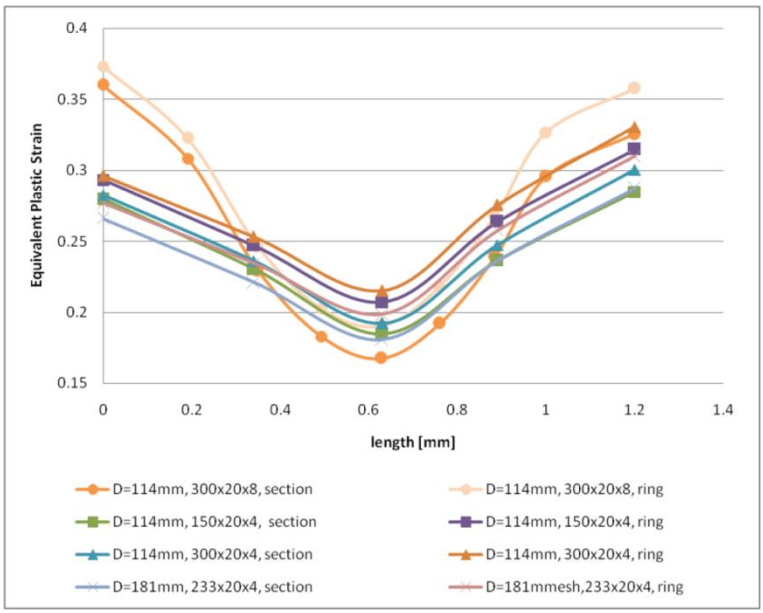

Figure 3-33: Plastic strain in section and ring forming stage at through thickness

This effect can also be noticed when comparing the amount of plastic strain induced during ring formation, with more elements giving a much smoother graph, and showing more details. The graphs for the three meshes of the small band clamp (114mm) in Figure 3-34 confirm the phenomena spotted in the previous two cases, where more strain is induced at the outside than inside of the bent area, as the latter is closer to the neutral axis where less deformation during ring formation took place.

The fourth graph for the larger clamp (181mm) also supports this observation as well as it shows that less plastic deformation is induced during ring formation as the diameter being formed increases.

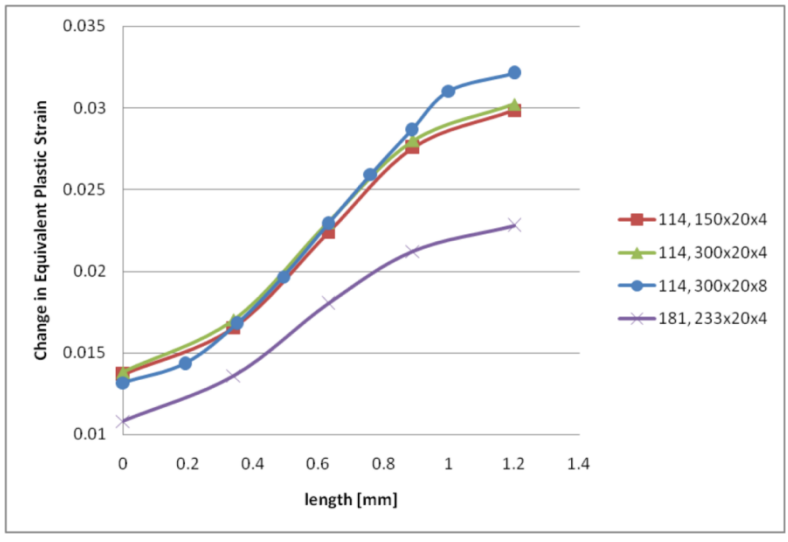

Figure 3-34: Change in equivalent plastic strain between section and ring forming at through the thickness

Moreover, it was found during the finite element analysis that the back of the V-band cross section widens as the mesh density is increased.

3.7 Conclusion

The 2 dimensional finite element model allowed the use of very fine mesh densities whilst not exceeding a sensible CPU time to solve the analyses. This allowed the strip cross section to be examined in great detail, which showed that the larger equivalent plastic strains (PEEQ) appeared, as expected where the greatest material deformation took place in the bend regions. It was also found that hydrostatic stresses induced by contact pressure from the rollers bending the band strip lead to localised decreases of the plastic strain. These highly localised peaks and valleys of the strain distribution on the inside of the bent area may to be one of the reasons for the crack growth in this region that has been observed in the field. The mesh convergence study demonstrated that even the coarsest mesh was giving results of sufficient accuracy.

The 3 dimensional finite element model on the other hand did not provide as much detailed information on the cross section of the band strip but was able to successfully simulate the whole manufacturing process of section and ring formation. For the section forming stage, the 3 dimensional plastic strain results were compared to those of the 2 dimensional one, and showed good agreement, though slightly over-predicting the strain. In a mesh convergence study, the chosen mesh densities, along with the strip length were shown to have only little, and very localised impacts. Moreover, it was found that the amount of plastic strain induced into the strip during ring formation depended on the formed ring diameter, and reduced as the diameter increased. For each node, all meshes predicted slightly different absolute values for section and ring deformation when compared to each other. For the same ring diameter on the other hand, they predicted the same increase in plastic strain induced during ring forming. Moreover, it was found during the finite element analysis that the back of the V-band cross section widens as the mesh density is increased

4 Finite Element Models Predicting the Ultimate Axial Load Capacity of V-band Retainers

In this chapter finite element (FE) models predicting the Ultimate Axial Load Capacity, F_{UALC}, of V-band joints are specified, using axisymmetric and three dimensional approaches. The numerical analyses took into account several parameters introduced during the manufacturing process of the V-band retainers and flanges, such as different diameters and thicknesses, as well as parameters occurring during the assembling and use of V-band joints, such as the coefficient of friction and the axial clamping load, F_{ACL}. Only the V-band of the retainer was simulated, not accounting for the trunnion loops and T-bolt. The F_{UALC} of V-band retainers is defined in section 1.1, as the maximum axial load that leads to unrecoverable separation of the flanges, and hence total failure of the V-band joint.

More details about sizes and associated initial dimensions of V-band retainers and flanges used in this project can be found in Shoghi (2003).

4.1 Definition of Axisymmetric Finite Element Model

Parts of this section are taken from Barrans and Muller (2009).

Although Shoghi (2003) has pointed out that the contact load distribution between the retainer and the flanges is non uniform around the circumference due to friction, the finite element model presented here assumed the contact pressure to be uniform as a first approximation. In order to simulate the joint, a finite sliding contact interaction was applied. Figure 4-1 shows that the V-band joint cross section is symmetrical where the flanges mate, hence the retainer was approximated to be axisymmetric and the plane of symmetry between the two flanges was used to reduce the model size.

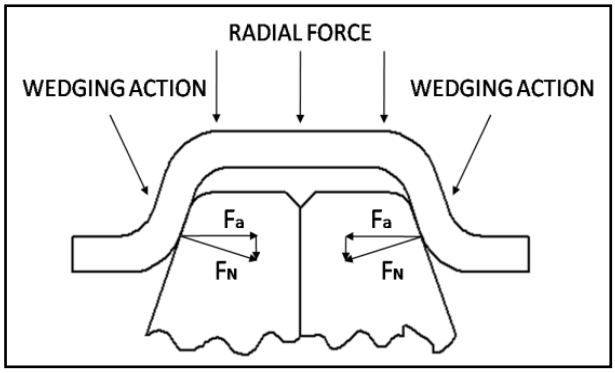

Figure 4-1: Symmetrical cross section of assembled V-band retainer

Figure 4-2 shows the axisymmteric FE model, consisting of half the V-band cross section and one flange, in which the V-band was constrained by a symmetry boundary condition (BC) at the plane of symmetry, to prevent it from moving in the axial direction. The V-band was modelled using a solid body, applying linear elements with reduced integration as suggested by Dassault Systems (2007a) and as recommended by Konter (2000) for similar cases of contact analyses, along with a penalty algorithm as these tend to converge more easily as stated by Konter (2005). In most applications the flange is made of a much harder material than the retainer such as cast iron (e.g. GGG 25) and also has a more substantial geometry. It can therefore be treated as a rigid body. This approximation was also made by Shoghi (2003) when developing a theoretical model for flat and V-section band clamps. Hence, the flange was defined as an analytical rigid body that does not require any sort of meshing, reducing computing time, and the complexity of the contact analysis, enabling it to converge faster. A displacement BC was applied to the reference point (RP) to keep the flange in position. The figure also shows all geometrical parameters referred to in this chapter.

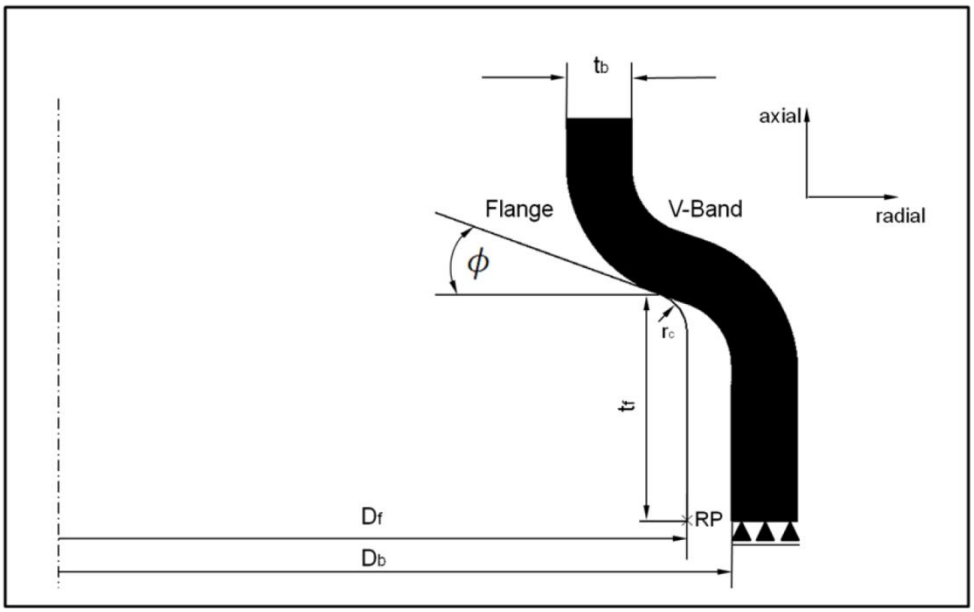

Figure 4-2: Axisymmetric finite element model of V-band joint

In reality the V-band retainer is assembled onto a pair of flanges by tightening the T-bolt nut, as discussed in section 1.1. In the simulation this process was enforced by generating an artificial thermal strain in the band to shrink it onto the flange. This part of the simulation can be seen in Figure 4-3, where in a) a retainer is loosely placed around the flange in the initial position, and b) the retainer is fully assembled and contact established.

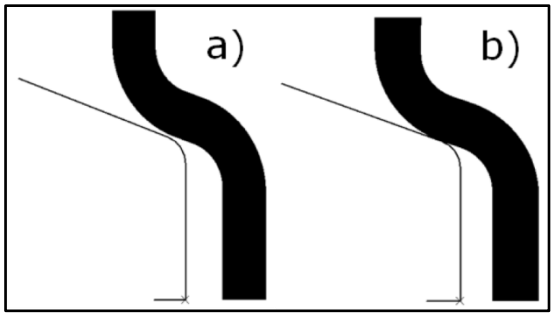

Figure 4-3: Assembling process of V-band retainer in axisymmetric finite element model, a) un-assembled, b) assembled (T-bolt nut tightened)

The T-bolt tightening generates an axial load pushing both flanges together, called the axial clamping load F_{ACL}, and in the finite element model was reported at the flange's reference point (RP). An iterative process was then required to determine the thermal load necessary to obtain the correct induced load for each analysis as due to the change of geometry (e.g. different diameter or flange thickness) or coefficient of friction, the contact point between flange and retainer changed. In reality and in the 3 dimensional model, the contact point mentioned here for the axisymmetric model is in fact a contact line along the circumference of the band.

After the retainer was assembled and the axial clamping force, F_{ACL}, acting, a displacement had to be applied to the flange's RP, which then moved the flange in the positive axial direction, deforming the cross section of the V-band. This axial movement of the flange simulated failure of the joint, while still reporting the axial reaction force on the RP. The undeformed (not assembled) and deformed (fully failed) modes of a joint with a band diameter, D_b, of 235mm are shown in Figure 4-4.

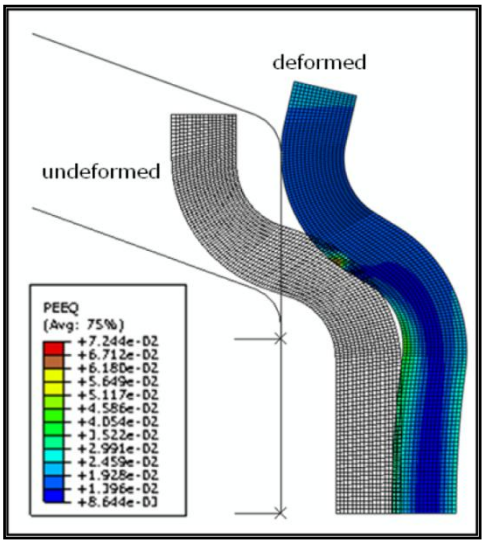

Figure 4-4: Initial and deformed geometry and equivalent plastic strain (PEEQ) of FE model for D_b=235mm

Simulating irrecoverable separation of the flanges, and, hence failure of the whole V-band joint, the F_{UALC} could be defined as the maximum axial reaction force acting between the retainer and the flange as indicated by a red arrow in Figure 4-5, which also shows the position of the axial clamping load F_{ACL}.

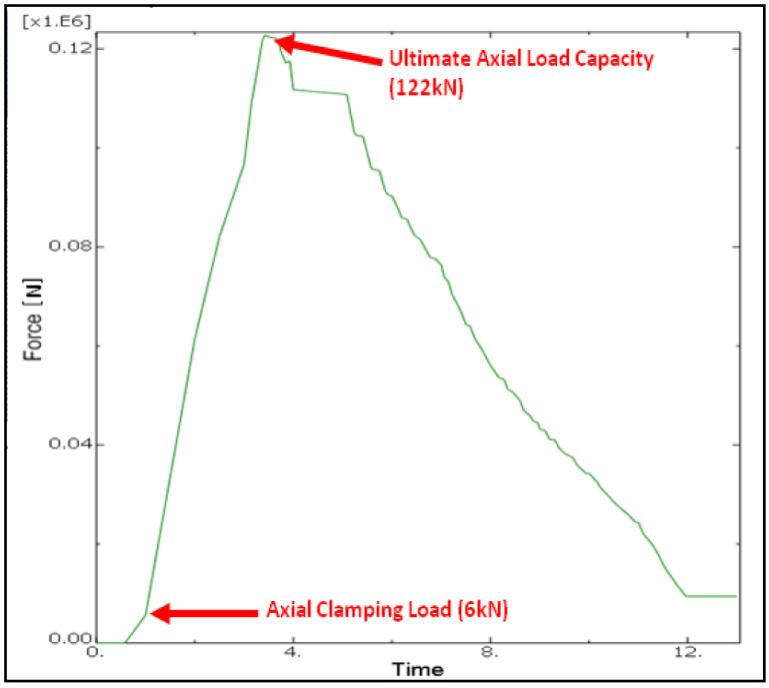

Figure 4-5: Predicted ultimate axial load capacity and axial clamping load reported from the axial reaction force between retainer and flange

4.2 Mesh Convergence Study for Axisymmetric Model

This section is entirely taken from the authors own publication Barrans and Muller (2009).

Using a fixed band diameter D_b = 250 mm, analyses were carried out for coefficients of friction of 0 and 0.3, for flange corner radii r_c of 0.3 and 0.5 mm, and for several element thicknesses along the sliding contact surface.

4.2.1 Ultimate Axial Load Capacity

The analyses generated appeared to be highly dependent on the mesh type and mesh element thickness especially along the contact sliding surface. Figure 4-6 shows the results for the ultimate axial load capacity F_{UALC} for a model with r_c = 0.5 mm and a coefficient of friction μ of 0.3. As can be seen in this figure the graph for the structured mesh seems to converge to a certain load value for decreasing element size. The graph for the free mesh oscillates with decreasing element size.

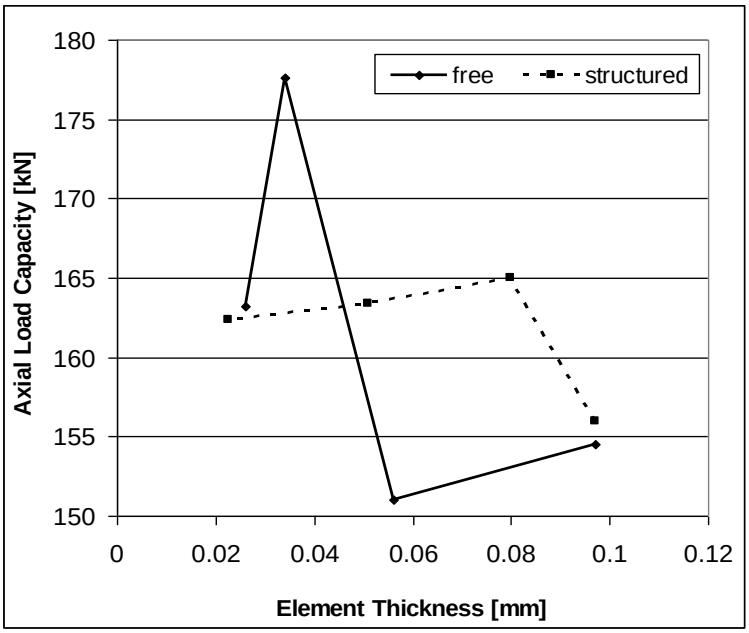

Figure 4-6: Axial Load Capacity depending on Element Thickness for free and structured mesh, μ =0.3 and r_c = 0.5 mm.

Figure 4-7a and b indicate the problems that occurred during this analysis work for this small band diameter and therefore needed further investigation. Figure 4-7a shows the axial reaction force at the flange reference point. The very high peak at 255 kN is clearly erroneous. The relative positions of flange and band at this peak are shown in Figure 4-7b. It can be seen that once the flange starts to slide the elements along the band clamp surface become heavily deformed. In further analyses these erroneous peaks were noted but were not reported as ultimate axial load capacity, and could be reduced by a finer mesh. Ignoring this peak, the ultimate axial load capacity F_{UALC} of this model is 162 kN.

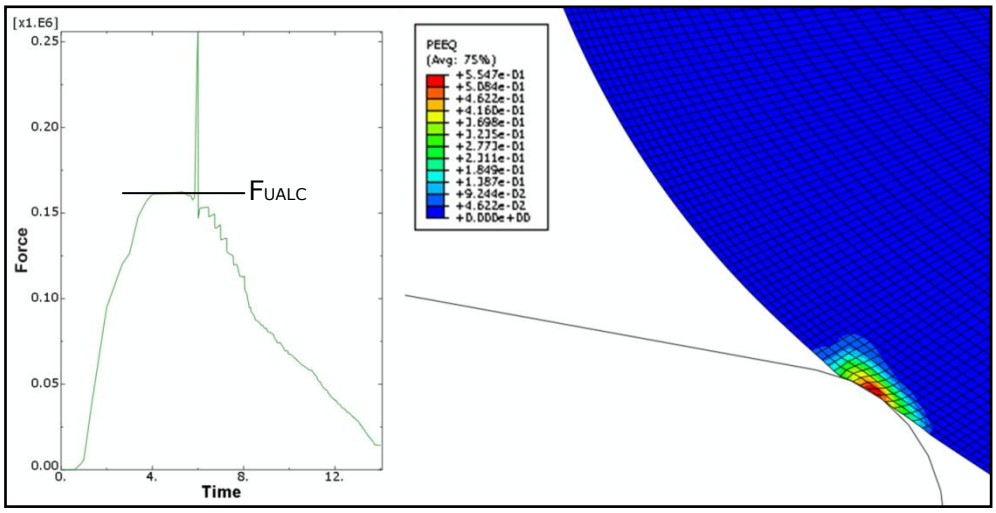

Figure 4-7: Results for r_c = 0.5 mm, μ= 0.3, structured mesh, high mesh density a) Axial load at reference point during failure b) position of flange at peak axial load.

Figure 4-8 shows the results for the same model but with a free, unstructured mesh with nearly the same element size. Again, there is an erroneous peak at the same position in the failure process but it is just at 175kN (Figure 4-8a), whereas the more reliable axial load capacity seems to be at 163kN almost the same as for the structured mesh. Figure 4-8b also indicates the same phenomenon of elements starting to deform as the flange starts to slide.

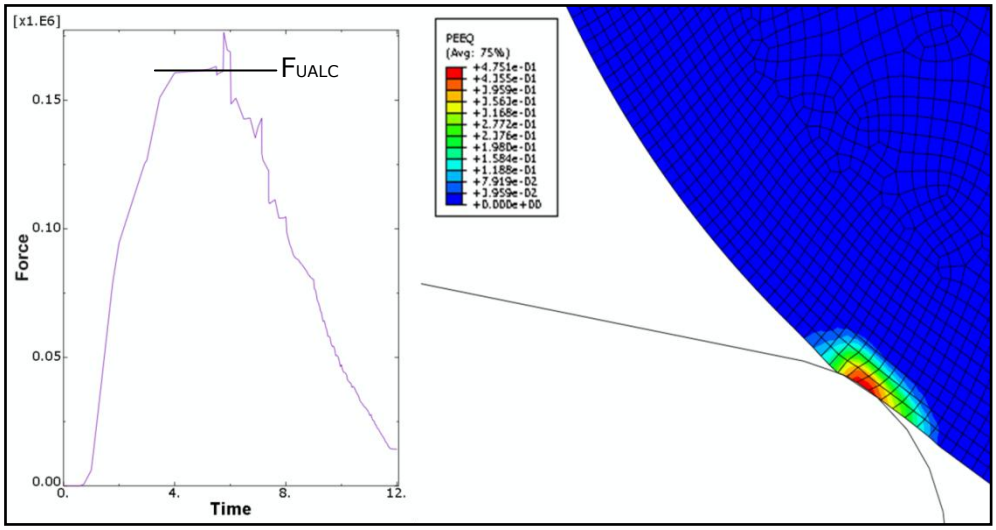

Figure 4-8: Results for r_c = 0.5 mm, μ = 0.3, free mesh, high mesh density a) graph of axial load during failure, b) detailed view of position of flange at axial load

In both cases mentioned above the peak axial load capacity occurs before the flange starts to slide. This shows that as soon as plastic deformation starts in the V-band material, as shown in Figure 4-8b the ultimate axial load capacity has been reached. This phenomenon has been observed for models of this band diameter and below.

4.2.2 Plastic Strain along inner Surface ε_{ps}

In this section the effect of element thickness along the contact sliding surface of the V-band on the development of plastic strain in the band clamp is analysed, for a model with r_c=0.3 mm and μ=0.3. Unlike the models for r_c=0.5 mm these models generated many more problems. Figure 4-9 identifies the position of the maximum plastic strain ε_{ps} (PEEQ) on the contacting surface.

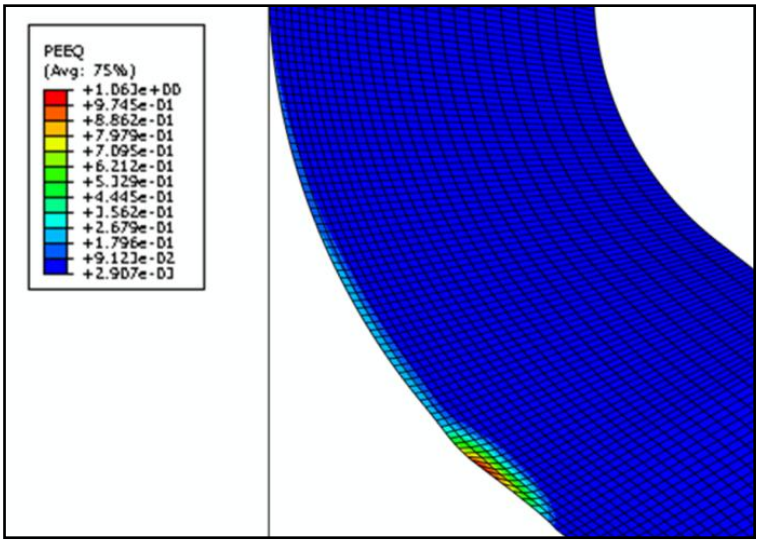

Figure 4-9: Plastic strain ε_{ps} development at contact surface.

These values are shown in Figure 4-10. The two graphs show that the maximum plastic strain increases as the element size decreases. This is due to the one integration point of the reduced integrated linear elements getting closer to the contacting surface, giving much more accurate results. The two meshing methodologies can be seen to give very similar results.

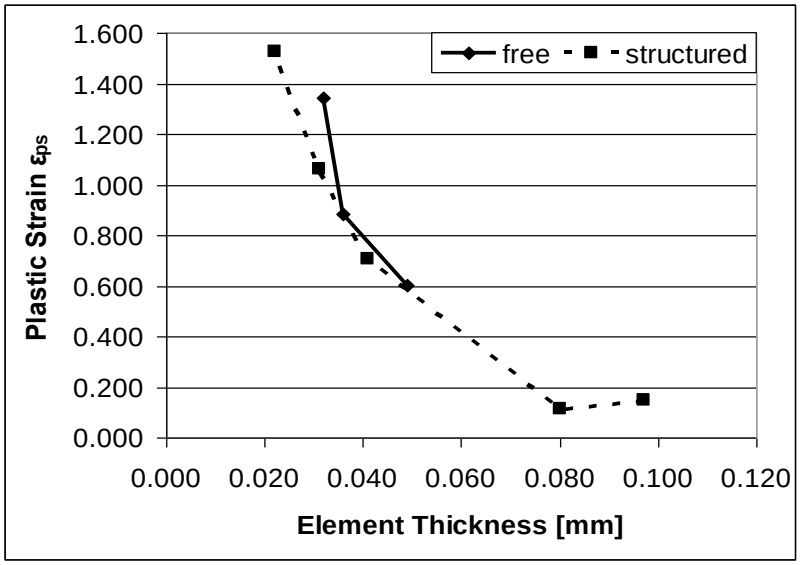

Figure 4-10: Maximum plastic strain along contact sliding surface for free and structured mesh for r_c= 0.3 mm and μ =0.3

The peak plastic strain described above is particularly interesting when discussing the contact pressure between flange and band. It was also observed, that reducing the element thickness along the sliding surface reduced the effects of the plastic strain. Figure 4-11 identifies the point on the band where large plastic strains, ε_{pr}, caused substantial band deformations and hence joint failure. This point stays the same for all

models used in this analysis work and as discussed in chapter 3, is very likely to be in the region where a crack through the whole thickness of the band may start to develop.

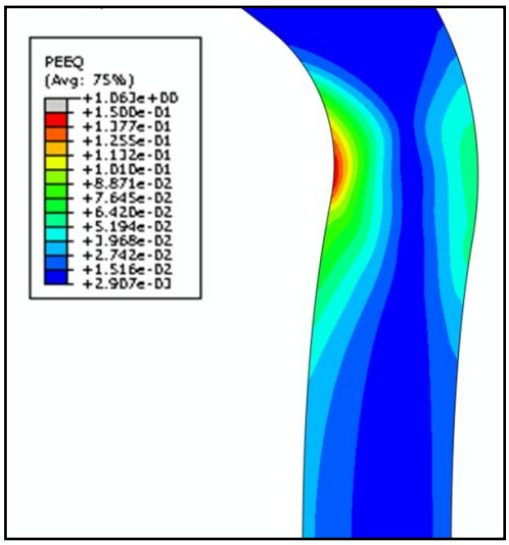

Figure 4-11: Position of maximum plastic strain ε_{pr} sampling point for Figure 4-12

Although the two graphs in Figure 4-12 seem to differ slightly, they still indicate the same tendency of plastic strain development. Again the plastic strain increases as the element size in this region has been reduced. The results for the structured mesh seem to be slightly more reliable because the element thickness along the whole inside of the band was reduced whereas for the free mesh only the element size along the contact surface itself was decreased. Moreover, the structured mesh allowed a much larger range of element thicknesses to be applied, whereas the free elements restricted the thickness to a much lower range.

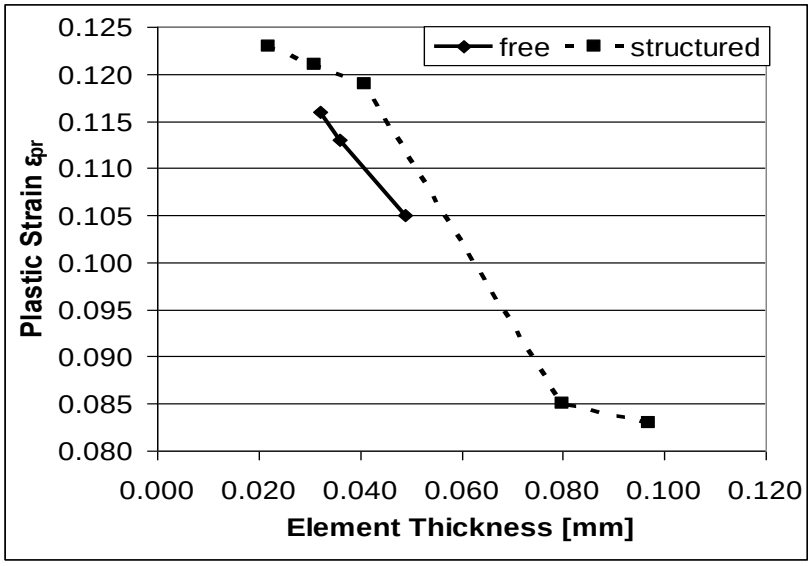

Figure 4-12: Maximum plastic strain taken from end point of radius for r_c =0.3 mm and μ= 0.3

4.2.3 Comparison of Explicit and Implicit Analysis

In sub-sections 4.2.4 to 4.2.6 the analyses for flange corner radii r_c= 0.1mm, 0.3mm, and 0.5 mm along with coefficients of friction μ= 0, 0.15, and 0.3, with a band diameter D_b = 114 mm are discussed and compared. The analyses were each solved using explicit and implicit solvers. The time periods for applying load were taken from an initial frequency analysis of the band where the first natural frequency f_n was predicted to be about 6850 cyc/time. The corresponding time period was t_n=0.000146 sec, which in this section is referred to as normal time. Time periods ten and fifty times slower (t_{10}=0.00146 sec and t_{50}=0.0073 sec) were also used.

4.2.4 Explicit Analysis Mesh Structure

Figure 4-13a and b show models that have reached the full failure state having the two extreme cases of very small radius r_c= 0.1mm combined with a very high coefficient of friction μ= 0.3, and a model with a relatively large radius r_c= 0.5mm and μ= 0.3, using an explicit solver. As can be seen in a) the small radius and high friction create a large distortion of the elements along the contact surface of the band clamp generating large plastic strain ε_{ps}= 180 whereas in b) the contact surface seems to be deformed as expected with a maximum plastic strain of ε_{ps}= 0.934, which seems much more realistic. This demonstrates that the reliability and accuracy of the explicit analyses is highly dependent on the contact edge radius. During this analysis work it has been experienced that a larger r_c results in a more stable solution giving more realistic results.

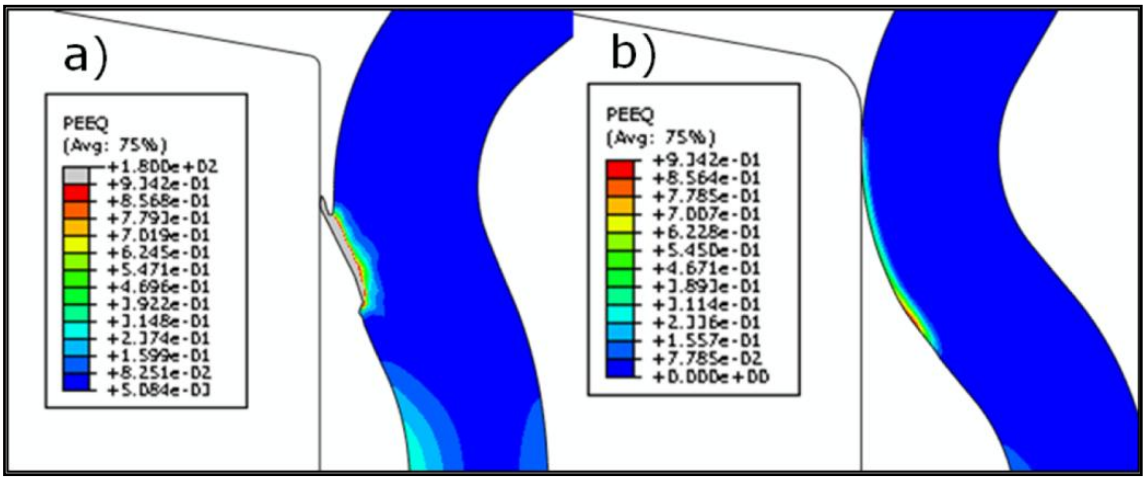

Figure 4-13: Full failure state using explicit solver and free mesh, 10 times slower a) r_c=0.1 mm μ =0.3 and b) r_c=0.5 mm μ =0.3

As can be seen in Figure 4-14a and b also the coefficient of friction has a significant influence to the accuracy of the results. Figure 4-14b indicates that for the same corner radius r_c=0.3 the higher coefficient of friction μ=0.3 results in significantly deforming the elements along the contact surface and giving too large plastic strain results

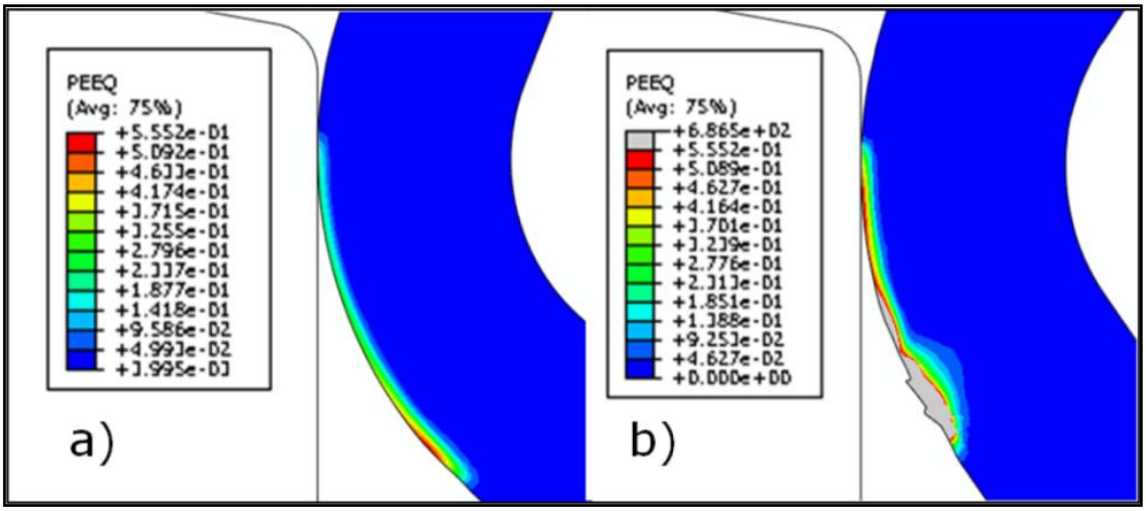

Figure 4-14: Model of V-section band clamp reached full failure mode using explicit solver for free mesh, 50 times slower a) r_c=0.3 mm μ =0 and b) r_c=0.3 mm μ = 0.3

Several explicit analyses have shown that the type of mesh had only a minor effect on the accuracy of the results. Comparing the maximum plastic strain values along the contact surface of two explicit models, the strain values are nearly the same. This demonstrates that the mesh type has almost no effect on the accuracy of the results generated.

As obtained in this subsection the results for contact in an explicit analysis highly depends on the radius of the rigid master surface (flange), the coefficient of friction, whereas the mesh type has no significant influence.

4.2.5 CPU (Run) Time

All the analyses using an implicit solver and a free mesh ran faster than their explicit counterparts which were set to run 10 times slower than the time t_n associated with the first natural frequency f_n. Moreover, the run time for the explicit solver increased as the mesh was changed from free to structured. This increase was due to an increase of elements since for the free mesh only the elements along the sliding surface were kept small with larger elements being allowed away from this surface. For the structured mesh, all elements in the model were kept the same size as those at the contacting surface.

4.2.6 Reliability of Results

In Table 4-1 results for explicit and implicit models with a band diameter D_b =114 mm are compared, for flange corner radius r_c=0.5 mm, a range of coefficients of friction and 10 times slower than t_n for the explicit analyses.

As stated in the previous sub-section, the CPU time increases a lot as the mesh density gets finer but comparing the results for ε_{pr} to the implicit results there is no significant

difference. The results obtained here along with the results from both sub-sections before support the knowledge of the accuracy and reliability increasing as the coefficient of friction decreases and the contact edge radius r_c increases. The mesh type for explicit analyses has only a minor influence on the accuracy but significantly increases the CPU time.

Table 4-1: Comparison of implicit and explicit solver for band diameter D_b=114 mm.

Flange Corner Radius r_c [mm]	Coefficient of Friction μ	Max. Plastic Strain at Corner End ε_{pr}	Mesh Type	Load Time, x times slower than t_n (only for Explicit)	Solver Type	CPU (Run) Time [min]
0.5	0.3	0.1381	free	---	Implicit	9.0
0.5	0.3	0.1512	free	10	Explicit	19.0
0.5	0.3	0.1519	structured	10	Explicit	32.0
0.5	0.15	0.1021	free	---	Implicit	9.5
0.5	0.15	0.1182	free	10	Explicit	14.0
0.5	0.15	0.1183	structured	10	Explicit	31.0
0.5	0	0.0773	free	---	Implicit	9.2
0.5	0	0.0804	free	10	Explicit	14.0
0.5	0	0.0812	structured	10	Explicit	30.0

After carrying out these convergence studies, the decision was made to apply a fairly fine structured mesh to the axisymmetric FE-models, since it proved to be sufficiently accurate and was reliable. An implicit solver was chosen, as it was found to converge much faster, whilst providing accurate results.

4.3 Three Dimensional Finite Element Model

4.3.1 Definition of Model

The 3 dimensional model predicting the F_{UALC} discussed in this section is the same model as in section 3.5, in which the cold roll forming process was investigated, hence it had the same material properties as in section 3.2 including the density mentioned in section 3.5. The mesh densities and diameters (D_b=114mm) were the same as listed in Table 1, using 8-node linear brick elements with reduced integration, and the analyses were carried out in an explicit environment. When compared to the previously discussed

model, it has two major benefits. It contained all residual stresses and strains induced during the manufacturing process, and accounted for the non-uniform contact pressure distribution between band and flange.

The model consisted of three stages, moving, tightening and failing the V-band retainer, and started after the ring was formed in the previous simulation as shown by Figure 4-15a. The formed V-band (ring) was then moved so that it was loosely placed around a flange, as can be seen in Figure 4-15b.

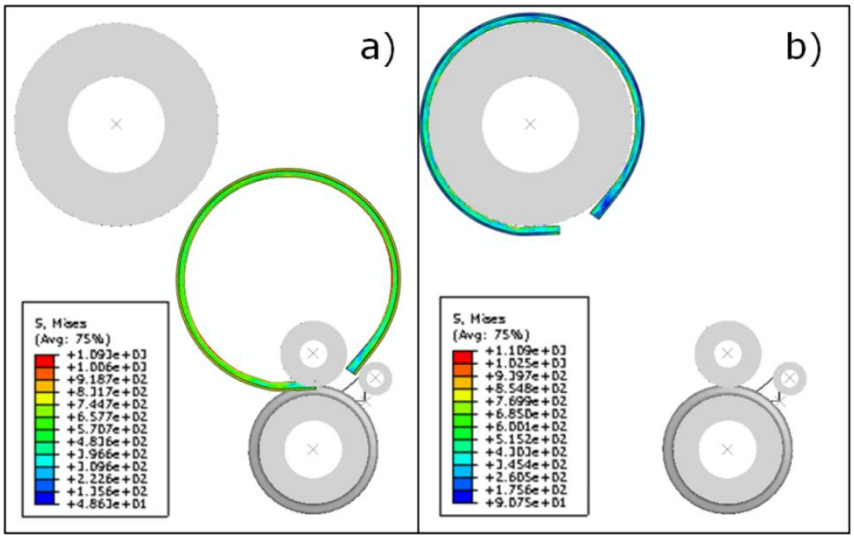

Figure 4-15: Moving formed ring away from final rolling stage in a) and placing loosely around the flange in b)

The 3 dimensional model had in common with its axisymmteric counterpart, the fact that only one flange and one half of the V-band were modelled due to the symmetry of the joint. In order to prevent rigid body motion, the flange was constrained in all directions on the reference point (RP) in its centre, and the band was given a symmetry boundary constraint in the axial direction on its symmetry-surface. After placing the band around the flange (Figure 4-16a), a surface traction was then applied at both ends of the band simulating the T-bolt force, F_β, being generated during assembling when the T-bolt nut is tightened, establishing contact between band and flange (Figure 4-16b). Thereupon, the flange was moved in the axial direction, simulating a failing V-band joint (Figure 4-16c), constantly reporting the axial reaction force on the flange's RP. In the same way as for the axisymmetric model, the maximum force reported was then defined to be the F_{UALC}. The contact interaction and properties were the same as for the previous model in 3.5, for a coefficient of friction, μ, of 0.2, and r_c=0.8mm.

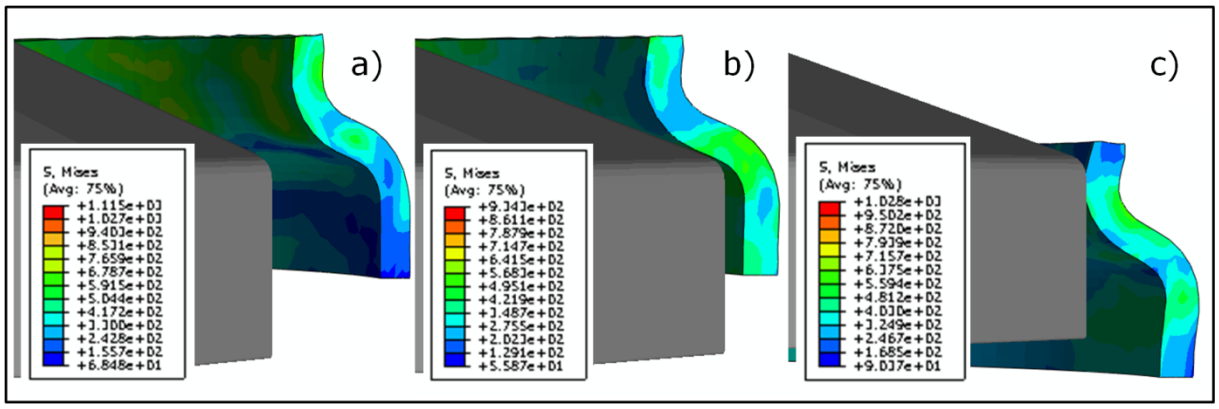

Figure 4-16: Assembling procedure in 3D FE model for D_b=114mm, a) placing band loosely around flange, b) tightening it onto the flange, and c) applying an external axial load by displacing flange

4.3.2 Mesh Convergence Study

In this sub-section, the impact of the mesh density on the ultimate axial load capacity F_{UALC} is presented over a range of different flange thicknesses t_f starting from 3mm to 5mm. The mesh densities here are the same as for the finite element models used to investigate the cold roll forming process in section 3.5.

Figure 4-17 illustrates three graphs for models with an axial clamping load F_{ACL} of 15kN, a coefficient of friction μ of 0.2, and a band diameter D_b of 114mm as well as the three different mesh densities. The graphs display results of the ultimate axial load capacity F_{UALC} over the flange thickness t_f.

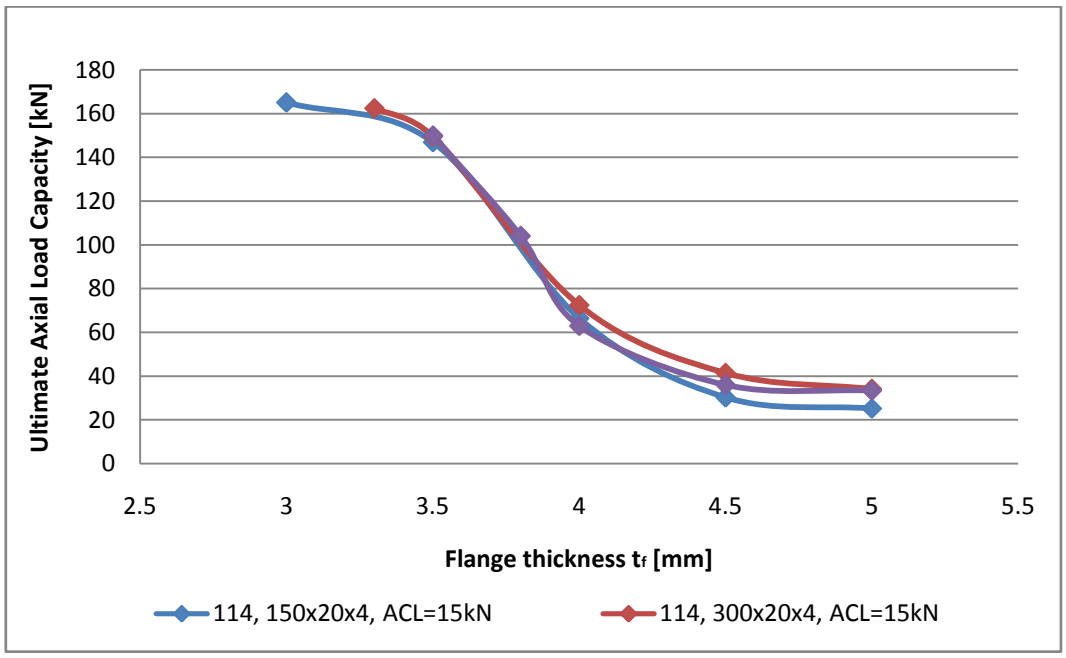

Figure 4-17: Mesh convergence study for 3D finite element model

For the bands (114mm) a finer mesh (reducing element size) results in only minor increases of the ultimate axial load capacity. However, increasing the mesh densities prevented the finite element models from applying the required axial clamping load of 15kN for smaller flange thicknesses. Therefore the graphs for the medium mesh (300x20x4 elements) do not give any results below 3.3mm, and for the fine mesh (300x20x8 element) below 3.5mm (Figure 4-17). This happens because during the roll forming simulation discussed in chapter 3, the back of the V-band cross section becomes wider for finer meshes. When tightened onto a thin flange the bands with a finer mesh are incapable of applying an axial clamping load of 15kN as contact is established between the back and the flange rather than the flat part of the leg and the flange, so that the wedging action of the V-shape cannot apply, as shown for the cross section on the opposite side of the T-bolt in Figure 4-18. The cross sections in this figure are the same as those used in chapter 3 described by the length l_c. Furthermore, it was observed that the T-bolt force applied to free ends of the V-band increased with the mesh density, in order to establish the same amount of axial clamping load. This is because the V-band looses stiffness as the elements through the section and along the circumference are increased, especially since linear elements with reduced integration were used. Hence, less T-bolt force is needed for the stiffer band with the coarse mesh and fewer elements.

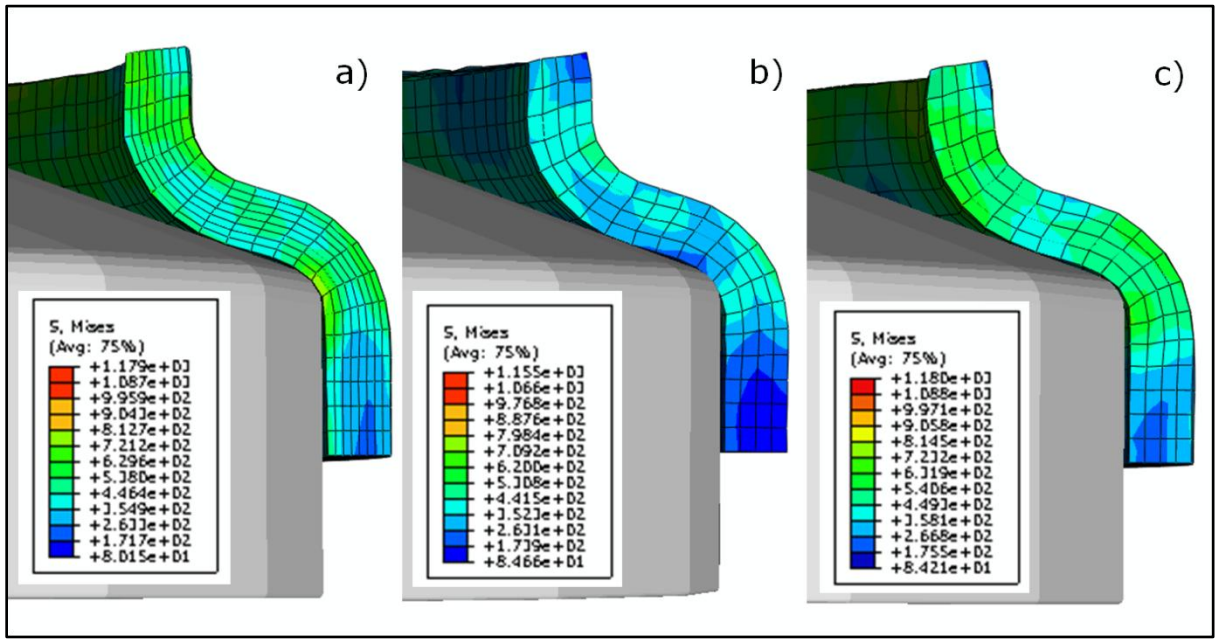

Figure 4-18: 3D FE models when tightened onto flanges for, a) fine mesh with 300x20x8 elements, b) medium mesh with 300x20x4 elements, and c) coarse mesh with 150x20x4 elements

4.4 Comparison of Axisymmetric and 3D Results

The results of the 3D model with medium mesh density (300x20x4) are compared to the axisymmetric FE model presented in sections 4.1 and 4.2, for F_{ACL}=15kN, and a coefficient of friction μ=0.2.

It must be noted here that the initial flange thickness for the 3D model was t_f=3.8mm, whereas for the axisymmetric model it was t_f=4.5mm, a difference of approximately 0.7mm. This was mainly due to the fact that the cross section of the 3D model was created through the cold roll forming process, for which the rolls were modelled using average dimensions gathered from drawings. The cross section of the axisymmetric model on the other hand was created from dimensions directly taken from drawings showing the desired end product and final formed cross section after the rolling operation. Taking into account tolerances in these drawings the average values for each dimension were then used. The difference of 0.7mm was therefore introduced by a combination of simulating the rolling process for the 3D model and two different sets of tolerances. In Figure 4-19, the results for the 3D and axisymmetric models are compared and it can be noticed that both graphs show a similar distribution of the F_{UALC} when varying the flange thickness. For band diameters between 4.5mm and 4.8mm the difference between both graphs is only minor. However, for band diameters below 4.5mm, the difference significantly increases, as the axisymmetric results settle for a constant value of approximately 98kN, whereas the results for the 3D model increase up to 162kN.

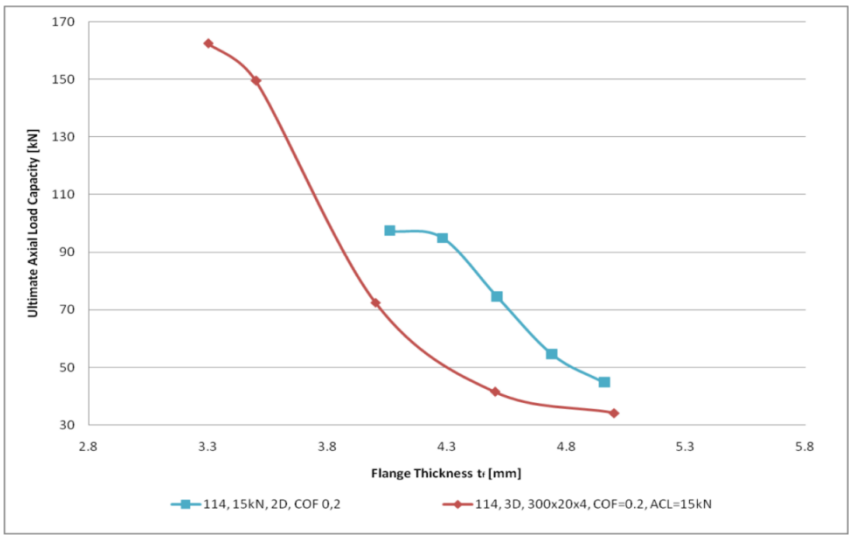

Figure 4-19: F_{UALC} over the flange thickness t_f for 3D and axisymmteric model

There are a number of reasons why the results behave this way. First of all the V-band back is narrower in the 3D than in the axisymmetric model. This means that when applying the same axial clamping load F_{ACL}, for the same flange thickness t_f, the gap

between the flange and the band back is smaller in the axisymmetric and larger in the 3D analysis. As especially for small band diameters, such as 114mm in this case, the cross section can be compared to that of a cantilever, reducing this gap between band and flange is equal to reducing the lever of the force acting as a bending moment on that cantilever. To create the same bending moment, and deform the cantilever by the same amount, the force needed for a small lever must therefore be larger than for a large lever. Applying this knowledge on the V-band, the ultimate axial load capacity of the axisymmetric model must be larger than of the 3D model, which was observed. The narrower back also explains the increasing results for the 3D model below 4mm, as the band leg is still in contact with the flange for thin flanges so that the wedging action of the V-shape can be acting, whereas for the axisymmetric model the flange and the band back rather than the leg are in contact, for which no wedging action is acting.

Moreover, a narrower back results in a shorter cantilever. In order to generate the same amount of deflection on the end of a long and a short cantilever, the latter must be deformed by a larger amount for which a larger force is required. This increases the effect of larger ultimate axial load capacities for 3D models for flange thicknesses t_f below 4mm. A detailed explanation of the working principle using the cantilever model is discussed in section 4.5.1.

The second reason for the larger and lower values of the ultimate axial load capacity is the way the axial clamping load is applied. In the axisymmetric model the axial clamping load is applied by shrinking the V-band onto a pair of flanges as discussed in depth in section 4.1, for which the whole V-band cross section is equally shrunk on resulting in a straightforward linear loading. In the 3D model on the other hand, the axial clamping load is generated by applying a surface traction force at both ends of the band (discussed in sub-section 4.3.1), which due to the large contact area between band and flange results in a highly complex analysis, creating a lot of noise in the data during loading process. The process of applying the axial clamping load itself is also greatly influenced by the geometry of the joint, where in the axisymmetric model a whole ring is assumed, and in the 3D model an open ring with a gap is modelled. The whole ring is therefore stiffer than the open ring, resulting in a larger ultimate axial load capacity than the 3D counterparts for flange thicknesses between 4.1mm and 4.9mm.

Another factor to consider when comparing both types of analysis is the average CPU running time. For axisymmetric models it lay between approximately 8min and 70min, and for 3D models between 60min and 180min (not taking into account the initial roll forming analyses), greatly depending on the mesh densities.

The bulk of the analyses, investigations, and experiments discussed in this thesis are undertaken for the initial reference flange thickness of 4.5mm, for which there is a

difference in ultimate axial load capacity results between 3D and axisymmetric models. However, for the investigation undertaken in this thesis the run times of the axisymmetric models greatly outweigh the small inaccuracies when compared to the 3D models. Therefore, it was concluded that the axisymmetric models are the better choice for further analyses, discussed in the subsequent section 4.5.

4.5 Numerical Investigation of F_{UALC} (Axisymmetric Model)

As the previous discussion of results has shown that the axisymmetric model is the better choice over the 3D model, the former was chosen along with a structured mesh to investigate the V-band joint in further detail, analysing the influence of several geometric and contact parameters.

4.5.1 Band Diameter D_b

Analysing a V-band joint when no friction was present between band and flange, applying an axial clamping load, F_{ACL}, of 6kN, for a band thickness of t_b 1.3mm, it can be seen in Figure 4-20 that the V-band diameters, D_b, had a significant influence on the ultimate axial load capacity, F_{UALC}. For clarification of the geometrical parameters, see Figure 4-2. There is quasi-linear increase between 114mm and 235mm and a peak at approximately 250mm. From this diameter on there is non-constant reduction in F_{UALC} with changing gradient.

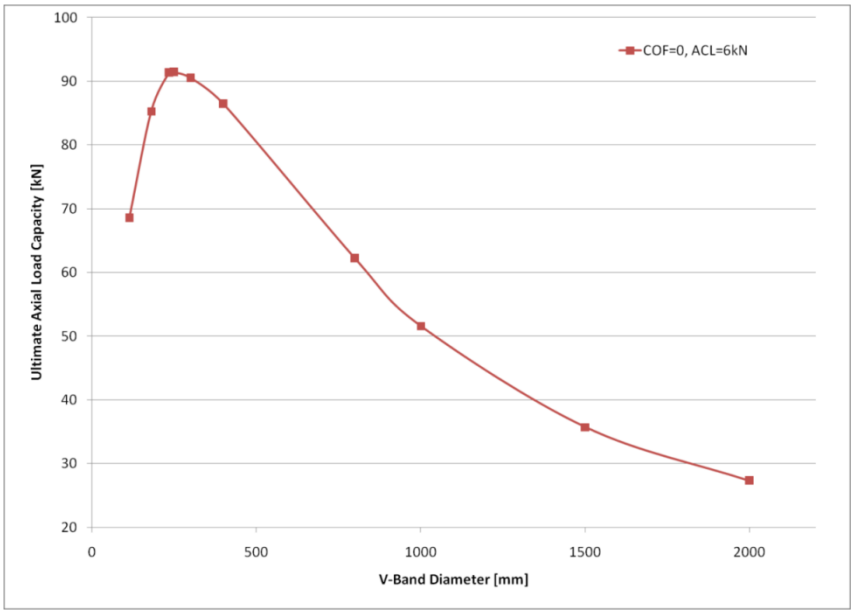

Figure 4-20: F_{UALC} over V-band diameter for F_{ACL}=6kN, and μ =0

The reasons for this behaviour can be explained when examining the deformed sections of failed V-band joints. Figure 4-21 displays sections for a small diameter, D_b=114mm , a medium-sized diameter, D_b=235mm, and a very large diameters. It is apparent that these three models have significantly different deformed shapes; the small one merely features a pure deformation of the section, whereas the large one shows no deformation of the section at all, but a pure ring deformation, which is an overall increase of the band diameter, D_b. The medium-sized model indicates a mixed deformed shape of section and ring deformation, and was chosen here for display as it was a standard-sized V-band retainer closest to the peak in F_{UALC} (shown in Figure 4-20).

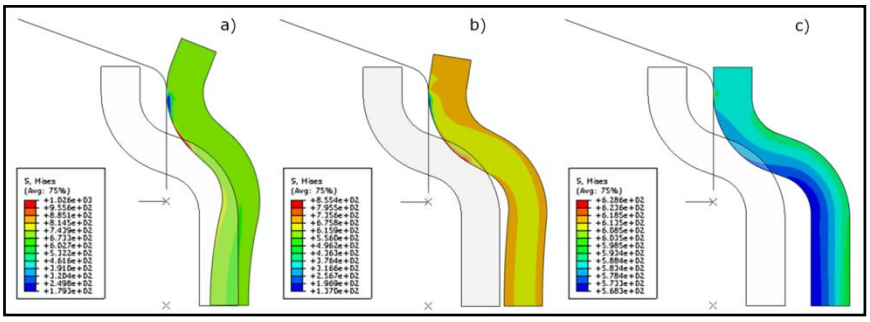

Figure 4-21: Fully deformed and undeformed shapes of axisymmetric model for F_{ACL} = 6kN, μ =0, and a) D_b=114mm, b) D_b=235mm, and c) D_b=2000mm

This behaviour is mainly due to the complexity of the load being applied to and acting inside the V-band. For a better understanding of this problem, a brief explanation is given in the following paragraphs, but it is discussed in greater detail in the subsequent chapter 5, where a theoretical model is developed.

A V-band can be compared to a 3 dimensional cantilever with a very large width being loaded on one end with a point load creating a bending moment, whilst at the same time a tensile load is applied on both sides in parallel to the bending moment tensor, generating a tension in the cantilever and increasing its width. In the V-band, the bending moment is introduced by the flange tip pushing against the inside of the band. Considering that the cantilever width is represented by the band length l_b, the tensile load is acting in the circumference and is generated due to the ring shape and T-bolt load F_β applied.

For small-sized V-bands, the bending moment can be said to be more influential than the circumferential tensile load. Considering a constant cross section, the force needed to deflect the cantilever by the same amount is directly related to the width. Therefore, the load needed to deflect the V-band cross section by the same amount is directly related to D_b, and l_b. This section deformation is mainly responsible for the quasi-linear increase of F_{UALC} between D_b =114mm, and D_b =235mm.

For larger diameter bands on the other hand, the influence of the tensile load in the circumference becomes more important. For total failure of a V-band joint, all sizes of V-bands need to be deflected in the radial direction by approximately the same amount. For large band sizes, the change in circumferential band length, Δl_b, required to generate this radial deflection is constant and hence independent of D_b. However, the circumferential strain required to generate this change in length is inversely proportional to the original length (and hence the diameter D_b). This ring deformation leads to the effect that between 250mm and 2000mm, the ultimate axial load capacity F_{UALC} reduces with increasing band diameter, D_b.

The peak at approximately 250mm and at its boundaries, is a result of the mixed effects of both section and ring deformation.

4.5.2 Friction Coefficient μ

The results presented previously in Figure 4-20 are shown in Figure 4-22 along with the results of analyses with coefficients of friction μ=0.1, and 0.2. The same clamping load (F_{ACL}=6kN) was used.

First of all it can be observed that friction highly impacts on the F_{UALC}. Secondly, the peak at D_b =250mm, for μ=0 is shifted, to D_b =300mm, for μ=0.1, and D_b =350mm for μ=0.2. Moreover, the increase in F_{UALC} is largest at the peak loads, and reduces for smaller and larger D_b. These three phenomena are very much related to the effects of the geometry and the nature of how the load was applied. The reason why friction impacts so greatly on the F_{UALC} is due to a very simple cause. When the joint is failing and the flanges are separating, the flange tip is sliding along the inside of the V-band, and more friction is then acting in the opposite sliding direction, meaning that the flange needs to be separated with a larger force.

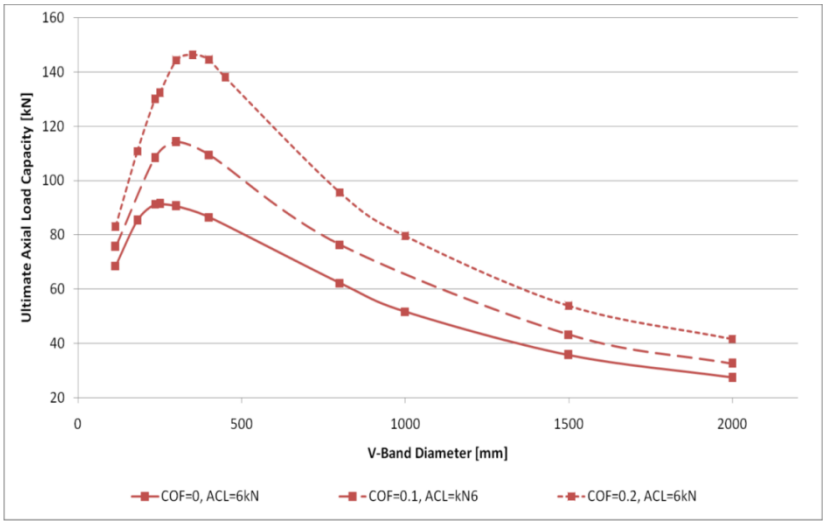

Figure 4-22: F_{UALC} over V-band diameter for F_{ACL}=6kN and μ =0, 0.1, and 0.2

4.5.3 Axial Clamping Load F_{ACL}

For the same models previously used, as a third parameter, the axial clamping load F_{ACL} was varied to investigate its influence on the F_{UALC}. Figure 4-23 displays results for models with no friction apparent and for varying axial loads of F_{ACL}=6kN, 15kN, and 25kN, in which the impact of the F_{ACL} is very small for small diameter bands, but has an increasing the effect for larger diameters with F_{UALC} increasing with F_{ACL}.

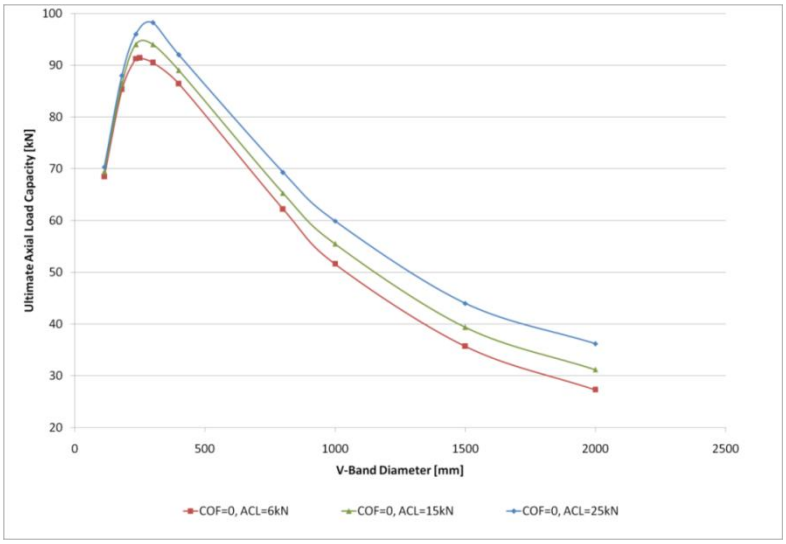

Figure 4-23: F_{UALC} over V-band diameter for F_{ACL}=6 kN, 15 kN, and 25kN, and μ= 0

As the coefficient of friction μ was increased to 0.1 the impact of the F_{ACL} for moderately sized bands increased as well, as can be seen in Figure 4-24. When compared to the previous diagram, Figure 4-24 shows that the effect of the clamping load increases between D_b =114mm and the peak at 235mm, but then remains to be nearly constant.

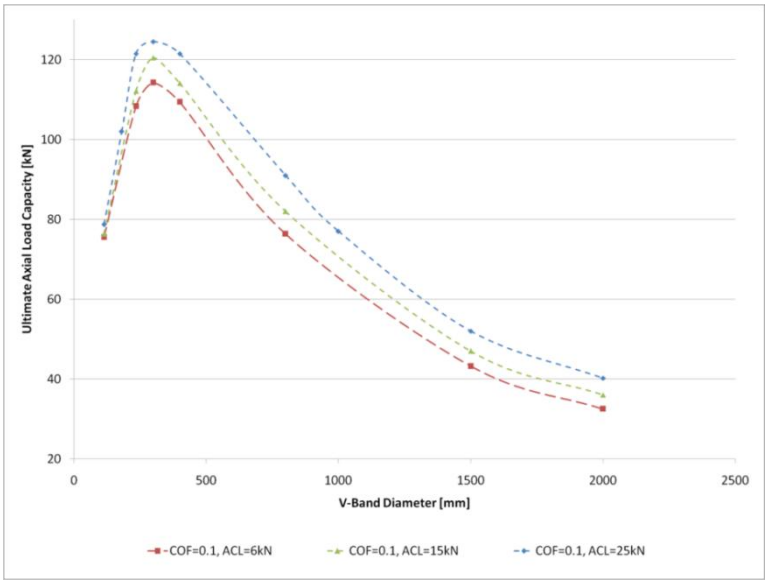

Figure 4-24: F_{UALC} over V-band diameter for F_{ACL} =6 kN, 15 kN, and 25kN, and μ=0.1

In Figure 4-25, for μ=0.2, the clamping load increases the F_{UALC} only slightly between D_b =114mm and approximately 300mm, but shows high impacts from 300mm on, also shifting the peak from 350mm to 400mm. Moreover, the impact reduces from approximately 1000mm on.

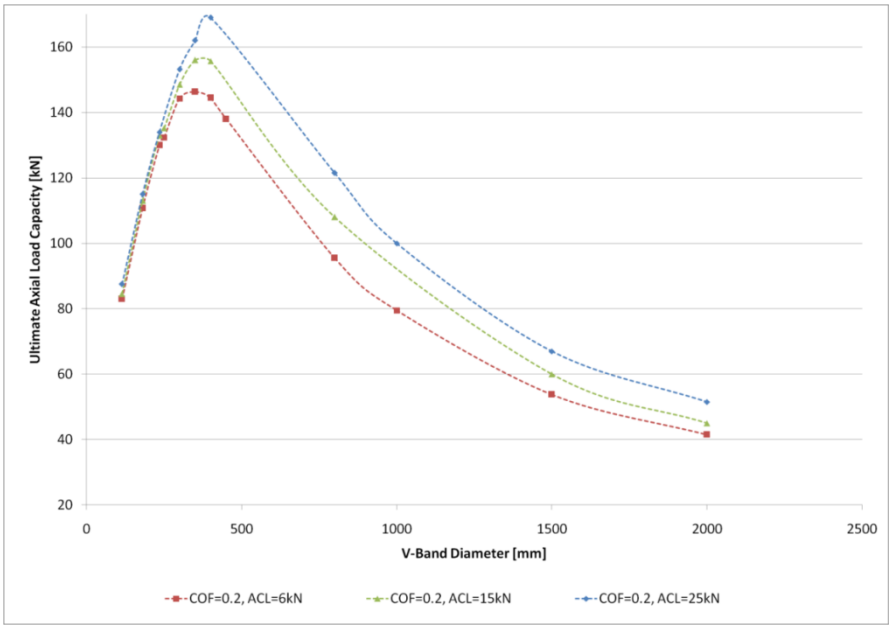

Figure 4-25: F_{UALC} over V-band diameter for F_{ACL} =6 kN, 15 kN, and 25kN, and μ=0.2

An increasing F_{UALC} resulting from larger F_{ACL}, is mainly due to the fact that the gap between flange diameter D_f and band diameter D_b (see Figure 4-2) is reduced. This impacts on F_{UALC} in two ways. Firstly, the lever of the point load acting on the cantilever is reduced. As the same bending moment is required with a smaller lever apparent, the force required to overcome this bending moment needs to be higher. Hence, the force required to deform the cross section (the failure mode for smaller bands) is increased.

The second effect for larger diameter bands, is that the radial expansion due to ring deformation δ_r required to fail the band joint is larger as the gap between band flange decreases.

It can be said that so far, the friction coefficient, μ, and band diameter, D_b, have a significant and large influence on the F_{UALC}, whereas the axial clamping load, F_{ACL} increases its influence with larger D_b.

4.5.4 V-Band Thickness t_b

The next band parameter investigated was the band thickness, t_b. Figure 4-26 compares previously discussed models for t_b =1.3mm, μ=0.2, and F_{ACL} =6kN, to models where t_b was reduced to 1.2mm. Again this shows the F_{UALC} reducing for thinner bands. Moreover, the impact is larger close to the peak values and decreases for smaller and larger sized

band retainers, and seems to reach a constant value for larger values. A shift of the peak capacity cannot be observed for these particular conditions.

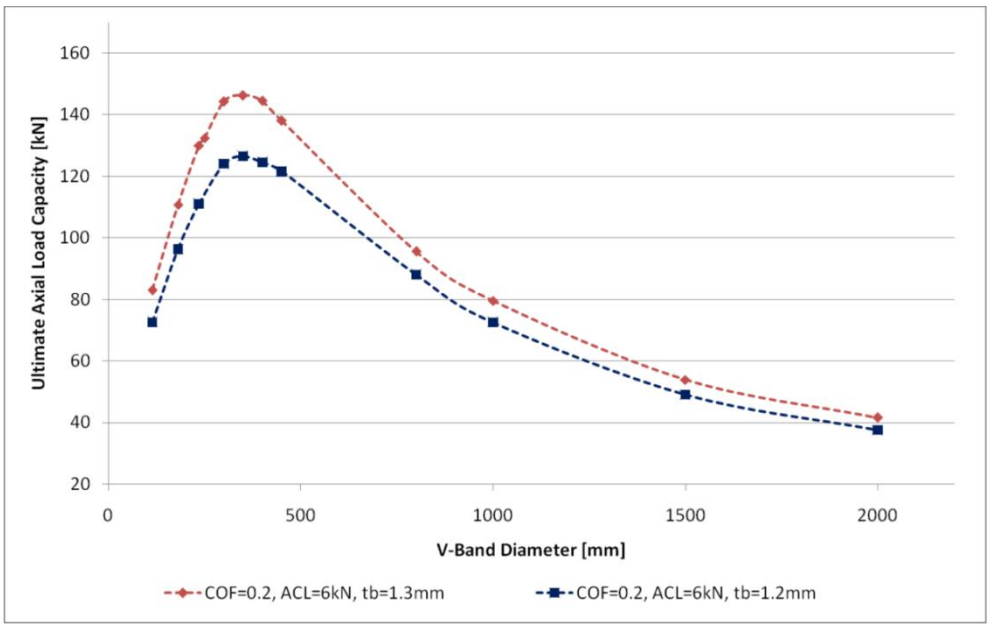

Figure 4-26: F_{UALC} over V-band diameter for F_{ACL} =6 kN, μ=0.2, and t_b = 1.2mm, and 1.3mm

Figure 4-27 shows the previously presented models with t_b =1.3mm and 1.2mm, and μ =0.2, but for a larger axial clamping force F_{ACL} =15kN. The effects are very similar to those seen in the previous diagram. However, the difference in F_{UALC} for larger band sizes does not settle to a constant value, but steadily reduces.

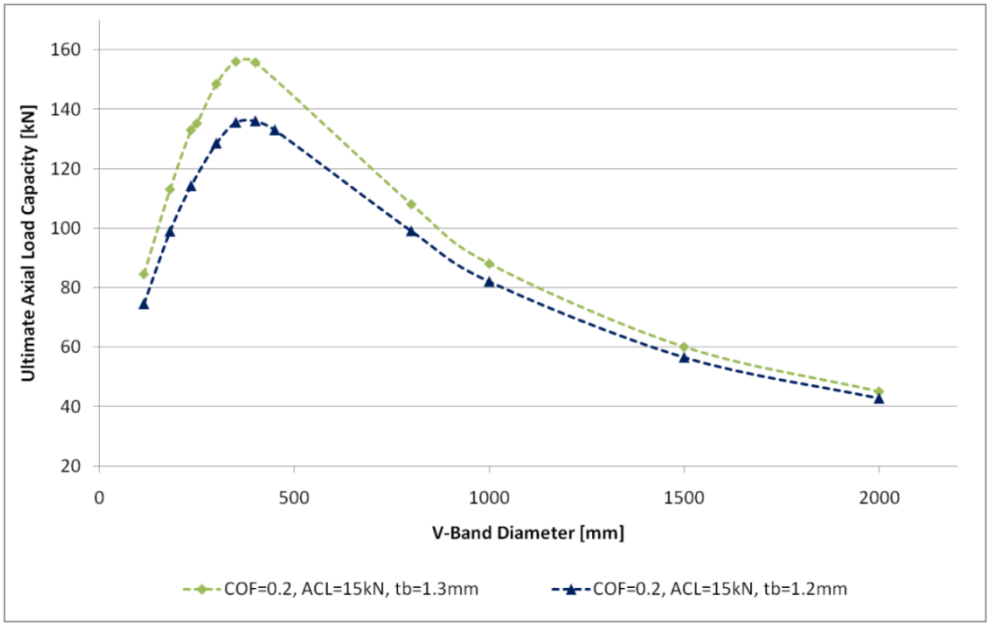

Figure 4-27: F_{UALC} over V-band diameter for F_{ACL} =15 kN, μ=0.2, and t_b = 1.2mm, and 1.3mm

For even larger axial clamping loads, F_{ACL} of 25 kN the behaviour is similar again, but the difference between the two different thicknesses reduces for larger band diameters, and finally reaches zero, as can be seen in Figure 4-28.

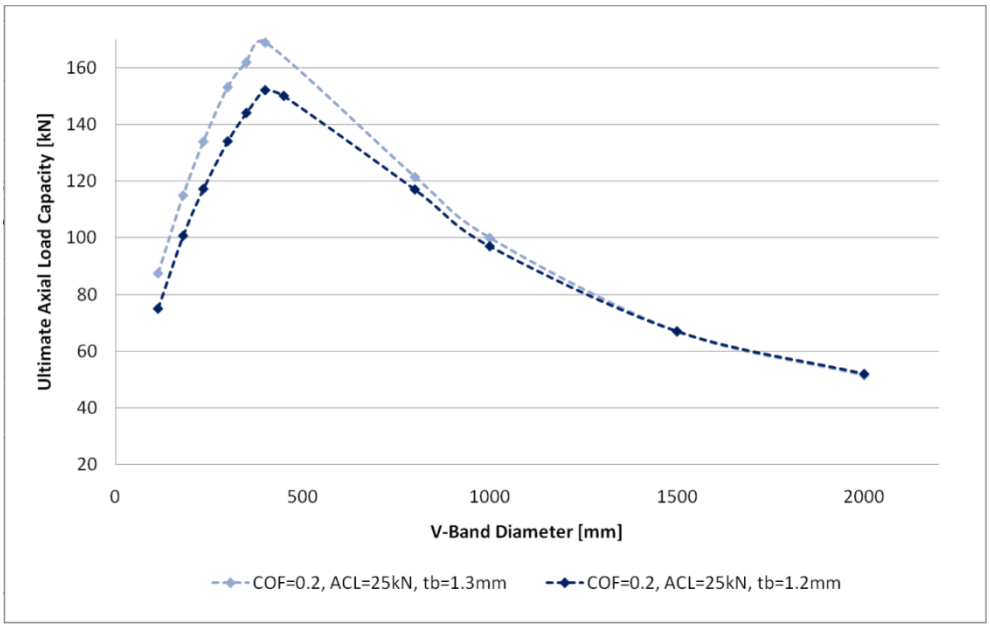

Figure 4-28: F_{UALC} over V-band diameter for F_{ACL} =25 kN, μ=0.2, and t_b = 1.2mm, and 1.3mm

This effect can be explained as:

Assembly process (T-bolt tightening):

When applying the same axial clamping load to bands with two different thicknesses of 1.2mm and 1.3mm, the reaction force F_θ created in the circumference inside the band is the same as well. However, the stress σ_θ due to F_θ is lower for the thick band and higher for the thin band as the band cross section area A_B changes and:

$$\sigma_\theta = \frac{F_\theta}{A_B}$$

Failure process (of V-band joint during flange separation):

For large bands, the radial deformation δ_r due to ring expansion required to fail the band is the same for thin and thick bands. The strain caused inside the band in the circumference ε_θ and the associated stress σ_θ are the same as well. However, the force F_θ and hence the ultimate axial load capacity F_{UALC} are lower for small and higher for thicker bands.

Applying only small axial clamping loads F_{ACL} such as 6kN, the effect due to the pretension is only very small, and the hence there is a large difference for the ultimate

axial load capacity between thin and thick bands. However, applying larger axial clamping loads such as 15kN and even 25kN increases the impact of the assembly process, and therefore resulting in similar ultimate axial load capacities for thick and thin bands.

4.5.5 V-Band Radius r_b

Figure 4-29 shows two graphs in which the cold rolled bending radius on the inside of the V-band r_b is reduced from 2.78mm to 1.3mm, for the given parameters of F_{ACL}=6kN, and μ =0. It should be noted here, that in a real cold roll forming process with the given V-band thickness this radius could not be reduced to 1.3mm because the band thickness itself is 1.3mm. This change is included here to predict and estimate the impact of even seemingly unimportant geometrical parameters. It can be seen in the graphs that the change in radius has only minor influence on the ultimate axial load capacity for V-bands sizes D_b=114mm and 181mm, but increases its impact tremendously for larger diameters. This leads to the conclusion that the radius has a particular effect on and is largely related to the elastic ring deformation, which starts to increase its presence significantly from 300mm on. A reduction in bending radius r_b largely increases the ultimate axial load capacity for band sizes above 235mm.

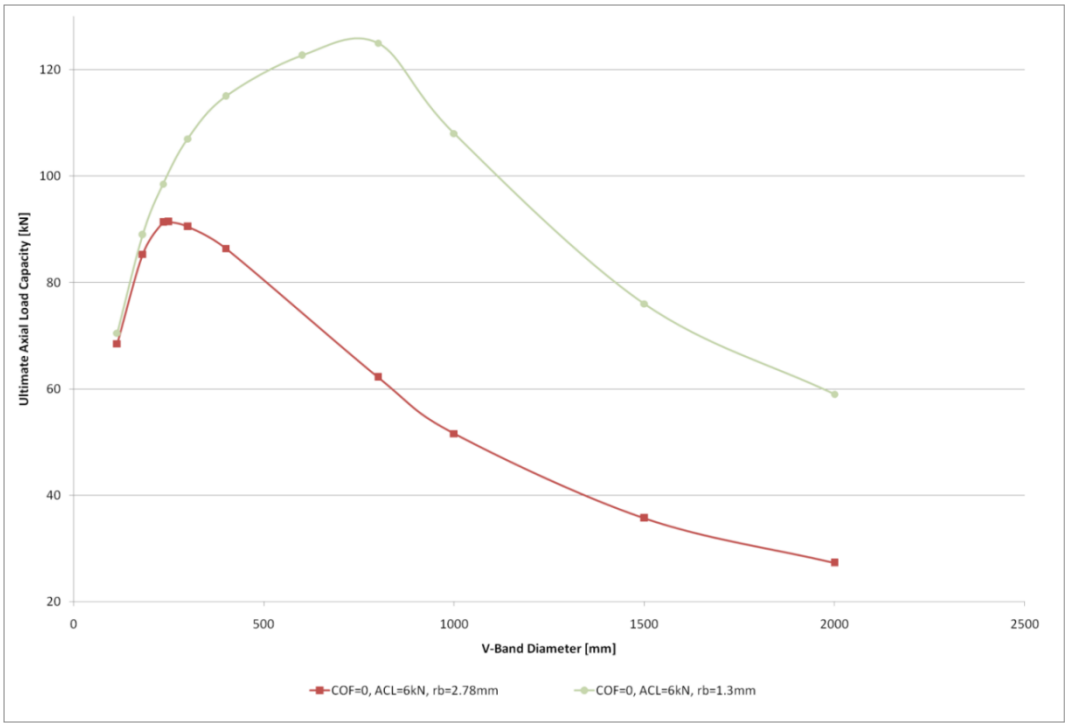

Figure 4-29: V-band bending radius r_b changed from 2.78mm to 1.3mm

This happens because the flat part on the V-band leg increases as the bending radius is reduced, which can also be seen in Figure 4-30 showing deformed FE models with both radii for D_b=800mm. This deformed stage is where the ultimate axial load capacity

occurs, and for the smaller radius in a) the flange has moved a smaller distance in the axial direction than for the larger radius in b). Moreover, in a) the ultimate axial load capacity occurs when the flange is still in contact with the flat part of the V-band leg, whereas in b) the flange has already moved around the radius r_b. Therefore, in a) the angle between radial and axial force remains at approximately 20°, whereas in b) it changes to an angle between 40° and 45°. This means that when the flange is at the same axial position in both models in the contact zone the radial force is smaller in a) than in b). Hence, the axial force needed to deform both cross sections by the same amount in the radial direction is larger for the smaller radius in a) than for the larger radius in b).

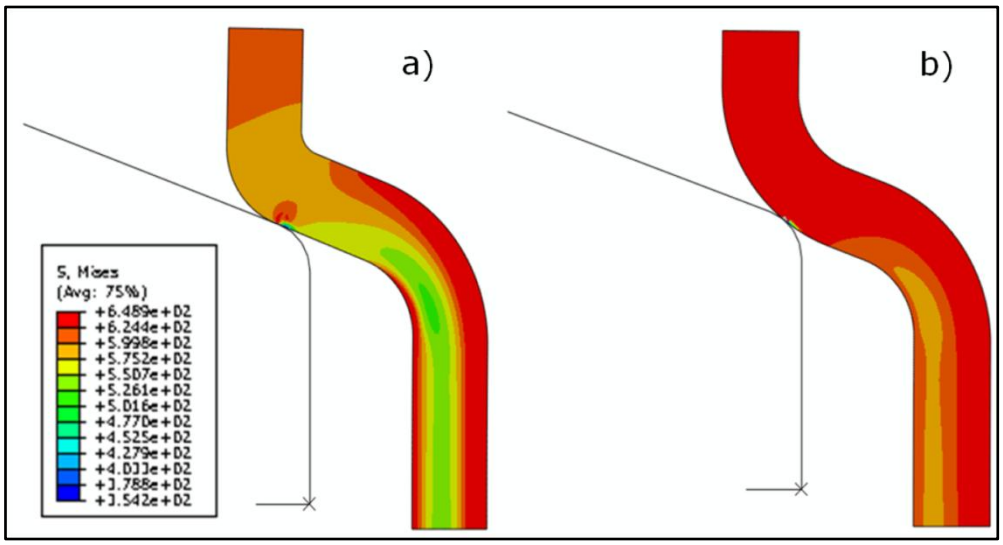

Figure 4-30: Deformed cross section in axisymmetric FE model at ultimate axial load capacity, for μ=0, D_b=800mm, and F_{ACL}=6kN, a) r_b=1.3mm, and b) r_b=2.78mm

4.5.6 Flange Parameters

The bulk of this sub-section is taken from the author's own publication, Muller and Barrans (2010a).

A further three joint parameters are investigated in this section. These parameters define the flange and are the flange thickness, t_f, the flange corner or contact radius, r_c, and the flange angle, ϕ. The flange angle, ϕ usually is manufactured to fit the V-band clamp angle of 20°, Shoghi (2003), which was taken as the reference value. The whole range was set from 18° to 22°, using steps of 1°. The corner radius r_c for turbocharger applications is normally 0.8 mm, as stated by Brown (2009). The range for r_c was from 0.6 mm to 1.0 mm. The reference value for the flange thickness t_f, as stated by Shoghi (2003), was 4.5 mm with a tolerance of +2.5%. In this investigation the range for tolerance was set higher, from -10% to +10%. All results were gathered for a coefficient of friction μ of 0.2.

Figure 4-31 shows the F_{UALC} to be highly dependent on flange thickness, with 125kN being the reference value at the initial flange thickness of 4.5mm, for D_b =235mm. From this reference value increasing the thickness by up to 10% highly reduced the F_{UALC} to approximately 68kN almost half of the initial value, and decreasing the thickness by 10% increased the F_{UALC} to 172kN (a 38% increase).

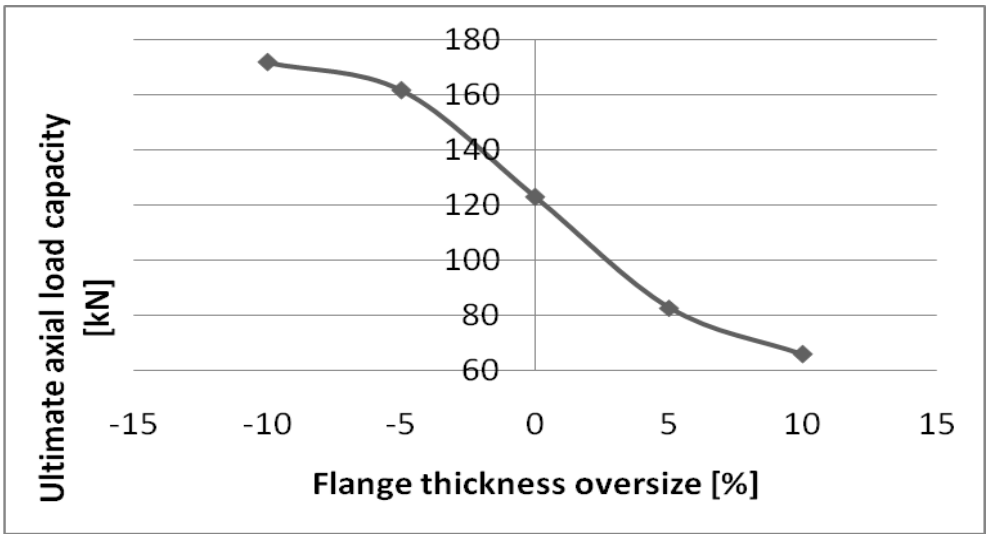

Figure 4-31: Predicted F_{UALC} over the flange thickness oversize for a corner radius r_c of 0.8mm and an angle of 20°, D_b =235mm

At the upper boundary the graph seems to converge to 180kN, so that any further reduction of the thickness would not increase the F_{UALC} anymore, as can be seen in Figure 4-32 a), where the outer diameter of the flange D_f is already in contact with the inner diameter of the V-band retainer D_b leaving no clearance between the two. An infinite increase of the flange thickness on the other hand would reduce the F_{UALC} to 0kN as the contact point would move towards the leg of the retainer, generating less axial clamping force F_{AACL}, as can be seen in Figure 4-32 c), when compared to the reference point in Figure 4-32 b).

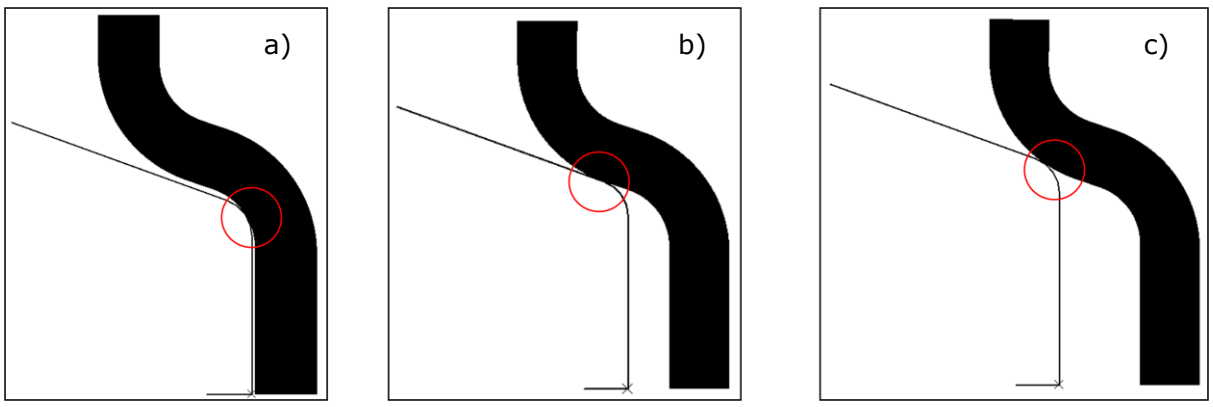

Figure 4-32: Different oversizes for flange thicknesses, t_f,a) -10%, b) 0%, and c) 10%

To gain additional support for these statements, the same convergence study as in Figure 4-31 was carried out for a retainer diameter D_b =114mm in Figure 4-33, showing the same tendencies, though for lower values overall, also presented and discussed in section 4.4.

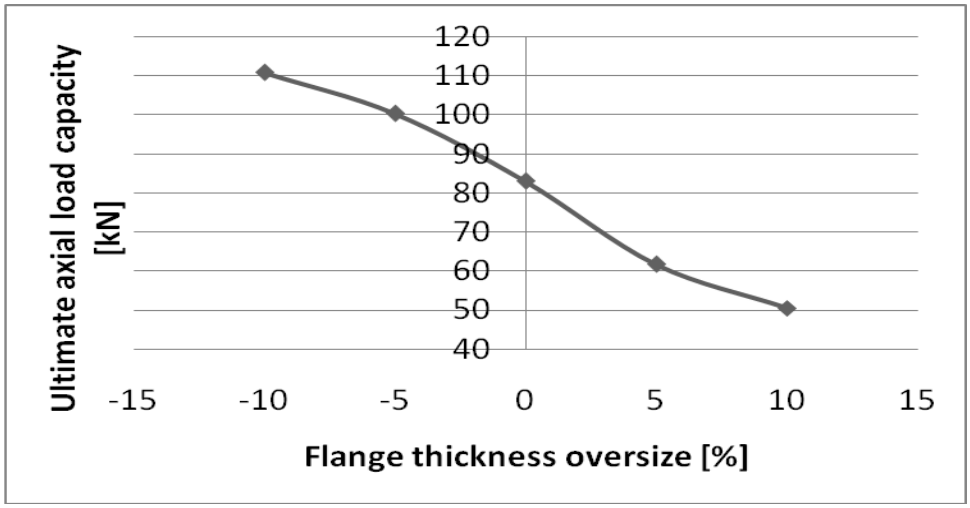

Figure 4-33: Predicted F_{UALC} over the flange thickness oversize, for a corner radius of r_c =0.8mm and an angle ϕ of 20°, D_b =114mm

In contrast, for the given ranges, the corner radius, r_c, and flange angle, ϕ, were found to have very little impact on the F_{UALC}, as shown in Figure 4-34 and Figure 4-35.

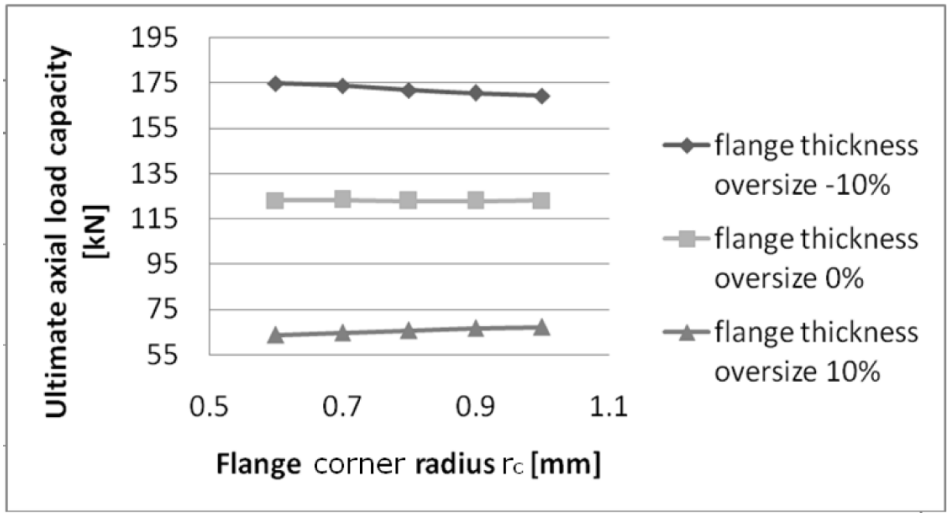

Figure 4-34: F_{UALC} over the flange corner radius r_c, for a flange thickness oversize of -10%, 0% and 10% and an angle ϕ of 20°

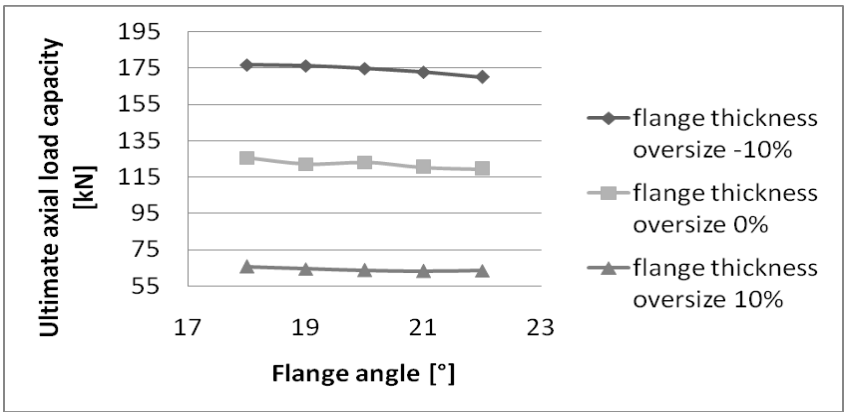

Figure 4-35: Predicted F_{UALC} over the flange angle ϕ for a flange corner radius r_c = 0.6mm and varying flange thickness oversize

4.5.7 Impact of Material Properties

Figure 4-36 shows three graphs of the axisymmetric FE model predictions with no friction apparent, for the original elastic-plastic material behaviour, for one where the yield stress σ_Y was increased to 1100 $\frac{N}{mm^2}$, and a third one for linear material behaviour. It can clearly be seen that all graphs correlate very well for band diameters above 800mm. The increase of yield point from 648 $\frac{N}{mm^2}$ to 1100 $\frac{N}{mm^2}$ increases the ultimate axial load capacity for band diameters below 800mm. This happens because the section deformations required to result in ultimate failure for smaller band diameters requires plastic deformation in the section. This is supported by the model with purely elastic material properties, for which the ultimate axial load capacity vastly increases for smaller V-band diameters.

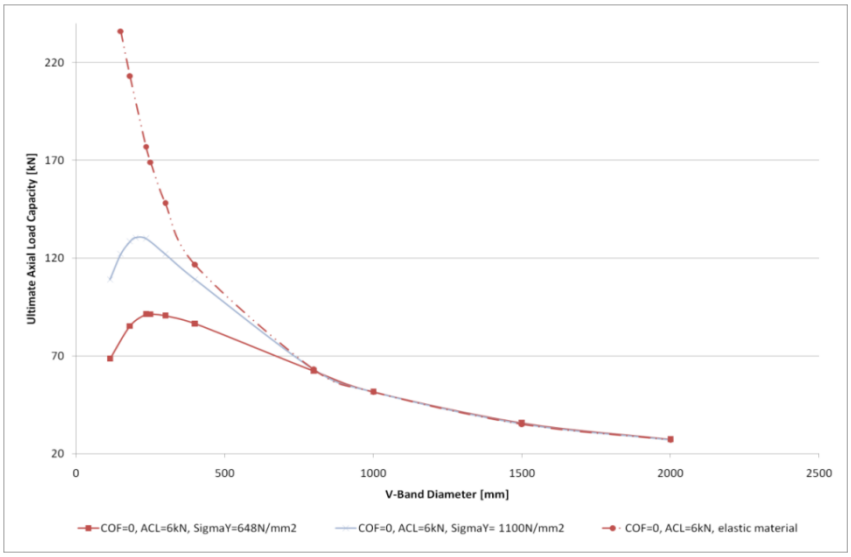

Figure 4-36: Ultimate axial load capacity results over the V-band diameter for finite element models with D_b=181mm for elastic-plastic material and yield point σ_Y changed to 1100N/mm²

In order to better understand the changes in ultimate axial load capacity associated with changing the material properties it is worth analysing the stress levels at the end of the V-band failure process, as predicted by the finite element model in Figure 4-37, for a V-band diameter D_b of 181mm. In a) for the elastic material, it can be noticed that the overall stress level is approximately 12.5 times larger than for the original model properties in a), due to the longer elastic part of the stress strain curve, which is supported by the model in c) with elastic-plastic material with 1100 $\frac{N}{mm^2}$ yield point σ_Y, where the over stress level is 8.5 times larger.

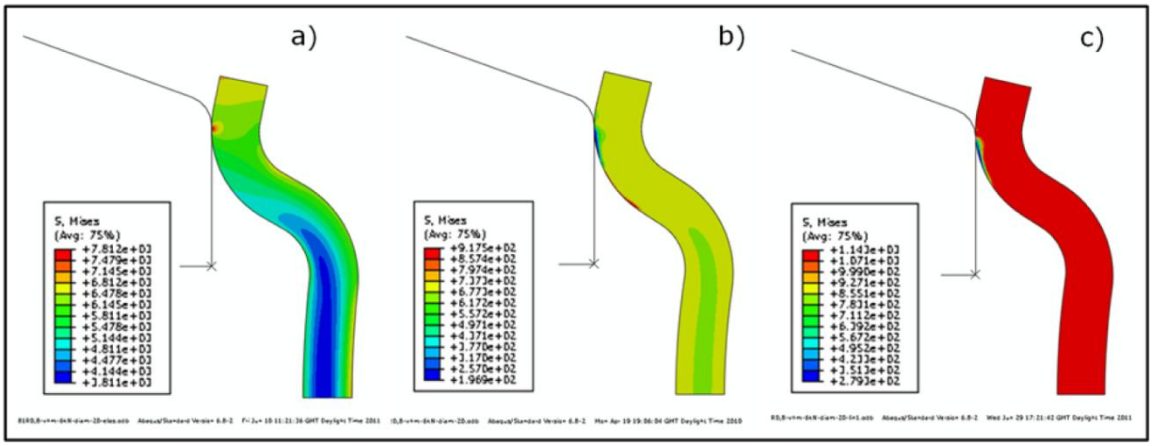

Figure 4-37: D_b=181mm, a) elastic, b) elastic-plastic material, c) yield point σ_Y changed to 1100N/mm²

4.5.8 Contact Pressure Distribution between V-Band and Flange

This sub-section is taken from the author's own publication Muller and Barrans (2010b).

In this sub-section the impact of the contact pressure on the contact surface is studied. As stated by Shoghi *et al*. (2004) during the assembly process, the contact pressure between the band and flanges around the circumference is expected to be larger next to the T-bolt due to friction effects. Therefore, the finite element model presented here is supposed to predict if any plastic deformation can be detected at the contact surface of the V-band. In the future the data gathered may then help to find methods to measure the plastic deformation and hence the contact pressure distribution on the inside of the band. The finite element model was set up to model assembly and removal of the V-band retainer from a joint with a diameter of 235mm.

Figure 4-38 a and b show the V-band contact zone after it has been taken off the flanges. In Figure 4-38a in which no friction has been assumed, almost no residual von-Mises stress can be seen at the surface. The peak stress lies beneath the surface. This phenomenon is due to the stresses acting at the surface during loading. Considering the von-Mises yield cylinder in three dimensional principal stress space, two stresses are

generated due to the bending of the band during assembly onto the flanges, one in the radial direction out of the plane, and one in parallel to the surface. The third stress is introduced by the contact force of the flange, acting directly normal to the surface. This third contact stress leads to an increase in hydrostatic stress, reducing the residual stress. This becomes clearer when taking into account friction as shown in Figure 4-38b (μ=0.2) adding an extra shear stress at the surface, leading to larger residual stresses at the surface as well, and increasing the peak stress by a ratio of about 3. This effect is explained in more detail sub-section 3.4.2.

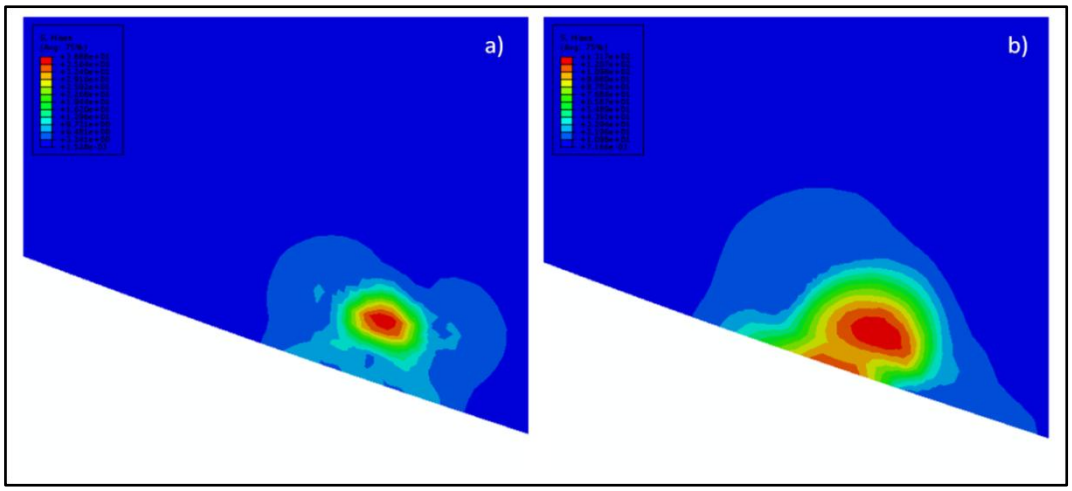

Figure 4-38: Residual von-Mises stress after V-band clamp is taken off the flanges and axial clamping load of 60kN has been applied, a) μ=0, b) μ=0.2

This assumption is confirmed by Figure 4-39a and b, showing no plastic strain at the surface for the non friction case, and larger plastic strain at the surface for the case where friction has been included. A series of FE analyses undertaken for this thesis have shown that below 30kN no plastic deformation in or close to the contact zone appears at all. As this shows, depending on the coefficient of friction and an axial clamping load of 30kN (16Nm), the plastic deformation would be hard to detect by surface roughness measurement. Even in the interest of research increasing the axial clamping load to 60kN (32Nm), which in a real application would never be that high, the plastic deformation shown in Figure 4-40a and b is very small for both no friction and friction case, and therefore hard to detect.

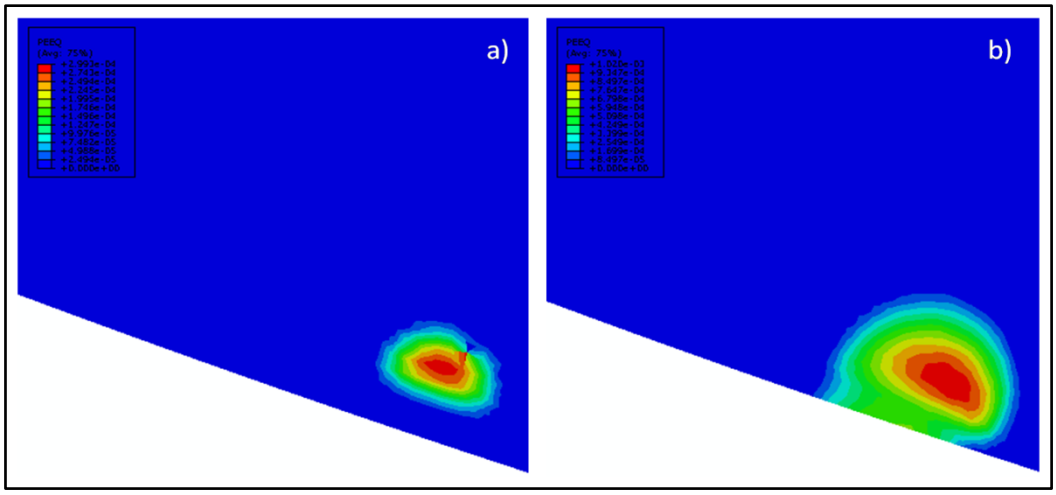

Figure 4-39: Plastic strains (PEEQ) after V-band clamp is taken off the flanges and axial clamping load of 30kN has been applied, a) μ=0, b) μ=0.2

For the 60kN case, the influence of the hydrostatic stress and, when taking into account friction, the influence of shear stress on the plastic strain is similar to that of 30kN, as shown in Figure 4-40a and b.

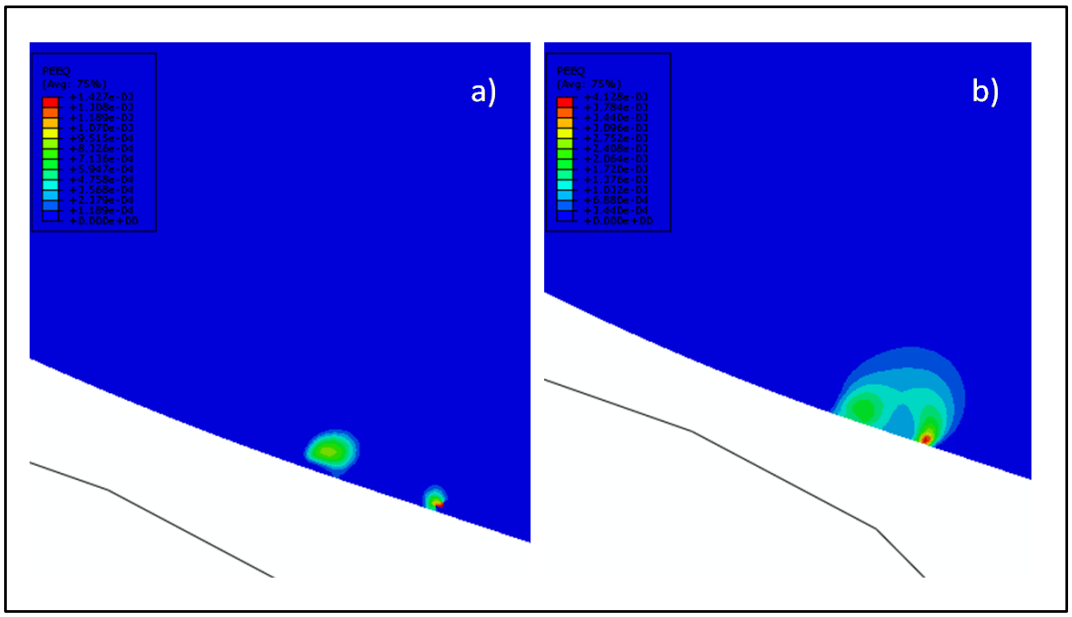

Figure 4-40: Plastic strains (PEEQ) after V-band clamp is taken off the flanges and axial clamping load of 60kN has been applied, a) μ=0, b) μ=0.2

In order to further investigate the contact surface for the case of F_{ACL}=60kN, the deformation of the corner nodes after the flange was taken off was reported. Figure 4-41 shows the global x-and y-coordinates of the nodes along the surface where contact could occur. As the contact surface was along the flat part of the surface, the nodes there must form a flat surface as well before deformation occurs. Figure 4-41 shows that there is only very minor deformation of the node coordinates when compared to a straight line,

as especially the nodes between x= 116.12mm and 116.15mm seem to be placed slightly above the line.

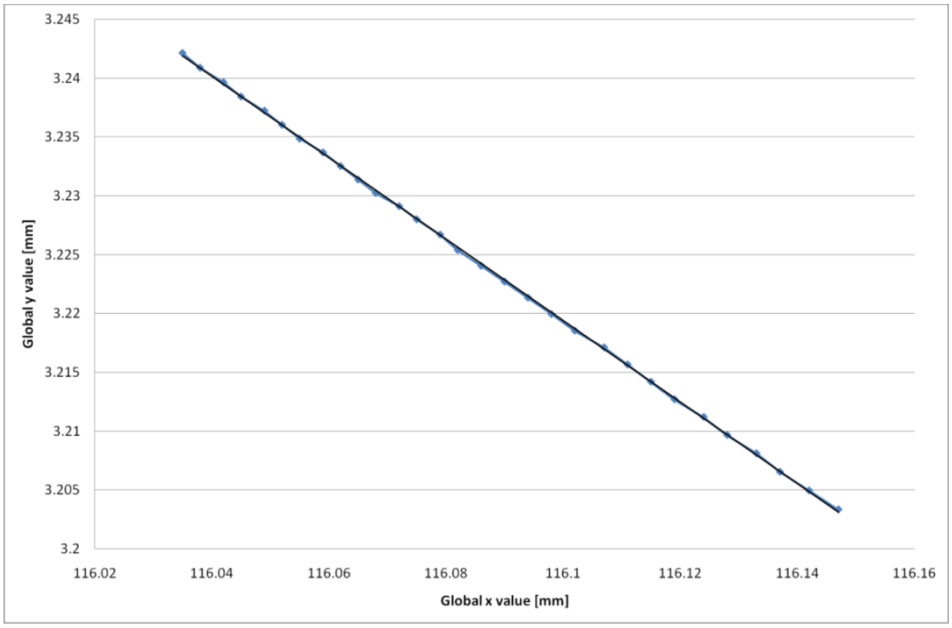

Figure 4-41: Global x- and y-values of nodes at contact surface after deformation for FE model with D_b=235mm, μ=0, F_{ACL}=60kN

For the case where friction is apparent in Figure 4-42 this deformation is still minor but slightly more detectable and more wide spread rather than localised between x= 116.10mm and 116.15mm.

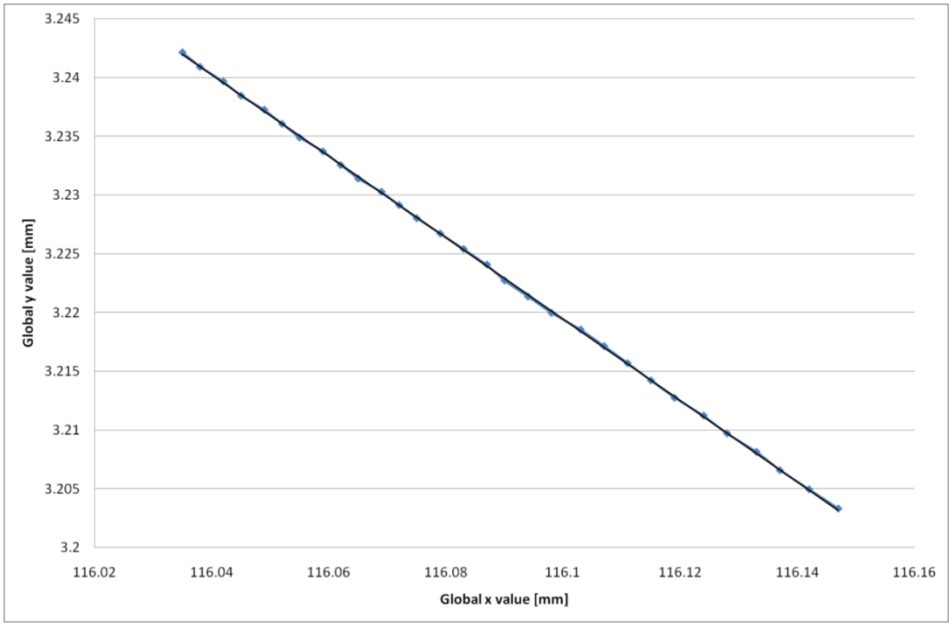

Figure 4-42: Global x- and y-values of nodes at contact surface after deformation for FE model with D_b=235mm, μ=0.2, F_{ACL}=60kN

However, this means that it might still be very difficult to be picked up and measured by surface metrology, as in case of the real band cross section, the flat part will not necessarily be flat, but will have valleys and scratches from the cold roll forming process. This means that the inside surface of the cross section needs to be measured at exactly the same spot before and after assembly onto the flanges.

In both cases the bulk of the plastic deformation was found underneath the contact surface. This phenomena was also found by Moore (1948) who points out that in accordance with Hertz's classical equations describing elastic deformation (Hertz 1896), and Timoshenko (1934), plastic deformation occurs below the centre of contact in the softer material once the maximum shear strain exceeds its elastic limit (also see section 2.5 for references).

4.6 Conclusion

In this chapter, the impact of several geometrical parameters of the V-band joint on the ultimate axial load capacity F_{UALC} was studied, using finite element analysis. Axisymmetric and 3D FE-models were defined, both including the assembly of the band onto a pair of flanges, and the subsequent axial separation of flanges, which then led to total failure of the whole joint. The major difference between the two types of model was that the axisymmetric models consisted of a closed and the 3D models of an open ring.

For the axisymmetric model it was shown that the F_{UALC} was strongly dependent on the mesh type and size of elements along the contact surface. It was also found that the plastic strain along the inner contact surface of the V-band, where the flange was sliding along, was strongly dependent on the size of elements along this surface, but independent of the mesh type. A much localised large peak of plastic strain ε_{pr} at the inner side of the V-band back close to the radius was predicted. Moreover, for this model, an implicit solver was favourable over an explicit one as the latter destroyed the contact surface and the implicit solver proved to be much faster. For all further work, a structured mesh was used.

The 3D model also included plastic stresses and strains from the cold roll forming process, as it was taken from the 3D FE analysis of the manufacturing process in chapter 3. A mesh convergence study was carried out to investigate the impact of flange thickness t_f on F_{UALC}, always using the same F_{ACL}. For finer meshes, small flange thickness could not be predicted, as F_{ACL}=15kN could not be applied. The F_{UALC} was found to increase as the flange thickness t_f decreased.

A comparison between both model types over a range of flange thicknesses showed a significant difference in the results for the ultimate axial load capacity. With the 3D

models, it was possible to simulate smaller flange thicknesses, and for the same thicknesses, results were larger for the 3D than those of the axisymmetric models. However, for the flange thicknesses used for the bulk of the analyses presented in this chapter, the 3D and axisymmetric models showed similar ultimate axial load capacities, and the latter proved to converge up to 22 times faster. Therefore, the decision was made to carry out all subsequent work using the axisymmetric model

The V-band diameter, D_b, had a significant influence on the ultimate axial load capacity, F_{UALC}, which increased between 114mm and 235mm, reached a peak, and then for larger diameters decreased again. This was mainly related to the deformation modes, as for small and medium band diameters the cross section deforms due to section and ring deformation, whereas for bands with larger diameters it deforms due to ring deformation only. The coefficient of friction had a large impact, and for the same axial clamping load the F_{UALC} increased with μ. A larger axial clamping load F_{ACL} increases the F_{UACL} as well, but its impact increases for larger μ. Overall it was found that reducing the band thickness t_b also reduced the F_{UACL}. However, a larger impact is found for bands with D_b between 114mm and 400mm, and a much smaller impact for larger bands. Moreover, this impact reduces as the axial clamping load is increased. The FE analyses have also shown that decreasing r_b highly increased F_{UACL}, as this decrease resulted in a larger sliding length l_s. More detailed investigations confirm the findings made previously, that the F_{UACL} was highly dependent on the flange oversize/ thickness. On the other hand, the flange corner radius r_c and flange angle γ were considered to have had very little impact on the F_{UACL}. Increasing the yield point σ_Y however increased the $F_{UACL}$for band diameters D_b <800mm, whereas above this diameter no changes were found. When investigating the impact of the contact pressure on the contact surface of the band by assembling and disassembling the band, the bulk of the plastic deformation was found underneath the contact surface, with only minor deformation at the surface.

5 Theoretical Models Predicting Ultimate Axial Load Capacity

5.1 Introduction

In the previous chapter, section 4.4, the finite element analyses revealed the F_{UALC} to be largely dependent on the band diameter, D_b. Moreover, it was shown that the deformation during failure can be split into two main parts, a pure ring deformation in radial direction for very large D_b, and for smaller band sizes a combination of both ring and section deformation. Based on this knowledge, this chapter presents a mathematical description predicting the F_{UALC} using classical engineering equations. For both types of deformation the discussion includes their individual development, as well as comparing them to the finite element work from the previous chapter 4. An experimental validation is given in the subsequent chapter 6.

5.2 Ring Theory Development

For the purpose of this analysis and to reduce the complexity of this problem it is assumed that, due to an external force the pair of flanges separates in the axial direction only. The band cross section is assumed to be rigid, deforming only in the circumference, and thereby increasing the band diameter/ radius. Moreover, friction and the axial clamping load are not considered.

5.2.1 Definition of Axial Load F_A using an Equilibrium Approach

Failure of the V-band joint is defined to occur due to separation of the flanges in the axial direct, by which they apply an axial load F_A onto the inner side of the V-band. This axial force, F_A, is distributed along the inside circumference of the V-band as a force per unit length f_a. The relationship between these two forces can be expressed in equation 5.1

$$F_A = f_a R_c 2\beta \tag{5.1}$$

where R_c is the radius at which contact is established between flange and band, and in which f_a is acting (as shown in Figure 5-1), and where β is the subtended angle of half the V-section band in the circumference.

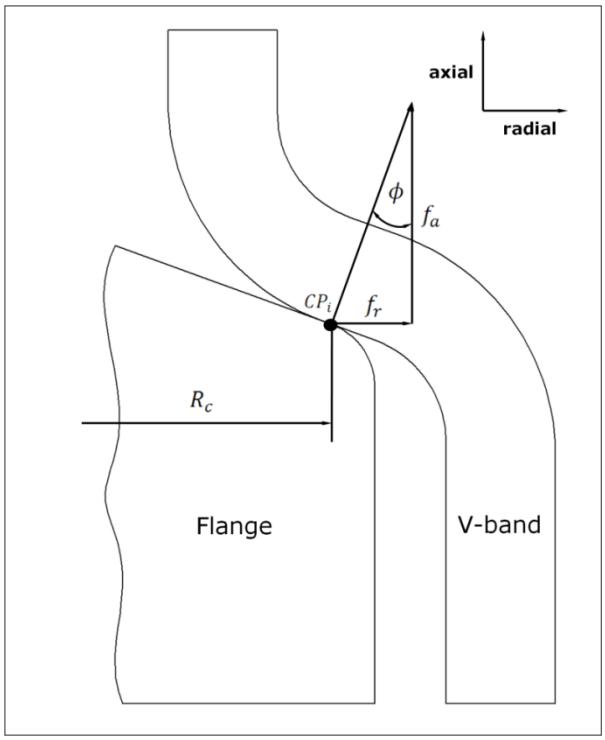

Figure 5-1: Axial and radial external forces at contact point between V-band retainer and flange for initial contact after V-band assembly

Rearranging equation 5.1 in to 5.2 gives:

$$f_a = \frac{F_A}{2R_c\beta} \tag{5.2}$$

Apart from the force per unit length in the axial direction f_a the contact force between the band and flange can be split in a second component f_r in the radial direction. The angle between these two components is, ϕ^*, and equals half the angle of the V-section, ϕ, only when initial contact is established along the flat part of the V-band section. The importance of this distinction taking into account the geometrical shape of the V-band cross section is discussed in further detail in the subsequent sub-section 5.2.2. The relationship between the forces can then be described by the following equation

$$f_r = f_a tan\phi^* \tag{5.3}$$

and can also be seen in Figure 5-1 for initial contact at the point, CP_i, on the flat section of the V-band leg. Substituting equation 5.2 in 5.3 then gives a new equation for the radial force per unit length:

$$f_r = \frac{F_A}{2R_c\beta} tan\phi^* \tag{5.4}$$

Considering this segment of the V-band retainer with an infinitesimal angle, $d\theta$, this externally generated radial force, f_r, creates a reaction force, F_θ, inside the V-band acting on both ends of the segment in the circumferential direction.

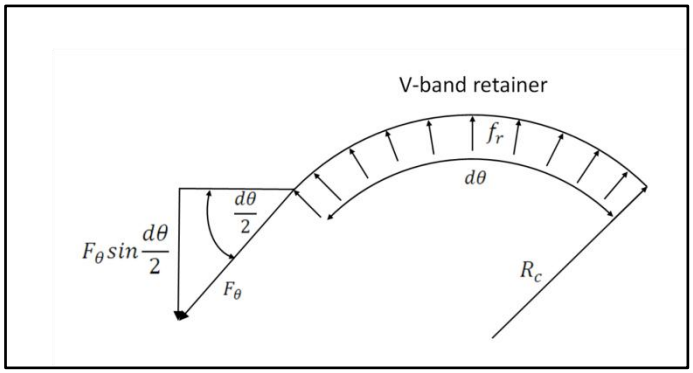

Figure 5-2: Internal and external forces acting on the V-band retainer

Using the radius of the contact point between band and flange, R_c, and equilibrium of this segment, the relationship between these two forces is found to be:

$$2F_\theta sin\frac{d\theta}{2} = f_r R_c d\theta \tag{5.5}$$

For small angles of, $d\theta$, it can be said that:

$$sin\frac{d\theta}{2} \rightarrow \frac{d\theta}{2} \tag{5.6}$$

Therefore, the complexity of equation 5.5 can be reduced to:

$$F_\theta = f_r R_c \tag{5.7}$$

Assuming that the stress in the circumferential direction, σ_θ, is uniform over the V-band cross section area, A_B, gives:

$$\sigma_\theta = \frac{F_\theta}{A_B} \tag{5.8}$$

In a pure ring deformation the change of the radial expansion, δ_r, in relation to the contact radius, R_c, equals the strain in the circumferential direction, ε_θ, and is thus related to the circumferential stress, σ_θ, as:

$$\frac{\delta_r}{R_c} = \varepsilon_\theta = \frac{\sigma_\theta}{E} \tag{5.9}$$

Where E = Young's modulus

Substituting equations 5.8, and 5.7 into 5.9, it can be said that

$$\frac{\sigma_\theta}{E} = \frac{F_\theta}{EA_B} = \frac{f_r R_c}{EA_B} \tag{5.10}$$

Equation 5.4 together with 5.10 can be substituted in 5.9 leading to the new relation:

$$\frac{\delta_r}{R_c} = \frac{F_A}{2EA_B\beta} tan\phi^* \tag{5.11}$$

As the aim of this part of the work is to generate a single equation describing the axial load, including parameters that could easily be gathered from literature, equation 5.11 is re-arranged to:

$$F_A = \frac{\delta_r}{R_c} \frac{2EA_B\beta}{tan\,\phi^*} \tag{5.12}$$

It is worth noting, that the relationship between, δ_r, and ϕ^* is largely dependent on the V-section shape and the position of the contact point. This is discussed in the next sub-section.

5.2.2 Definition of Contact Radius R_c

Since the reference point for defining δ_r is the contact point between band and flange with the radius, R_c, the latter has to be defined also. This can be done using the dimensions of the flange. As shown in Figure 5-3, on the flange initial contact can be defined to take place at the point where the flat part with the V-angle ϕ, and the corner radius, r_c, meet.

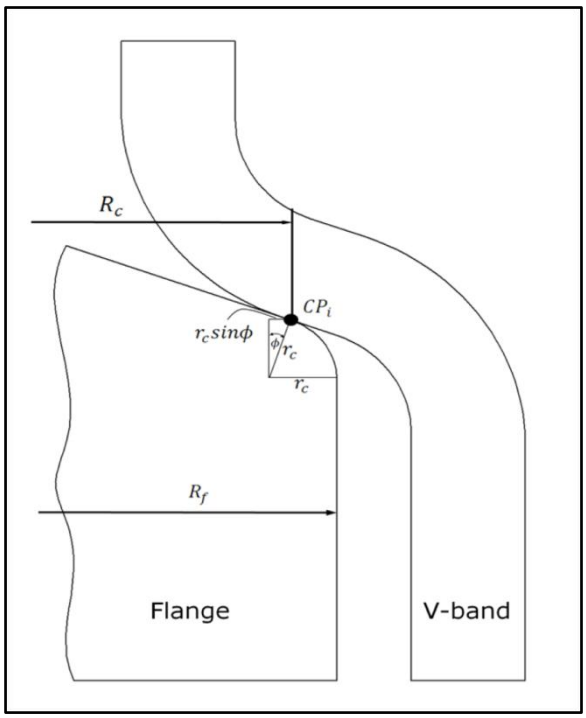

Figure 5-3: Definition of R_c for initial contact between V-band and flange

It is important to remember that the following definition is only valid for initial contact after the retainer has been assembled to a pair of flanges and a T-bolt tension applied, prior to the application of any external loads. Moreover, the angle of the flat part on the flange must match the V-angle, ϕ, which is an assumption also used by Shoghi (2003). R_c can then be defined using the flange dimensions as:

$$R_c = R_f + r_c(sin\phi - 1) \tag{5.13}$$

It is clear from this discussion that the contact radius, R_c, and hence the contact point depend on the shape of the flanges and V-band cross section, although for large joint diameters, small deviations and errors of R_c only have a minor influence on the axial load, F_A. After defining R_c using equation 5.13, the results can then be substituted into equation 5.12.

5.2.3 Definition of Radial Expansion due to Ring Deformation

Defining the radial expansion, δ_r, is probably the most complex part of this section of the theory. Figure 5-4 shows one half of the cross section of a joint in which the flange is separated axially and sliding over the inner side of the V-band. The initial contact, CP_i, (also see Figure 5-1) is marked on both the band and flange as, CP_{ib}, and CP_{if} respectively. The current subsequent contact point is marked with CP_s.

Since this theory assumes the flange and band cross sections to be rigid, the contact force is always normal to both surfaces, and its direction can be described by the angle, ϕ^*.

In order to define radial expansion, δ_r, the geometrical V-band cross section parameters, radius, r_b, and the radial sliding length, l_s, as indicated in Figure 5-4 are required. Radius r_b can easily be obtained from drawings, and for a given cross section remains constant. The definition of l_s is not straightforward and its accurate definition is vital for predicting the correct F_{UALC}. l_s describes the length on the flat part of the leg between initial contact CP_i and the start of radius r_b, for which the current angle between axial and radial force, ϕ^*, remains constant, and equals the V-band angle ϕ. Its length depends on several parameters, such as the flange thickness, t_f, and the axial clamping load, F_{ACL}, and for the current methods needs to be obtained either from finite element simulations, or experimental data .

Since the current theory focuses on the geometrical definition of the change in position of the contact point during failure, parameters such as the flange or band thickness are not yet accounted for.

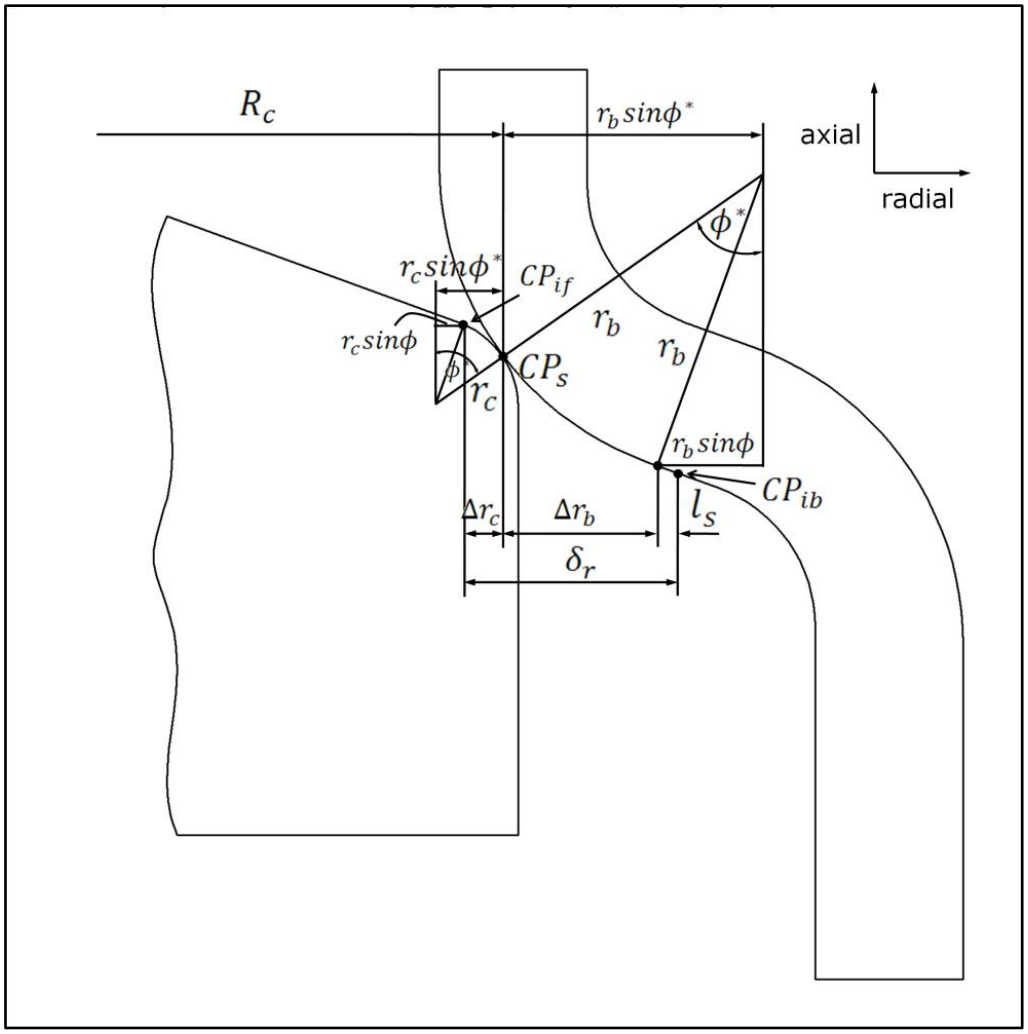

Figure 5-4: Cross section area of deformed V-band joint

The radial expansion δ_r can then be obtained as the sum of Δr_b, and Δr_c, which represent the change of radius of the contact point on the band and flange respectively, and the radial sliding length l_s. This relationship can then be expressed as

$$\delta_r = \Delta r_b + \Delta r_c + l_s = (r_b + r_c)(sin\phi^* - sin\phi) + l_s \tag{5.14}$$

Where:

$$\Delta r_b = r_b(sin\phi^* - sin\phi) \tag{5.15}$$

and

$$\Delta r_c = r_c(sin\phi^* - sin\phi) \tag{5.16}$$

5.2.4 Definition of the Ultimate Axial Load Capacity

In the previous chapter 4, the ultimate axial load capacity, F_{UALC}, was defined as the maximum axial force during flange separation. Combining equations 5.12 and 5.14, considering the shape of V-band and flanges, the axial load can expressed as:

$$F_A = \frac{[(r_b+r_c)(sin\,\phi^*-sin\phi)+l_s]}{R_c}\frac{2EA_B\beta}{tan\,\phi^*} \tag{5.17}$$

Since the only variable in equation 5.17 is the angle ϕ^*, F_A can be differentiated with respect to ϕ^*:

$$\frac{dF_A}{d\phi^*} = \frac{(r_b+r_c)cos\,\phi^*2EA_B\beta}{R_c}(-sin^2\phi^*) \tag{5.18}$$

And since

$$sin^2\phi^* = 1 - cos^2\phi^* \tag{5.19}$$

combining equations 5.17 and 5.18:

$$\frac{dF_A}{d\phi^*} = \frac{(r_b+r_c)cos\,\phi^*2EA_B\beta}{R_c}(cos^2\phi^* - 1) \tag{5.20}$$

In order to find the maximum of 5.17, equation 5.20 must be set to equal 0:

$$\frac{dF_A}{d\phi^*} = 0$$

which is valid for $\phi^* = \frac{\pi}{4}(= 45°)$, since $\cos(45°) = 0$.

Following this method, it can be concluded that $F_A = F_{UALC}$, when $\phi^* = \frac{\pi}{4}$, as expressed by:

$$F_{UALC} = \frac{\left[(r_b+r_c)\left(\sin\left(\frac{\pi}{4}\right)-sin\phi\right)+l_s\right]}{R_c}\frac{2EA_B\beta}{tan\left(\frac{\pi}{4}\right)} \tag{5.21}$$

5.3 Ring Theory Results

In this section, the results for equation 5.12 are compared to numerical results of the axisymmetric finite element model presented in chapter 4, for several flange and band parameters, and the differences between the methods are compared and discussed. The properties used in this section are listed in Table 5-1. For each axial clamping load, the associated sliding length l_s was obtained from the finite element model. It should be noted that the sliding length varies with band diameter for the same axial clamping load.

However, this variation is insignificant and therefore the theory assumes l_s not to change.

Table 5-1: Properties of V-band joint used in ring theory

V-band angle ϕ	20°
Sliding length l_s	0.09 mm (for 6kN), and 0.125mm (for 25kN)
V-band bending radius r_b	2.78 mm (1.3 mm)
Flange contact radius r_c	0.8 mm
Elastic modulus E	227000 N/mm^2
V-band cross section area A_B	13 mm^2
Subtended angle of half the band β	167°, (180°)

5.3.1 Axial Load Variation during V-Band Failure

As discussed previously in chapter 4, very large V-band joints deform mainly elastically due to ring expansion. Therefore, a joint with $D_b = 2000mm$ (the largest diameter analysed in chapter 4) was chosen in order to compare the variation in axial load during failure of a V-band joint predicted by the ring theory to the axisymmetric finite element model.

Using equation 5.17 the axial load variation is as shown in Figure 5-5. The two graphs reporting the ring theory values show small differences at the maxima when exchanging β=167° to 180°. When compared to the finite element model for an axial clamping load, $F_{ACL} = 6kN$, and $\mu = 0$, the results indicate that there is a closer correlation between the FEA data and the theory for β=180°, than 167°. This is mainly due to the fact that β =167° is a measured value used by Shoghi *et al.* (2004) for real V-band applications, and β=180° is what was assumed in the axisymmetric finite element analysis. It can be observed that the main difference between finite element and theoretical graphs lies closest to the start of deformation. This difference occurs because the axial clamping load, F_{ACL} is not included in the theory so it is to be expected that the FEA results should always be 6kN higher than the β=180° degree theory. However, the theory assumes a rigid cross section whereas the FEA has a deformable cross section (even though that deformation is small). The deformation of the section increases ϕ and hence decreases F_{UALC} (i.e. reduces the preload effect of the clamping load F_{ACL}) and also reduces the δ_r,at which F_{UALC} occurs (equation 13).

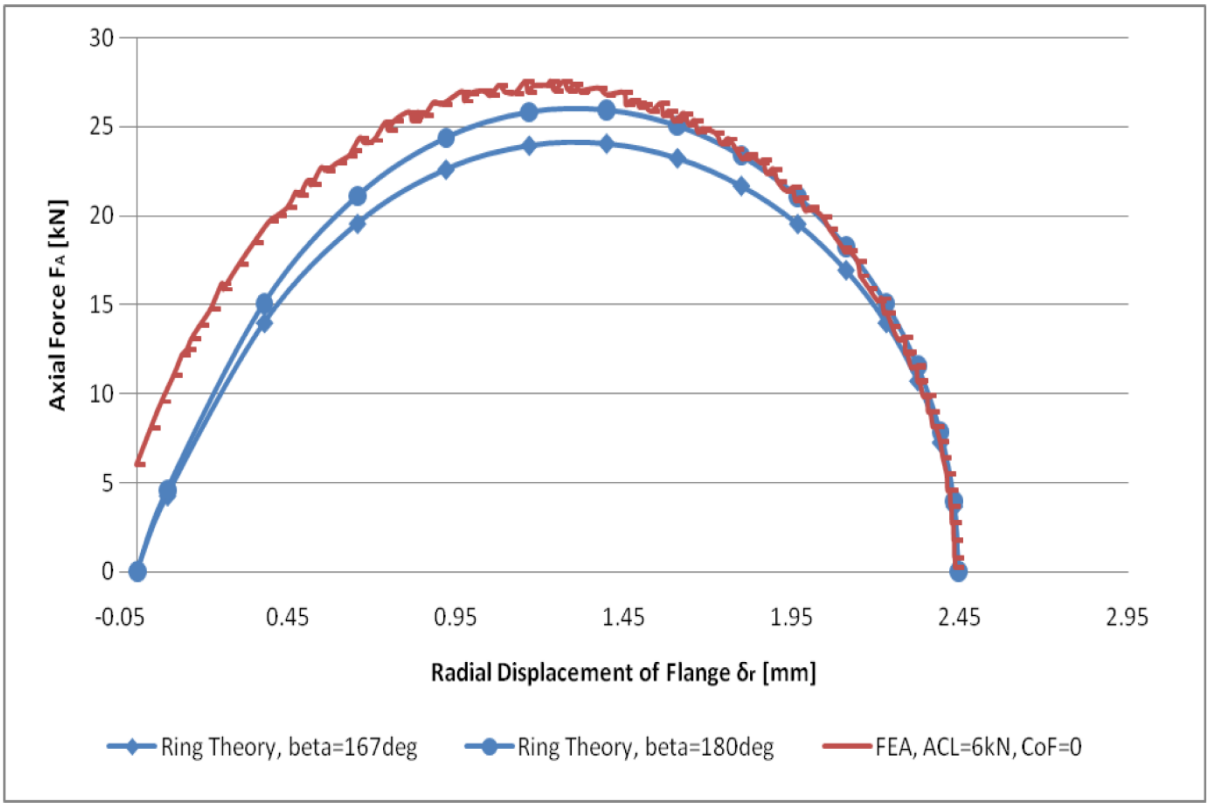

Figure 5-5: Predicted ultimate axial load capacity for axisymmetric FEA model compared to Ring Theory, $D_b = 2000mm$

Table 5-2 gives the radial expansion where the ultimate axial load capacity occurs and the capacity itself, showing good correlation between both methods used.

Table 5-2: Results of Ring theory and finite element analysis for F_{UALC} and δ_r

Method of calculation	Ultimate Axial Load Capacity F_{UALC} [kN]	Radial expansion δ_r [mm] where F_{UALC} occurs
Ring theory ($r_b = 2.78mm, r_c = 0.8mm$, $l_s = 0.06mm$, $D_b = 2000mm$, $\beta = 167°$)	24.07	1.397
Ring theory ($r_b = 2.78mm, r_c = 0.8mm$, $l_s = 0.06mm$, $D_b = 2000mm$, $\beta = 180°$)	25.94	1.397
Axisymmetric finite element model. ($F_{ACL} = 6kN$, $\mu = 0$, $D_b = 2000mm$)	27.53	1.23

5.3.2 Effect of Band Diameter D_b, on Ultimate Axial Load Capacity

Calculating the ultimate axial load capacity F_{UALC} from equation 5.21

$$F_{UALC} = \frac{\left[(r_b+r_c)\left(\sin\left(\frac{\pi}{4}\right)-sin\phi\right)+l_s\right]}{R_c}\frac{2EA_B\beta}{tan\left(\frac{\pi}{4}\right)} \tag{5.21}$$

for a wide range of band diameters D_b, it can be seen in Figure 5-6 that the value increases rapidly as the diameter decreases. Very good correlation between finite element and theoretical predictions predominates for band diameters D_b between 800mm and 2000mm.

This confirms the finding in chapter 4, that large V-bands deform purely elastically due to ring expansion, without deforming the cross section. Moreover, it can be seen that the theoretical results for $\beta = 180°$ correlate better with the finite element data, as presented in the previous sub-section 5.3.1.

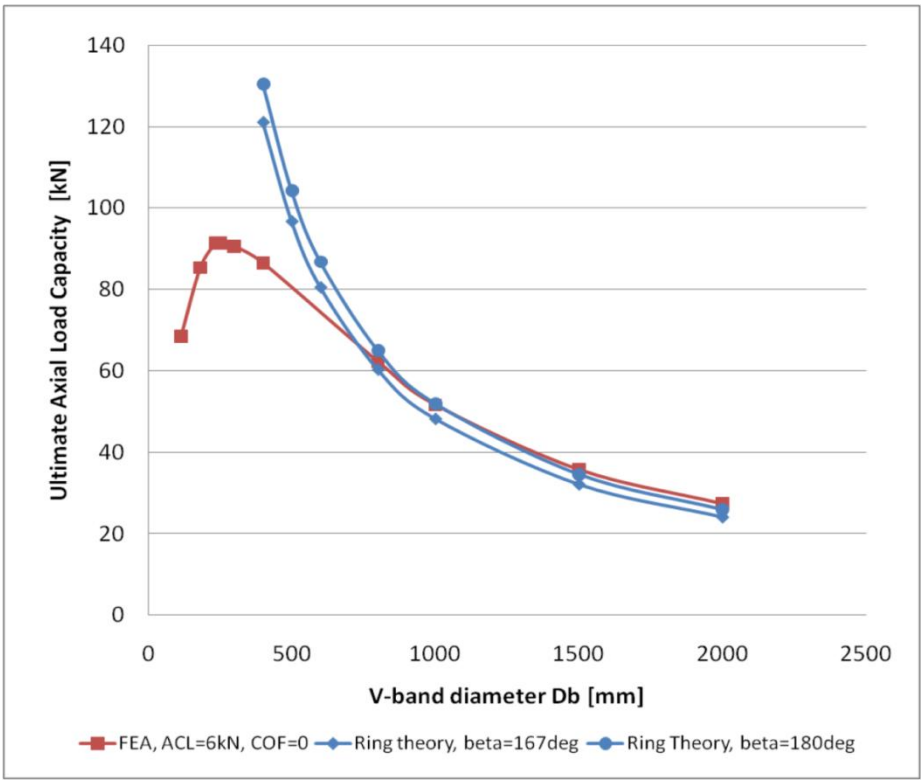

Figure 5-6: Predicted ultimate axial load capacity over band diameter for axisymmetric FEA model compared to Ring Theory

Figure 5-7 shows the impact on the ultimate axial load capacity F_{UALC} when changing the band bending radius r_b from 2.78mm to 1.3mm. It should be noted here, that, for the given section, changing r_b to 1.3mm is not possible in reality due to the cold roll forming manufacturing process. This modification of the section increases l_s from 0.06mm to 1.02. As can be seen, reducing r_b has a minor impact on V-band joints with D_b between

114mm and 181mm, but increases its effect significantly on bands with medium and large diameters. A more detailed discussion of the impact of r_b on the ultimate axial load capacity is given in sub-section 4.5.5.

This change of radius was included merely to point out firstly the importance of defining the correct band section geometry as a whole, the importance of the interaction between r_b and l_s in particular, and the capability of the derived Ring Theory to consider this change successfully.

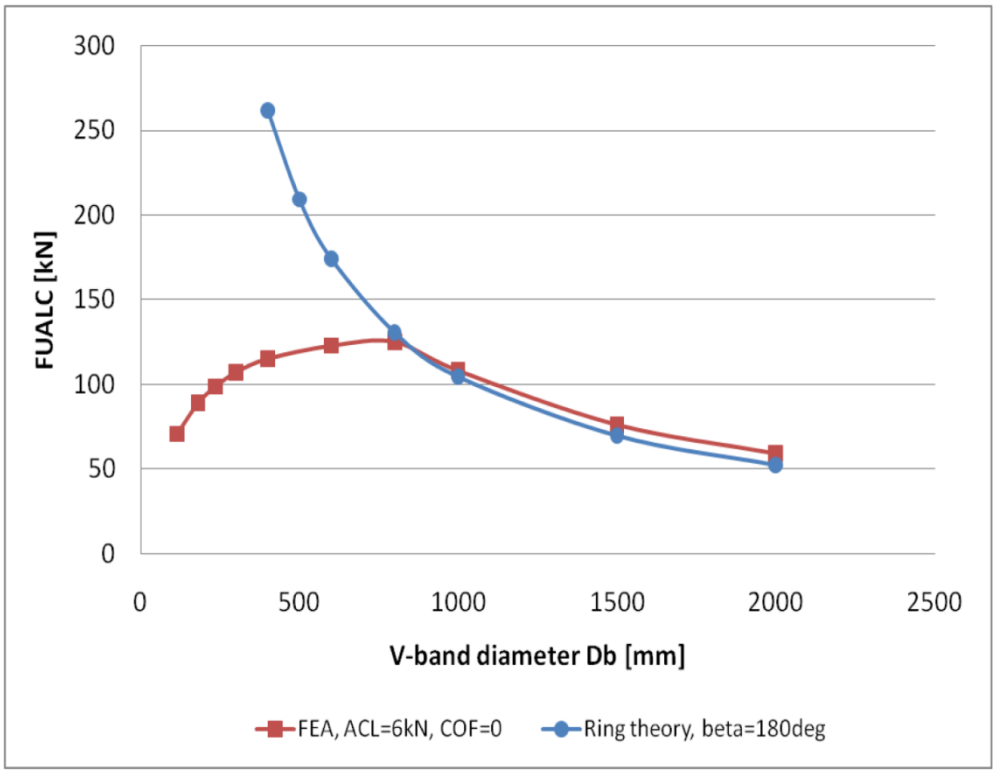

Figure 5-7: Predicted ultimate axial load capacity over band diameter for axisymmetric FEA model compared to Ring Theory, r_c=1.3mm

In the next case, the ring theory is compared to the finite element model from sub-section 4.5.7, and shows very good correlation between both graphs. As discussed for this FE-model, the linear elastic material properties shifted the deformation behaviour of the band section for bands with a diameter below D_b = 800mm, to increase the amount of deformation due to ring expansion δ_r, and reduce the deformation due to section bending δ_s. This statement can be validated by the two graphs in Figure 5-8, where for V-bands below 800mm, the correlation is still very good, but there is a divergent trend. This minor difference is due to the fact that the theory assumes the band to deform as a rigid cross section ring, whereas the finite element analysis includes a small but significant amount of section deformation.

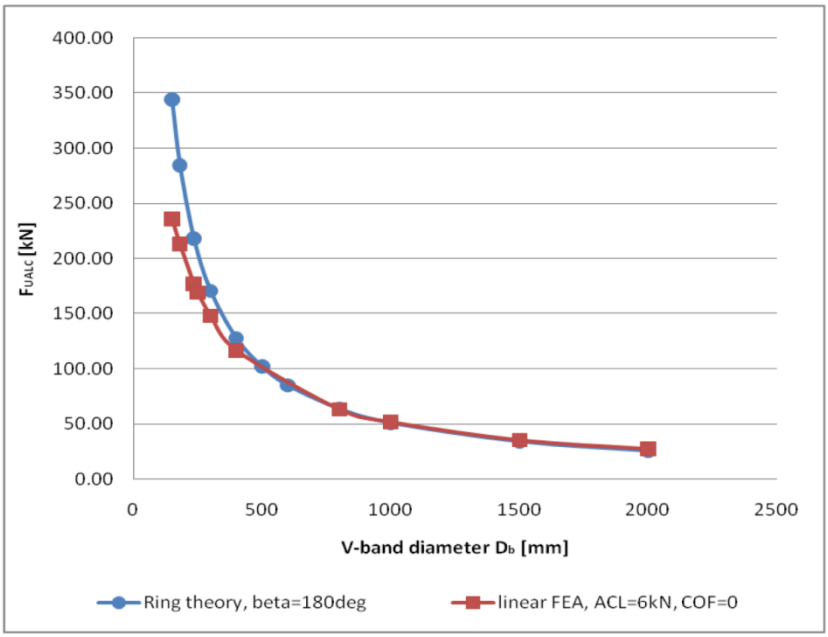

Figure 5-8: Predicted ultimate axial load capacity over band diameter for linear axisymmetric FEA model compared to Ring Theory

As mentioned previously, in the theory, the effect of the axial clamping load is taken into account by manipulating the sliding length l_s. For an axial clamping load of F_{ACL}=25kN, the sliding length was set to l_s=1.25mm, which was obtained from the axisymmetric finite element model. As can be seen in Figure 5-9 for larger clamping loads the difference between theoretical and finite element data increases. The current theory does not yet manage to include this effect sufficiently, but shows correct distributions and trends.

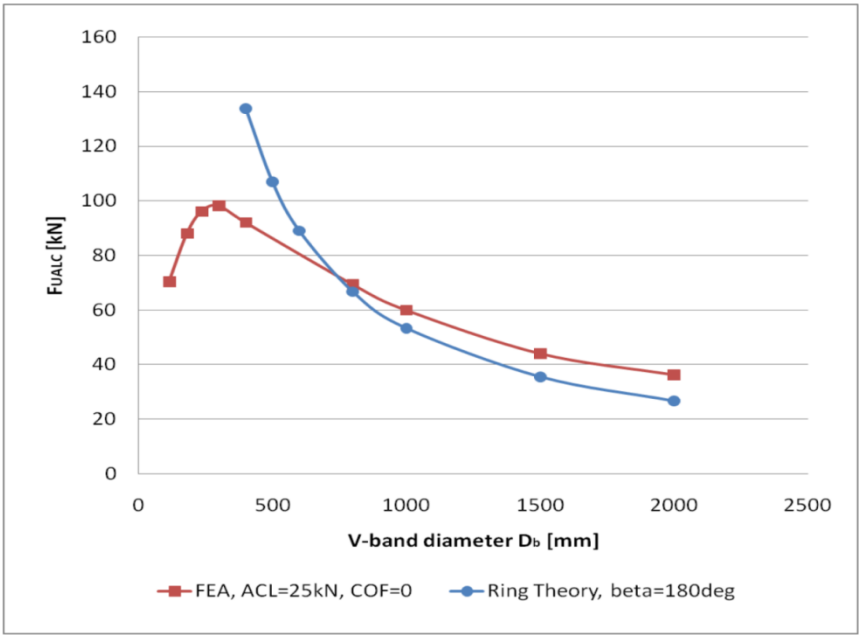

Figure 5-9: Predicted ultimate axial load capacity over band diameter for axisymmetric FEA model compared to Ring Theory

It was shown, that the Ring theory developed here is capable of successfully predicting the ultimate axial load capacity of V-band joints, for diameters D_b equal to and larger than 800mm.

5.4 Development of Combined Section and Ring Theory

In this section, a combined theory taking into account section deformation due to bending of the back of the section, and the previously discussed elastic ring deformation is presented, as this is a deformation behaviour investigated using finite element models in chapter 4. During the development of the theory, several assumptions were made, as listed here:

Assumptions:

- Section deformation:
    - V-band cross section is reduced to a wide rectangular cantilever
    - No friction
    - Flanges separate in axial direction only
    - Elastic deformation only, no plasticity included
    - Equations used are only valid for small deformations
    - Leg and foot taken into account to describe position of contact and predict axial and radial levers
    - Circumferential expansion of leg and foot not taken into account
    - No preload included
- Ring deformation (first half of this chapter):
    - Uniform circumferential stress in whole V-band cross section
    - No friction
    - Rigid cross section
    - Flanges separate in axial direction only
    - Deforming only in the circumference
    - Elastic deformation

5.4.1 Definition of Section Deformation in Initial Stage

The part of the theory presented in this sub-section is only concerned with the section deformation, and assumes the V-band cross section to be a rectangular cantilever as shown for the initial stage in Figure 5-10 (red rectangle), with length L, thickness t_b (equal to the V-band thickness), width l_b (equal to the V-band length), elastic modulus E, and second moment of area I. The foot and leg are only considered to calculate K and H, which represent the levers for the radial F_R and axial force F_A respectively. The relationship between radial and axial force in the initial stage can be expressed as:

$$F_R = F_A \tan \phi \tag{5.22}$$

which is a modified version of equation 5.7. Moreover, during the failure process, the foot and leg are assumed to remain rigid in relation to the free end of the cantilever (back of V-band).

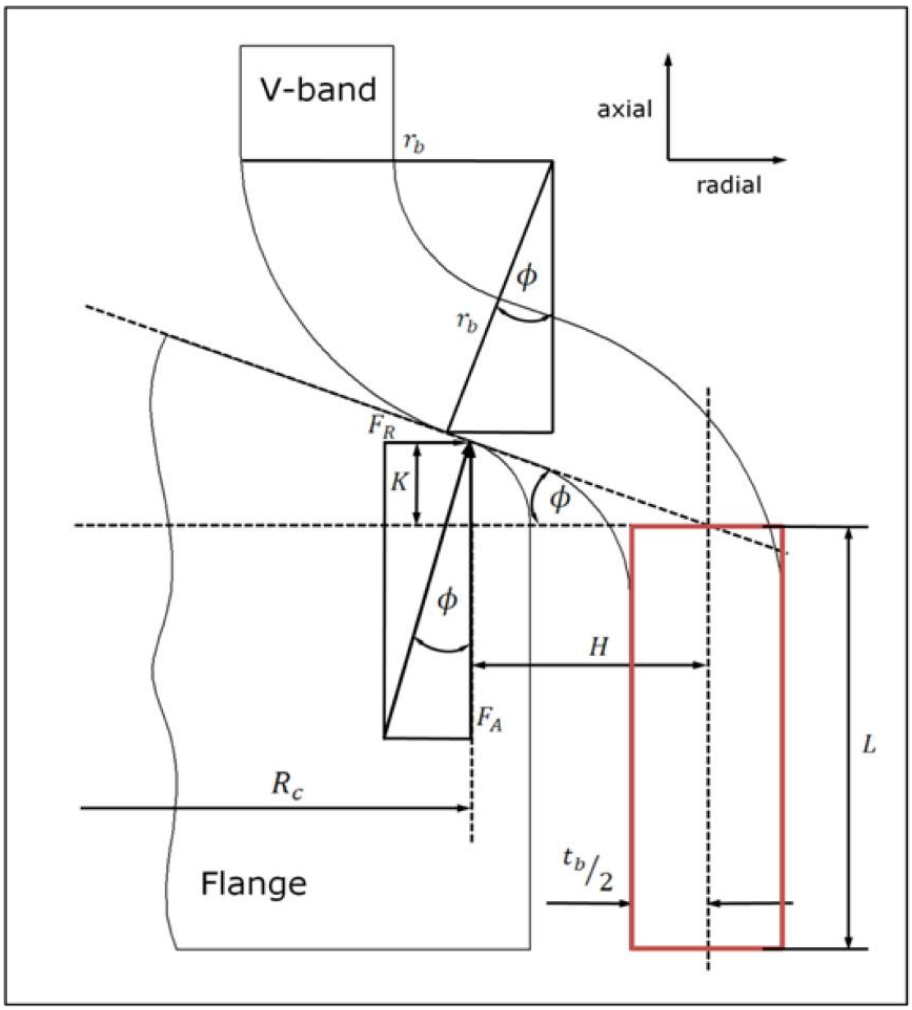

Figure 5-10: V-band cross section with cantilever (red) assumed in the back

A suitable method of calculating the cantilever deflection is the unit-load method as presented by Gere and Timoshenko (1991) and given in equation 5.23:

$$\Delta = \int \frac{M_U M_L}{EI} dx \tag{5.23}$$

where Δ represents a displacement, M_L the moment due to the actual loads, and M_U the moment due to a fictitious unit load applied at the point where the deformation is to be found.

As the cantilever is subjected to a bending moment M_L its free end rotates by the angle θ_a, and deflects by δ_s which can be seen in Figure 5-11a and b.

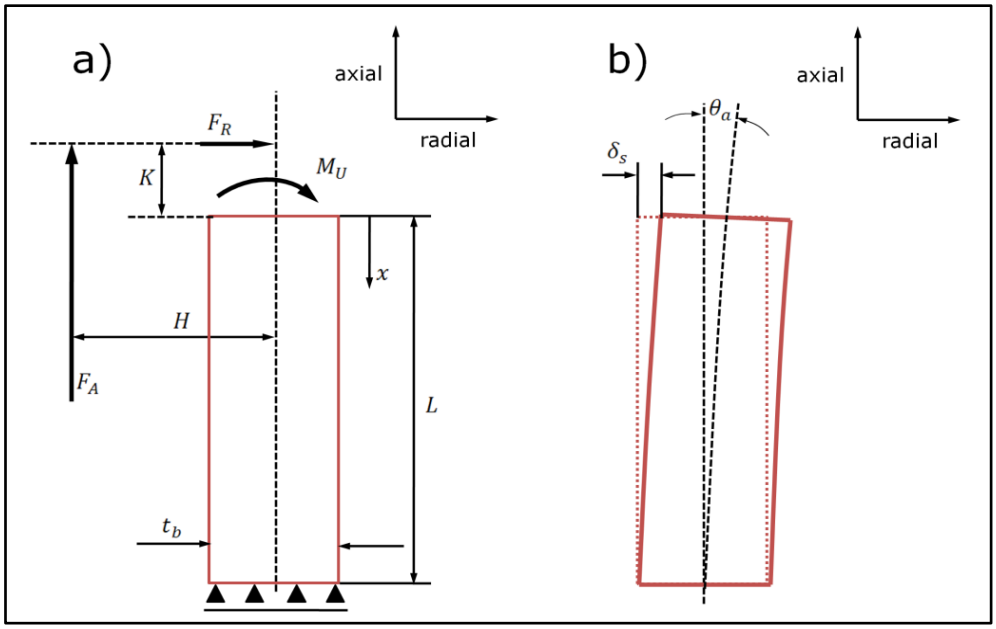

Figure 5-11: Assumed cantilever of flat part of V-band section

In order to calculate the rotation, Δ is replaced by θ_a, $M_U = 1$ and substituting this into equation 5.23 gives:

$$\theta_a = \int \frac{M_L}{EI} dx \tag{5.24}$$

Where: $M_L = F_R(K + x) + F_A H$ (5.25)

Substituting 5.25 into 5.24 the gives:

$$\theta_a = \frac{1}{EI} \int_0^L [F_R(K + x) + F_A H]\, dx \tag{5.26}$$

After solving the integral it can be written as:

$$\theta_a = \frac{1}{EI} \left[F_R K x + F_R \frac{x^2}{2} + F_A H x \right]_0^L \tag{5.27}$$

And inserting the limits leads to

$$\theta_a = \frac{1}{EI} \left(F_R K L + F_R \frac{L^2}{2} + F_A H L \right) \tag{5.28}$$

The second moment of the area I is given in equation 5.29

$$I = \frac{{t_b}^3 l_b}{12} \tag{5.29}$$

Where the band length l_b is the circumference is considered as

$$l_b = 2\beta R_c \tag{5.30}$$

Substituting equation 5.22 into 5.28, the angle can be expressed as

$$\theta_a = \frac{L}{EI}\left[(F_A \tan\phi\left(K+\frac{L}{2}\right)+F_A H)\right] \quad (5.31)$$

Rearranging equation 5.31 the axial force can be expressed as:

$$F_A = \frac{\theta_a EI}{\tan(\phi+\theta_{a\,n})L\left(K+\frac{L}{2}\right)+HL} \quad (5.32)$$

In addition to the angular deformation θ_a, the radial deflection δ_s at the free end of the cantilever, as shown in Figure 5-11b, is derived in a similar way. In the original equation 5.23, Δ is then replaced by δ_s and $M_U = 1x$. This can then be expressed in equation 5.33.

$$\delta_s = \frac{1}{EI}\int_0^L [F_R(K+x)+F_A H]x\,dx \quad (5.33)$$

And including x and solving the bracket gives

$$\delta_s = \frac{1}{EI}\int_0^L [F_R Kx + F_R x^2 + F_A Hx]\,dx \quad (5.34)$$

Solving the differential the results in

$$\delta_s = \frac{1}{EI}\left[F_R K\frac{x^2}{2}+F_R\frac{x^3}{3}+F_A H\frac{x^2}{2}\right]_0^L \quad (5.35)$$

and inserting the limits leads to

$$\delta_s = \frac{L^2}{EI}\left[F_R\left(\frac{K}{2}+\frac{L}{3}\right)+F_A\frac{H}{2}\right] \quad (5.36)$$

Again substituting equation 5.22 into 5.36 then gives the radial deflection as:

$$\delta_s = \frac{L^2}{EI}\left[F_A \tan(\theta_r)\left(\frac{K}{2}+\frac{L}{3}\right)+F_A\frac{H}{2}\right] \quad (5.37)$$

which is very similar to the angular deflection expressed in equation 5.21.

5.4.2 Contact along Sliding Length of V-Band Leg (Combined Section and Ring Deformation)

In this sub-section, a method is presented to combine both parts of the theory for radial expansion due to section deformation (sub-section 5.4.1) and ring deformation (section 5.2). Considering the symmetry of the V-band joint, as one flange is moved out in the axial direction it slides along the inside of the V-band. For the results obtained by the combined theory the difference between contact along the flat part of the leg and the

radius r_b is very important. This sub-section is therefore particularly focussing on the flat part, whereas movement around the radius r_b is discussed in the subsequent sub-section.

Let the cross section be deformed at a point in time n, then the relationship between radial and axial force changes by rearranging 5.22 into equation 5.38 , where ϕ is now replaced with $\phi + \theta_{a\,n}$ due to the angular deflection $\theta_{a\,n}$:

$$F_{Rn} = F_{A\,n}\tan(\phi + \theta_{a\,n}) \tag{5.38}$$

As the V-band cross section starts to deform the lengths of levers H, and K for the axial and radial force increase to H_n and K_n respectively. This can be seen in Figure 5-12a for the whole cross section, and in Figure 5-12b considering radial deflections δ_s and δ_r due to section and ring deformation only for the cantilever. $\delta_{s\,n}$ can be calculated using equations 5.37 only considering the cantilever, and $\delta_{r\,n}$ can be calculated using equation 5.39, which is a rearranged version of 5.12 considering the whole V-band cross section.

$$\delta_{r\,n} = \frac{F_{An}\ R_c\tan(\phi+\theta_{an})}{2EA_B\beta} \tag{5.39}$$

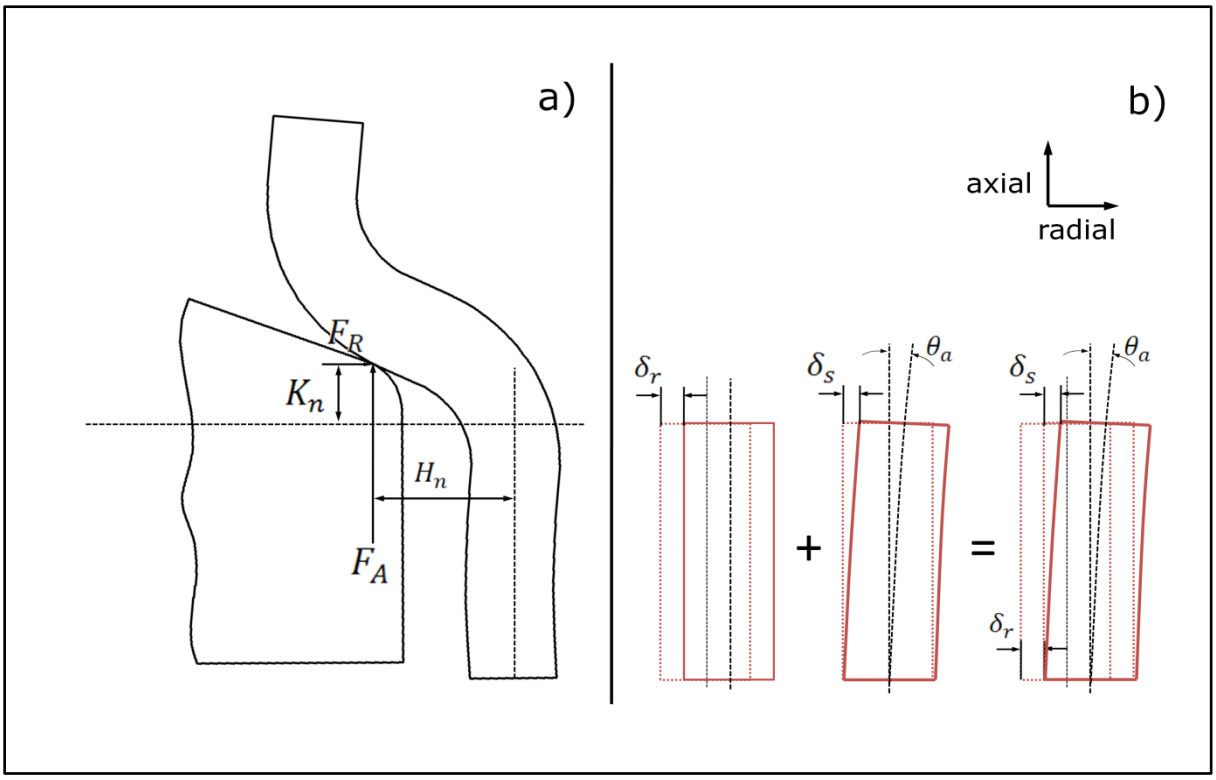

Figure 5-12: Deformed V-band with contact along flat part of leg, a) full V-band cross section and flange, and b) assuming only a cantilever

The lever H_n (at time n) for the axial force can be expressed as the sum of the original lever length at initial position H_0, section $\delta_{s\,n}$ and ring $\delta_{r\,n}$ deformation, and the subtraction of the distance the V-band has slid over the flange $r_c[\sin(\phi + \theta_{a\,n}) - \sin(\phi)]$. The

derivation of the subtraction including the flange radius r_c can be explained much better using the diagram shown in Figure 5-13, where a) includes the flange, and b) excludes the flange for a better view. There, CP_{if} describes the initial contact point on the flange, and CP_{fn} describes the contact point at a point in time n. The radial distance between both points is then defined as $r_c[\sin(\phi + \theta_{a\,n}) - \sin(\phi)]$.

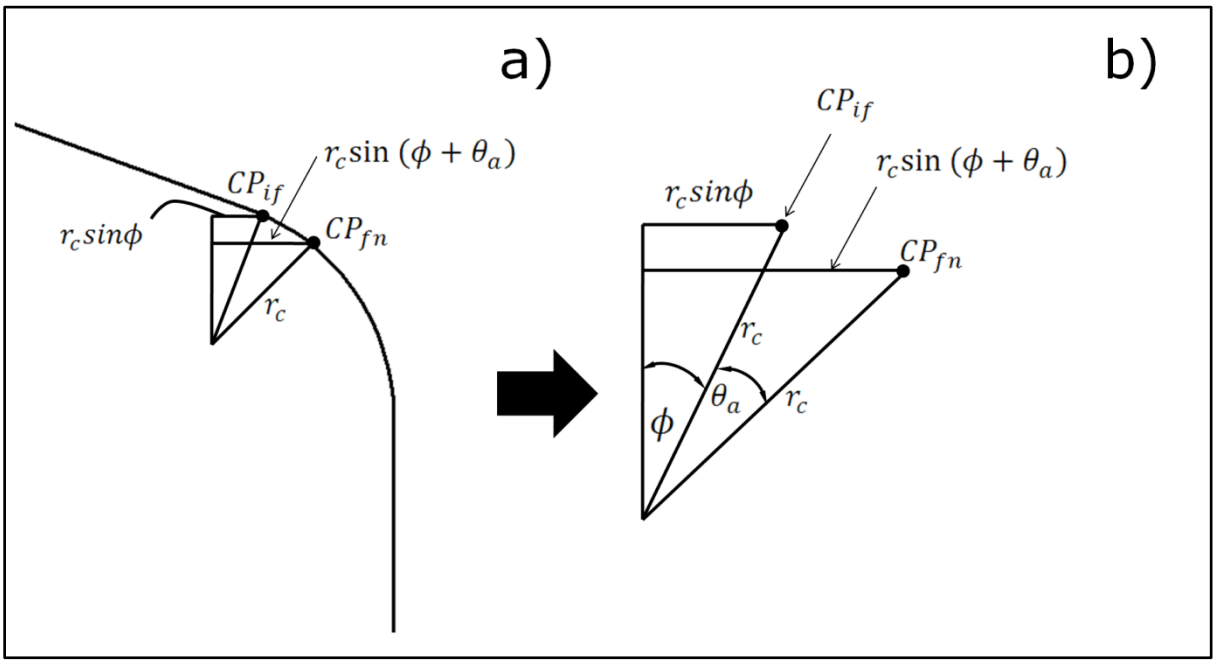

Figure 5-13: Detailed view of change in contact point at flange radius when in contact with flat part of V-band leg, a) including, and b) excluding the flange

H_n can then be given by equation 5.40.

$$H_n = H_0 + \delta_{s\,n} + \delta_{r\,n} - r_c[\sin(\phi + \theta_{a\,n}) - \sin(\phi)] \qquad (5.40)$$

As the relationship and angle $\phi + \theta_{a\,n}$ between the levers is the same as for the associated forces, lever K_n can be given as:

$$K_n = H_n \tan(\phi + \theta_{a\,n}) \qquad (5.41)$$

The change in section geometry described above will be large leading up to joint failure. An incremental process is therefore required to predict the deformation. This is explained in the following paragraphs and shown in Figure 5-14.

Step 1 of the methodology used to predict axial and radial behaviour of a V-band joint is to assume a value for $\theta_{a\,n}$ at a given point in time n and calculate the axial load F_{An} using the previously derived equations 5.32.

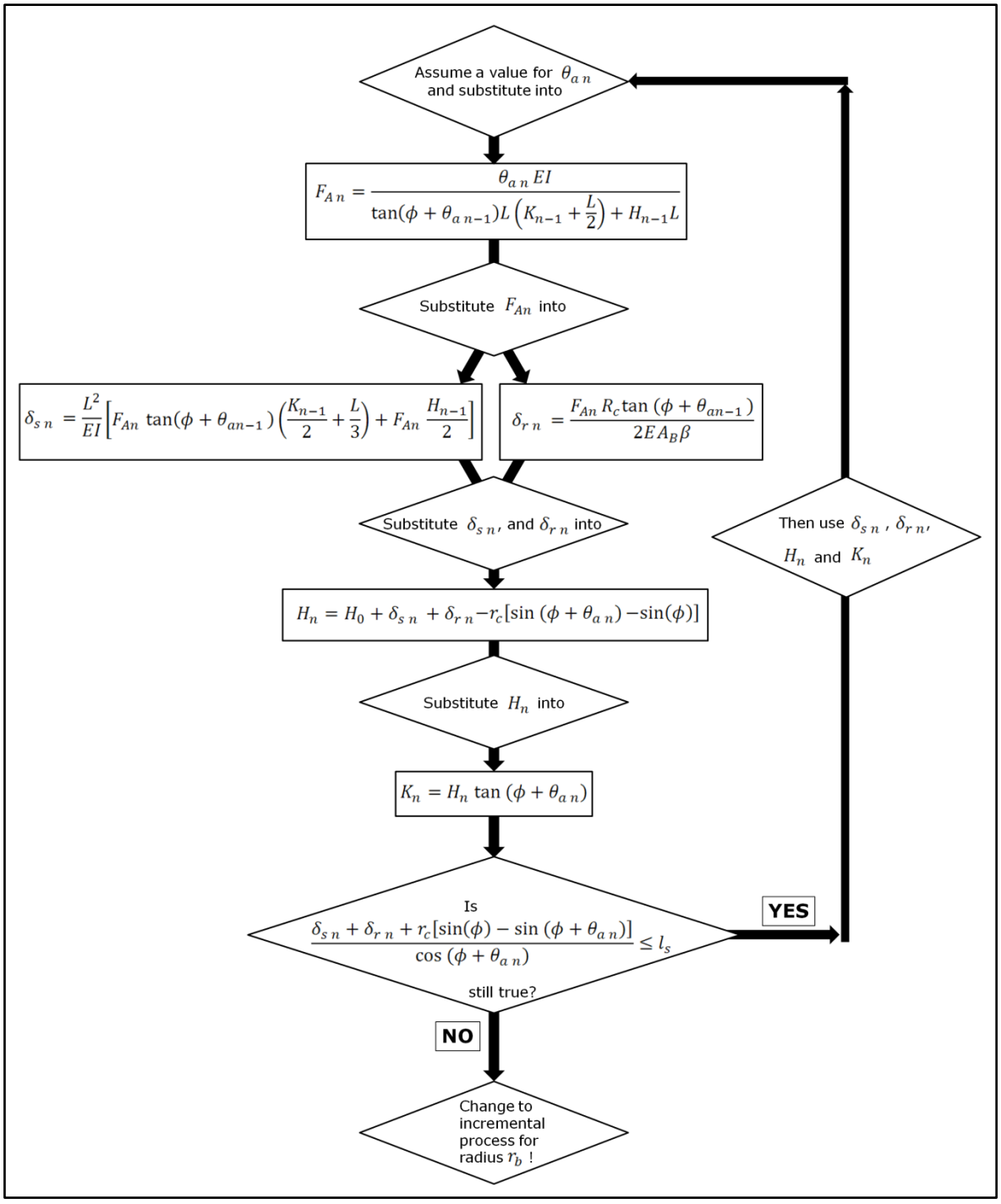

Figure 5-14: Method used to calculate axial load variation along flat part of V-band leg

Step 2 then uses F_{An} in order to calculate radial section δ_{sn} and ring δ_{rn} deflection as given by equations 5.37 and 5.39. For both equations, K_{n-1}, H_{n-1}, and $\theta_{a\,n-1}$ are again taken from the previous increment, and for the first increment K_{n-1}, and H_{n-1}, are equal to their initial values K_0 and H_0.

In step 3 the two radial deflections $\delta_{s\,n}$ and $\delta_{r\,n}$ are then used to gather the current levers H_n and K_n as defined by equations 5.40 and 5.41, however using the $\theta_{a\,n}$ rather than the previous $\theta_{a\,n-1}$.

Step 4 then consists of repeating steps 1 to 3.

However, this methodology is valid only as long as contact is established along the flat part of the leg with the radial sliding length l_s, which is defined in Figure 5-15. It should be noted that in this case and only for this particular definition $l_s/\cos(\phi+\theta_{a\,n})$ is replaced with l_s as the angle $\theta_{a\,n}$ at this specific position is unknown. Due to the small values used, this assumption has only a minor impact on the results. For all subsequent definitions l_s is the correct radial component again. In there a) describes the radial difference between initial contact and contact at the end of the sliding length for $r_c[\sin(\phi)-\sin(\phi+\theta_{a\,n})]$ on the flange. In b) the relationship of the lever distances for the initial position and the position at the end of the flat part are shown. The red triangle from b) is drawn to a larger scale in c), and the relationship of this triangle is expressed in d), which defines l_s.

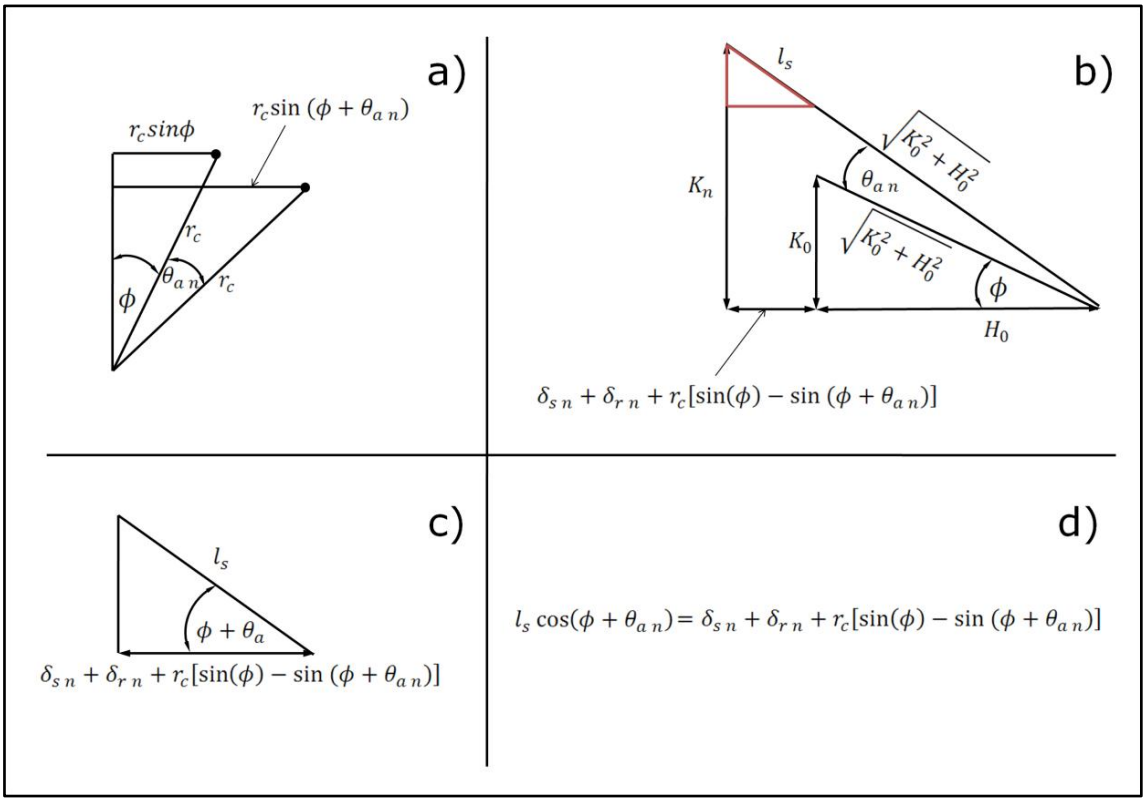

Figure 5-15: Limit of contact region, a) Sliding along flange (taken from figure 1-14), b) relationship between levers at initial position and at end of flat part, c) enlarged view of red triangle from b), and d) relationship of triangle in c)

This can be expressed equation 5.42 and as long as the left term is smaller or equal to l_s, contact is established along the flat part.

$$\frac{\delta_{s\,n}+\delta_{r\,n}+r_c[\sin(\phi)-\sin(\phi+\theta_{a\,n})]}{\cos(\phi+\theta_{a\,n})} \leq l_s \tag{5.42}$$

Once equation 5.42 is no longer true, the incremental process along the flat part has finished, and needs to be changed to the method described in the subsequent sub-section.

5.4.3 Contact along Radius r_b (Combined Section and Ring Deformation)

Once the contact between flange and band moves off the flat surface of the band and onto the radius r_b the angle of the normal contact direction is no longer the sum of $\phi + \theta_{a\,n}$ but changes to θ_r, which is not as straightforward to calculate.

In order to calculate θ_r several geometrical parameters must be introduced, mainly L_b, which represents the distance between the end of the cantilever EC_i and the centre point $C_i r_b$ of radius r_b, and its associated angle γ, as shown in Figure 5-16. Both these parameters are calculated in the initial position, and hence are assumed to remain constant throughout the deformation process, as the leg is assumed to stay rigid with only the back of the section deforming.

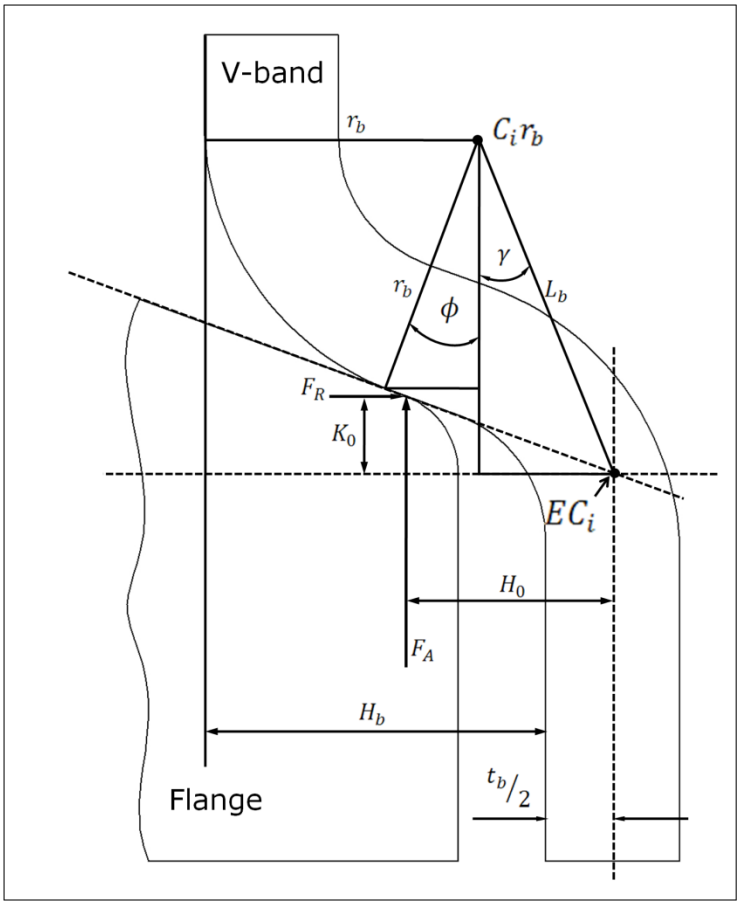

Figure 5-16: Half a V-band and flange section for initial contact showing geometrical parameters required during prediction of deformation

L_b can be calculated employing equation 5.43 and is assumed to remain constant

$$L_b = \sqrt[2]{(H_b + {}^{t_b}/_2 - r_b)^2 + (K_0 + l_{sv} + r_b cos\phi)^2} \quad (5.43)$$

Where, H_b, is the depth of the V-band section, and l_{sv} is the axial component of the sliding length l_s.

$$l_{sv} = l_s \, tan\phi \quad (5.44)$$

The angle γ can be expressed as:

$$\gamma = atan \frac{H_b + {}^{t_b}/_2 - r_b}{K_0 + l_{sv} + r_b cos\phi} \quad (5.45)$$

Figure 5-17a shows the undeformed initial position with the initial contact point on the flange CP_{if}, and the end point of the cantilever EC_i. There it can be seen that the distance between the centre $C_i r_b$ of radius r_b and the centre $C_i r_c$ of radius r_c is the sum of $r_b + r_c$. Transferring the four points into Figure 5-17b it can be seen how they change during deformation of the cross section at any time n.

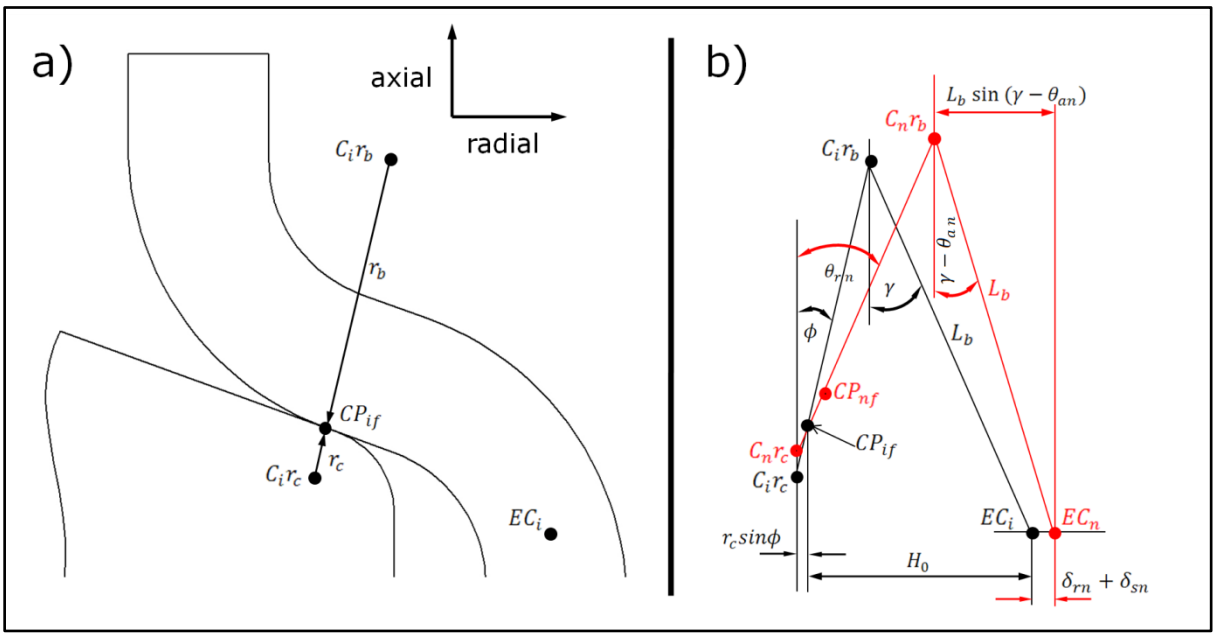

Figure 5-17: a) initial undeformed V-band joint cross section, b) schematic superimposition of initial undeformed section and deformed section at time n

It is very important to note that even for the deformed stage, the distance between the two radius-centres $C_n r_b$ and $C_n r_c$ remains as $r_b + r_c$, and the latter centre only moves in axial but not radial direction. The end point of the cantilever changes from EC_i to EC_n, and only moves in radial but not axial direction. Moreover, as stated previously the distance L_b between $C_n r_b$ and EC_n remains constant. In order to calculate θ_{rn} at time n the distance between $C_n r_b$ and $C_n r_c$ is required. It is calculated as a sum of the radial distance $r_c \, sin\phi$

between $C_i r_c$ and CP_{if}, the initial lever H_0, the radial deflections δ_{rn} and δ_{sn} which both define the distance between EC_i and EC_n, and subtracting $L_b \sin(\gamma - \theta_{an})$. The angle between this and $r_b + r_c$ is θ_{rn} which can be calculated as:

$$\theta_{rn} = asin\left[\frac{r_c\, sin\phi + H_0 + \delta_{rn} + \delta_{sn} - L_b \sin(\gamma - \theta_{an})}{r_b + r_c}\right] \tag{5.46}$$

The deformed cross section where contact is established around the radius r_b is shown in Figure 5-18a, from which it can be seen that the absolute angle θ_{rn} also defines the relation between axial and radial force.

Moreover, it also shows how both levers H and K increase, where H_n can be expressed by equation 5.47, which is the same as 5.40, but exchanging $\theta_{an} + \phi$ with $\theta_{r\,n}$.

$$H_n = H_0 + \delta_{s\,n} + \delta_{r\,n} - r_c[\sin(\theta_{r\,n}) - \sin(\phi)] \tag{5.47}$$

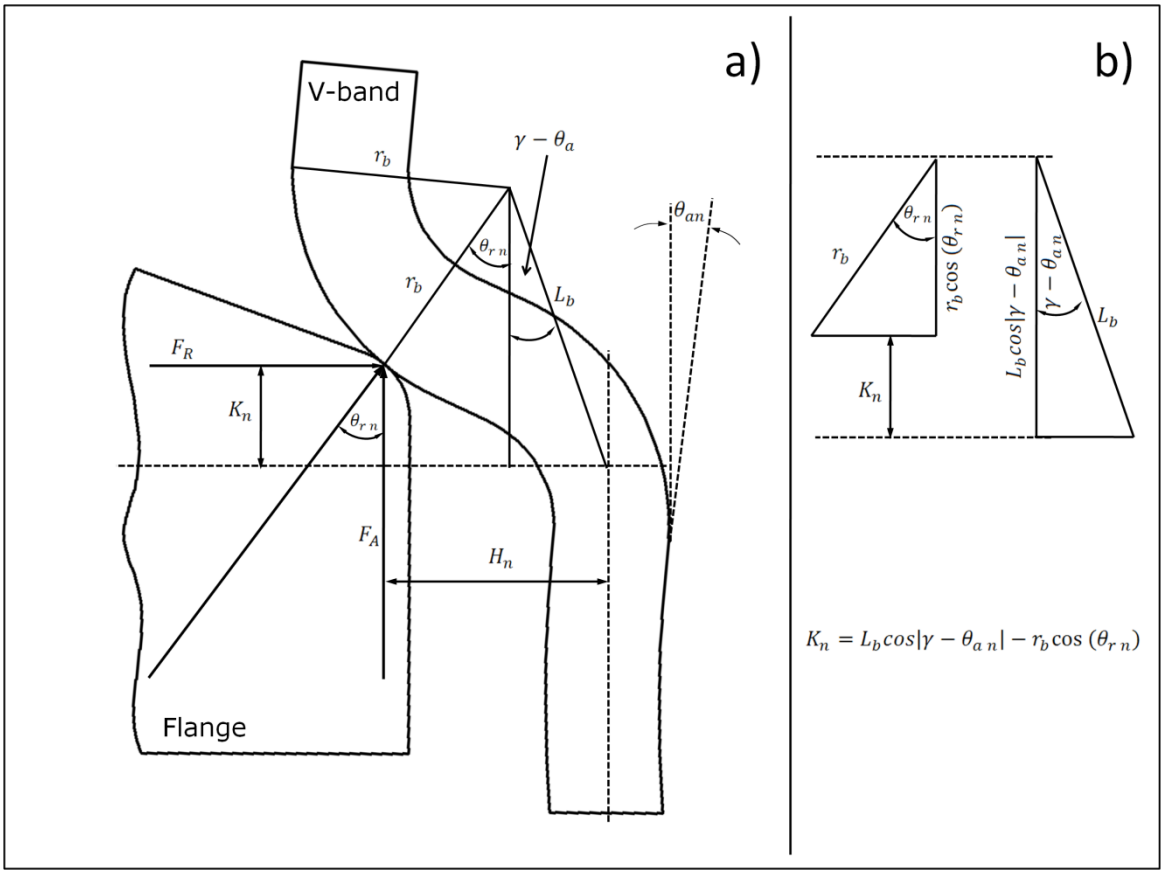

Figure 5-18: a) Deformed cross section as contact is established around radius r_b, and b) derivation of equation 5.50b for lever K

Lever K_n can be given as:

$$K_n = L_b cos|\gamma - \theta_{a\,n}| - r_b \cos(\theta_{r\,n}) \tag{5.48}$$

And its derivation is presented in Figure 5-18b.

Apart from changing the angle $\theta_{an} + \phi$ to $\theta_{r\,n}$ and calculating this angle, the methodology is similar as previously discussed for the flat part of the leg in sub-section 5.4.2. The methodology is shown in Figure 5-19.

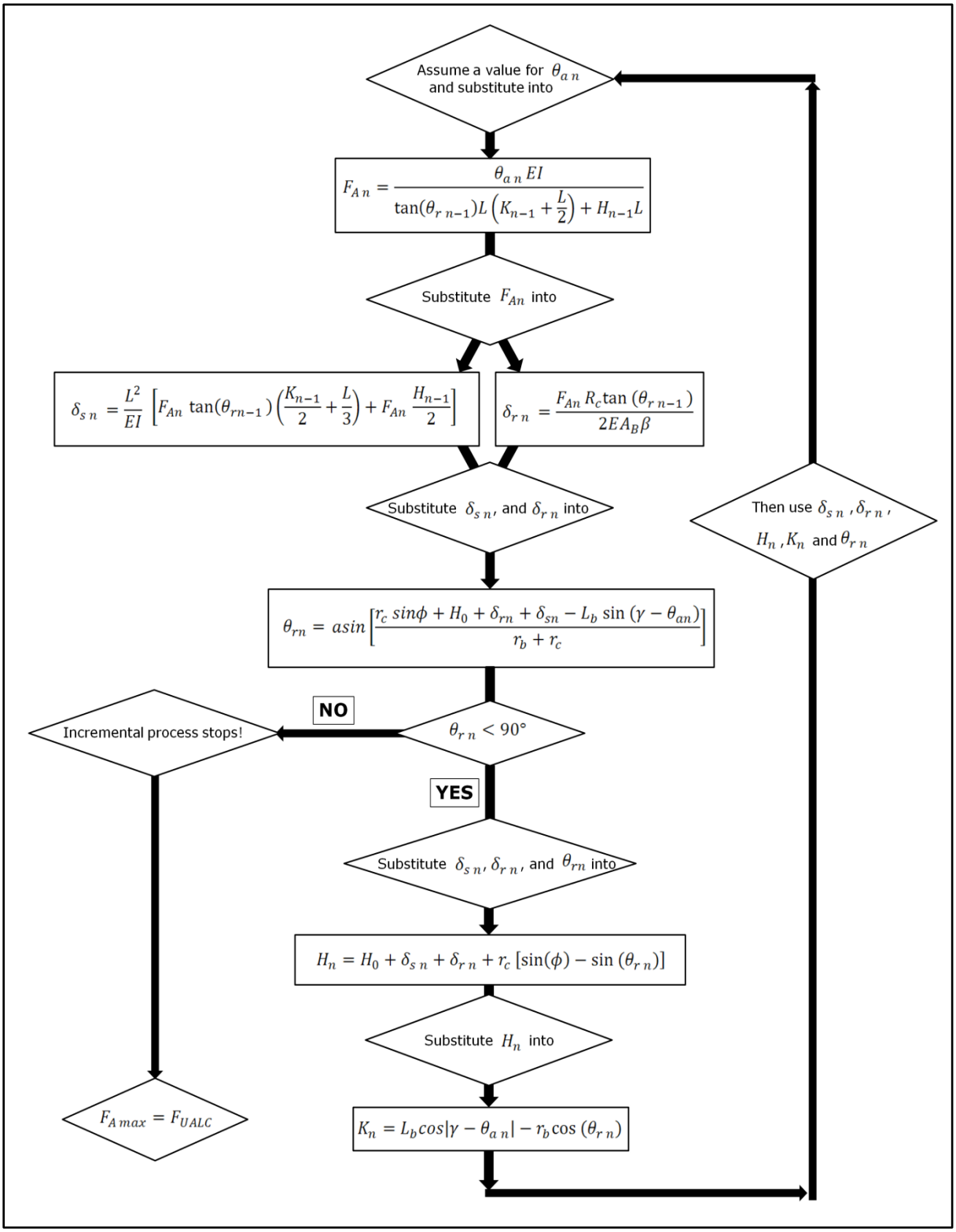

Figure 5-19: Method used to calculate axial load variation along radius r_b of V-band leg

In step 1 again assume a bending angle $\theta_{a\,n}$ to get the axial load $F_{A\,n}$ at a point in time n, using equation 5.32 for which θ_a is replaced with θ_r. For the first increment of this radius part of the methodology, θ_r is equal to $\phi + \theta_{a\,n}$ of the final increment of the previous sliding length methodology.

In step 2 the axial load $F_{A\,n}$ is used to gather $\delta_{s\,n}$ and $\delta_{r\,n}$, equally by employing equations 5.37 and 5.39, and replacing θ_a with θ_r.

In step 3 $\delta_{s\,n}$ and $\delta_{r\,n}$ are then used to gather the current angle θ_{rn} around the radius r_b at time n, which in step 4 is then substituted into equations 5.47 and 5.48, to find the current levers H_n and K_n.

In step 5 the previous steps 1 to 4 need to be repeated until the flange has deformed the V-band cross section to be able to freely separate the joint.

The ultimate axial load capacity F_{UALC} is defined as the maximum value that is found throughout this incremental process.

5.5 Results of Combined Theory

This section discusses the results obtained from the combined section and ring theory, and compares them to the numerical results obtained from the axisymmetric finite element model from chapter 4. The material and geometrical properties used in the theoretical model are listed in Table 5-3.

Table 5-3: Properties used in combined theory

K_0	0.7596 mm (F_{ACL} =6 kN) 0.7264 mm (F_{ACL} =25 kN)	H_b	3.3 mm
H_0	2.087 mm (F_{ACL} =6 kN) 1.996 mm (F_{ACL} =25 kN)	t_b	1.3 mm
r_b	2.78 mm	L_b	3.59 mm
r_c	0.8 mm	L	3.763 mm
ϕ	20°	E	227000 N/mm^2
l_s	0.06 mm	A_B	13 mm^2

5.5.1 Effect of Increment Size $\Delta\theta_a$ on F_A

Axial load values and radial deformations in the combined theoretical model are gathered by assuming a certain increment $\Delta\boldsymbol{\theta_a}$ size for the bending angle $\boldsymbol{\theta_a}$. Figure 5-20 illustrates the impact of increment size on the ultimate axial load capacity F_{UALC}, V-band joints with D_b=114mm, 235mm, and 800mm. First of all, it can be noticed that for all three band sizes larger increments increase the predicted values of the ultimate axial load capacity F_{UALC}, leading to less accurate results. Secondly, it can be said that changes in increment size have a larger impact on bands with larger diameters D_b.

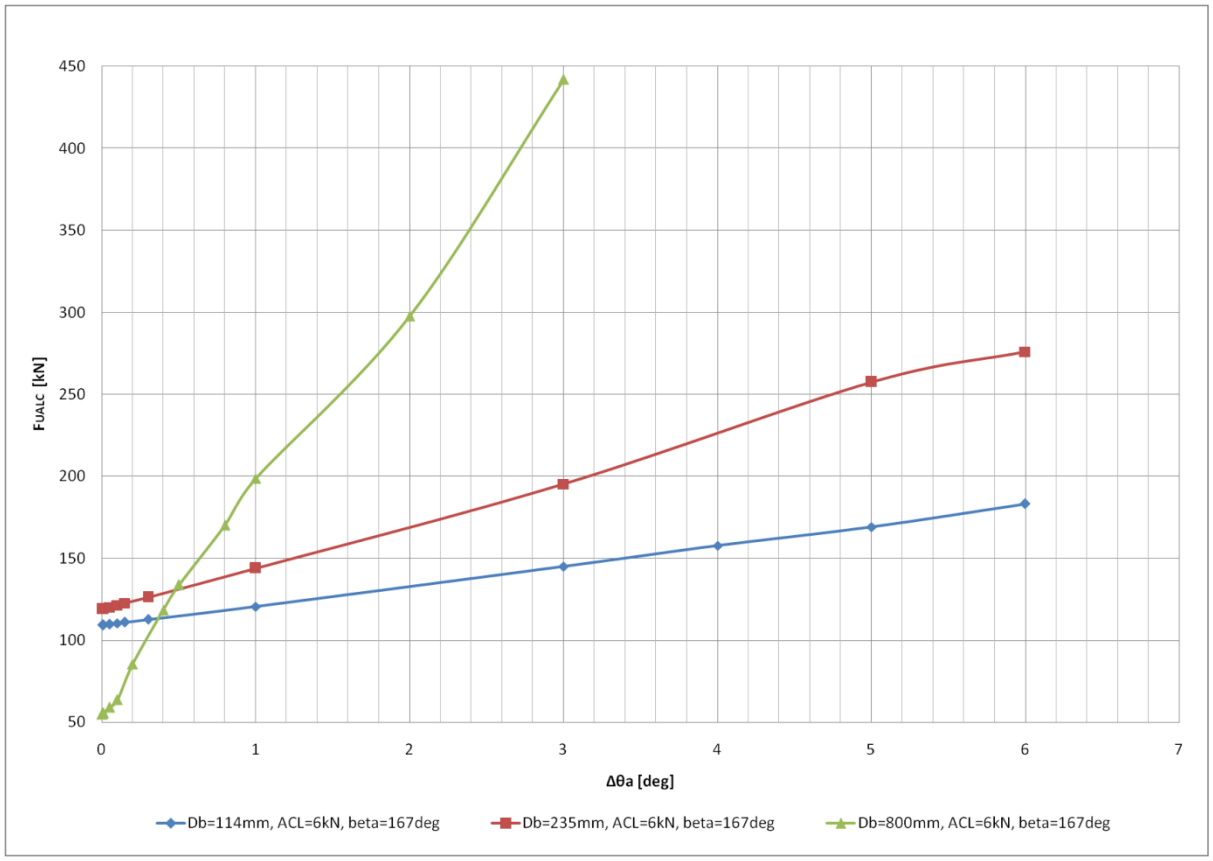

Figure 5-20: Effect of increment size of $\Delta\theta_a$ on the ultimate axial load capacity F_{UALC}

From these two findings it can be concluded that the increment size $\Delta\theta_a$ must be reduced as the band diameter D_b increases. This is very important to consider as bending of the back is greater in small V-bands resulting in larger angles θ_a, and smaller in larger V-bands as demonstrated in Figure 5-21, where the graph converges to approximately zero for with increasing band diameter D_b.

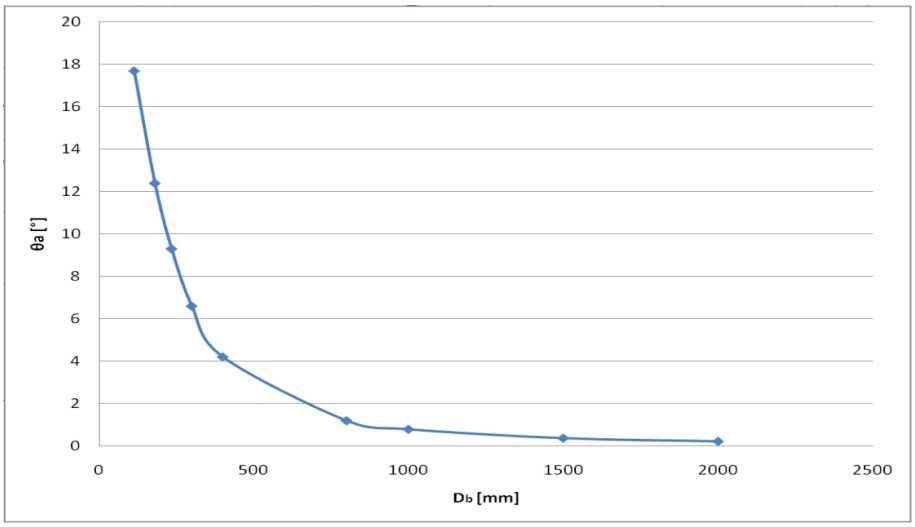

Figure 5-21: Relationship of bending angle θ_a and V-band diameter D_b

5.5.2 Effect of δ_r and D_b on Axial Load

These results can be confirmed by Figure 5-22, where the amount of radial deformation due to ring expansion is larger in large bands (e.g. D_b=800mm), and greatly reduces for small band sizes (D_b=235mm and 114mm). This suggests, too, that the impact of ring deformation increases with the band diameter D_b.

Moreover, it shows an increase in F_{UALC} from 114mm to 235mm, and then a drop from 235mm to 800mm, suggesting that the interaction and correlation of section and ring deformation is not straightforward. This phenomenon is discussed in further detail in sub-section 5.5.4 when theoretical and finite element results are compared.

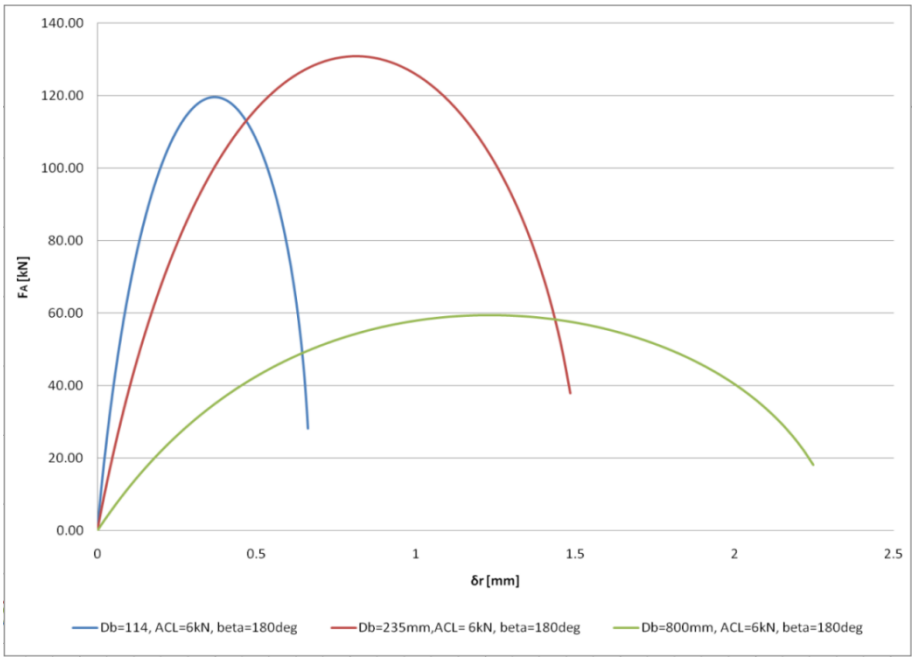

Figure 5-22: Axial load variation in relation to radial deformation due to ring expansion

Figure 5-23 shows the component of the maximum radial deformation due to ring expansion $\delta_{r\,max}$ over the V-band diameter ranging from 114mm to 2000mm. It can be seen that $\delta_{r\,max}$ increases significantly between 114mm and 400mm, and then starts to converge to a constant value of approximately 2.5mm, which is the same as the difference between the inside of the V-band $D_b - 2H_b$ and the flange diameter D_f.

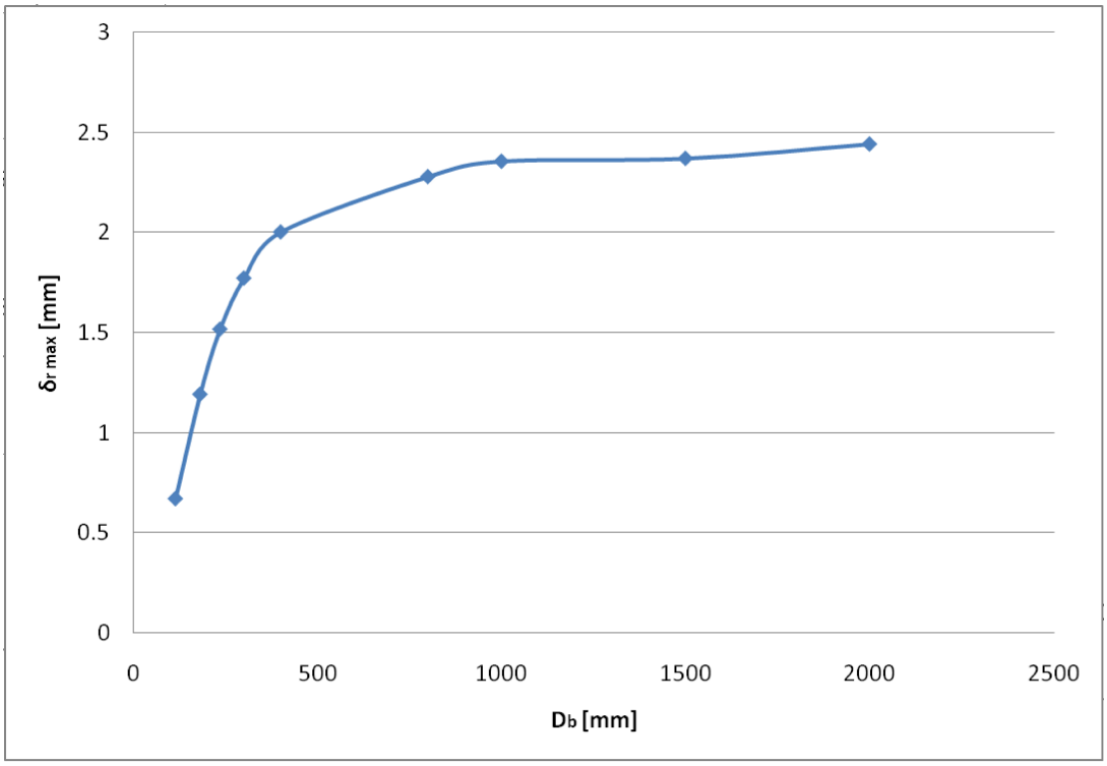

Figure 5-23: Effect of the band diameter D_b on radial deformation due to maximum ring expansion $\delta_{r\,max}$.

This leads to the outcome that for large V-band joints irrecoverable separation of the flanges is reached when the band diameter increases by $2\delta_{r\,max}$, as defined by:

$$2\delta_{r\,max} = D_f - (D_b - 2H_b) \tag{5.49}$$

As shown in Figure 5-22, the axial load at $\delta_{r\,max}$ is significantly smaller than the ultimate axial load capacity. The graph in Figure 5-23 is not very smooth which is mainly due to the different increment sizes $\Delta\theta_a$ used for different diameters.

As stated in sub-section 5.4.3 the incremental process ends when θ_r becomes equal to 90°, and this is where $\delta_{r\,max}$ would appear. However, Figure 5-24 shows that the process stops at a level below 90°, which is due to the nature of the incremental process itself. It was found that reducing the increment size $\Delta\theta_a$, θ_{rmax} was closer to 90°.

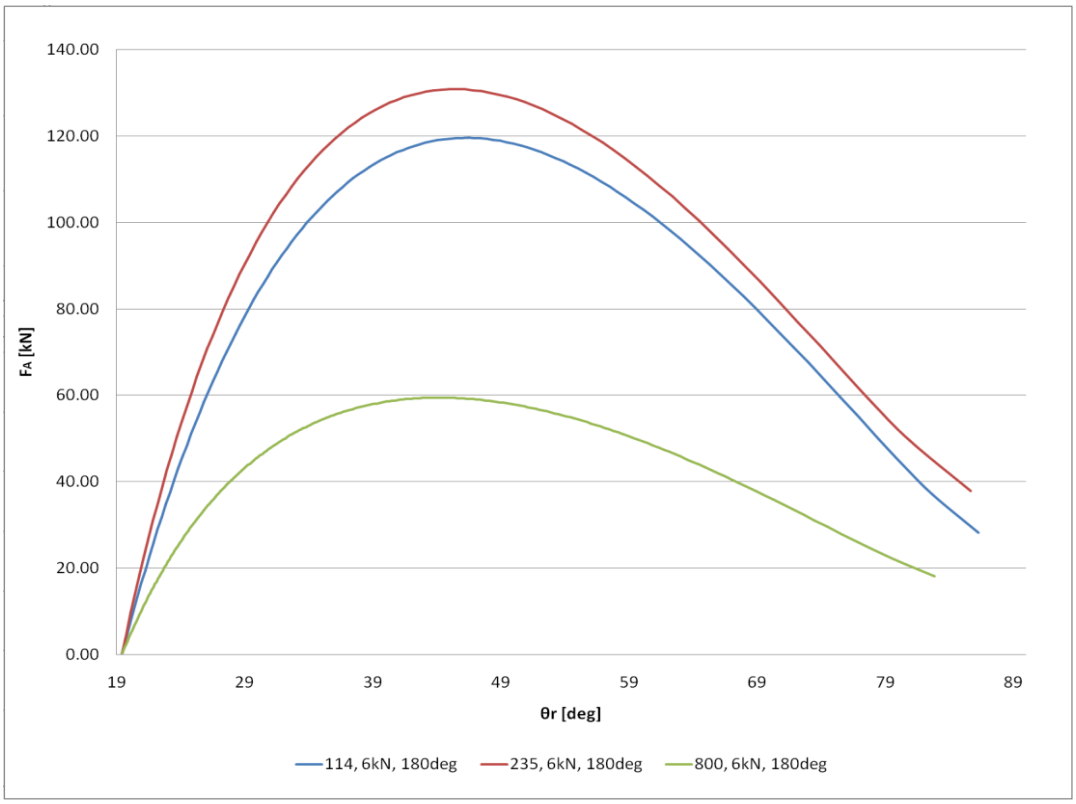

Figure 5-24: Axial load variation in relation to θ_r due to ring expansion

5.5.3 Comparison of Combined and Ring Theory

In Figure 5-25 the combined and ring theories are compared, for an axial clamping load F_{ACL}=6kN, and β=180°. Both graphs agree very well for ultimate axial load results between diameters 80mm and 2000mm, where mainly ring deformation δ_r takes place. Below 800mm however the effect of the section deformation δ_s becomes more influential and the graphs deviate largely as the ring theory only accounts for the ring deformation. It can therefore be said, that for band diameters above 800mm, the much more straightforward ring theory gives accurate results for the ultimate axial load capacity.

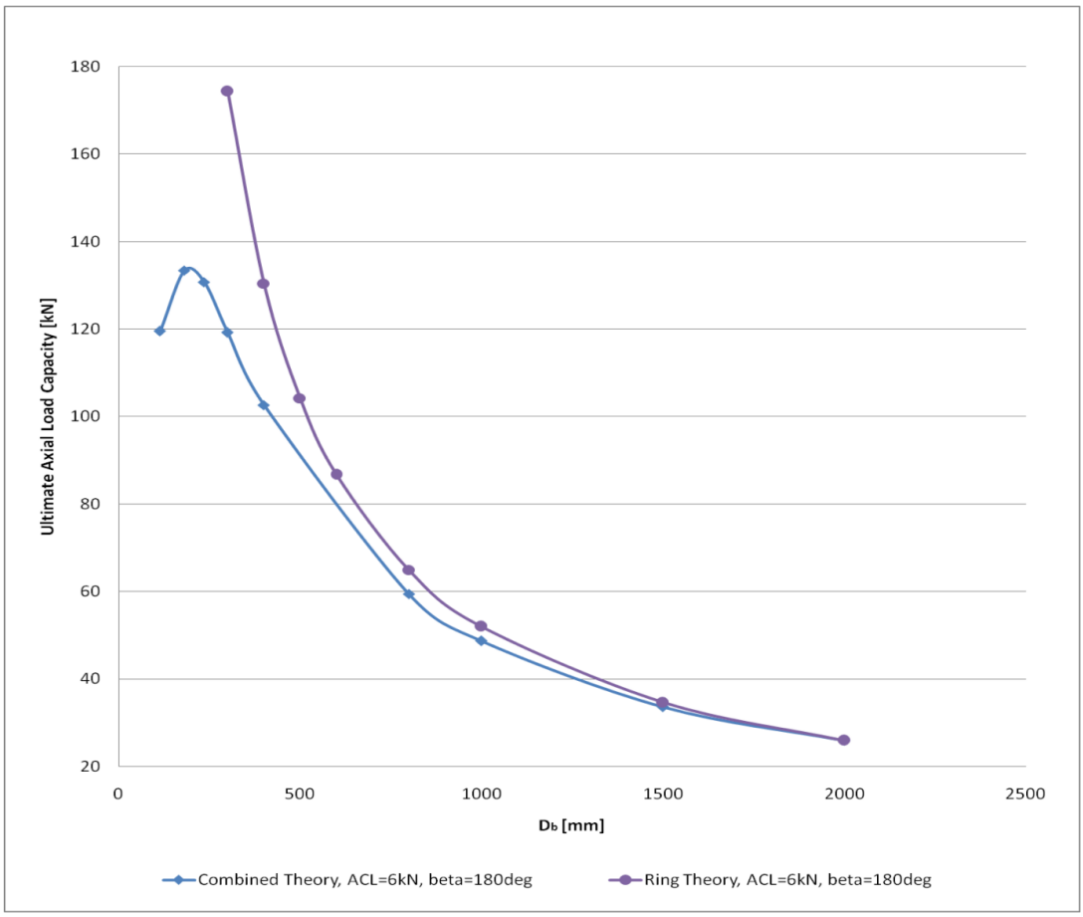

Figure 5-25: Comparison of combined and ring theory for axial clamping load F_{ACL}=6kN and β=180°

5.5.4 Comparison of Finite Element and Combined Theoretical Model

The results for the combined theory presented in this sub-section are for β=180° to enable direct comparison with the axisymmetric finite element models.

Figure 5-26 compares the results of the ultimate axial load capacity, F_{UALC}, gathered from the theoretical model to the finite element model from chapter 4, for F_{ACL}=6kN, and no friction present. The graphs indicate very good correlation between V-band sizes D_b= 800mm and 2000mm due to the predominance of elastic ring expansion, which was confirmed in sub-section 5.3.2. For band diameters below 400mm on the other hand, the difference between the graphs increases. This is due to a number of the assumptions made during the development of the theory.

As discussed in chapter 4 for the axisymmetric finite element model, plastic deformation starts to occur at very small bending angles θ_a and increases rapidly. Material deforming plastically offers significantly less resistance to deformation than elastic material. Hence

the finite element results can be expected to be lower than the theoretical results, particularly for small band diameters where there is significant section deformation.

In addition, the small V-bands undergo relatively large bending deformations resulting in geometric non-linearity. The theoretical model does not account for this and hence over-predicts the ultimate axial load capacity.

The third most significant assumption is that the leg and foot (used to calculate the leverage) remain with the same angle of ϕ in relation to the free end of the back, whereas the finite element model has shown that the angle increases. These three simplifications in the development of the theoretical model are interlinked and eliminating them is not straightforward.

However, even though the absolute values of the results predicted by the theoretical model seem to differ from the finite element analysis, the theory is capable of giving a similar distribution with a peak load at approximately D_b=181mm.

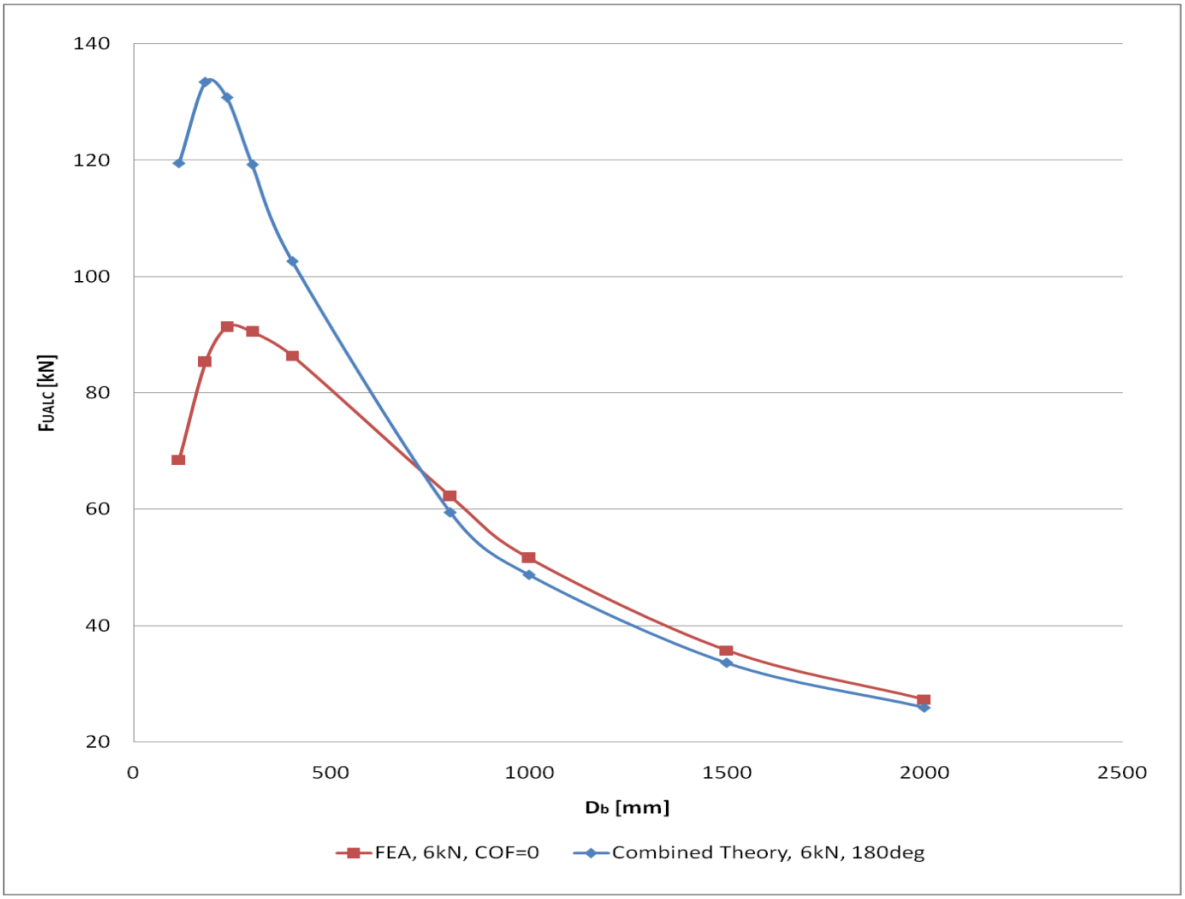

Figure 5-26: Comparison of combined theory and finite element model, for axial clamping load of 6kN, and no friction

The graphs in Figure 5-27 compare the theoretical to the finite element model for an axial clamping load F_{ACL} of 25kN. In the combined theory the clamping load is simulated

by reducing the initial levers H_0 and K_0, as well as increasing l_s. It can be seen that similar to the ring theory, the results of the combined theory are starting to differ more for larger axial clamping loads. However, the combined theory still shows a similar distribution, and predicts an increase of the ultimate axial load capacity as the axial load is increased.

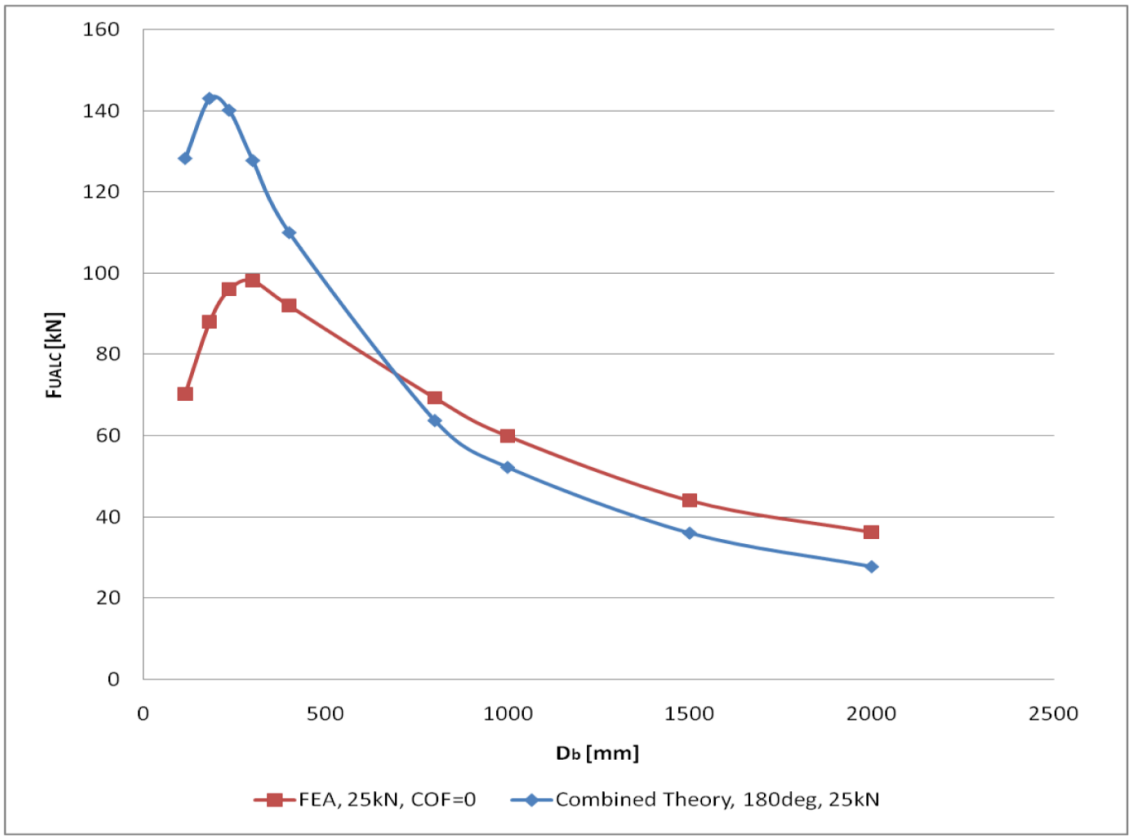

Figure 5-27: Comparison of combined theory and finite element model, for axial clamping load of 25kN, and no friction

In Figure 5-28 the combined theory is compared to the finite element model with pure elastic material properties, for no friction, and an axial clamping load of 6kN. These results correlate well for D_b=400mm and larger, whereas below this diameter, the graphs start to differ significantly.

The good agreement between both graphs above 400mm, is mainly due to elastic ring deformation being dominant for these large band diameters. For smaller diameters the FE model will include the effect of the leg and foot of the section straining in the circumferential direction. This effect increases as the diameter decreases, hence the ultimate axial load capacity increases. As the foot and leg are not included in the combined theory their effect is not accounted for, hence, the peak at 181mm.

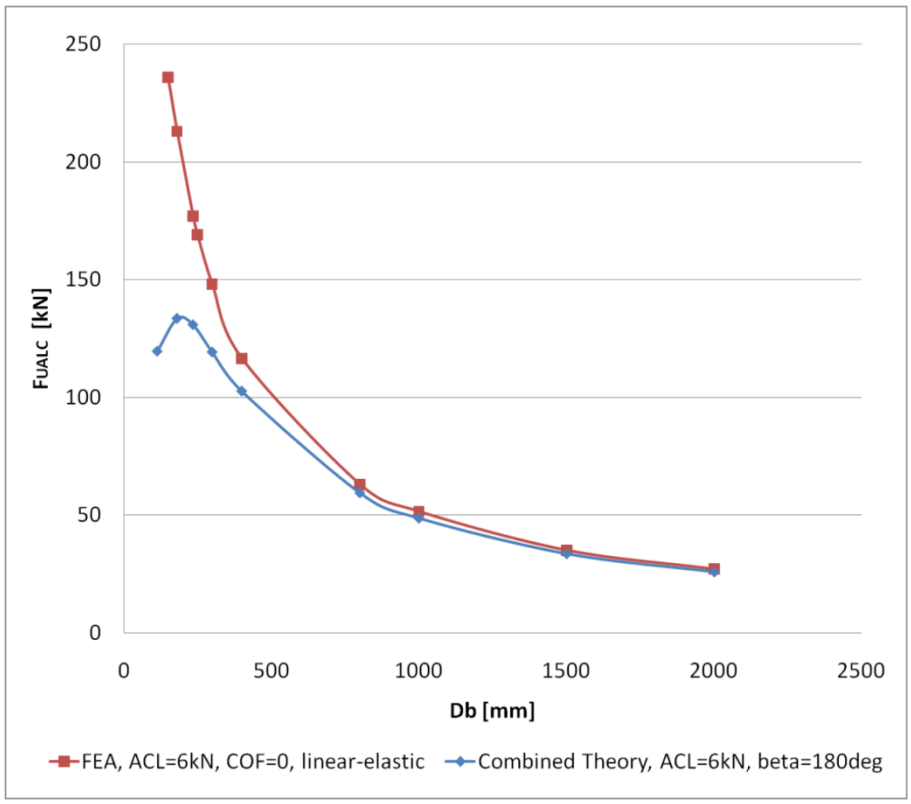

Figure 5-28: Comparison of combined theory and finite element model, for axial clamping load of 6kN, no friction, and elastic material behaviour

5.6 Conclusion of Theoretical Model Results

In this chapter it was shown that the ring theory was able to give very good correlation with the finite element work, for band diameters between 800mm and 2000mm. Below 800mm, the ring theory over-predicted the ultimate axial load capacity, as it only considered ring deformation, whereas the finite element work combined ring and section deformation.

Therefore, a combined theory was developed in the second part of this chapter, taking into account ring and section deformation. This combined theory showed very good correlation to the finite element models and the ring theory for band diameters between 800mm and 2000mm, as well. Below this diameter range, it also over-predicted the ultimate axial load capacity, but to a much smaller amount than the ring theory. Moreover, it was able to successfully predict a peak ultimate axial load at approximately 181mm, which agreed with the finite element model that predicted a peak at 250mm. It can therefore be concluded that even though many assumptions were made in the combined model, it proved to be a useful means of quickly predicting the ultimate axial load capacity.

6 Experimental Validation

In this chapter experimental tests are presented which were used to validate firstly the finite element work investigating the cold roll forming process in chapter 3, and secondly the finite element work in chapter 4 and theoretical work in chapter 5 both predicting the ultimate axial load capacity of V-band retainers.

Sections 6.1 to 6.2 are entirely taken from the author's own publication Muller et al. (2011).

6.1 Material Investigation Test Set Up

A tensile test for austenitic stainless steel AISI 304 was carried out to establish data to validate the finite element simulations described in chapter 3. Using a tensile test machine a standard test sample of the initial flat band was extended in increments of plastic strain. The sample was taken off the machine to measure the work hardness (HMV) at each increment. All hardness measurements used the Vickers hardness scale and were taken using a Microhardness Tester Buehler 1600-6100. For the tensile test specimens, care was taken to ensure that the sample had not started to neck before measurements were taken.

The second set of hardness measurements can be sub-divided into two categories. The first showed the increase in work hardness throughout the cold roll forming process starting from the initial flat band to a sample of the sixth roll pass. The second was used to establish a new method to validate the finite element results for the sixth pass. For both categories the hardness was measured at several points through the cross-section of the band perpendicular to the rolling direction. The samples were obtained by taking a strip out of the roll forming machine including all six passes. The position of each pass was marked on the strip and after that small samples were cut off the string close to each marked position. Figure 6-1 shows at which positions the samples were taken. Figure 6-2 gives an overview of the measuring points in the cross-section for the final section forming stage, pass 6.

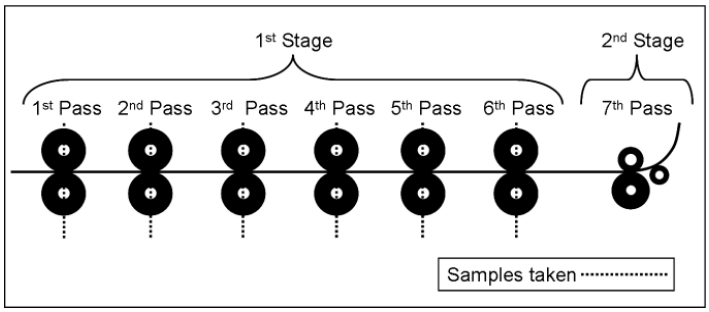

Figure 6-1: 2 dimensional schematic of rolling process including 1st stage of forming the V-section and 2nd stage of forming circular shape

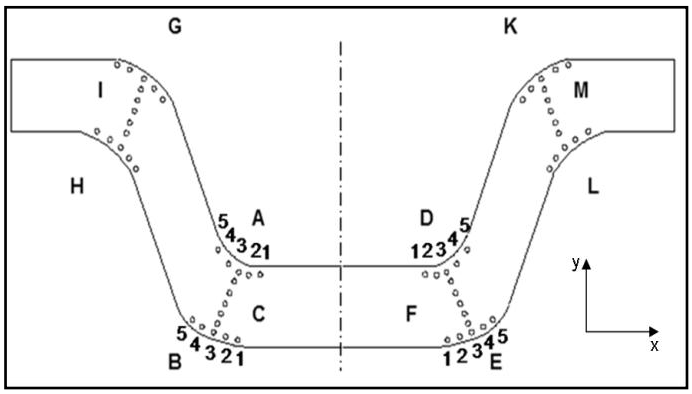

Figure 6-2: Work Hardness measuring points to show increase throughout roll forming process (6th pass)

The regions measured in the cross-section, A to M were chosen because the finite element results showed large changes in plastic deformation, so these are likely to have the largest change in hardness through the forming process. The points of regions A, B, D, E, G, H, K and L were measured with a distance to the outside surface between 0.08 and 0.15mm. Using an optical microscope with a micro adjustable x-y stage on the hardness machine, the position of the right and left hand side of each sample was set. It was then possible to define the plane of symmetry and from there the x-distance to each point was defined. A similar process using the upper and lower edges of the samples was used to define the y-coordinate for each point. Considering that each machining process has certain tolerances it was not possible to measure the hardness of a specific point at exactly the same position for each pass. This thesis focuses especially on regions A, B, C, D, E, and F, as they are expected to have the largest impact on the actual strength of the joint and crack development in the V-band cross section. Five measuring points in each region were assumed to be sufficient to show the work hardness progression, whereas between 6 and 16 points were required to establish an accurate validation for the finite element work, as shown in Figure 6-3.

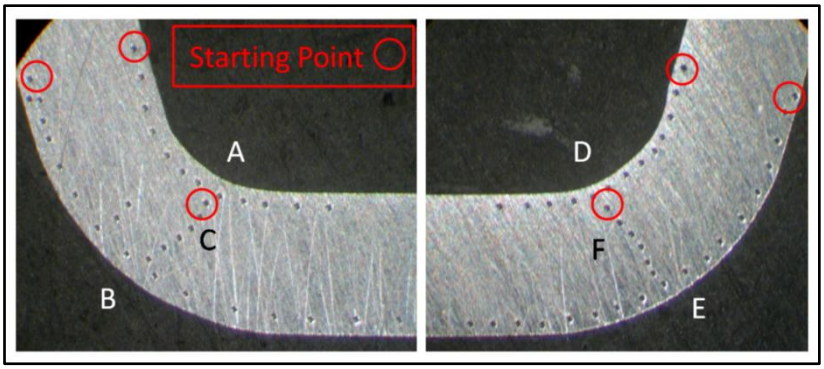

Figure 6-3: Work Hardness measuring points for validating finite element analyses (6th pass)

6.2 Material Investigation Test Results

6.2.1 Tensile and Hardness Test to establish Validation Method

Using equations (2.26), (2.33), and (3.1) and undertaking the same procedure as for the finite element model (see section 3.2), all engineering values gathered from the tensile test sample were transformed into true values and the plastic behaviour could be calculated. This allowed the relationship between plastic strain and work hardness to be established, as shown in Figure 6-4. In this figure the change in material behaviour shown on the vertical axis is directly related to the development of the material yield stress during plastic deformation.

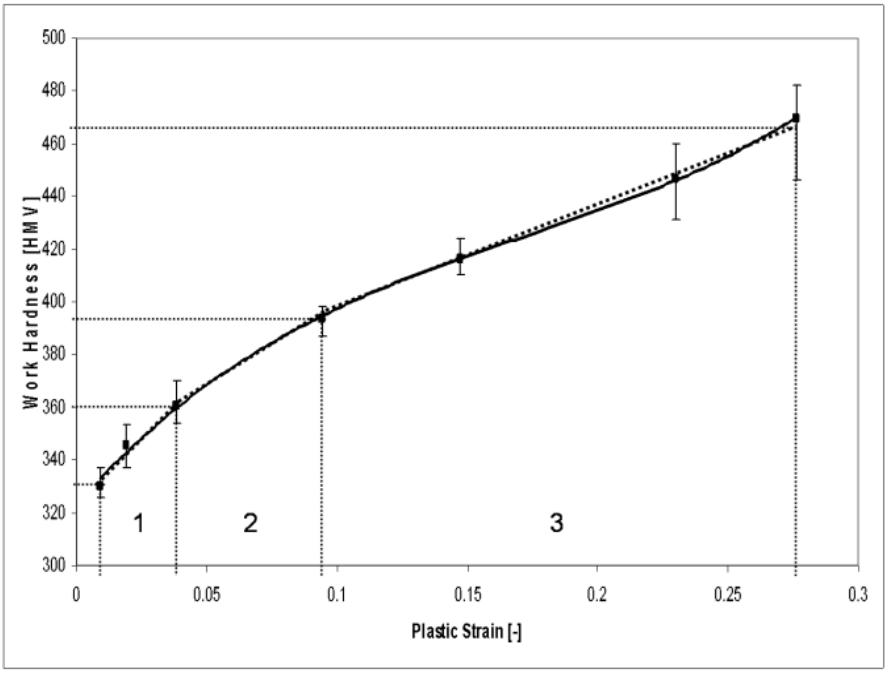

Figure 6-4: Correlation between work hardness and plastic strain for AISI 304

The hardness values in Figure 1-4 were determined for plastic strain values between 0.009 and 0.0277 and then partially linearised (dashed lines) in three regions, generating equations (6.1) to (6.3):

Region 1 $0.009 \leq \varepsilon_{pl} < 0.039$

$$H_1 = \varepsilon_{pl} x 1000 + 320 \quad (6.1)$$

Region 2 $0.039 \leq \varepsilon_{pl} < 0.095$

$$H_2 = \varepsilon_{pl} x 643 + 336 \quad (6.2)$$

Region 3 $0.095 \leq \varepsilon_{pl} < 0.277$

$$H_3 = \varepsilon_{pl} x 362 + 360 \quad (6.3)$$

6.2.2 Determination of Work Hardness throughout Cold Roll Forming Process

Figure 6-5 to Figure 6-7 display the experimental results for the development of work hardness in three regions through the six pass roll forming process. The ordinate shows the Vickers Hardness and the abscissa the number of the sample point. Figure 6-5 indicates that for region A the greatest work hardening is in the centre of the fillet. This is the area predicted by the FE analysis as having the largest plastic deformation. The further away the sample points are from the centre, the smaller is the work hardness. Only the graph for the initial flat band has a relatively constant value of hardness taking account of measurement uncertainty.

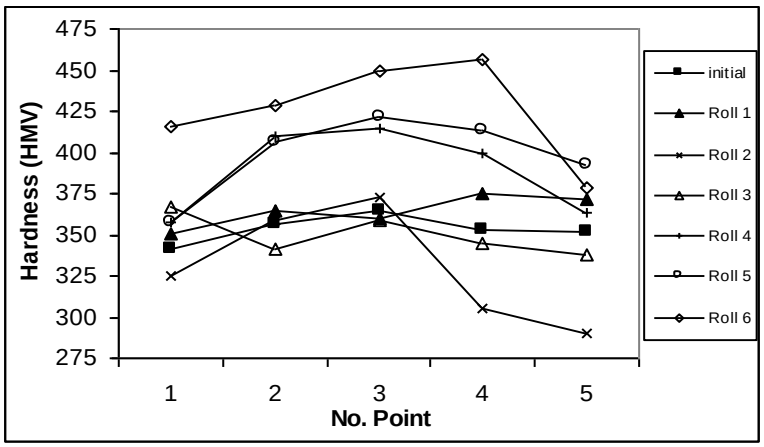

Figure 6-5: Hardness measured at region A (all passes)

The behaviour observed for region A can also be seen for area B in Figure 6-6. The largest magnitude of hardness occurred at the centre of the fillet indicated as number 3. Again, this is where the FE analysis predicts the largest plastic strain.

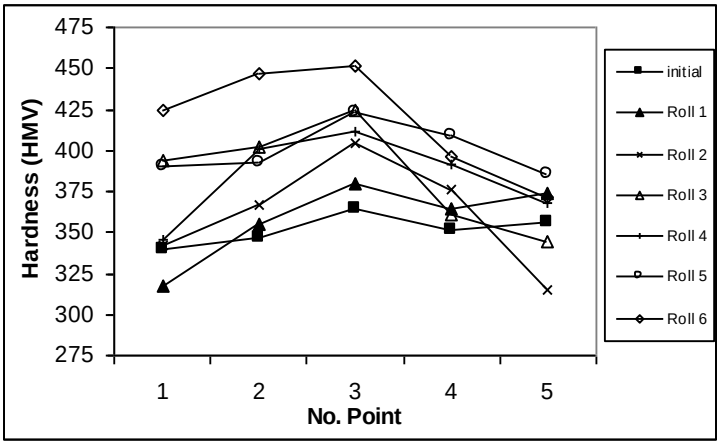

Figure 6-6: Hardness measured at region B (all passes)

The graphs in Figure 6-7 show the development of work hardening through the thickness of the band in region C. The graph for the initial flat band indicates that the band has already had a range of hardness through the thickness, with the magnitude decreasing towards the neutral plane. This range was due to the preceding flat rolling process. As the graphs for the six pairs of rollers display, this trend develops further as the band undergoes more deformation.

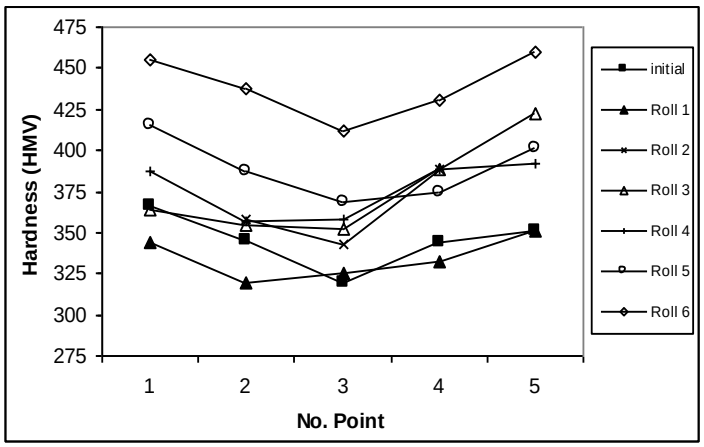

Figure 6-7: Hardness measured at region C (all passes)

The trends shown by the experimental results obtained in this investigation agreed with the numerical results obtained from FE analysis in sub-section 3.4.1. In order to get a quantitative comparison a further experimental investigation was undertaken to relate work hardness and plastic strain directly.

6.2.3 Experimental Validation of Numerically Predicted Plastic Strain Values and Tested Hardness Values

Using the relationship established in sub-section 6.2.1, it was then possible to convert the plastic strain values found by the FE analysis into hardness values. The transformed numerical hardness results taken from pass six were then compared to the measured hardness values at regions A, B, C, D, E, and F.

The Hardness values for areas A and D (see Figure 3-7 and Figure 6-3) determined in the experimental tests compared to their 2D finite element counterparts (with a 48x360 element mesh) from chapter 3 are shown in Figure 6-8. The values for the hardness are shown over the length as the distance between the points was measured, starting at zero with the point at the top of the areas A and D. The same was done for the finite element results, but there the distance between the nodes was taken as the length value. The overall trend of the measured hardness fits well with the predicted results with differences of less than 10%. However, it can be noticed that there is some deviation between the predicted and measured results. This may be due to the difficulty of precisely and repeatably locating position of each experimental measurement point.

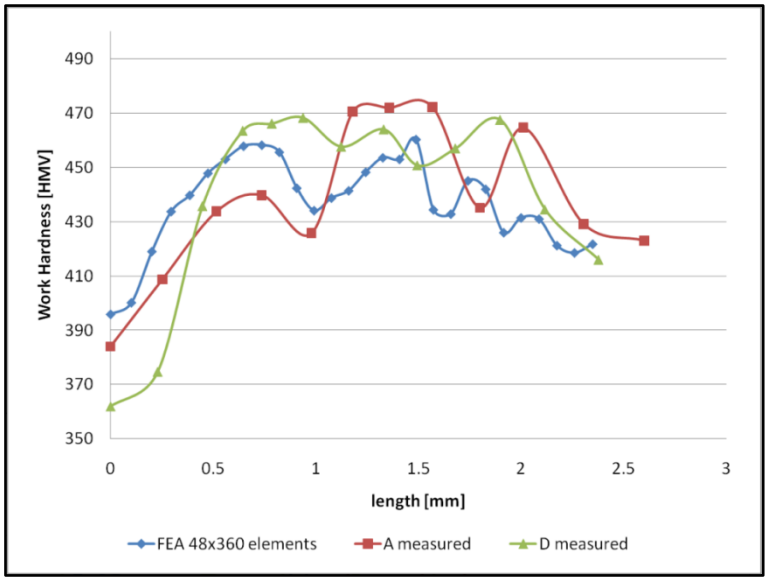

Figure 6-8: Comparison of Hardness determined for regions A, D and Hardness obtained by predicting plastic strain (6th pass)

The same good correlation of overall trend of measured areas B and E compared to the finite element results can be seen in Figure 6-9, with the peaks in the centre of the fillet.

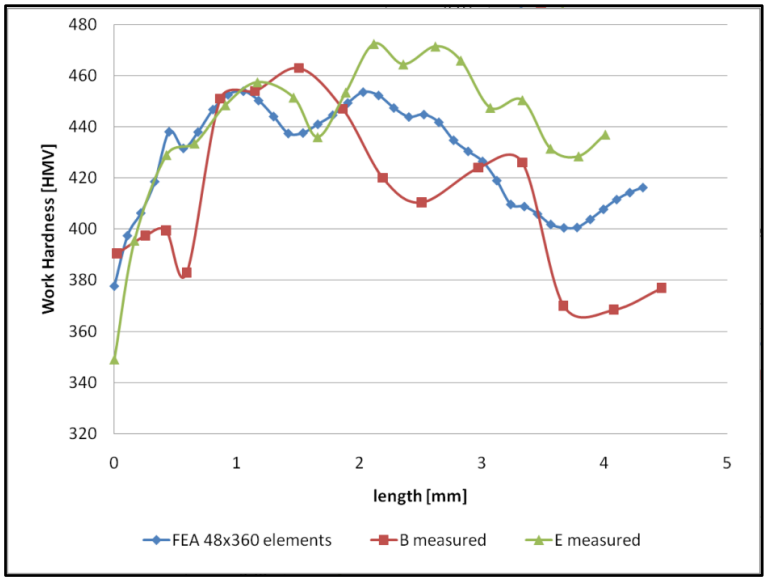

Figure 6-9: Comparison of Hardness determined for regions B, E and Hardness obtained by predicting plastic strain (6th pass)

Very good correlation in the overall trend as well as the absolute values between predicted and measured hardness for regions C and F can be observed from Figure 6-10. All three graphs show the expected distribution through the thickness of the cross section as a parabola, with the hardness values decreasing towards the neutral line.

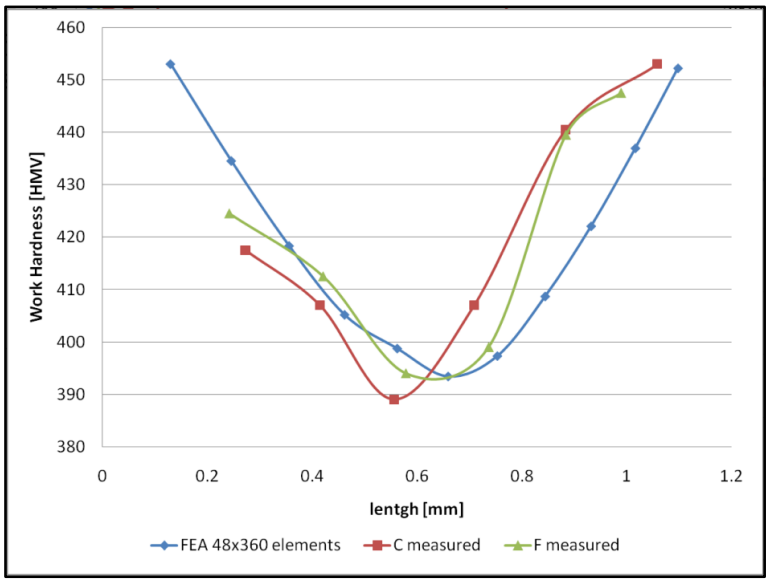

Figure 6-10: Comparison of Hardness determined for regions C, F and Hardness obtained by predicting plastic strain (6th pass)

Although the experiments carried out in the presented work have shown partial deviations between predicted and measured hardness, it is clear that validating predicted plastic strain in finite element analysis by measuring the work hardness is a useful technique.

6.3 Ultimate Axial Load Capacity Tensile Test Set Up

Tests were carried out on an Instron tensile test machine to determine the ultimate axial load capacity of V-band retainers, with initial geometrical values as given by Shoghi (2003). The V-band retainers were mounted on a pair of circular test flanges, as indicated in Figure 6-11.

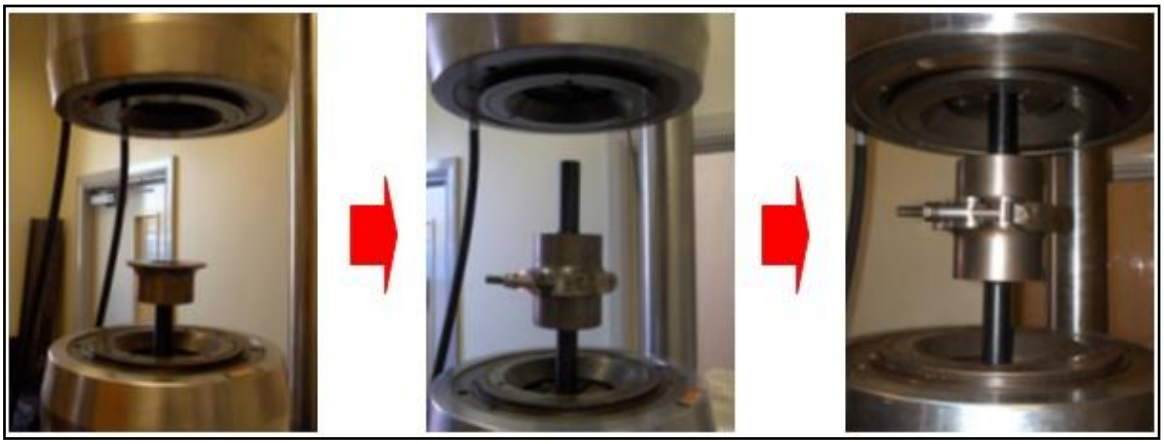

Figure 6-11: Process of setting up ultimate axial load test, and assembling V-band retainer

An axial load was then applied until irreversible separation of the flanges occurred, leading to total failure of the joint, very much like the finite element work presented in chapter 4.

The tests were undertaken for V-band diameters D_b of 114mm, 181mm, and 235mm and for a range of T-bolt torques T_t ranging from 4Nm to 20Nm, in increments of 2Nm.

6.4 Experimental Ultimate Axial Load Capacity Results

6.4.1 Determination of Ultimate Axial Load Capacity F_{UALC} depending on V-Band Diameter D_b and Axial Clamping Load F_{ACL}

The results of the ultimate axial load capacity tests can be seen in Figure 6-12 for all three band diameters and the whole range of T-bolt torques T_t. Considering that the graphs show a very large amount of scatter (which is discussed in more detail for Figure 6-13) it can still be observed that for small torques between 4 and 8Nm the largest bands (235mm) have the lowest F_{UALC} values, the medium sized bands (181mm) have the largest values, and the small bands (114mm) have intermediate F_{UALC} values. For torques between 8Nm and 20Nm this order changes slightly, so that the small bands (114mm)

have the smallest capacities, the largest bands (235mm) have the intermediate capacity values, and the medium bands (181mm) have the largest F_{UALC} values.

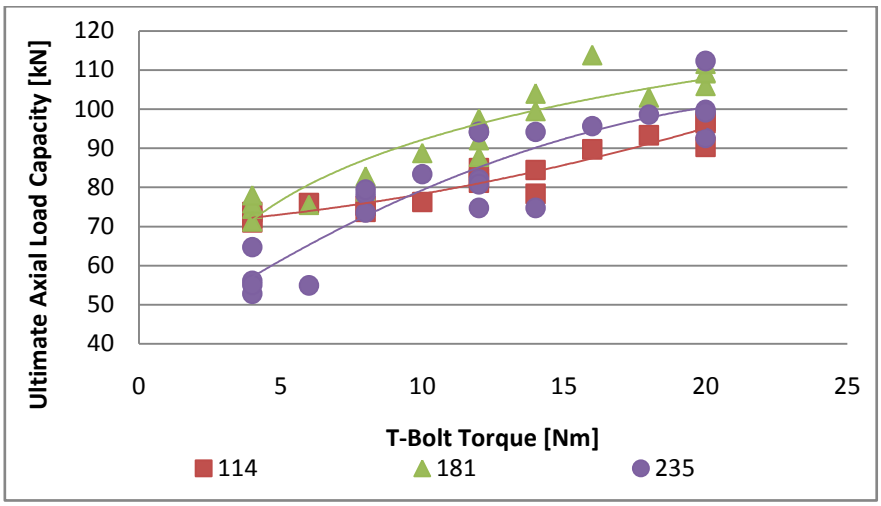

Figure 6-12: Determined ultimate axial load capacities of V-band joints over the T-bolt torque T_t

The large amount of scatter can be better evaluated using Figure 6-13. This shows the same results as Figure 6-12 but presents them as ultimate axial load capacity over the V-band diameter D_b. The points shown there are the average measured values along with lines of best fit, and error bars indicating scatter. These graphs illustrate that there is a peak value for F_{UALC} at medium sized joints and that this peak is moving and highly dependent on the T-bolt torque. For small T-bolt torques, the peak occurs at flange diameters of approximately 155mm, and for larger clamping load shifts to 180mm and slightly above. A similar trend was observed in the finite element work presented in chapter 4. Moreover, as the error bars show the amount of scatter increases with the band diameter D_b.

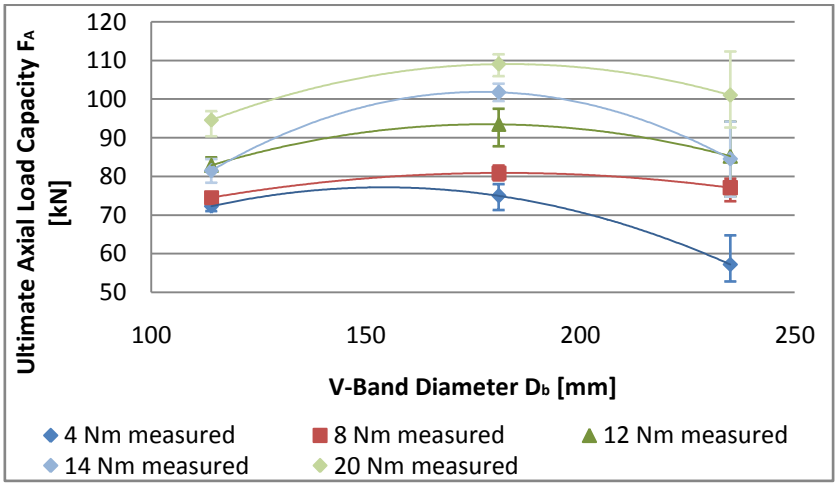

Figure 6-13: Lines of best fit for ultimate axial load capacity values of V-band joints over the band diameter D_b

As stated in chapter 1 V-band retainers consist of an open ring, which is the V-band itself, where the gap is located between the trunnion loops, which themselves hold the T-bolt. Figure 6-14 shows cross sections of the end of the bands situated in the gap, after the V-band joint had failed, the external force had been removed and the bands had been taken off the pair of flanges.

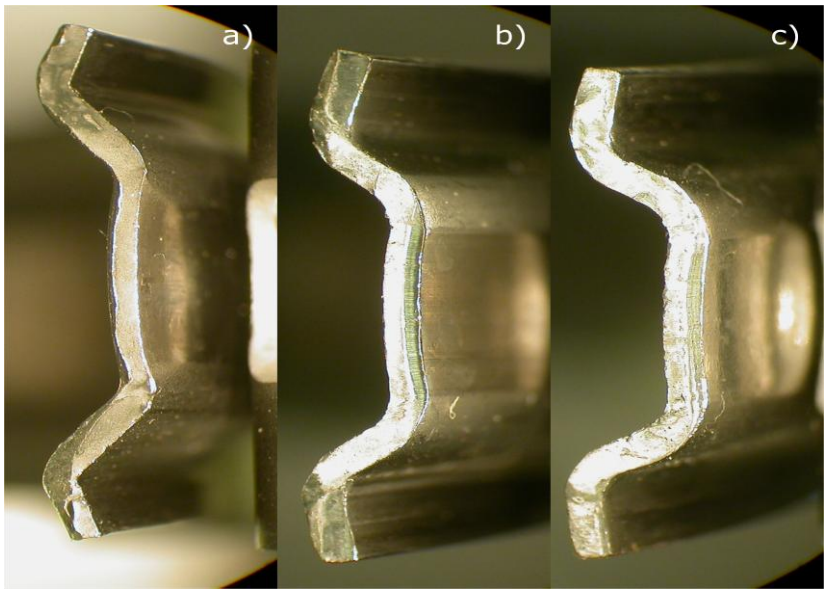

Figure 6-14: Plastic deformation of failed V-band retainers after tensile test for T_t=4Nm and for a) 114mm, b) 181mm, and c) 235mm

It can be seen that all three pictures show a permanent bending of the back of the band, resulting in opening of the section and increasing the V-band angle, ϕ. Moreover, this bending is larger for the small bands (114mm) and becomes smaller for the larger bands. This can also be seen for T-bolt torques of 12Nm, as shown in Figure 6-15.

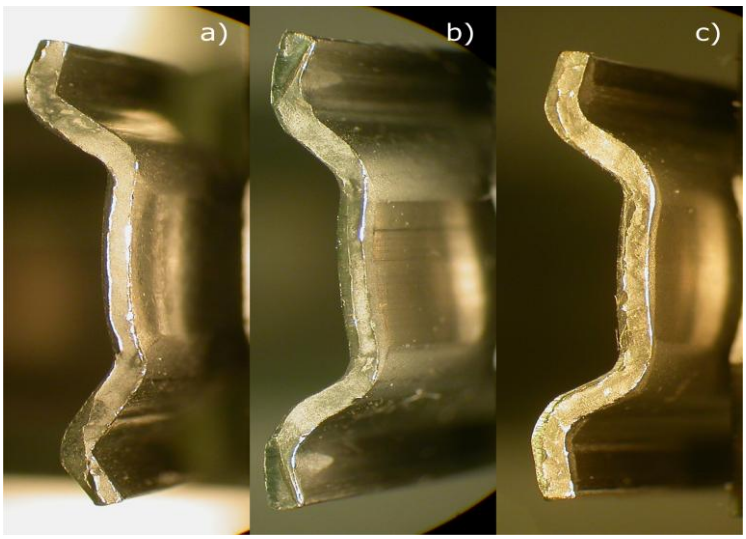

Figure 6-15: Plastic deformation of failed V-band retainers after tensile test for T_t=12Nm and for a) 114mm, b) 181mm, and c) 235mm

Furthermore, it was observed that significant plastic deformation occurred only at these ends of the band next to the gap, whereas the rest of the cross section remained in its initial shape. When analysing this phenomenon, the actual design of the V-band retainer should be considered. Figure 6-16 shows that the trunnion loops are spot-welded onto the V-band, and once assembled to a pair of flanges; this means that there is a significant distance between the weld spots of both sides. Along the gap between the weld spots, no radial force is applied, making this part of the cross section the weakest link. During failure of the joint as both flanges separate, the V-band therefore shifts towards the side of the gap between the weld spots, bending the back of the band there first and opening the section, as this is the part where the wedging effect of the V-shape is reduced due to the lack of radial force. The whole V-band joint is therefore weakened, leading to a reduced strength and load capacity.

This can be better understood when compared to the theoretical and finite element models, which assume perfect conditions, and constant radial force around the circumference of the V-band joint.

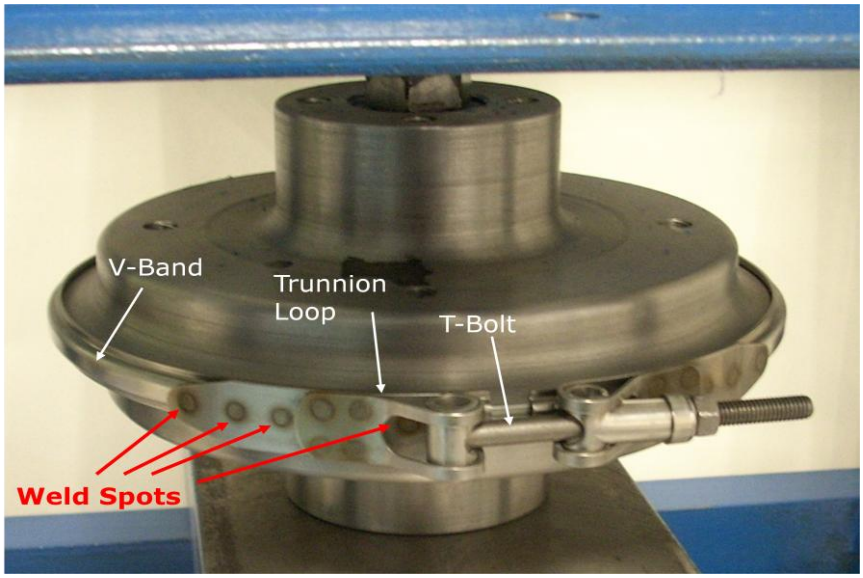

Figure 6-16: V-band retainer assembled to a pair of test flanges before applying an external load

6.4.2 Method used to Compare Axial Clamping Load F_{ACL} and T-bolt Torque T_t Applied

In order to enable the comparison of the finite element and experimental work it is necessary to create a direct link between the T-bolt torque T_t and axial clamping load F_{ACL}. This is important as the joint assembly process was controlled by reporting the axial clamping load F_{ACL} in the finite element models. In the experiments on the other hand, the torque applied to the T-bolt T_t was measured, which generated a circumferential

force F_β. F_β itself then generated an axial clamping load due to the wedging action of the cross section V-shape. This comparison was undertaken using equations 6.4, 6.5, 6.6, and 2.5 as presented in the author's own publication Muller and Barrans (2010b), which was a method adapted from previous work of Shoghi *et al.* (2004)

$$T_t = F_\beta \left[\frac{d_p}{2}\tan(\alpha_h + \mu_{th}) + \mu_h R_m\right] \quad (6.4)$$

where

F_β = clamping load in the T-bolt

T_t = torque applied to the T-bolt

R_m = mean radius of the fastener under-head bearing surface

d_p = pitch diameter of the bolt

α_h = helix angle

μ_h = underhead coefficient of friction

μ_{th} = coefficient of friction of threads

The mean radius itself can be defined using equation 6.2:

$$R_m = \left[\frac{d_1+d_2}{4}\right] \quad (6.5)$$

where

d_1 = inside diameter of the nut bearing surface

d_2 = outside diameter of the nut bearing surface

$$F_\beta = \frac{F_{ACL}\,\mu\,(\mu+tan\phi\,)}{(1-\mu tan\phi\,)(\mu cos\Phi+sin\phi\,)}\left\{\frac{1}{1-e^{\frac{-\mu\beta}{\mu cos\phi\,+sin\phi}}}\right\} \quad (6.6)$$

and

$$F_{ACL} = \frac{(1-\mu tan\phi\,)F_\beta\,(\mu cos\phi+sin\phi\,)}{\mu\,(\mu+tan\phi\,)}\left\{1-e^{\frac{-\mu\beta}{\mu cos\phi\,+sin\phi}}\right\} \quad (2.5)$$

where

F_{ACL} = axial clamping force due to tightening of T-bolt nut

β= subtended angle of half the V-section

μ= coefficient of friction between the V-section band clamp and rigid flanges

ϕ= angle of the V-section

6.4.3 Validation of Predicted Ultimate Axial Load Capacity Values

In this sub-section, the previously presented experimental results for the ultimate axial load capacity are compared to and used to validate the finite element and theoretical models presented in chapters 4 and 5.

Figure 6-17 includes experimental, finite element, and theoretical results of the ultimate axial load capacity for V-band sizes of D_b=114mm, 181mm, and 235mm. The experimental results shown are those taken from Figure 6-13, for T-bolt torques T_t=4, 8, 12, 14Nm. The finite element results for the axisymmetric model (discussed in section 4.5) are presented for a coefficient of friction μ=0.2, and for axial clamping loads of 6, 15, and 25kN. Employing the method proposed in the previous sub-section these clamping loads could be converted into T-bolt torques of 3.2, 8, and 13.3Nm respectively. The theoretical results are given for axial clamping loads of 6, and 25kN, not taking into account friction. For the smallest band diameter (114mm), experimental and finite element results correlate very well in their absolute values, though the FE models under-predicts the influence of increasing load capacity/ T-bolt torque. The theoretical results on the other hand differ by a factor of two in absolute values, but are capable of correctly predicting the increase of load capacity by increasing the T-bolt torque. As the band diameter increases to 181, and 235mm the finite element model predicts a nearly linear increase for the ultimate axial load capacity, with peak load capacity values between 350, and 400mm, whereas the theoretical model, in agreement with the experimental results show the ultimate axial load capacity to peak at approximately 181mm.

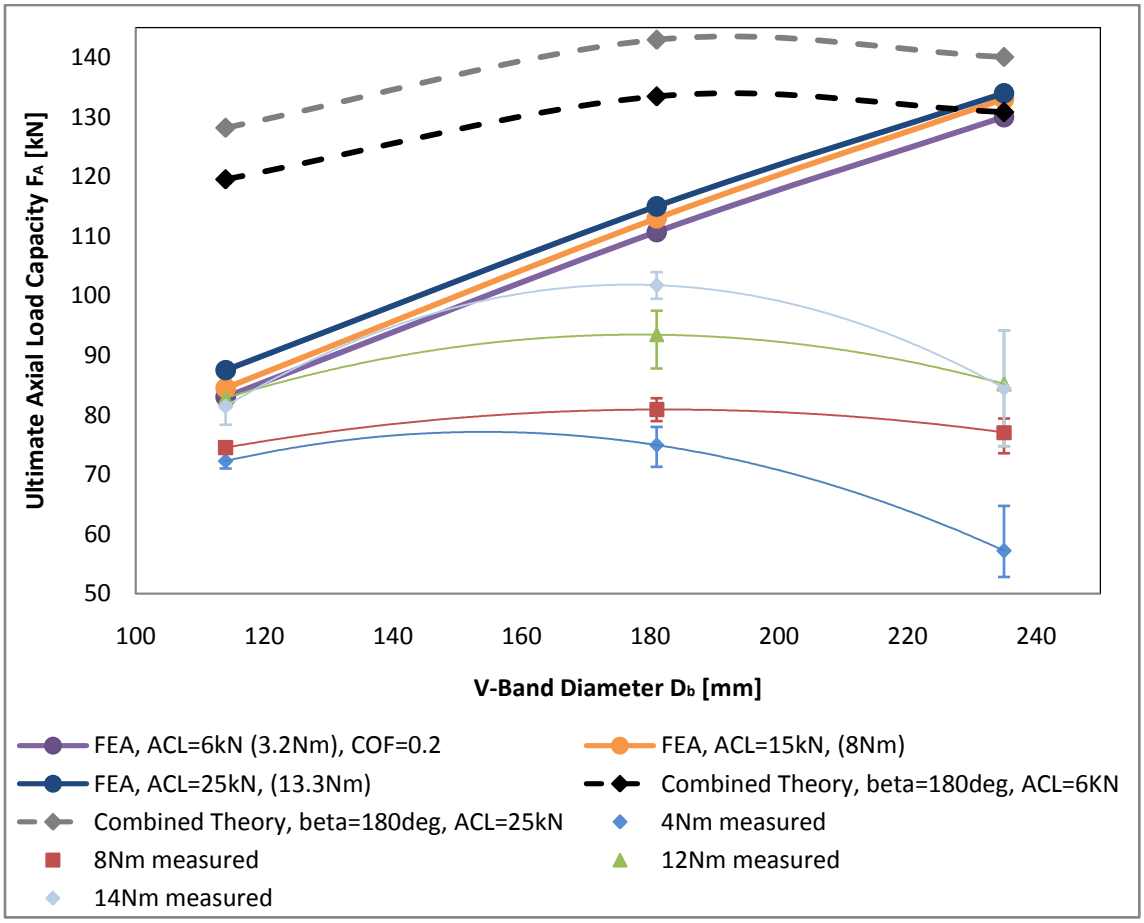

Figure 6-17: Comparison of experimental, finite element, and theoretical results of the ultimate axial load capacity over the band diameter

Comparing these experimental, finite element and theoretical results is a rather complex procedure, with many factors and parameters that need to be taken into consideration.

As found previously in this chapter the spot welds position was a major factor that impacted to the failure behaviour of V-bands during experiments. Therefore, angle β could be set to 167°, an average value also utilised in previous work such as Shoghi *et al.* (2004). The axisymmetric finite element model on the contrary employs an angle β of 180°, as a whole fully closed ring was assumed. For small band diameters of 114mm this difference has only a minor effect on the ultimate axial load capacity as the graphs show. These small bands are usually very stiff initially even before assembly due to the small diameter and the amount of plastic strain induced during ring formation in the roll forming process. This effect of the band rigidity due to the cold roll forming largely outweighs the effect of different angles β. This means that a large amount of the UALC is due to the initial rigidity of ring forming effect, and only to a certain amount due to tightening of the T-bolt. For larger bands, 181mm, and 235mm, this initial rigidity due to the forming process is largely reduced as less plastic strain is induced during the ring formation step, and the strength of the band depends to a larger extent on tightening of

the T-bolt, and the thereby induced wedging effect of the V-section. This means that the difference in β becomes much more important to the V-band failure behaviour, a factor that needs to be taken into account when designing and applying these bands in the real world. This finding is also supported by the experimental data provided in Figure 6-13 as the scatter increases with the band diameter. Moreover, support can be gathered from the experimental test data where the V-bands shifted towards the T-bolt side during failure largely reducing the ultimate axial load capacity, a factor not included in the finite element work. Furthermore, the FE models did not take into consideration the effect of the T-bolt itself.

Comparing the theoretical and experimental results the difference is much larger, due to many assumptions made in the development of the theory, as discussed in the previous chapter 5. The three most significant assumtions are not including plastic deformation, large deformation, and the change of the angle between leg and the free end of the V-band back during failure. This change of angle can best be understood by considering Figure 6-18, where in a) the inside of the V-band is shown as two black lines in the initial position and the angle between leg and back is made up of 90° plus half the subsquent V-band angle ϕ=20°, to give 110°. In b) the deformed shape is shown where due to flange separation the back is bent by an angle θ_a but the angle between back and leg remains at 110° as assumed in the combined theory. In c) however, the more realistic view is shown, again where the back is bent by an angle θ_a, but the angle between leg and back increases by an additional angle $\Delta\theta$, to give $110° + \Delta\theta$.

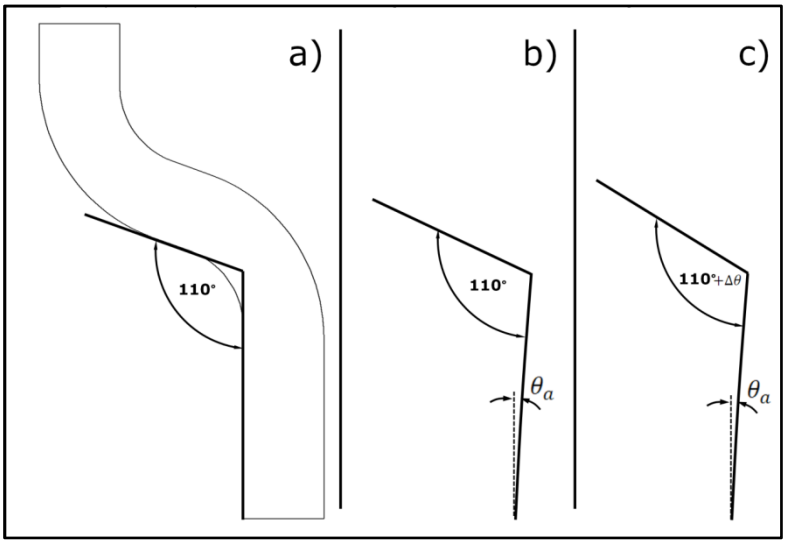

Figure 6-18: Angle between V-band back and leg for, a) initial position, b) deformed position as assumed in combined theory, and c) deformed position as believed to be reality

Including all these features in the combined theory would certainly largely decrease the predicted ultimate axial load capacity.

6.5 Conclusion of Experimental Validations

An experimental method was established to directly link plastic strain and work hardness for AISI 304 quarter hardened austenitic steel, using tensile testing and hardness measurements. When compared to classical strain gauge tests, the method presented here was able to pick up even small, very detailed and localised changes in hardness throughout the cross section. The hardness measurements of the cross section showed large hardness values where plastic deformation took place, especially in bent areas, as well as the hardness increasing throughout the section roll forming process. FEA and experiments correlated very well picking up even small peaks in hardness values. In the bent area tests showed large hardness values at the surfaces which reduced towards the neutral axis.

The tensile capacity tests revealed a peak of the ultimate axial load capacity for V-bands with diameters of 150mm, and the peak shifting towards 181mm as the axial clamping load was increased. During the experimental testing the bands showed plastic deformation of the cross section close to both ends of the V-band next to the T-bolt, but little irreversible deformation elsewhere along the circumference of the band, demonstrating that the band shifted towards the T-bolt side during failure. This shift largely reduced the ultimate axial load capacity, which means that the position of the T-bolt and the trunnion loops in particular are important and have a significant impact on the failure behaviour of V-band retainers. Moreover, it was found that plastic deformation of the cross section was most apparent for small band sizes such as 114mm, and reduced for larger diameters. When presenting the experimental results it was clear that the ultimate axial load capacity values scattered more for bands with 235mm than for small bands with 114mm. It was shown that larger axial clamping loads or T-bolt torques increased the ultimate axial load capacity significantly, and that the amount of influence itself also increased for larger bands, of 181mm, and 235mm.

The axisymmetric FE models correlated very well with experiments for small band retainers (114mm) but over-predicted the ultimate axial load capacity for larger bands (181mm, and 235mm). For the three tested band sizes the FE models predicted a linear increase in ultimate axial load capacity as the band diameter increased, but were not able to predict the peak in the ultimate axial load capacity. Moreover, the FE models under-predicted the impact of axial clamping load on the ultimate axial load capacity.

For the tested band sizes, the combined theory largely over-predicted the absolute values of the ultimate axial load capacity but successfully predicted the distribution depending on the diameter as well as the position of the peak at approximately 181mm.

The combined theory also successfully predicted the change of ultimate axial load capacity due to increasing axial clamping load/ T-bolt torque.

7 Conclusion

The literature survey in chapter 2 concluded that there were significant gaps in knowledge concerning the manufacturing, application, working behaviour, and failure modes of V-band joints. In particular it could be said, that all methods of predicting the ultimate axial load capacity F_{UALC} were rather rough approximations with little theoretical basis, as they were purely empirical and strongly based on experiments. Such methods are expensive and may be unreliable across a wide range of V-band retainers. Moreover, it was unknown how and if the plastic strain and work hardness generated during the cold roll forming process impacted on the ultimate axial load capacity.

Therefore, as stated in section 1.1, the overall aim of the work presented in this thesis was to provide a robust method of predicting the F_{UALC} of joints formed using V-band retainers.

This aim was achieved by addressing the following objectives:

1. To generate a finite element modelling technique able to predict the work hardening development during the manufacture of V-section band clamps.
2. To produce finite element models, validated by experimental data that allow V-band joint ultimate axial load capacity to be accurately predicted and also allow the internal stresses within the band to be studied.
3. To extend the existing theory of V-band behaviour to encompass ultimate axial load capacity, taking into account plastic deformation effects.
4. To generate an empirical understanding of the relationship between V-band tightening force, V-band internal stresses and V-band joint ultimate axial load capacity by conducting experimental tests on samples from different sizes of V-band.

7.1 Forming Models

In order to address objective 1, 2D and 3D finite element models were carried out to predict the plastic deformation and work hardening development during a V-band roll forming process. The 2 dimensional finite element model analysed the first stage of the process in which section forming took place, and allowed the use of very fine mesh densities whilst not exceeding a sensible CPU time to solve the analyses. This enabled the strip cross section to be examined in great detail. These analyses showed that the larger equivalent plastic strains (PEEQ) appeared, as expected where the greatest material deformation took place in the bend regions. It was also found that hydrostatic stresses induced by contact pressure from the rollers bending the band strip lead to

localised decreases of the plastic strain. These highly localised peaks and valleys of the strain distribution on the inside of the bent area may be one of the reasons for the crack growth in this region that has been observed in the field.

These 3 dimensional finite element models did not provide as much detailed information on the cross section of the band strip as the plane strain models but were able to successfully simulate the whole manufacturing process of section and ring formation. The plastic strains predicted by the 3D models were in broad agreement with those predicted by the plane strain models. An explicit solver was used to carry out these analyses, which was able to simulate dynamic effects and greatly reduced problems associated with very complex contact interactions. Despite being very stable, the explicit analyses needed between 6 and 15 hours to be solved, strongly dependent on the mesh densities. These ranged from using 150x20x4 elements for the coarsest and 300x20x8 elements for the finest mesh for a band diameter of 114mm, and 233x20x4 elements for a band diameter of 181mm.

An experimental method was established to directly link plastic strain and work hardness for AISI 304 quarter hardened austenitic stainless steel, using tensile testing and hardness measurements. When compared to classical strain gauge tests, the method presented here was able to pick up very detailed and localised changes in hardness throughout the cross section. The plastic strain results from the finite element work, in particular from the more detailed plane strain analyses were in good agreement with the hardness measurements of samples of the band taken throughout the roll forming process.

The major outcomes of this work were:

- Both 2D and 3D finite element models accurately predicted the plastic strain distribution in the V-band cross section throughout the cold roll forming process.
- The analyses revealed very localised peaks in plastic strain at the inner V-band surface, close to a region where cracking has occurred.
- An experimental technique was developed to validate finite element analyses of roll forming processes by generating a direct link between plastic strain and hardness values.

7.2 Numerical Prediction of Ultimate Axial Load Capacity

Objective 2 was addressed in two ways. Firstly an axisymmetric modelling technique was established simulating the interaction between a flange pair and a V-band section during separation. Secondly, the three dimensional roll forming model was extended to again simulate joint separation. The major difference between these methods was that the

axisymmetric models consisted of a closed ring and the 3D models of an open ring. A comparison of the methods over a range of flange thicknesses showed a significant difference in the results for the ultimate axial load capacity. With the 3D model, it was possible to simulate smaller flange thicknesses, and for the same thicknesses, results were larger for the 3D than those of the axisymmetric models. However, for the flange thicknesses used for the bulk of the analyses presented in this thesis, the 3D and axisymmetric models showed similar ultimate axial load capacities, and the latter proved to converge up to 22 times faster. Therefore, the decision was made to carry out all subsequent work using the axisymmetric model.

Using the axisymmetric modeling methodology it was found that the V-band diameter, D_b, had a significant influence on the ultimate axial load capacity, F_{UALC}, which increased between 114mm and 235mm, reached a peak, and then for larger diameters decreased again. This was mainly related to the deformation modes, as for small and medium band diameters the cross section deforms due to section and ring deformation, whereas for bands with larger diameters it deforms due to ring deformation only. The coefficient of friction, μ, had a large impact, increasing ultimate axial load capacity F_{UALC} for the same axial clamping load F_{ACL}. A larger axial clamping load F_{ACL} increases the F_{UALC} as well, with its impact increasing for larger μ. Overall it was found that reducing the band thickness t_b also reduced the F_{UALC}. However, a larger impact was found for bands with D_b between 114mm and 400mm, and a much smaller effect for larger bands. Moreover, this impact reduces as the axial clamping load F_{ACL} is increased. The FE analyses also showed that decreasing $r_b$highly increased F_{UALC}, as this decrease resulted in a larger sliding length l_s.

In terms of flange geometry, the FE analyses showed that ultimate axial load capacity was highly dependent on the flange oversize/ thickness t_f. On the other hand, the flange corner radius r_c and flange angle ϕ were shown to have very little impact on the F_{UALC}.

The major outcomes of this work were:

- Geometric differences between axisymmetric and 3D models can be significant but the results gained by the two model types agree well.
- The 3D models included the plastic strains induced by the roll forming process, and showed that these plastic strains had little impact on the ultimate axial load capacity F_{UALC}.
- The finite element analyses found two different modes of failure, a pure ring deformation for large V-band retainers, and a combined section and ring deformation for small and medium retainers.
- The flange geometric parameters including thickness t_f, corner radius r_c, and angle ϕ were shown to impact on F_{UALC} with thickness being the most significant.

- The ultimate axial load capacity F_{UALC} was strongly dependent on the band diameter D_b.
- An increase in friction μ and axial clamping load F_{ACL} also strongly increased the F_{UALC}.
- Reducing the band thickness t_b also reduced the F_{UALC}, although this change was strongly dependent on the coefficent of friction μ and axial clamping load F_{ACL}.

7.3 Theoretical Models

Objective 3 was addressed by developing two theoretical models. The first one assumed that the band deformed as a pure ring elastically in the radial direction, and the second one combined section and ring deformation. For the ring deformation model the full V-band cross section was included but was assumed to remain rigid with uniform circumferential stress in the whole V-band cross section, and deformation was taking place only in the circumference. This model showed very good correlation with the finite element work for band diameters between 800mm and 2000mm. Below 800mm, the ring theory largely over-predicted the ultimate axial load capacity.

For the section deformation model the V-band cross section was reduced to a wide, straight, rectangular cross section cantilever. The leg and foot were only considered to describe the position of contact and predict axial and radial levers. The circumferential expansion of leg and foot or bending of the leg were not accounted for. This combined theory showed very good correlation to the finite element models for band diameters between 800mm and 2000mm, as well. Below this diameter range, it also over-predicted the ultimate axial load capacity, but to a much smaller amount than the ring theory. Moreover, it was able to successfully predict a peak ultimate axial load at approximately 181mm, which agreed with the finite element model that predicted a peak at 250mm.

For both models friction and the amount of the axial clamping load were not included.

The major outcomes of this work were:

- A theoretical model was developed which assumed a radial ring deformation and correlated very well with the finite element models for V-band joints with large diameters.
- A theoretical model was developed which accounted for combined section and ring deformation.
- Both theoretical models predicted a very large impact of small changes in both flange and band geometry on the F_{UALC}, resulting in load distributions which were similar to those found by the numerical work from objectives 2

7.4 Empirical Study

In order to meet objective 4, experimental tensile tests were carried to determine the ultimate axial load capacity F_{UALC} of V-band joints, and to validate the finite element models from objective 2 and theoretical models from objective 3. The tests revealed a peak of the ultimate axial load capacity for V-bands with diameters of 150mm, and the peak shifting towards 181mm as the axial clamping load was increased. During the experimental testing the bands showed plastic deformation of the cross section close to both ends of the V-band next to the T-bolt, but little irreversible deformation elsewhere along the circumference of the band, demonstrating that the band shifted towards the T-bolt side during failure. This shift largely reduced the ultimate axial load capacity, which means that the position of the T-bolt and the trunnion loops in particular are important and have a significant impact on the failure behaviour of V-band retainers. Moreover, it was found that plastic deformation of the cross section was most apparent for small band sizes such as 114mm, and reduced for larger diameters.

When presenting the experimental results it was clear that the ultimate axial load capacity values scattered more for bands with 235mm than for small bands with 114mm. It was shown that larger axial clamping loads or T-bolt torques increased the ultimate axial load capacity significantly, and that the amount of influence itself also increased for larger bands, of 181mm, and 235mm.

The axisymmetric FE models correlated very well with experiments for small band retainers (114mm) but over-predicted the ultimate axial load capacity for larger bands (181mm, and 235mm). For the three tested band sizes the FE models predicted an increase in ultimate axial load capacity as the band diameter increased, but were not able to predict the peak in the ultimate axial load capacity. The FE models under-predicted the impact of axial clamping load on the ultimate axial load capacity.

For the tested band sizes, the combined theory largely over-predicted the absolute values of the ultimate axial load capacity but successfully predicted the distribution depending on the diameter as well as the position of the peak at slightly above 181mm. The combined theory also successfully predicted the change of ultimate axial load capacity due to increasing axial clamping load/ T-bolt torque.

The major outcomes of this work were:

- The scatter in the experimental results indicated that uncontrolled variables were highly significant.
- For the tested diameter range, smaller bands failed mainly due to deformation of the section, whereas for larger bands ring expansion increased its impact.

- An increase in the axial clamping load also increased the ultimate axial load capacity.
- The experiments validated the numerical and theoretical work undertaken in objectives 2 and 3.

8 Further Work

The work presented in this thesis has managed to fill a large gap in knowledge concerning V-band joints. However, in this field there are still plenty of questions remaining that need answering, and the thesis itself has raised some new interesting questions. Therefore, based on this work there are some suggestions of what further research should focus on, discussed in this chapter.

8.1 Additional Validation

Hardness tests were undertaken in which the hardness development throughout the roll forming process was measured and used to validate the finite element simulation of this process. The method should be refined by introducing more measurement points, as well as including the ring forming stage and comparing them to the existing finite element work, presented in chapter 3.

The experiments also included tensile tests to determine the ultimate axial load capacity of V-band joints, which were undertaken for three band sizes and a range of axial clamping loads. However, in the future further tests should be carried for a larger range of band diameters, especially for band sizes beyond 400mm. Therefore, larger V-band retainers and flanges need to be manufactured.

The impact of the flange thickness should be tested by producing slightly undersized flange pairs and then increasing their thickness with the use of shims.

Prior to all tests undertaken in the future, the cross section of the flange pair should be measured precisely. These measurements should also focus on determining the precise V-band cross section of every band before and after all tests, in order to determine the amount of irreversible deformations during failure. This would make it possible to determine the impact of certain V-band and flange geometric parameters - such as the band thickness and length of the flat part of which the sliding length is a part - on the ultimate axial load capacity. This may also include measuring the surface roughness and form of the inner V-band surface, and detecting differences along the circumference, and hence proving that the contact pressure distribution around the circumference is non-uniform.

8.2 Parameter Investigation

The finite element and theoretical work undertaken in this thesis, has shown that there were a number of geometric parameters, such as the sliding length l_s that was difficult to control as it is strongly dependent on the coefficient of friction and the axial clamping load, and other parameters that are determined by the rolling process. However, these parameters were shown to have a significant impact on the ultimate axial load capacity.

Hence, this needs further analyses including a carefully constructed investigation by expanding the existing theoretical and finite element work. This should be validated by detailed physical testing, and could be part of the experiments mentioned in the previous section. In particular the existing 3D FE models should be extended to analyse V-band joints with larger band diameters, include a finer mesh and should then be compared to the axisymmetric analyses.

Currently, the V-band cross section varies between the axisymmetric and 3D models, and should be made the same. This could include photographing the real V-band cross section, scanning it into a CAD package, and based on these photographs designing a new improved V-band cross section for the FE models, which is closer to reality.

The work undertaken here has also shown a large impact of band thickness and hence should be included in the comparison between two models. Fully investigating this parameter was beyond the scope of this thesis and therefore for the further work it is suggested to analyse a range of variability in manufactured bands as well as numerical investigations.

8.3 Theoretical Model Development

Both theoretical models showed good agreement with the finite element work but lack certain parameters. Therefore, in both models friction and the axial clamping load should be included.

The section deformation part of the combined theory on the other hand requires much more additional work. So far, the theory uses a classical elastic approach combined with large deflections. However, both the FEA and the physical experiments have shown that there is significant plastic deformation for smaller bands. Hence, the effects of plasticity should be included. It is believed that this will largely reduce the predicted ultimate axial load capacity. This would affect especially bands with D_b<400mm, as the section deformation is most apparent at these diameters, and would result in much better correlation between FE and experimental data.

Furthermore, the section theory only assumes a rectangular cantilever, but for further work should include the full half of the V-band cross section (using the joint symmetry).

The combined theory presented in this thesis is solved by using an incremental process. In there, small increments of the angle due to bending are assumed, which makes the accuracy of the results highly dependent on the increment size. This can be avoided by introducing an iterative process to refine the incremental process.

Initially the angle between the leg and the back is set due to the design. However, the angle is believed to change during separation of the flanges. The amount of change should be determined from the axisymmteric FE model and the significance of this with regard to the theoretical model should be considered. The circumferential expansion of the leg and foot due to section deformation should be investigated in a similar way. If necessary, the theoretical model should be expanded to incorporate both effects.

8.4 Additional Parameters

So far, neither the theoretical nor the finite element models included the effects of the T-bolt and the trunnion loops on the overall failure mechanism. However, these may strongly impact on the ultimate axial load capacity and overall performance of the V-band joint.

To begin with, in the 3D model, the T-bolt load could be included by introducing connection elements, connecting both free ends of the band. Once assembled to the flanges, the T-bolt load could then be applied by using the bolt tension feature in ABAQUS. In more sophisticated subsequent models, the T-bolt and trunnion loops could be fully designed.

In the theoretical models, these parameters could be included by adding another term to the equations, accounting for the different cross section of the T-bolt and trunnion loops.

8.5 Other Failure Modes

For the hardness development analyses, the peaks and valleys in plastic strain in the bent area of the 2D FE models should be further analysed. Particular investigations should be directed at the impact of the plastic strain distribution on crack growth in the bent area, ideally linked with an explicit dynamic analysis.

These investigations should also include the development and growth of cracks, by defining their exact starting point and measuring the hardness near by. This may lead to better understanding how these cracks in the bent area can be prevented, by introducing improvements and changes in the manufacturing process.

Directly associated to crack growth is the impact of fatigue due to vibrations and service loads while the turbocharger is running.

Therefore both, axiymmetric and 3D FE models should also include the impact of dynamic behaviour and vibrations on the ultimate axial load capacity, using an explicit solver.

All work in this thesis focused on axial separation of the flanges, applying an axial load to the V-band retainer. However, in real applications such as exhaust pipes and turbochargers, other failure modes will occur. These include torsional movement of the flanges relative to each other, and failure of the joint due to an applied bending moment, which will be particularly significant for larger joints.

Theoretical and finite element models, as well as experimental validations should therefore focus on predicting and determining the ultimate rotational load capacity and ultimate bending load capacity. Especially for the latter, the position of the bending moment relative to the position of the T-bolt load might have a significant impact on the load capacity, considering that the contact pressure around the circumference is non-uniformly distributed. Furthermore, for all geometric parameters investigated in this thesis their impact on ultimate load capacities due to rotation and bending should be analysed.

References

Atkinson, P. J., W. N. Newberry, et al. (1998). "A method to increase the sensitive range of pressure sensitive film." Journal of Biomechanics **31**: 855-859.

Bachus, K. N., A. L. DeMarco, et al. (2006). "Measuring contact area, force, and pressure for bioengineering applications: Using Fuji Film and TekScan system." Medical Engineering & Physics **28**: 483-488.

Barrans, S. M. and M. Muller (2009). Finite element prediction of the ultimate axial load capacity of V-section band clamps. 7th International Conference on Modern Practice in Stress and Vibration Analysis. Cambridge.

Becker, A. A. (2004). An Introductory Guide to Finite Element Analysis. London, Professional Engineering Publishing Limited.

Belytschko, T., W. K. Liu, et al. (2000). Chapter 10 Contact-impact. Nonlinear Finite Elements for Continua and Structures. Chichester, John Wiley & Sons Ltd.

Bhattacharyya, D., P. D. Smith, et al. (1984). "The Prediction of Deformation Length in Cold Roll-Forming." Journal of Mechanical Working Technology **9**: 181-191.

Bicanic, N. (1992). Chapter 3 Time Independent Material Nonlinearities. NAFEMS Introduction to Nonlinear Finite Element Analysis. E. Hinton. Glasgow.

Black, J. T. and R. A. Kohser (2008). DeGarmor's Materials & Processes in Manufacturing. USA.

Budinski, K. G. and M. K. Budinski (2010). Engineering Materials Properties and Selection, Vernon R Anthony Pearson Prentice Hall.

Bui, Q. V., L. Papelux, et al. (2004). "Numerical simulation of springback using enhanced assumed strain elements." Journal of Materials Processing Technology(153-154): 314-318.

Bui, Q. V. and J. P. Ponthot (2008). "Numerical simulation of cold roll-forming processes." Journal of Materials Processing Technology **202**: 275-282.

Cook, R. D., D. S. Malkus, et al. (2002). Chapter 17 Nonlinearity: An Introduction. Concepts and applications of finite element analysis. W. Anderson, John Wiley & Sons. Inc.

Cruise, R. B. and L. Gardner (2008). "Residual stress analysis of structural stainless steel sections." Journal of Constructional Steel Research **64**: 352-366.

Dassault-Systems (2007a). "Getting Started with ABAQUS v6.7 Section 12 Contact."

Dassault-Systems (2007b). "Getting Started with ABAQUS v6.7 Section 4 Using Continuum Elements."

Dassault-Systems (2007d). "Getting Started with ABAQUS v6.7 Section 10 Materials."

Di Tolla, R. and M. Ernst (1994). Nonlinear Finite Element Evaluation of Marman Clamp Structural Capabilty. AIAA/ASME/ASCE/AHS/ASC Structures, Structural Dynamics and Materials Conference 1**:** 320-330.

Dixit, P. M. and U. S. Dixit (2008). Modeling of Metal Forming and Machining Processes by Finite Element and Soft Computing Methods. London, Springer-Verlag.

Dowen, D., C. Chrisriansen, et al. (2001). Development of a Reusable, Low-Shock Clamp Band Separation System for Small Spacecraft Release Applications. European Space Mechanisms and Tribology Symposium. Liege.

Durelli, A. J., E. A. Phillips, et al. (1958). Introduction to the Theoretical and Experimental Analysis of Stress and Strain. New York, McGraw-Hill Book Company, Inc.

Fagan, M. J. (1992). Chapter 10 Further applications of the finite element method. Finite Element Analysis. Essex, Pearson Education Limited.

Farzin, M., M. S. Tehrani, et al. (2002). "Determination of buckling limit of strain in cold roll forming by the finite element analysis." Journal of Materials Processing Technology(125-126): 626-632.

Fritskey, J. (2003). "Clamping and coupling with V-band retainers." Machine Design **75**(8): 68-70,72.
Gere, J. M. and S. Timoshenko (1991). Mechanics of Materials, Chapman & Hall. **Third SI Edition:** p636.
Han, Z. W., C. Liu, et al. (2002). "Simulation of a multi-stand roll-forming process for thick channel section." Journal of Materials Processing Technology **127**: 382-387.
Han, Z. W., C. Liu, et al. (2005). "Spline finite strip analysis of forming parameters in roll forming a channel section." Journal of Materials Processing Technology **159**: 383-388.
Heislitz, F., H. Livatyali, et al. (1996). "Simulation of roll forming process with the 3-D FEM code PAM-STAMP." Journal of Materials Processing Technology **59**: 59-67.
Hertz, H. (1896). Miscellaneous Papers. London, MacMillan.
Hinton, E. and T. Hellen (1992). Chapter 6 Further Complexities. NAFEMS Introduction to Nonlinear Finite Element Analysis. E. Hinton. Glasgow, NAFEMS.
Hoffmann, K. and K. Decker (2007). "Inaccuracies in measurement of contact pressure due to the measuring grid of a foil sensor." Int. J. Intelligent Systems Technologies and Applications **3**(2/3): 80-94.
Johnson, W. and P. B. Mellor (1983). Engineering Plasticity. West Sussex, Ellis Horwood Ltd.
Kain, V., K. Chandra, et al. (2004). "Effect of cold work on low-temperature sensitization behavior of austenitic stainless steel." Journal of Nuclear Materials **334**: 115-132.
Kiuchi, M. (1973). Analytical study on cold roll forming process. Report of Inst. Ind. Sci., University of Tokyo.
Kiuchi, M. and T. Koudabashi (1984). Automated design system of optimal roll profiles for cold roll forming Poceedings of the Third International Conference on Rotary Metalworking Processes. Kyoto, Japan**:** 423-436.
Komi, E. R., J. R. Roberts, et al. (2007). "Evaluation of thin, flexible sensors for time-resolved grip force measurement." Proc. IMechE Part C: J. Mechanical Engineering Science **221**: 1687-1699.
Konter, A. (2000). How to undertake a Contact and Friction Analysis. Glasgow, NAFEMS.
Lancho, M., J. Larrauri, et al. (2000). "CRSS: a separation system for launching very heavy payloads." Acta Astronautica **47**(2-9): 153-162.
Laursen, T. A. (2002). Computational Contact and Impact Mechanics: Fundamentals of Modeling Interfacial Phenomena in Nonlinear Finite Element Analysis. Heidelberg Berlin, Springer.
Li, S. H., G. Zeng, et al. (2009). "Residual stresses in roll-formed sqare hollow sections." Thin-walled structures **47**: 505-513.
Lin, C. S. and T. R. Cole (1997). "Dynamic Model for Global Positioning System Block IIR Space Vehicle." Journal of Spacecraft and Rockets **34**(3): 354-359.
Lindgren, M. (2005). Finite element model of roll forming of a U-channel profile. International Conference on Tech. of Plasticity. Verona.
Lindgren, M. (2007a). "Cold roll forming of a U-channel made of high strength steel." Journal of Materials Processing Technology **186**: 77-81.
Lindgren, M. (2007b). "An improved model for the longitudinal peak strain in the flange of a roll formed U-channel developed by FE-analysis." Steel Res Int **78**(1): 82-7.
Marciniak, Z., J. L. Duncan, et al. (2002). Mechanics of Sheet Metal Forming. Oxford, Butterworth-Heinemann.
McClure, C. K. and H. Li (1995). "Roll Forming Simulation using Finite Element Analysis." Manufacturing Review **8**: 114-119.
Meyer, R. X. (1999). Elements of Space Technology. San Diego, Academic Press**:** p.104.
Milad, M., N. Zreiba, et al. (2008). "The effect of cold work on structure and properties of AISI 304 stainless steel." Journal of Materials Processing Technology **203**: 80-85.
Moen, C. D., T. Igusa, et al. (2008). "Prediction of residual stresses and strains in cold-formed steel memebers." Thin-walled structures **46**: 1274-1289.
Moore, A. J. W. (1948). "Deformation of Metals in Static and in Sliding Contact." Proceedings of the Royal Society of London. Series A, Mathematical and Physical Sciences **195**: 231-244.
Mountford, R. (1980). "Design of clamp joints." Engineering Designer: 37-39.

Muller, M. and S. M. Barrans (2009). Ultimate Axial Load Capacity of V-Band Clamp Joints. Proceedings of Computing and Engineering Annual Researchers' Conference, Huddersfield, University of Huddersfield

Muller, M. and S. M. Barrans (2010). Impact of flange geometry on the ultimate axial load capacity of V-band clamps. 9th International Conference on Turbochargers and Turbocharging. London, UK.

Muller, M. and S. M. Barrans (2010b). PREDICTING AND DETERMINING OF CONTACT PRESSURE DISTRIBUTION IN JOINTS FORMED BY V-BAND CLAMPS. Proceedings of Computing and Engineering Annual Researchers' Conference, Huddersfield, University of Huddersfield.

Muller, M., S. M. Barrans, et al. (2011). "Predicting plastic deformation and work hardening during V-band formation." Journal of Materials Processing Technology **211**(4): 627-636.

NASA (2000). Marman clamp system design guidelines. Guideline GD-ED-2214, Goddard Space Flight Centre.

Panton, S. M., J. L. Duncan, et al. (1996). "Longitudinal and shear strain development in cold roll forming." Journal of Materials Processing Technology **60**: 219-224.

Papeleux, L. and J.-P. Ponthot (2002). "Finite element simulation of springback in sheet metal forming." Journal of Materials Processing Technology: 785-791.

Paralikas, J., K. Salonitis, et al. (2009). "Investigation of the effects of main roll-forming process parameters on quality for a V-section profile from AHSS." International Journal of Advanced Manufacturing Technology **44**: 223-237.

Paralikas, J., K. Salonitis, et al. (2010). "Optimization of roll forming process parameters - a semi-empirical approach." International Journal of Advanced Manufacturing Technology **47**: 1041-1052.

Polakowski, N. H. and E. J. Ripling (1966). Strength and Structure of Engineering Materials. Englewood Cliffs, N.J., Prentice-Hall, Inc.

Pullen, J. and J. B. P. Williamson (1972). "On the Plastic Contact of Rough Surfaces." Proceedings of the Royal Society of London. Series A, Mathematical and Physical Sciences **327**: 159-173.

Qin, Z. Y., S. Z. Yan, et al. (2010a). "Dynamic analysis of clamp band joint system subjected to axial vibration." Journal of Sound and Vibration **329**: 4486-4500.

Qin, Z. Y., S. Z. Yan, et al. (2010b). "Dynamic characteristics of launch vehicle and spacecraft connected by clamp band." Journal of Sound and Vibration **doi: 10.1016/j.jsv.2010.06.011**.

Quach, W. M., J. G. Teng, et al. (2004). "Residual stresses in steel sheets due to coiling and uncoiling: a closed-form analytical solution." Engineering Structures **26**: 1249–1259.

Quach, W. M., J. G. Teng, et al. (2006). "Finite element predictions of residual stresses in press-braked thin-walled steel sections." Engineering Structures **28**: 1609-1619.

Redford, G. D., J. G. Rimmer, et al. (1969). Mechanical Technology, The macmillan press ltd.

Roylance, D. (1996). Chapter 6 Yield and Plastic Flow. Mechanics of Materials. New York, John Wiley & Sons, Inc.

Schuler (1998). Metal forming handbook. Berlin, Heidelberg, Springer-Verlag.

Shanley, F. R. (1957). Strength of Materials. New York, McGraw-Hill Book Company.

Shoghi, K. (2003). Stress and Strain Analysis of flat and V-section band clamps. Huddersfield, University of Huddersfield. **PhD**.

Shoghi, K., S. M. Barrans, et al. (2006). Axial load capacity of V-section band clamp joints. 8th International Conference on Turbochargers and Turbocharging London.

Shoghi, K., S. M. Barrans, et al. (2003). Classical and finite element analysis of V-band retainers. NAFEMS World Congress. (Orlando) Florida.

Shoghi, K., S. M. Barrans, et al. (2004). "Stress in V-section band clamps." Journal of Mechanical Engineering Science, Part C **218**: 251-261.

Shoghi, K., H. V. Rao, et al. (2003). "Stress in a flat section band clamp." International Journal of Mechanical Science **217**(c): 821-830.

Skrzypek, J. J. (2000). Chapter 4 Basic Equations of Plastic Hardening. Plasticity and Creep Theory, Examples, and Problems. R. B. Hetnarski, CRC Press, Inc.

Skrzypek, J. J. (2000). Plasticity and Creep Theory, Examples, and Problems CRC Press, Inc.

Stavrinidis, C., M. Klein, et al. (1996). "TECHNICAL AND PROGRAMMATIC CONSTRAINTS IN DYNAMIC VERIFICATION OF SATELLITE MECHANICAL SYSTEMS." Acta Astronautica **38**(1): 25-31.

Suzuki, H., M. Kiuchi, et al. (1972). Experimental investigation on cold-roll-forming process. Report of the Institute of Industrial Science. Tokyo, University of Tokio**:** 82-172.

Takeuchi, S. and J. Onoda (2002). "Estimation of Separation Shock of the Marman Clamp System by Using a Simple Band-Mass Model." TRANSACTIONS OF THE JAPAN SOCIETY FOR AERONAUTICAL AND SPACE SCIENCES **45**(147): 53-60.

Tehrani, M. S., P. Hartley, et al. (2006). "Localised edge buckling in cold roll-forming of symmetric channel section." Thin-walled structures **44**: 184-196.

Timoshenko, S. (1934). Theory of Elasticity. New York, MacGraw-Hill.

Timoshenko, S. P. and J. M. Gere (1973). Inelastic Bending. Mechanics of Materials. London, Van Nostrand Reinhold Company Ltd.

Wempner, G. (1995). Mechanics of solids. Boston, PWS Publishing Company.

Weng, C. and T. Pekoz (1990). "Residual stresses in cold-formed steel members." Journal of Structural Engineering **116**(6): 1611-1625.

Weng, C. and R. White (1990a). "Residual stresses in cold-bent thick steel plates " Journal of Structural Engineering **116**(1): 24-39.

Weng, C. and R. White (1990b). "Cold-bending of thick high-strength steel plates." Journal of Structural Engineering **116**(1): 40-54.

Wilkey, J. W. (1966). Velocity Package. United States of America.

Wittman, A. (1987). Clamping Connection Assembly for Spacecraft. U.S.A. **4,715,565**.

Wriggers, P. (2006). Computational Contact Mechanics. Berlin Heidelberg, Springer-Verlag.

Wriggers, P. (2008). Nonlinear Finite Element Methods, Springer.

Zeng, G., S. H. Li, et al. (2009). "Optimization design of roll profiles for cold roll forming based on response surface method." Materials and Design **30**(6): 1930–1938.

Zhang, L., N. Tan, et al. (2010). "A New Model for Simulation of Cold Roll-Forming of Tubes by Using Spline Strip Method." Journal of Shanghai Jiaotong University **15**(1): 70-75.

Zhu, S. D., S. M. Panton, et al. (1996). "The effects of geometric variables in roll forming a channel section." Proc. Inst. Mech. Engrs. **210**: 127-134.

Zienkiewicz, O. C. and R. L. Taylor (2005). The Finite Element Method for Solid and Structural Mechanics. Oxford, Elsevier Butterworth-Heinemann

Appendix (Conference and Journal Papers)

7th International Conference on Modern Practice in Stress and Vibration Analysis. Cambridge. 2009:

Finite element prediction of the ultimate axial load capacity of V-section band clamps

S M Barrans[1] and M Muller[1]

[1] University of Huddersfield, School of Computing and Engineering, Queensgate, Huddersfield, HD1 3DH, UK

E-Mail: s.m.barrans@hud.ac.uk

Abstract. Band clamps with a flat bottomed V-section are used to connect a pair of circular flanges to provide a joint with significant axial strength. Despite the wide application of V-band clamps, their behaviour is not fully understood and the ultimate axial strength is currently only available from physical testing. This physical testing has indicated that the ultimate strength is determined by two different types of structural deformation, an elastic deformation mode and a plastic deformation mode. Initial finite element analysis work has demonstrated that analysis of this class of problem is not straightforward. This paper discusses the difficulties encountered when simulating this type of component interaction where contact is highly localised and contact pressures are high.

1. Introduction

V-section band clamps are used in a wide range of applications in the aerospace and automotive industries. As stated by Shoghi [1] they were invented during the Second World War by the Marmon Corporation and are nowadays used to connect together the housings of diesel engine turbochargers and also to assemble satellites to their launching device [2]. The process of assembling V-band clamps to a pair of circular flanges has recently been investigated using classical analysis [3], finite element analysis [4] and experimental validations [5]. Figure 1 shows a V-section band clamp assembled to a pair of flanges in an experimental test rig.

Figure 1: V-section band clamp assembled to a pair of circular flanges for initial experimental testing

Despite their wide application, once assembled to a pair of flanges little is known about the interaction between flange and band. Moreover the failure mode of V-band clamps when undergoing

an axial load is not fully understood. Work has therefore been initiated to generate a finite element model able to predict the ultimate axial load capacity and deformation of V-band Clamps.

2. Initial Finite Element Analyses

To get a first understanding of the structural behaviour of V-band clamps initial finite element analyses were generated using the package ABAQUS. The bands were approximated as being axisymmetric and the plane of symmetry between the two flanges was used to reduce the model size. Whilst Shoghi [1] has demonstrated that the contact load between the bands and flanges is not uniform around the band, the load variation was judged to be small for this first approximation. A sliding contact interaction between the flange and the band clamp was defined and to simulate tightening of the band, it was shrunk on to the flanges. The band clamp was meshed with 2D axisymmetric linear plain strain elements with reduced integration as suggested by Dassault Systems [6] because as observed by Konter [7], second order elements do not distribute the contact pressure uniformly between the mid-side and corner nodes. No meshing was needed for the flange because it was set up as an analytical rigid body. For these initial analyses an implicit solver and a penalty contact algorithm were used with the knowledge that penalty contacts tend to converge more easily and to be more stable as stated by Konter [8].

The material for the band clamp was AISI 304 stainless steel, with a Young's Modulus of 227 GPa, and a Poisson's Ratio of 0.29. The material was modelled as being elastic-plastic with the hardening approximated as linear as explained by Dixit and Dixit [9]. Material data was taken from experimental tests carried out by Shoghi [1]. Using Ludwik's theorem as presented by Meyer [10] these were transformed from engineering to true stress and strain values.

These finite element analyses were set up for a range of different flange diameters, D_f, from 55 mm to 2000 mm with a flange contact edge radius R of 0.1 mm. In practice flange contact radii vary from 0.1 to 0.7 mm. Dassault Systems [11] state that the contact algorithm in ABAQUS requires that the master surface should not contain sharp edges. In the first step of each analysis a boundary condition (BC) was applied to the band at its symmetrical edge to prevent it from moving in the axial direction as shown in Figure 2.

The flange was restrained at its reference point (RP) to prevent it from moving in the radial and axial directions and to prevent it from rotating. Initially there was a gap of about 0.1 mm between the band and the flange. The band was then shrunk onto the flange using an applied reduction in temperature to generate a thermal contraction. This was done to simulate the assembly procedure of tightening the T-bolt nut, which generates an axial load. Using several steps the flange was then moved in the axial direction to simulate a failure of the V-band clamp joint. For these contact interactions the V-band clamp was set as the deformed slave-surface and the flange was set to be the deforming rigid, master-surface. Throughout this paper only the flange diameter D_f rather than the band clamp diameter D_b is used because D_b highly depends on the T-bolt load. After performing these analyses the maximum value of the reaction force in the axial direction at the flange's reference point (RP) could be recorded. This represents the ultimate axial load capacity of the joint. These results are summarized in Figure 3 which indicates that the highest load capacity exists with a flange diameter, D_f of 250 mm.

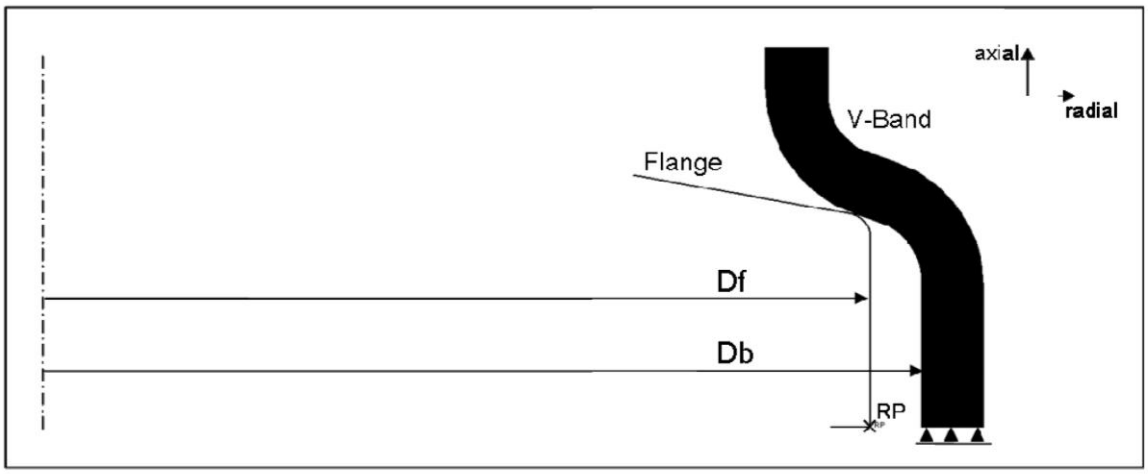

Figure 2: Axisymmetric model arrangement.

It is worth mentioning at this point that these initial analyses were carried out with no friction, a single edge contact radius, R, and a relatively low mesh density using a free, unstructured mesh.

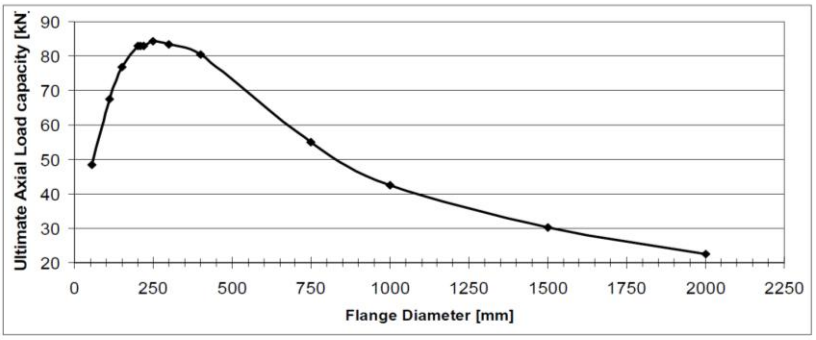

Figure 3: Predicted Axial Load Capacity of V-Section Band Clamps over varying Flange Diameters for Initial FE-Analyses.

3. Implicit Analysis

Using a fixed flange diameter D_f = 250 mm, analyses were carried out for coefficients of friction of 0 and 0.3, for contact edge radii R of 0.3 and 0.5 mm, and for several element thicknesses along the sliding contact surface. Although a contact edge radius of 0.1 mm was used in the initial analyses, these analyses failed with a coefficient of friction of 0.3 and a change in mesh density applied.

3.1. Axial Load Capacity

The analyses generated appeared to be highly dependent on the mesh type and mesh element thickness especially along the contact sliding surface. Figure 4 shows the results for the ultimate axial load capacity for a model with R = 0.5 mm and a coefficient of friction μ of 0.3. As can be seen in this figure the graph for the structured mesh seems to converge to a certain load value for decreasing element size. The graph for the free mesh oscillates with decreasing element size.

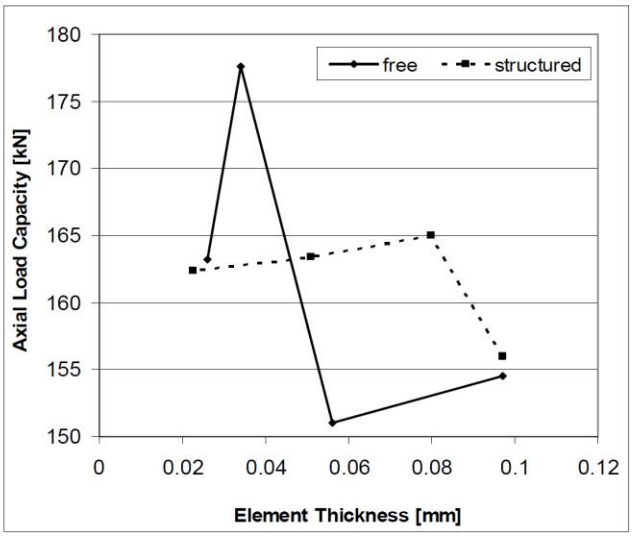

Figure 4: Axial Load Capacity depending on Element Thickness for free and structured mesh, μ = 0.3 and R = 0.5 mm.

Figure 5 indicates the problems that occurred during this analysis work and therefore needed further investigation. Figure 5a shows the axial reaction force at the flange reference point. The very high peak at 255 kN is clearly erroneous. The relative positions of flange and band at this peak are shown in Figure 5b. It can be seen that once the flange starts to slide the elements along the band clamp surface become heavily deformed, especially as the flange slides over the surface. In further analyses these erroneous peaks were noted but were not reported as ultimate axial load capacity. Ignoring this peak, the ultimate axial load capacity of this model is 162 kN.

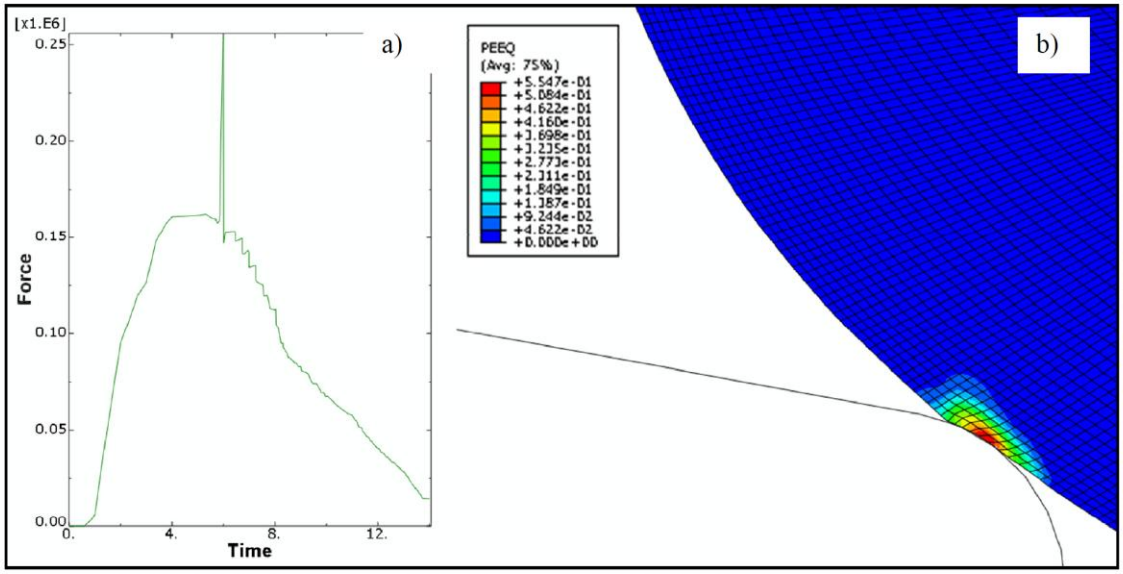

Figure 5: Results for R = 0.5 mm, μ = 0.3, structured mesh, high mesh density a) Axial load at reference point during failure b) position of flange at peak axial load.

Figure 6 shows the results for the same model but with a free, unstructured mesh with nearly the same element size. Again, there is an erroneous peak at the same position in the failure process but it is just at 175kN (Figure 6a), whereas the more reliable axial load capacity seems to be at 163kN almost the same as for the structured mesh. Figure 6b also indicates the same phenomenon of elements starting to deform as the flange starts to slide.

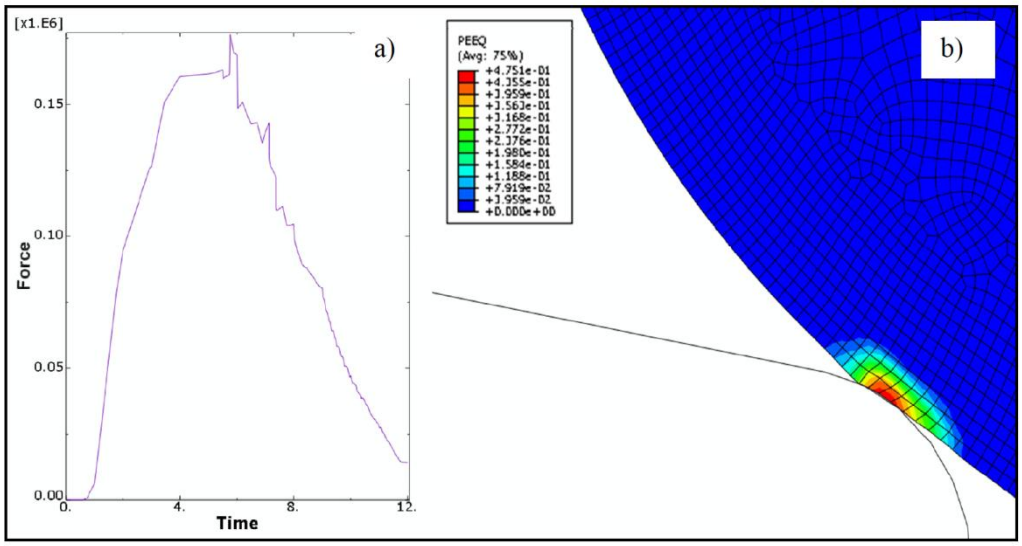

Figure 6: Results for R = 0.5 mm, μ = 0.3, free mesh, high mesh density a) graph of axial load during failure, b) detailed view of position of flange at axial load.

In both cases mentioned above the peak axial load capacity occurs before the flange starts to slide. This shows that as soon as plastic deformation starts in the V-band material, as shown in Figure 5b the ultimate axial load capacity has been reached. This phenomenon has also been seen for models with R = 0.5 mm and μ = 0.

3.2. Plastic Strain

In this section the effect of element thickness along the contact sliding surface of the V-section band clamp on the development of plastic strain in the band clamp will be analysed, for a model with R = 0.3 mm and μ = 0.3. Unlike the models for R = 0.5 mm these models generated many more problems. Figure 7 identifies the position on the contacting surface of the maximum plastic strain ε_{ps}. These values are shown in Figure 8. The two graphs show that the maximum plastic strain increases as the element size decreases. This is due to the one integration point of the reduced integrated linear elements getting closer to the contacting surface, giving much more accurate results. The two meshing methodologies can be seen to give very similar results.

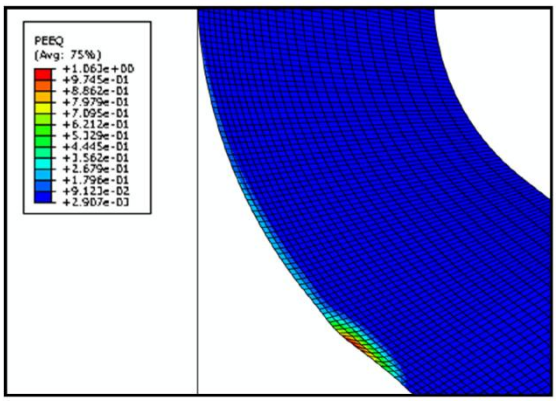

Figure 7: Plastic strain development at contact surface.

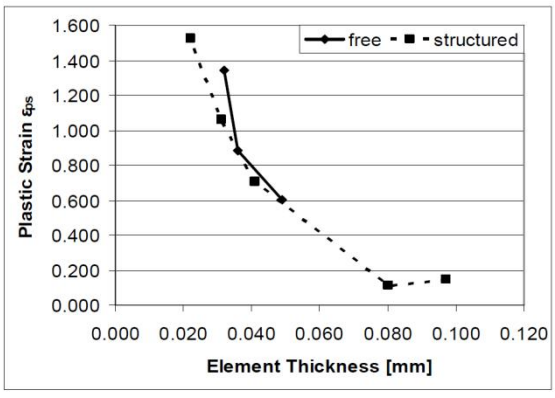

Figure 8: Maximum plastic strain along contact sliding surface for free and structured mesh for R = 0.3 mm and μ = 0.3.

The peak plastic strain described above is only of academic interest as it is not responsible for ultimate failure of the band. Figure 9 identifies the point on the band where large plastic strains ε_{pr} will lead to substantial band deformations and hence joint failure. This point stays the same for all models used in this analysis work and as shown in industrial applications of band clamps [12], is very likely to be in the region where a crack through the whole thickness of the band clamps starts to develop. Although the two graphs in Figure 10 seem to differ slightly, they still indicate the same tendency of plastic strain development. Again the plastic strain increases as the element size in this region has been reduced. The results for the structured mesh seems to be slightly more reliable because the element thickness along the whole inside of the band clamp was reduced whereas for the free mesh only the element size along the contact surface was decreased.

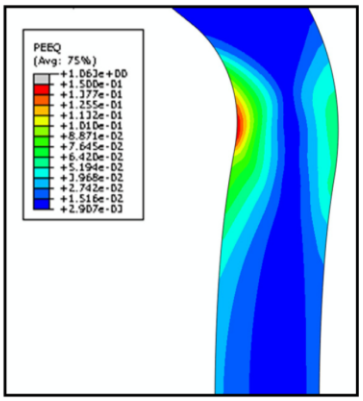

Figure 9: Position of maximum plastic strain sampling point for Figure 10

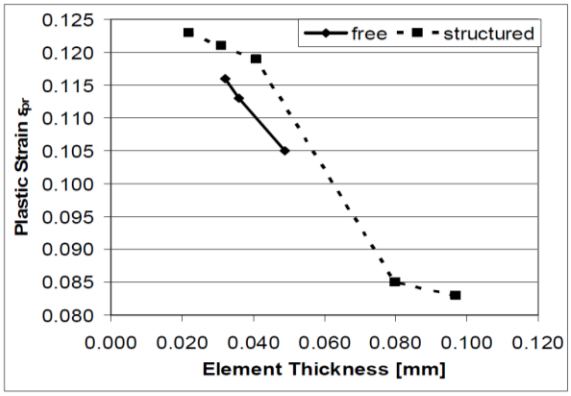

Figure 10 Maximum plastic strain taken from end point of radius for R = 0.3 mm and μ = 0.3.

4. Comparison of Explicit and Implicit Analysis

In this section the analyses for contact edge radii R = 0.1, 0.3 and 0.5 mm along with coefficients of friction μ = 0, 0.15 and 0.3, with a flange diameter D_f = 111 mm will be discussed and compared. The analyses were each solved using explicit and implicit solvers. The time periods for applying load were taken from an initial frequency analysis of the band where the first natural frequency f_n was predicted to be about 6850 cyc/time. The corresponding time period was t_n = 0.000146 sec, which in this paper is referred to as normal time. Time periods ten and fifty times slower (t_{10} = 0.00146 sec and t_{50} = 0.0073 sec) were also used.

4.1. Explicit Analysis Mesh Structure

Figures 11a and b show models that have reached the full failure state having the two extreme cases of very small radius R = 0.1mm combined with a very high coefficient of friction μ = 0.3, and a model with a relatively large radius R = 0.5mm and μ = 0.3, using an explicit solver. As can be seen in a) the small radius and high friction create a large distortion of the elements along the contact surface of the band clamp generating large plastic strain ε_{ps} = 180 whereas in b) the contact surface seems to be deformed as expected with a maximum plastic strain of ε_{ps} = 0.934, which seems very much more realistic. This demonstrates that the reliability and accuracy of the explicit analyses is highly dependent on the contact edge radius. During this analysis work it has been experienced that a higher edge radius R results in a more stable solution giving more realistic results.

As can be seen in Figure 12a and b also the coefficient of friction has a significant influence to the accuracy of the results. Figure 12b indicates that for the same contact edge radius R = 0.3 the higher coefficient of friction μ = 0.3 results in significantly deforming the elements along the contact surface and giving too large plastic strain results.

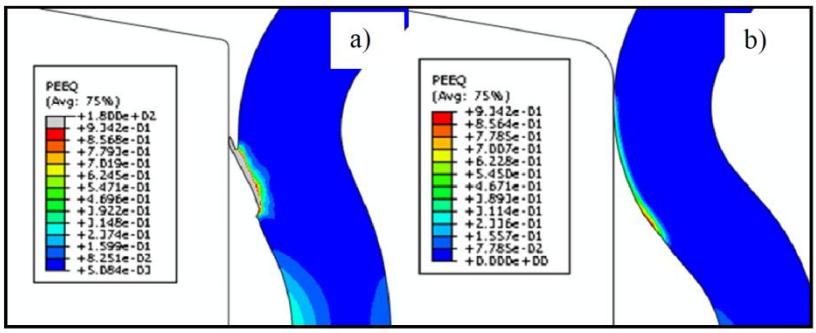

Figure 11: Full failure state using explicit solver and free mesh, 10 times slower a) R=0.1 mm μ = 0.3 and b) R = 0.5 mm μ = 0.3

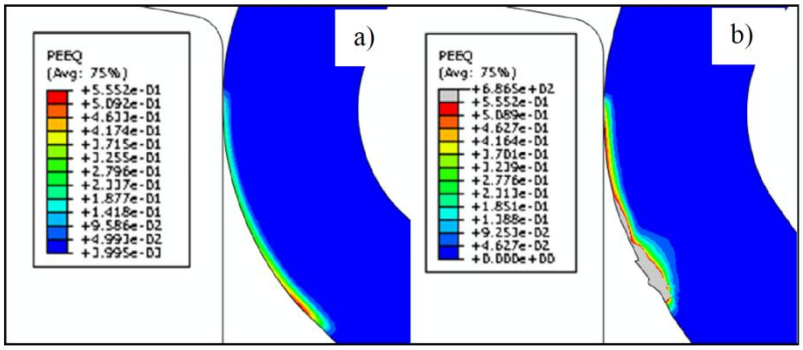

Figure 12: Model of V-section band clamp reached full failure mode using explicit solver for free mesh, 50 times slower a) R = 0.3 mm μ = 0 and b) R = 0.3 mm μ = 0.3

Several explicit analyses have shown that the type of mesh had only a slight effect on the accuracy of the results. Comparing the maximum plastic strain values along the contact surface of two explicit models, the strain values are nearly the same for both. This proofs that the mesh type does have almost no effect for a time t_{10} on the accuracy of the results generated.

As obtained in this subsection the results for contact in an explicit analysis highly depend on the radius of the rigid master surface (flange), the coefficient of friction, whereas the mesh type has no significant influence.

4.2. CPU (Run) Time

All analyses using an implicit solver and a free mesh were always running faster than their explicit counterpart which was set to run 10 times slower. Moreover the run time for the explicit solver increases as the mesh was changed from free to structured. This increase was due to an increase of elements as for the free mesh only the elements along the sliding surface were kept small and getting bigger the more they were away from this surface and for the structured mesh all elements in the model were kept the same size as at the contacting surface.

4.3. Reliability of Results

In Table 1 all explicit and implicit results for the models with a flange diameter $D_f = 111$ mm are compared, for contact edge radius R = 0.5 mm, all possible coefficients of friction and 10 times slower for the explicit.

As stated in the subsection before the CPU time increases a lot as the mesh density gets finer but comparing the results for ε_{pr} to the implicit results there is no significant difference. The results obtained here along with the results from both subsections before support the knowledge of the accuracy and reliability increasing as the coefficient of friction decreases and the contact edge radius R increases. The mesh type for explicit analyses has only a slight influence on accuracy but significantly increases the CPU time.

Table 1: Comparison of implicit and explicit solver for flange diameter D_f = 111 mm.

Contact Edge Radius R [mm]	Coefficient of Friction μ	Max. Plastic Strain at Corner End ε_{pr}	Mesh Type	Load Time (only for Explicit)	Solver Type	CPU (Run) Time [min]
0.5	0.3	0.1381	free	---	Implicit	9.0
0.5	0.3	0.1512	free	10	Explicit	19.0
0.5	0.3	0.1519	structured	10	Explicit	32.0
0.5	0.15	0.1021	free	---	Implicit	9.5
0.5	0.15	0.1182	free	10	Explicit	14.0
0.5	0.15	0.1183	structured	10	Explicit	31.0
0.5	0	0.0773	free	---	Implicit	9.2
0.5	0	0.0804	free	10	Explicit	14.0
0.5	0	0.0812	structured	10	Explicit	30.0

5. Conclusion

In this paper a model capable of predicting the ultimate axial load capacity and structural deformation of V-band Clamps using finite element analysis has been generated. It has been shown that the accuracy of analyses using implicit and explicit solver were highly depending on the contact edge radius R. Moreover the coefficient of friction μ had a significant influence on the stability of implicit analyses. Using explicit or implicit solver for contact analysis the contacting radius should be smooth enough. The accuracy of the results also depended on the element size and amount of elements along the sliding contact surface. Moreover the results were found to be depending on the type of mesh.

6. Further Work

The work presented in this paper has provided an understanding of how a model should be set up to investigate the ultimate axial load capacity of V-section band clamps. In further work the model should be improved to predict the interplay of elastic and plastic deformation mode, taking into account the influence of several V-band diameters.

References

[1] Shoghi K 2003 Stress and Strain Analysis of flat and V-section band clamps *PhD Thesis* Huddersfield

[2] NASA 2000 *Marman clamp system design guidelines*. Guideline GD-ED-2214, Goddard Space Flight Centre

[3] Shoghi K, Barrans S M, Rao H V 2004 Stress in V-section band clamps *Proceedings of the Institution of Mechanical Engineers* **218** 251-261

[4] Shoghi K, Barrans S M, Rao, H. V. 2003 Classical and finite element analysis of V-band retainers *NAFEMS World Congress* (Orlando Florida)

[5] Shoghi K, Barrans S M, Ramasamy P 2006 Axial load capacity of V-section band clamp joints *8th International Conference on Turbochargers and Turbocharging* (London) pp273-285

[6] Dassault Systemes 2007 Getting Started with Abaqus, v6.7 Section 12.4

[7] Konter A 2000 *How to Undertake a Contact and Friction Analysis* (Glasgow: NAFEMS) p 12

[8] Konter A 2005 *Advanced Finite Element Contact Benchmarks* (Glasgow: NAFEMS) p 19

[9] Dixit P M and Dixit U S 2008 *Modeling of Metal Forming and Machining Processes by Finite Element and Soft Computing Methods* (London: Springer) p 101

[10] Meyers M A and Chawla K K 1999 *Mechanical Behavior of Materials* (London: Prentice-Hall International UK Ltd) p 116

[11] Getting Started with Abaqus 2007 v6.7 Section 12.4 Dassault Systemes

[12] Brown I 10-12-2008 Teconnex Ltd. Keighley UK personal conversation

School of Computing and Engineering Researchers' Conference, University of Huddersfield, Dec 2009

Ultimate Axial Load Capacity of V-Band Clamp Joints

M. Muller[1] and S. M. Barrans[1]
1 Centre for Precision Technologies, University of Huddersfield, Queensgate, Huddersfield HD1 3DH, UK

ABSTRACT

Band clamps with a flat bottomed V-section are used to connect a pair of circular flanges to provide a joint with significant axial strength. Despite the wide application of V-band clamps, their behaviour is not fully understood and the ultimate axial strength is currently only available from physical testing. This physical testing has indicated that the ultimate strength is determined by two different types of structural deformation, an elastic deformation mode and a plastic deformation mode. Initial finite element analysis work has demonstrated that analysis of this class of problem is not straightforward. This paper discusses the difficulties encountered when simulating this type of component interaction where contact is highly localised and contact pressures are high and therefore presents a finite element model to predict the ultimate axial load capacity of V-band clamps.

Keywords V-band retainer, plasticity, finite element analysis, cold roll forming

1 INTRODUCTION

V-section band clamps are used in a wide range of applications in the aerospace and automotive industries. As stated by Shoghi (2003) they were invented during the Second World War by the Marmon Corporation and are nowadays used to connect together the housings of diesel engine turbochargers and as stated by NASA (2000) to assemble satellites to their launching device. The process of assembling V-band clamps to a pair of circular flanges has recently been investigated using classical analysis by Shoghi et al. (2004), finite element analysis by Shoghi et al. (2003) and experimental validations by Shoghi et al. (2006).
Figure 1 shows a V-band clamp assembled to a pair of flanges in an experimental test rig. These band clamps are assembled by placing them loosely around the flanges, and then tightening the T-bolt nut. The band will then lessen its diameter and apply a radial load. Due to the V-shape of the section and the wedging action this radial load then generates an axial load, pressing both flanges together. Despite their wide application, once assembled to a pair of flanges little is known about the interaction between flange and band. Moreover the failure mode of V-band clamps when undergoing an axial load is not fully understood. Work has therefore been initiated to generate a finite element model able to predict the ultimate axial load capacity and deformation of V-band clamps.

2 PREDICTION OF THE ULTIMATE AXIAL LOAD CAPACITY

Theses band clamps are made of AISI 304 austenitic stainless steel quarter hard with a Young's Modulus of 227GPa, a Poisson's ratio of 0.29, a yield strength (0.2% offset) of 648MPa and an ultimate tensile strength of 857MPa, as mentioned in Shoghi (2003). In the FE analyses the material was assumed to be elastic-plastic with linear hardening, as described by Dixit and Dixit (2008). ABAQUS requires all material properties to be added as true stress and strain values so equations (1), (2) and (3) were used to convert the engineering values of the Yield point and the Ultimate tensile strength into true values, as demonstrated by Meyers and Chawla (1999) and Teherani et al. (2006).
In these equations σ_e and ε_e represent the engineering stress and strain values and σ_t and ε_t represent the true stress and strain values.

$$\sigma_t = \sigma_e(1+\varepsilon_e) \quad (1)$$

$$\varepsilon_t = \ln(1+\varepsilon_e) \quad (2)$$

$$\varepsilon_{pl} = \varepsilon_t - \varepsilon_{el} \quad (3)$$

For the finite element models described in this paper, the flange was assumed to be a rigid non deforming body, so it did not need to be meshed, and the band clamp was modelled using a solid body, for which a mesh was required. Assembling of the V-band clamp to the flanges, which in reality is done by tightening the T-bolt nut, was simulated by generating a thermal contradiction so the band clamp was shrunk onto the flanges by applying a reduction in temperature. The initial axial load generated by this procedure was set to 6 kN for all analyses. Failure of the band clamp was then simulated in ABAQUS by moving the flange in the axial direction. At the reference point RP shown in Figure 2, the resistance force of the band clamp acting against the movement of the flange was reported. The highest value of this resistance force represents the ultimate axial load (UALC). As the set up of this V-band joint simulation is a purely symmetrical problem, only one half of the clamp joint was modelled using a 2 dimensional axisymmetric model, in which only one flange was used, along with half a side of the band clamp section. For this half modelled band a boundary condition (BC) was applied to its symmetry plane, so any movement of the clamp in the axial direction was prevented, see Figure 2.

Using the commercial finite element program ABAQUS, initial numerical contact analyses have shown that the problem associated with these analyses is the flange sliding over the V-band clamp, as observed by Barrans and Muller (2009). In real application the contact radius R is usually up to 0.8mm when clamping together housings for turbocharger, whereas for the finite element work presented in this paper the contact radius R was chosen to be 0.5mm, as this is a radius which is a good average for all radii used. The flange angle γ was set to be 20° to match the angle of the V-section, along with the flange thickness t_f to be 4.5mm as suggested by Brown (2009).

Initial finite element analyses by Barrans and Muller (2009) have shown that the ultimate axial load capacity (UALC) highly depended on the diameter of the V-band clamp. As Figure 3 shows, assuming no friction at the contact area between the flanges and the band clamp, the UALC increases for small diameters up to 250mm and then starts to decrease again. It should be noted at this point that for the range of diameters shown in Figure 3 the cross section of the V-band clamp remains unchanged.

This behaviour has further been investigated in more detail by analysing the elastic-plastic failure mode of the clamp. Figure 4 shows that for smaller diameters e.g. 55mm the V-band deforms highly plastically with the V-section being bent so its behaviour was as that of a cantilever, whereas band clamps with large diameters e.g. 1500mm tend to deform only elastically and the V-section does not change its shape, but it deforms in the radial direction. This behaviour for large diameters is due to the cross section area being the same as for smaller diameters but more material exists in the circumferential. This problem is not straightforward as the failure mode is made of a mixture of the change from plastic-elastic deformation to purely elastically, and the deformation by bending the V-section or deforming strictly in the radial and circumferential direction without bending of the V-section. This is therefore important as the axial load must exceed the yield strength to deform a band clamp with a small diameter so it deforms mainly plastic and partially elastic. For larger diameters the axial load leading to failure of the joint can be below the yield strength so less force is needed to fail a joint than for smaller diameters.

Moreover these finite element predictions showed a high concentration of plastic strain on the inside of the flat section, next to the inner radius, as can be seen in Figure 5. This is obviously due to bending of the V-section as it happens for smaller band clamps. Keeping in mind that these analyses were purely static applying a single large force, this concentration occurred immediately after applying the load. In real turbocharger application it is very likely that over a long period of time smaller loads may occur regularly, which lead to smaller strain and stress concentrations. After such a dynamic loading even smaller stress and strain concentration can get higher values after a certain amount of time. Such a concentration could lessen the thickness of the flat section of the band. As it is well understood in literature and is frequently demonstrated at easy tensile tests, this lessen can lead to failure of a material by lessening the thickness even more and reducing the strength of the band clamp or it could even lead to small micro-cracks, which, lead to crack growth.

3 EXPERIMENTAL RESULTS

Experimental tests have been carried out in order to validate the finite element work. V-band clamps have therefore been assembled to a circular pair of flanges which were mounted in an Instron tensile test machine. The experiments were carried out in the same way as the numerical work. After assembling the band camps to the flanges, the flanges were then separated until the band clamp flipped over the flanges and hence failure of the whole joint occurred. The axial load created because of this separation was reported and the peak value of this force was shown to be the ultimate axial

load capacity (UALC). All experiments were carried out with V-band clamps with a diameter of 114 mm.
Figure 6 shows the UALC for a series of eight tests that were carried out. The values lie all in a range from 68 kN to 81 kN, which gives an average of 75.5 kN. Comparing these to the numerical value ca.68 kN shown in Figure 2, it can be seen that the experimental values are slightly higher because the contact area in finite element model was assumed to be frictionless whereas in the experiments a certain amount of friction always exists, even after lubricants were applied.
The crack theory with the concentration of plastic strain in Figure 5 can be proven to be correct as well. After investigating V-band clamps used at a diesel engine turbocharger in real application which failed because of a turbocharger burst, the band clamp in Figure 7 clearly shows a crack in the region as predicted before by the finite element model.

4 CONCLUSION

In this paper a finite element model able to predict UALC of V-band clamp joints has been developed and the problems associated with this type of analyses have been investigated.
It was shown that the ultimate axial load capacity highly depends on the flange/V-band diameter, because of the complex plastic-elastic failure mode. The numerical and experimental values for the UALC correlated very well.
The finite element prediction showed high concentrations of plastic strain at the edge of the flat section. It was shown that a crack occurred at V-band clamps mounted to turbochargers for diesel engines as the joint failed. This crack occurred in the flat section in the same region as the finite element model prediction high strain concentrations.

5 REFERENCES

Shoghi K (2003) Stress and Strain Analysis of flat and V-section band clamps *PhD Thesis* Huddersfield

NASA (2000) *Marman clamp system design guidelines*. Guideline GD-ED-2214, Goddard Space Flight Centre

Shoghi K, Barrans S M, Rao H V (2004) Stress in V-section band clamps *Proceedings of the Institution of Mechanical Engineers* **218** 251-261

Shoghi K, Barrans S M, Rao, H. V. (2003) Classical and finite element analysis of V-band retainers *NAFEMS World Congress* (Orlando Florida)

Shoghi K, Barrans S M, Ramasamy P (2006) Axial load capacity of V-section band clamp joints *8th International Conference on Turbochargers and Turbocharging* (London) pp273-285

Dixit, P.M. and U.S. Dixit, *Modeling of Metal Forming and Machining Processes by Finite Element and Soft Computing Methods*. 2008, London: Springer. p 101.

Meyers, M.A. and K.K. Chawla, *Mechanical Behavior of Materials*. 1999, London: Prentice-Hall International (UK) Ltd.

Tehrani, M.S., et al., *Localised edge buckling in cold roll-forming of symmetric channel section.* Thin-walled structures, 2006. **44**: p. 184-196.

Barrans, S.M. and M. Muller, *Finite element prediction of the ultimate axial load capacity of V-section band clamps*, in *7th International Conference on Modern Practice in Stress and Vibration Analysis*. 2009: Cambridge.

Brown, I. 11-05-2009, Teconnex Ltd.: Keighley.

School of Computing and Engineering Researchers' Conference, University of Huddersfield, Dec 2009

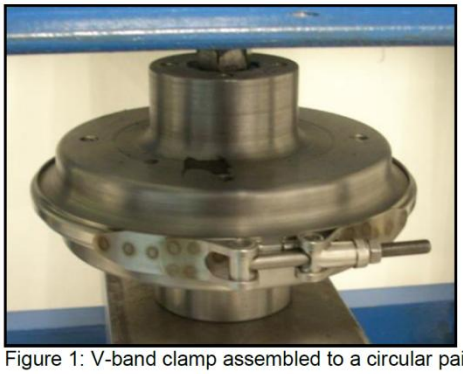

Figure 1: V-band clamp assembled to a circular pair of test flanges, taken from Barrans and Muller (2009)

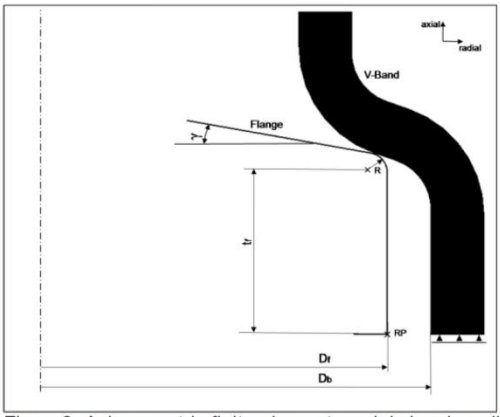

Figure2: Axisymmetric finite element model showing all geometrical parameters, taken from Barrans and Muller (2009)

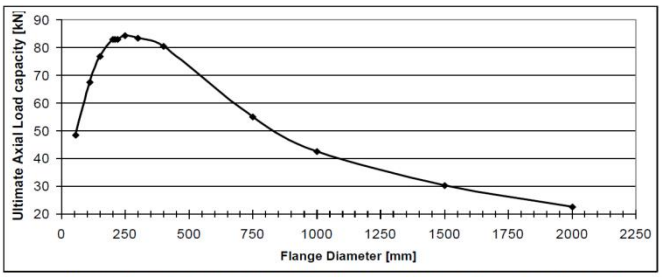

Figure 3: Predicted dependency of UALC on flange diameter, taken from Barrans and Muller (2009)

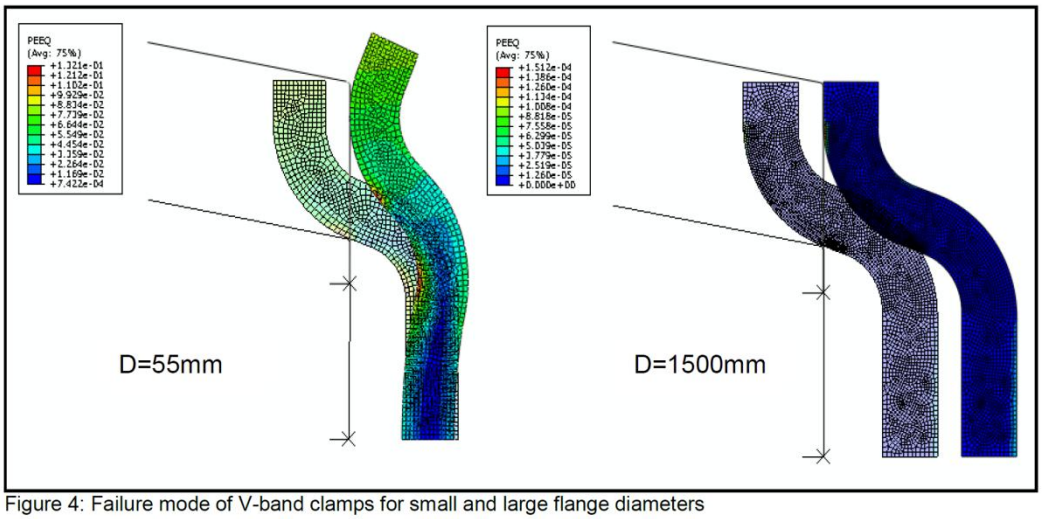

Figure 4: Failure mode of V-band clamps for small and large flange diameters

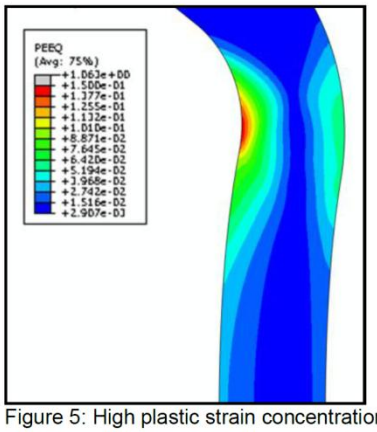

Figure 5: High plastic strain concentration at flat section of V-band clamp

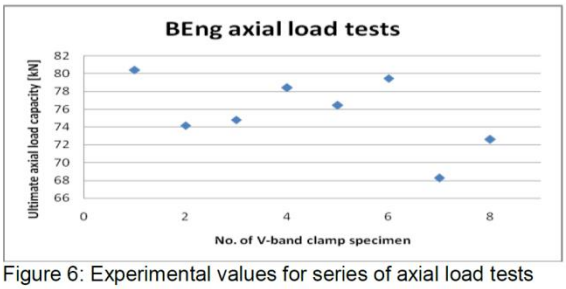

Figure 6: Experimental values for series of axial load tests

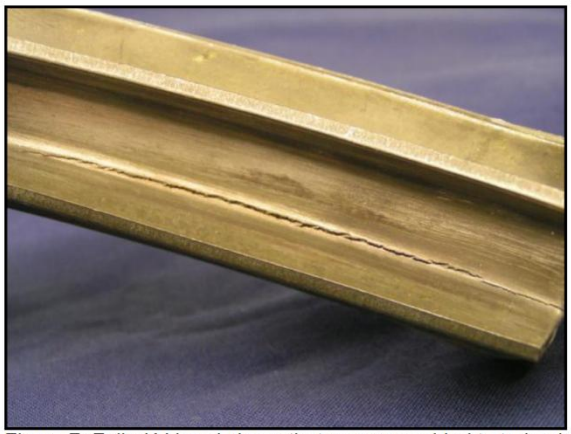

Figure 7: Failed V-band clamp that was assembled to turbocharger for a diesel engine

Impact of flange geometry on the ultimate axial load capacity of V-band clamps

M. Muller, S.M. Barrans
School of Computing and Engineering, University of Huddersfield, UK.

ABSTRACT

Modern turbochargers typically comprise a body in three parts; the turbine and compressor housings and the bearing housing. The preferred method of joining these three parts, in automotive applications, is to use a band clamp with a flat bottomed V-shaped cross section mating with appropriate flanges on the body sections. This method of clamping allows for rapid assembly and infinitely variable relative rotational orientation of the body parts. In this paper finite element analyses are carried out to predict the influence of different flange geometries to the ultimate axial load capacity (UALC), which show a significant dependency on the flange thickness.

1 INTRODUCTION

V-band clamps are widely used in automotive, aircraft and aerospace industries to connect a pair of circular flanges to provide a joint with good axial strength and torsional rigidity. The band clamps this paper focuses on are mainly used to connect together housings of turbochargers for diesel engines. During the assembly process a V-band clamp is first loosely placed around the flanges, after that the T-bolt nut (Figure 1) is tightened. This leads to a radial force being generated in the band clamp, and, due to the V-section of the band this results in the creation of an axial load. This axial load then pushes the flanges together.

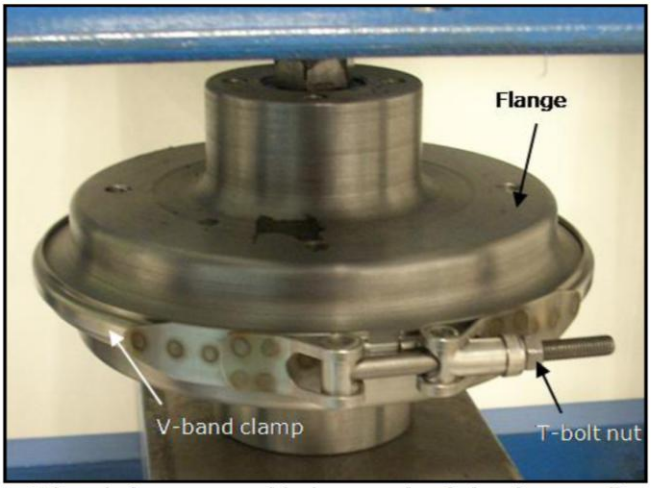

Figure 1: V-band clamp assembled to a pair of circular test flanges [1]

Several research papers by Shoghi et al. [2], [3] and [4] have been published concerning V-band clamps. In their work Shoghi et al. [2] present a classical analysis and Shoghi et al. [3] a finite element analysis to investigate stresses generated in the V-band during the assembly process. In Shoghi et al. [4] these results were backed up with experimental data and an updated method of determining the axial load generated by an assembled V-band clamp joint was presented.

Barrans and Muller [1] have recently developed an axisymmetric finite element model able to investigate the elastic-plastic material behaviour of V-band joints as the flanges are separated by an external force. This technique therefore allows the ultimate axial load capacity of V-band joints to be predicted. It should be noted that the work reported in [1] focused on setting up the model in the commercial FEA software ABAQUS and determining the appropriate settings for finite element parameters such as solver type, mesh density and especially the contact between the flanges and the band. The study was carried out with the V-band modelled as solid body using finite elements and the flange modelled using an analytical rigid body. It was found that an inappropriate mesh density or solver type would result in highly erroneous peak loads and hence potentially incorrect predictions of the UALC.

In this paper the influence of varying flange geometry to the ultimate axial load capacity of a V-band clamp joint has been investigated using the finite element model taken from Barrans and Muller [1]. The commercial finite element analysis package ABAQUS/Standard has been used to predict the UALC and model the differences in flange geometry.

2 FINITE ELEMENT MODEL

For the finite element models analysed in this paper a flange diameter of D_f= 235 mm was taken. This is a typical diameter for the V-band clamps that are used in turbocharger applications and it was shown by Barrans and Muller [1], that a maximum UALC appears to be at a flange diameter D_f of 250 mm. 235 mm is the closest standard diameter value.

2.1 Set up of FE model

The finite element model [1] used for this simulation was assumed to be axisymmetric and the symmetry plane between two flanges made it possible to model only one side (see also Figure 2). Hence the model size could be reduced. The flange was modelled using an analytical rigid body since in many applications it will typically have a thickness many times greater than the thickness of the V-band and will therefore deform only slightly compared to the band. The use of a rigid body also dramatically reduced the analysis time. For the V-band clamp a solid body has been used. As the models include contact analyses, Dassault Systems [5] suggest the use of 2D plane strain linear elements with reduced integration for the V-band clamp, because second order elements suffer from a non uniform load distribution between mid-side and corner nodes. This element choice is also recommended by Konter [6]. Moreover unlike fully integrated linear elements, reduced integration linear elements do not suffer from shear locking which usually leads to under predicted results. The problem of hour-glassing often associated with reduced integration elements [7] is avoided by introducing a small amount of artificial "hourglass stiffness" and using a relatively fine mesh. A penalty contact algorithm was used as Konter [8] states that these tend to converge easily and also are more stable. An implicit solver was used to solve the analyses as suggested by Barrans and Muller [1], since that work showed that especially for this application, an implicit solver compared to their explicit counterparts tended to give more accurate results and need less CPU time.

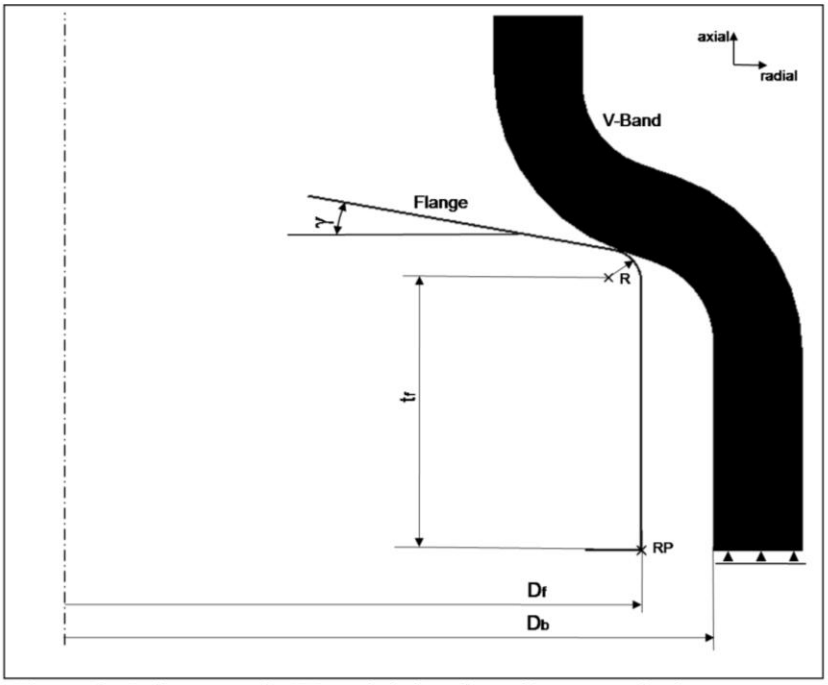

Figure 2: Axisymmetric FE model showing all geometrical parameters

In order to simulate the assembly process in which the T-bolt nut is tightened, an artificial thermal strain was generated in the band to shrink it onto the flanges. It was hereby assumed that deformation of the band and hence stresses are axisymmetric. The process of applying this thermal strain in ABAQUS/Standard is described in detail in section 2.4. A displacement boundary condition (BC) was applied at the reference point (RP in Figure 2) of the flange to prevent it from moving in the axial direction or rotating during assembly. The boundary condition needed to be applied only to the reference point as Dassault Systems [9] state that an analytical rigid body has two translational and one rotational degrees of freedom only at the reference point. As the flange is rigid, it needs to be constraint in theses three directions. A symmetry BC was applied at the symmetry plane of the V-band to prevent it from moving in the axial direction during the whole simulation. Being an analytical rigid body, the UALC can only be taken-up at the reference point RP of the flange.

2.2 Material Properties

AISI 304 stainless steel was used for the V-band clamp with a Young's Modulus of 227 GPa and a Poisson's Ratio of 0.29, which where taken from Shoghi [10]. In the FE analyses the material was assumed to be elastic-plastic with linear hardening, as described by Dixit and Dixit [11].

ABAQUS requires all material properties to be added as true stress, σ_t, and strain, ε_t, values so equations (1), (2) and (3) were used to convert the engineering values, σ_e and ε_e, of the yield point and the ultimate tensile strength into true values, as demonstrated by Meyers and Chawla [12] and Teherani et al. [13].

$$\sigma_t = \sigma_e(1+\varepsilon_e) \quad (1)$$

$$\varepsilon_t = \ln(1+\varepsilon_e) \quad (2)$$

$$\varepsilon_{pl} = \varepsilon_t - \varepsilon_{el} \quad (3)$$

According to equations (1), (2) and (3) above, the true stress σ_{ty} at the yield point was 648 MPa with no plastic strain, and the true stress σ_{tUTS} at the ultimate tensile strength was 1182.7 MPa with a true strain ε_t of 0.322 and a plastic strain ε_{pl} of 0.317. All stress and strain properties discussed above can also be seen in the stress and strain diagram representing the material model in Figure 3. In there σ_{tUTS} represents the true stress value of the ultimate tensile strength and σ_{ty} represents the true stress value at the yield point.

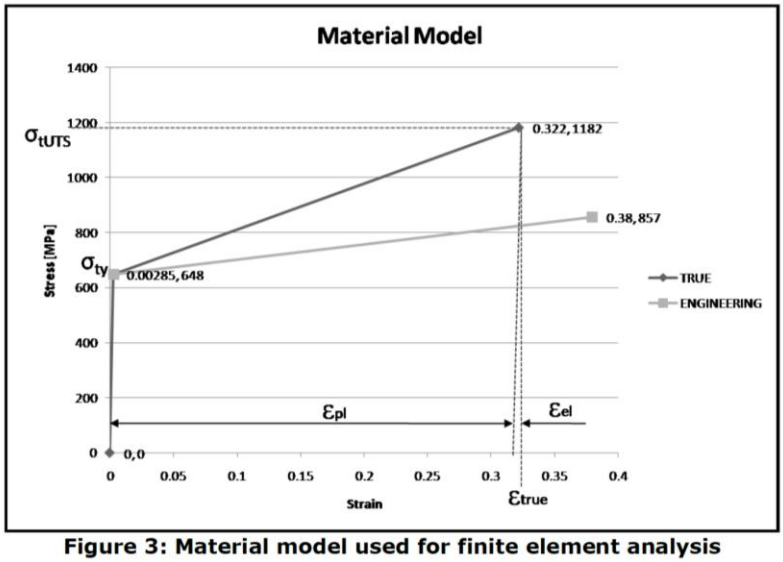

Figure 3: Material model used for finite element analysis

2.3 Flange geometry

The aim of this paper is to investigate how changes of the flange geometry affect the UALC. Therefore the three geometrical parameters of the flange angle, contact radius and thickness were chosen as variables. The flange angle, γ, usually is manufactured to fit the V-band clamp angle of 20°, [10], which was taken as the reference value. The whole range was from 18° to 22°, using steps of 1°. The contact radius R for turbocharger applications is normally 0.8 mm, as stated by Brown [14]. The range for R was from 0.6 mm to 1.0 mm. The reference value for the flange thickness t_f, as stated by Shoghi [10], was 4.5 mm with a tolerance of +2.5%. In this paper the range for tolerance was from -10% to +10%.

2.4 T-bolt load

As mentioned in section 2.1 the band clamp was shrunk onto the flange to simulate the process of tightening the T-bolt nut. The T-bolt induced load referred to in this paper is the axial load generated by the V-section pressing the flanges together as the nut is tightened. The value of this induced load in each analysis was measured using the axial reaction force at the reference point (RP) of the flange. An iterative process was required to determine the thermal load required to obtain the correct induced load for each analysis as due to the change of geometry, the contact point between flange and band clamp will change. If for example the thickness t_f is reduced, the flange will be smaller, hence the contact point will move more towards the flat part of the V-band clamp, and therefore reducing the gap between flange diameter D_f and band clamp diameter D_b (also see Figure 2). The band will therefore have to be shrunk further to generate the required induced load. For all analyses the induced load was set to 6kN taken from Shoghi et al. [4].

2.5 Mesh

In the finite element analyses structured meshes were used because Barrans and Muller [1] showed that with structured meshes the contact analysis for this model is more stable and has fewer convergence problems than with free meshes. A relatively coarse mesh was used to model the V-band clamp. As initial finite element analyses have shown the mesh density does have a significant influence on the prediction of the plastic strain (PEEQ), as the coarse mesh under-predicts the plastic deformation at the initial contact point by about three times. However as this paper focuses on the overall deformation of the band section and not on deformations at the contact point, this highly localised plastic strain distribution can be ignored. A typical mesh density chosen for the finite element model can be seen in Figure 4 and Figure 5, both showing the undeformed case before the V-band clamp is assembled to the flanges, as well as the deformed case once full load is applied and

the joint has failed. Figure 4 also shows the equivalent plastic strain (PEEQ) and Figure 5 the von Mises stress for the fully loaded and deformed case. The thickness of elements on the inner surface of the band clamp is 0.082mm, which with a band clamp thickness of 1.2mm, gives a ratio of 0.068.

The values for UALC on the other hand differ only slightly with different mesh densities, e.g. for varying structured mesh densities the range for UALC was from 156 kN to 162 kN and for free meshes the range was 151 kN to 177 kN, considering that the element size at the contact area was the same for both kinds of meshes. Analyses using different mesh densities have shown that for a relatively coarse mesh compared to a fine mesh the UALC values only differ by a maximum of 2%. Moreover coarse mesh densities require less solver time.

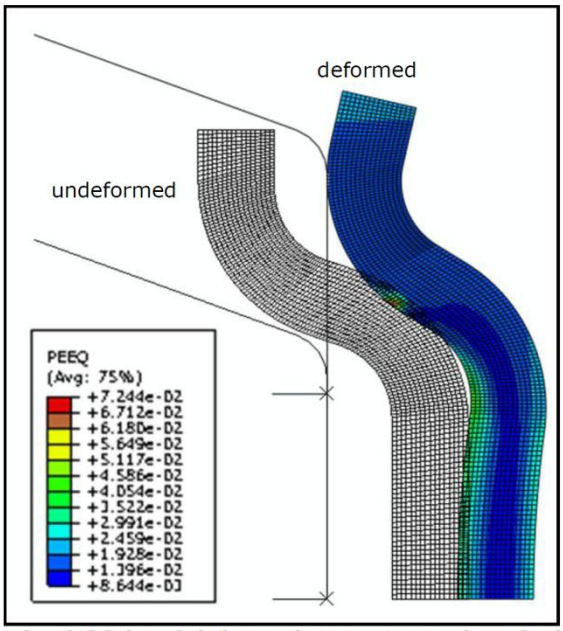

Figure 4: FE model showing initial and deformed geometry and equivalent plastic strain PEEQ

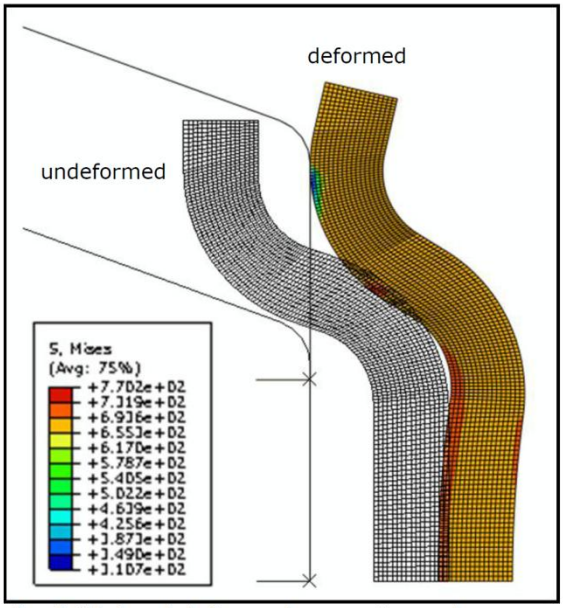

Figure 5: FE model showing initial and deformed geometry and corresponding von Mises stress

3 RESULTS

It can be seen in Figure 3 that the deformation of the V-band combines two modes. The first is an overall increase in the band diameter. The second is a bending of the V-band cross section. The presence of significant plastic strain only on the inner and outer surfaces of the band indicates that the bending mode is principally responsible for the stresses generated. However, it is clear that both deformation modes will have an impact on the UALC.

As the trend in Figure 6 shows, the UALC is highly dependent on the flange thickness t_f. It can be seen that the UALC drops as the flange gets thicker. Considering Figure 2 this is due to the flange contact point moving to the foot of the band section and hence increasing the lever responsible for bending the back of the section.

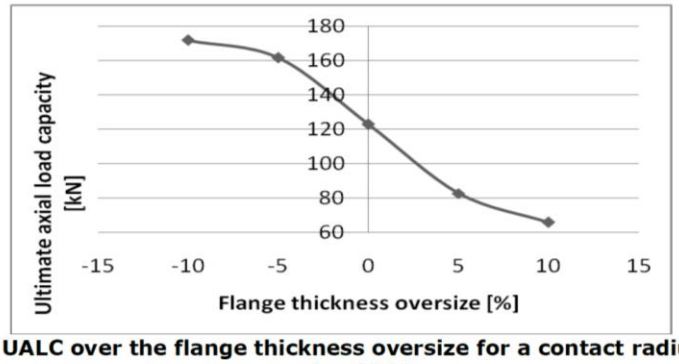

Figure 6: Predicted UALC over the flange thickness oversize for a contact radius of 0.8mm and an angle of 20°

Figure 7 shows the dependency of the UALC on the flange radius R. Although the influence of the radius is rather small compared to the flange thickness, it can be seen in Figure 7 that the UALC slightly drops for smaller flange thicknesses (-10% oversize) as the radius increases, stays the same for no oversize (0%), and increases for thicker flanges (+10% oversize).

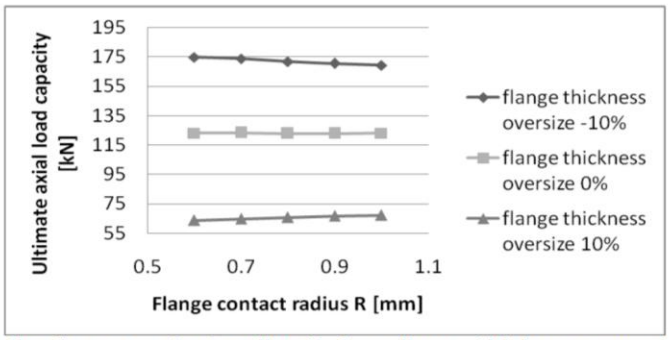

Figure 7: UALC over the flange contact radius R, for a flange thickness oversize of -10%, 0% and 10% and an angle of 20°

For a contact radius R of 0.6 mm, and several different flange thicknesses t_f, the graphs in Figure 8 show a minor dependency of the UALC on the flange angle γ. For all three thicknesses with oversize from 10% to -10%, the UALC drops as the flange angle γ increases. For these analyses only the flange angle changed but the angle of the band clamps V-section remained at 20°. This minor drop is due to the flange angle getting larger and hence the contact point moving away from the back of the section towards the flange legs. This again increases the lever and leads to less force being necessary to deform the band section.

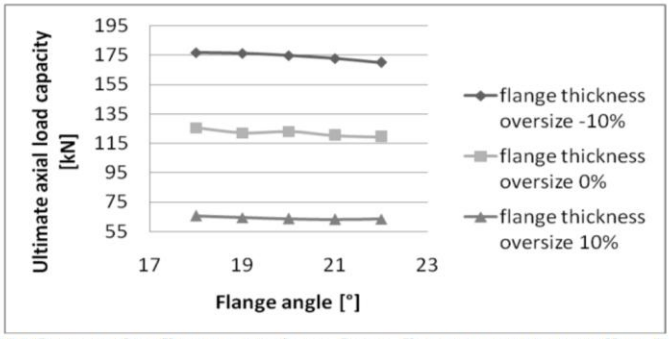

Figure 8: Predicted UALC over the flange angle γ, for a flange contact radius R=0.6mm and varying flange thickness oversize

Initial experimental validation of the finite element analysis methodology was obtained by investigating models with a flange diameter D_f of 112 mm. The results of the finite element analyses are shown in Figure 9 and show the same tendency as band clamps with a diameter D_f of 235 mm in Figure 10. Previous experimental work by Muller [15] produced the UALC values shown in Figure 10. Whilst there is significant scatter in the experimental results and the precise band geometry was not controlled, the results are within the range predicted by the finite element analysis (for D_f=112 mm).

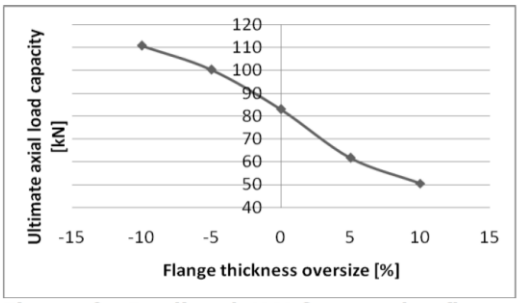

Figure 9: Predicted UALC over the flange thickness oversize, for a contact radius of R=0.8mm and an angle of 20°

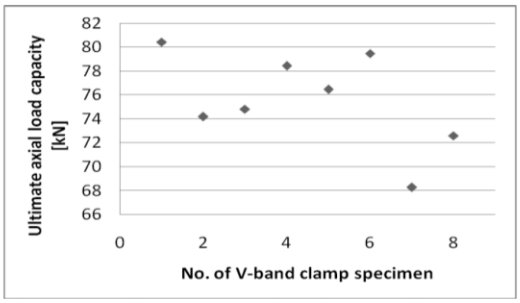

Figure 10: Determined UALC over specimens used in experimental tests on a tensile machine, Df=112mm

4 CONCLUSION AND FURTHER WORK

In this paper the influence of a number of geometrical parameters of flanges on the ultimate axial load capacity (UALC) of a V-band joint has been investigated. Using finite element analysis it was found that the thickness of the flange has the greatest influence and significantly reduces UALC as the flange gets thicker. The flange angle and contact radius only play a minor role in changing the UALC of a V-band joint.

Further work should now focus on investigating the influence of the geometrical parameters of the V-band clamp itself to the UALC. It was also noted that failure of the V-band joint was due to two effects: extension of the overall band circumference and bending of the band cross section. Further work should therefore be extended over a wide range of flange diameters to investigate the influence of these modes of failure. Additional experimental validation of the finite element work should also be established by testing bands with a range of diameters and measured geometry.

Moreover this numerical work assumed axisymmteric deformation and stresses in the V-band clamp, but in real applying deformation and stresses in the circumference do not distribute uniformly. Further work should focus on replacing the 2 dimensional model with a 3 dimensional, and investigate deformation and stresses in the circumference.

REFERENCES

1. Barrans, S.M. and M. Muller, *Finite element prediction of the ultimate axial load capacity of V-section band clamps*, in *7th International Conference on Modern Practice in Stress and Vibration Analysis*. 2009: Cambridge.
2. Shoghi, K., S.M. Barrans, and H.V. Rao. *Stress in V-section band clamps*. in *Proceedings of the Institution of Mechanical Engineers*. 2004.
3. Shoghi, K., S.M. Barrans, and H.V. Rao, *Classical and finite element analysis of V-band retainers*, in *NAFEMS World Congress*. 2003: (Orlando) Florida.
4. Shoghi, K., S.M. Barrans, and P. Ramasamy. *Axial load capacity of V-section band clamp joints*. in *8th International Conference on Turbochargers and Turbocharging* 2006. London.
5. Dassault-Systems, *Getting Started with ABAQUS v6.7 Section 12 Contact.* 2007.
6. Konter, A. *How to undertake a Contact and Friction Analysis*. in *NAFEMS*. 2000. Glasgow.
7. Dassault-Systems, *Getting Started with ABAQUS v6.7 Section 4 Using Continuum Elements.* 2007.
8. Konter, A., *Advanced Finite Element Contact Benchmarks*, in *NAFEMS*. 2005: Glasgow.
9. Dassault-Systems, *Getting Started with ABAQUS v6.7 Section 3.* 2007.
10. Shoghi, K., *Stress and Strain Analysis of flat and V-section band clamps*. 2003, University of Huddersfield: Huddersfield.
11. Dixit, P.M. and U.S. Dixit, *Modeling of Metal Forming and Machining Processes by Finite Element and Soft Computing Methods*. 2008, London: Springer. p 101.
12. Meyers, M.A. and K.K. Chawla, *Mechanical Behavior of Materials*. 1999, London: Prentice-Hall International (UK) Ltd.
13. Tehrani, M.S., et al., *Localised edge buckling in cold roll-forming of symmetric channel section.* Thin-walled structures, 2006. **44**: p. 184-196.
14. Brown, I. 11-05-2009, Teconnex Ltd.: Keighley.
15. Muller, M., *Ultimate Tensile Strength of V-Band Connectors*, in *School of Computing and Engineering*. 2007, University of Huddersfield: Huddersfield.

School of Computing and Engineering Researchers' Conference, University of Huddersfield, Dec 2010

PREDICTING AND DETERMINING OF CONTACT PRESSURE DISTRIBUTION IN JOINTS FORMED BY V-BAND CLAMPS

M. Muller, S.M. Barrans
University of Huddersfield, Queensgate, Huddersfield HD1 3DH, UK

ABSTRACT

V-band clamps are utilised in a wide range of industries to connect together a pair of circular flanges, for ducts, pipes, turbocharger housings and even to form a joint between satellites and their delivery vehicle. In this paper, using a previously developed axisymmetric finite element model, the impact of contact pressure on the contact surface of the V-band clamp was studied and surface roughness measurements were used to investigate the distribution of contact pressure around the circumference of the V-band.

Keywords: V-band clamp, finite element model, surface roughness, contact analysis

1 INTRODUCTION

Focussing on elastic deformation during the assembling of V-band clamps, Shoghi et al. (2003) and Shoghi et al. (2004) have recently generated finite element models and a classical analysis investigating this process, which where validated by experimental tests of Shoghi et al. (2006). This work then led to recently published research by Barrans and Muller (2009) presenting an axisymmetric finite element model which analysed the failure mechanism of V-band joints, proving that the ultimate axial load capacity, was dependent on the clamp diameter. Based on their work, Muller and Barrans (2009) showed that during failure of a V-band joint for small clamp diameters the cross section deformed plastically into a non recovering state, whereas towards larger diameters a pure elastic deformation could be noticed. As in real turbocharger applications cracks are very likely to occur on the inside surface close to where the V-band was bent due to the roll forming process. In the same area, their finite element model analysed a high concentration of plastic strain while failing of the V-band joint occurred. With the same FE model the impact of flange geometry could be analysed and it was found by Muller and Barrans (2010) that the flange thickness in the contact area had the highest influence on the ultimate axial load capacity, drawing attention to the importance of manufacturing tolerances to be taken into account when designing such a joint. For all analytical or numerical models presented previously, the contact pressure between the flanges and the V-band clamp was assumed to be uniformly distributed, although especially Shoghi et al. (2006) pointed out that this was a temporary assumption, because the V-band joint can be expected to have a non-uniform pressure distribution.

2 FINITE ELEMENT MODEL

Details about the set up of the finite element model can be taken from Muller and Barrans (2009), and is also shown in Figure 1. For the material, properties for AISI 304 stainless steel were taken from Shoghi et al. (2003), in which the Young's Modulus is of 227MPa and the Poisson's Ratio is 0.29. The finite element package ABAQUS (v6.8) was employed to carry out the numerical analysis, which requires all stresses and strains to be given as true values, so the yield stress $\sigma_y$was set to 648MPa and the true tensile strength $\sigma_{tUTS}$to 1182.7MPa. The finite element model presented in here simulates a joint with a diameter of 235mm. As in this paper the impact of the contact pressure on the contact surface was studied the finite element model was set up to model the assembling and removing of the V-band clamp. The V-band is assembled by tightening the T-bolt nut with a certain Torque T_w, which generates a force F_β in the T-bolt and the radial direction of the V-band. Due to the wedging action of the V-section, this radial force generates the axial clamping load F_{ac}, pushing the flanges together. All of these three forces can be calculated using equations (1) to (4), in which equation (3) is a modification of (3).

$$R_m = \left[\frac{d_1+d_2}{4}\right] \quad (1)$$

d_1 = inside diameter of the nut bearing surface

d_2 = outside diameter of the nut bearing surface
d_p = pitch diameter of the bolt
R_m = mean radius of the fastener under-head bearing surface

$$T_w = F_\beta \left[\frac{d_p}{2}\tan(\alpha_h + \lambda) + \mu_h R_m\right] \quad (2)$$

F_β = clamping load in the T-bolt
T_w = torque applied to the T-bolt
α_h = helix angle
μ_h = underhead coefficient of friction
λ = coefficient of friction of threads

$$F_\beta = \frac{F_{ac}\mu(\mu+tan\Phi)}{(1-\mu tan\Phi)(\mu cos\Phi+sin\Phi)}\left\{\frac{1}{1-e^{\frac{-\mu\beta}{\mu cos\Phi+sin\Phi}}}\right\} \quad (3)$$

$$F_{ac} = \frac{(1-\mu tan\Phi)F_\beta(\mu cos\Phi+sin\Phi)}{\mu(\mu+tan\Phi)}\left\{1-e^{\frac{-\mu\beta}{\mu cos\Phi+sin\Phi}}\right\} \quad (4)$$

F_{ac}= axial clamping force due to tightening of T-bolt nut
β= subtended angle of half the V-section
μ= coefficient of friction between the V-section band clamp and rigid flanges
Φ= angle of the V-section

This is important to remember in later stages of this paper, as assembling in the finite element work is measured in F_{ac}, and in the experimental testing in T_w.
Figures 2a and 2b show the V-band contact zone after it has been taken off the flanges. In Figure 2a in which no friction has been assumed, almost no residual Mises stress can be seen at the surface. The peak stress lies further towards the inside away from the surface. This phenomenon is due to the forces acting at the surface. Considering the Mises-cylinder in three dimensions, two stresses are acting due to the bending of the band during assembly, one in the radial direction out of the plane, and one in parallel to the surface. The third stress is introduced by the contact force of the flange, acting directly normal to the surface. This third contact stress leads to an increase in hydrostatic stress, reducing the residual stress. This becomes clearer when taking into account friction as shown in Figure 2b (μ=0.2) adding an extra shear stress at the surface, leading to larger residual stresses at the surface as well, and increasing the peak stress by a ratio of about 3. This assumption is confirmed by Figures 3a and 3b, showing no plastic strain at the surface for the non friction case, and larger plastic strain at the surface for the case where friction has been included. A series of FE analyses undertaken for this paper have shown that below 30kN no plastic deformation in or close to the contact zone appears at all. As this shows, depending on the coefficient of friction and an axial clamping load of 30kN (23.6Nm), the plastic deformation would be hard to detect by surface roughness measurement. Even in the interest of research increasing the axial clamping load to 60kN (47.1Nm), which in real application would never be that high, the plastic deformation shown in Figures 3a and 3b is very little for no friction and friction case, and therefore hard to detect. Despite of that, the peak plastic strain has increased by approximately 2.5 when compared to 30kN. For the 60kN case, the influence of the hydrostatic stress and, for taking into account friction, the influence of shear stress on the plastic strain is similar to those of 30kN, as shown in Figure 4a and 4b.
Finally it can be said that no noteworthy amount of plastic deformation can be seen on the contact surface of the V-band, hence this method is not useful to detect the contact pressure distribution between the flanges and the band clamp.

3 EXPERIMENTAL RESULTS

The surface roughness on the inside of the V-band was measured in ten zones, 5 equally distributed around each side of the V-section, in which the band is in contact with the flanges, to create a methodology which enables investigation of the contact pressure distribution around the inside of the V-band clamp. The purpose of this investigation is to show whether or not the contact pressure is distributed uniformly or non-uniformly around the circumference.
The set up of the V-band on the PGI stylus machine can be seen in Figure 5a, along with an example of the 25x25mm measured area shown in the red square in Figure 5b. Each band clamp was

measured before and after assembly and the results for each area were compared to each other. Bands were assembled with torques T_w of 5, 10, 15 and 20Nm.
An example measurement of one area measured close to the T-bolt can be seen in Figure 6, in which 6a shows the plot for the measured surface before assembling the band. In there the red line shows where the diagram for the x-direction has been measured from. These were compared to Figures 6c and 6d after the assembly, and showed very little difference. Especially 6b and 6d seem to be slightly different but this is mainly due to the difficulty of always measuring the same red line before and after assembly. Even small deviations in the measured position can give different results, and hence it is hard to compare both diagrams to each other. Comparing Figures 6a and 6b the roll forming process in which the band clamps are manufactured can clearly be identified, as the flat section (of the V-section) is clearly smother than the top part of the square, which represents the bent area and hence has a larger surface roughness. As no plastic deformation could be detected for the range of 5 to 20Nm, there seems to be only elastic deformation on the surface. The correlates very well with the findings of the finite element work in the previous section, in which plastic deformation could only be noticed from 30kN (23.6Nm), and even then the values were so little to be determinable. Another problem associated with this measurement type, were marks and fringes appearing in the y-direction of the tested areas (Figures 7a and 7b) which were either due to table-noise and/or the preceding cold roll forming process in which these V-band clamps were manufactured with.

4 CONCLUSIONS

In this paper a previously developed axisymmetric finite element model for predicting the ultimate axial load capacity was utilised to carry out to numerically investigate the influence of contact pressure on the inner surface of a V-band clamp. The predictions showed very little plastic deformation in the contact area after the band clamp was assembled and then taken off again, even for torques that would never be reached in real applications.
The surface roughness measurements correlate very well with the finite element analyses as it was not possible to pick up any plastic deformation of the inner contact surface. Moreover, table noise and influences of the cold roll forming process highly affected the results and made it impossible to give reliable and accurate readings.
In the future finite element analysis of the cold roll forming process should be carried out to compare residual plastic strains induced by manufacturing to strains predicted in paper, to see if either one of them is significantly smaller and, hence, can be neglected.
The measurement methodology should be improved to prevent table noise.

REFERENCES

Barrans, S.M., Muller, M., 2009. Finite element prediction of the ultimate axial load capacity of V-section band clamps. In: 7th International Conference on Modern Practice in Stress and Vibration Analysis, Cambridge, UK.

Muller, M., Barrans, S.M., 2009. Ultimate Axial Load Capacity of V-Band Clamp Joints. In: University of Huddersfield (Ed.), Proceedings of Computing and Engineering Annual Researchers' Conference, Huddersfield, UK, 14-18

Muller,M., Barrans,S.M., 2010. Impact of flange geometry on the ultimate axial load capacity of V-band clamps. In: 9th International Conference on Turbochargers and Turbocharging, London, UK.

Shoghi, K., Barrans, S.M., Rao, H.V., 2004. Stress in V-section band clamps. J. Mech. Eng. Sci. 218, part C, 251-261.

Shoghi, K., Barrans, S.M., Rao, H.V., 2003. Classical and finite element analysis of V-band retainers. In: NAFEMS World Congress, Orlando, Florida, USA.

Shoghi, K., Barrans, S.M., Ramasamy. P., 2006. Axial load capacity of V-section band clamp joints. In: 8th International Conference on Turbochargers and Turbocharging, London, UK, pp. 273-285

School of Computing and Engineering Researchers' Conference, University of Huddersfield, Dec 2010

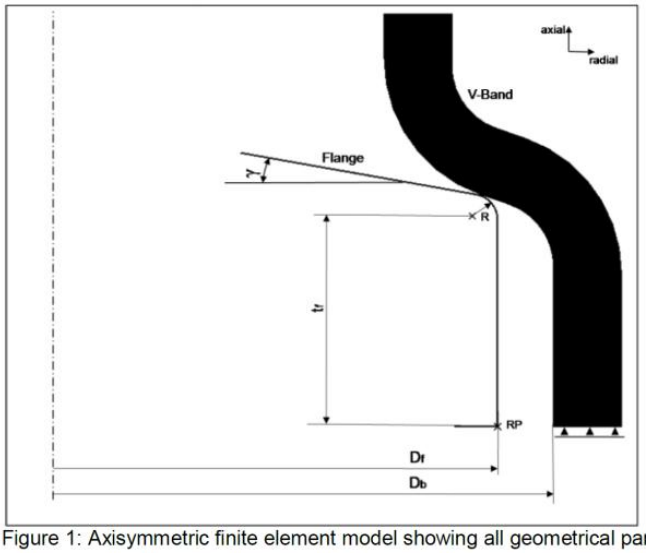

Figure 1: Axisymmetric finite element model showing all geometrical parameters, taken from Barrans and Muller (2009)

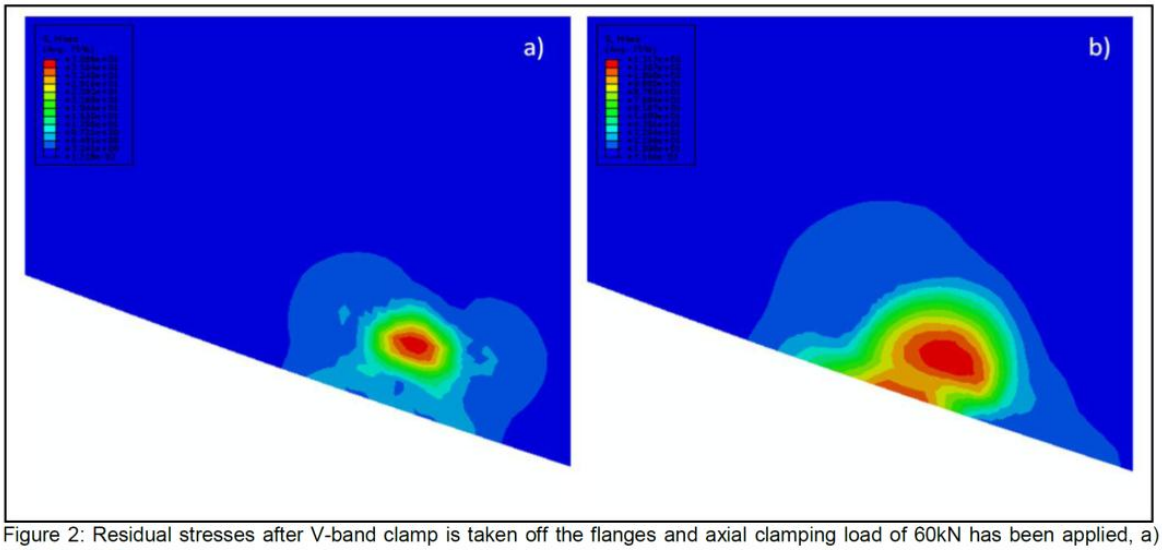

Figure 2: Residual stresses after V-band clamp is taken off the flanges and axial clamping load of 60kN has been applied, a) μ=0, b) μ=0,2

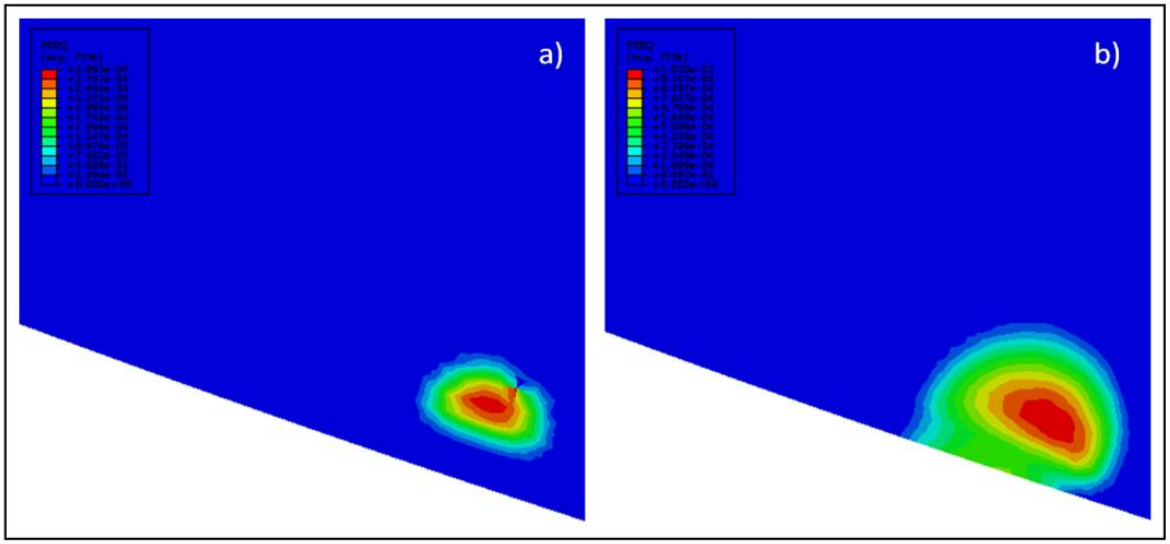

Figure 3: Plastic strains (PEEQ) after V-band clamp is taken off the flanges and axial clamping load of 30kN has been applied, a) μ=0, b) μ=0,2

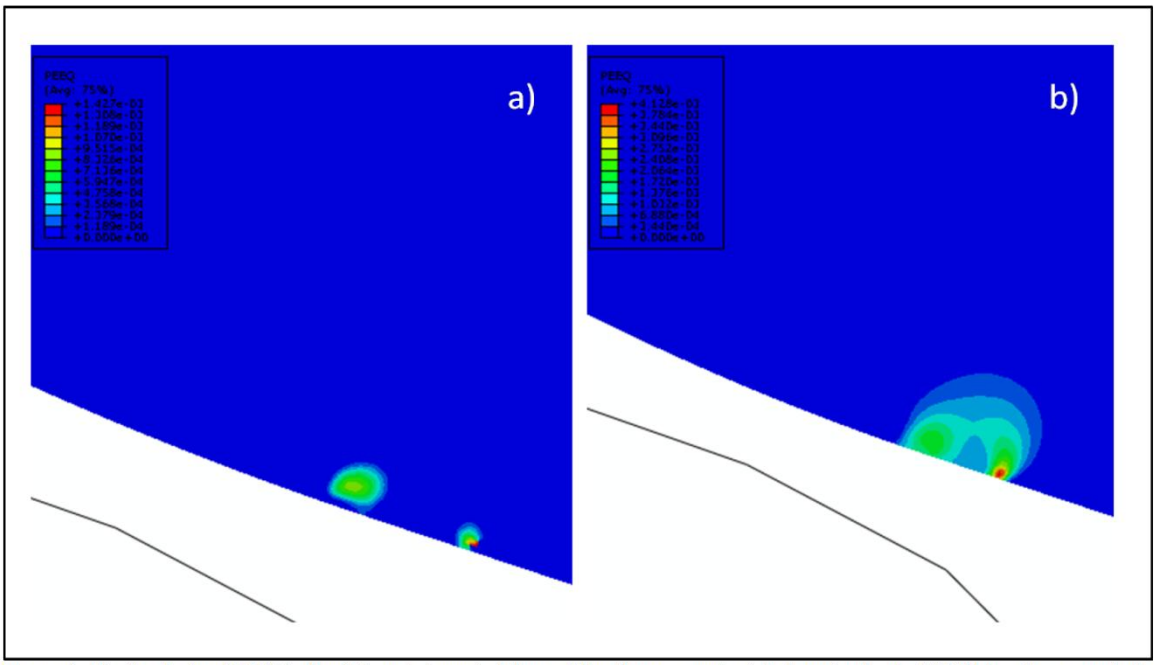

Figure 4: Plastic strains (PEEQ) after V-band clamp is taken off the flanges and axial clamping load of 60kN has been applied, a) μ=0, b) μ=0,2

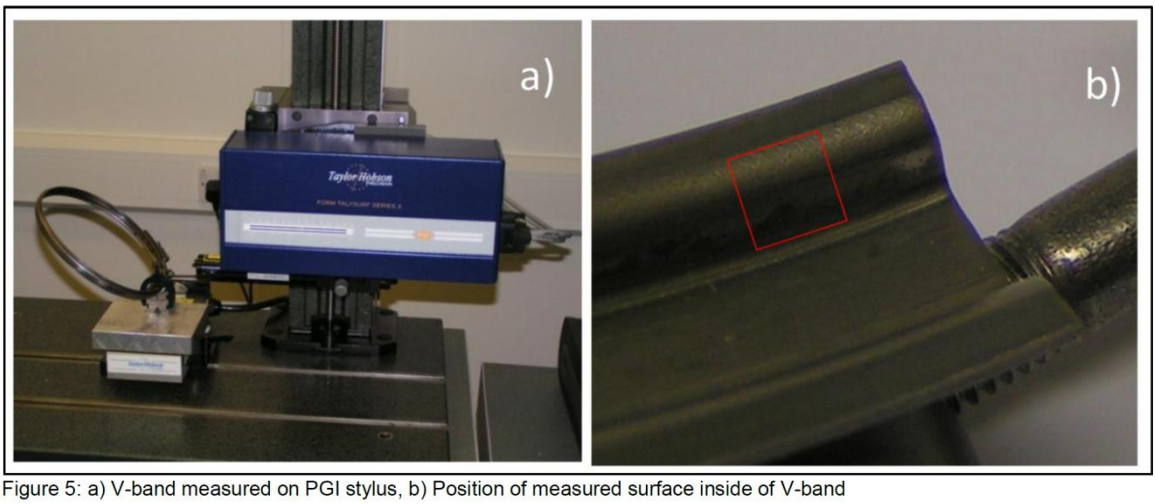

Figure 5: a) V-band measured on PGI stylus, b) Position of measured surface inside of V-band

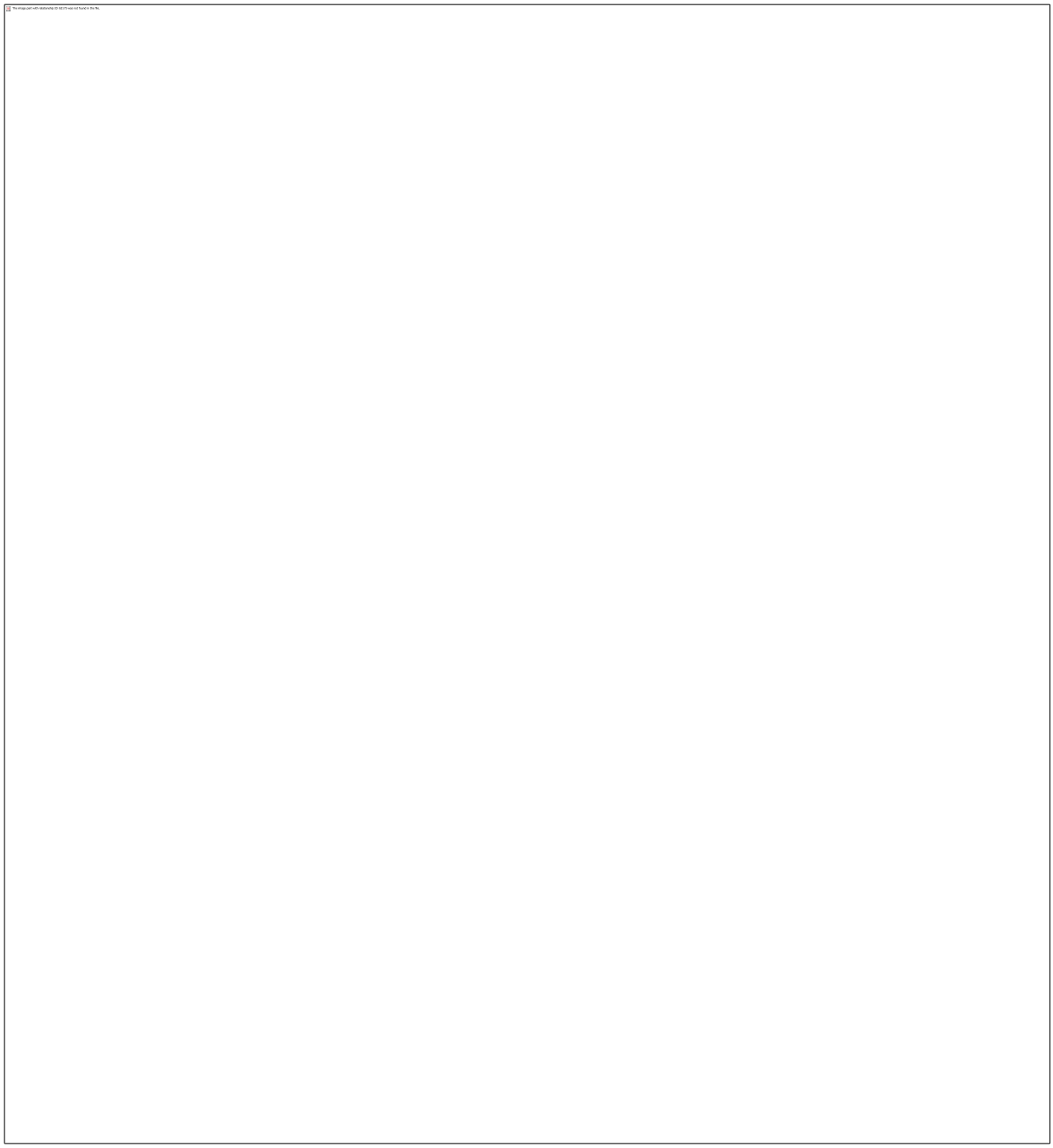
The image part with relationship ID rId19 was not found in the file.

Journal of Materials Processing Technology 211 (2011) 627–636

Contents lists available at ScienceDirect

Journal of Materials Processing Technology

journal homepage: www.elsevier.com/locate/jmatprotec

Predicting plastic deformation and work hardening during V-band formation

M. Muller*, S.M. Barrans, L. Blunt

Centre for Precision Technologies CPT, School of Computing & Engineering, University of Huddersfield, Queensgate, Huddersfield HD1 3DH, UK

ARTICLE INFO

Article history:
Received 28 April 2010
Received in revised form
22 November 2010
Accepted 27 November 2010
Available online 7 December 2010

Keywords:
V-band
Plastic deformation
Work hardening
Finite element analysis
Roll forming process

ABSTRACT

V-band clamps are manufactured using a cold roll forming process consisting of six passes which plastically deform an initially flat strip by bending to produce the band's V-section. In this paper a new method of validating numerically predicted plastic deformation in a cold formed metal strip is presented. Tensile testing of samples of the band's material was used to obtain a direct link between plastic strain and work hardness of this particular material. Using this correlation, the equivalent plastic strain (PEEQ) values predicted by finite element simulations were converted into hardness values. These values were compared to experimental work, in which samples of each pass of the roll forming process were taken to determine the work hardness in the cross section of the V-band using a micro-hardness machine. The error in strain predicted by the numerical method and hardness obtained by testing was found to be between 0.4% and 16.9%. This error was mainly due to uncertainty in material properties and the accuracy of the measurement technique. Compared to the more classical approach of measuring strain distribution with strain gauges, this method is more precise and accurate, as it is able to pick up even small changes in strain distribution.

1. Introduction

V-band clamps are widely used in the automotive, aircraft and aerospace industries to connect a pair of circular flanges to provide a joint with good axial strength and torsional rigidity. Offering the benefit of generating a fluid tight seal joint, they are used to clamp together the housings of turbochargers. Despite their well established benefits and wide use, there is still a lack of published knowledge about the working principle and behaviour of V-band clamps. Some work regarding the working principle of V-bands was originally presented by Mountford (1980) and more recently by Shoghi (2003). In the latter work the author presented a theoretical model able to predict the stresses and forces generated as the clamp is tightened around a pair of flanges. This was validated by Shoghi et al. (2004) using experimental data and Shoghi et al. (2003) using finite element analysis. The finite element work was developed further by Shoghi et al. (2006) to account for friction in the axial direction when tightening the T-bolt nut and applying an axial load. More recently Barrans and Muller (2009) and Muller and Barrans (2010) have analysed the ultimate axial load capacity of V-band clamps using the finite element method. However, it was partially recognised in this previous work that prediction of the ultimate axial load capacity of V-band joints would require knowledge of the state of the band material. This knowledge is essential if additional plastic deformation generated during joint failure is to be predicted and required an investigation of the manufacturing process. V-band clamps are made of austenitic stainless steel and manufactured using a cold roll forming process. In the first stage an initial flat band-strip is deformed using six passes to form the V-section. The second stage consists of a cold roll-bending process in which the band gets its circular shape as shown in Fig. 1.

Several authors have already investigated and numerically predicted similar cold roll forming processes, but have mainly focussed on longitudinal strain effects and the validation of these numerical models, as they have a large impact on wave edges, longitudinal curvature and end flare, hence reducing the quality of the metal strip.

One of the first computer aided simulations of a roll forming process allowed, Kiuchi and Koudabashi (1984) to optimise the production of circular tubes. The simulation enabled them to prevent the occurrence of edge waves, and it ensured that the energy dissipated in each roll pass was equal. McClure and Li (1995) analysed a roll forming process with three passes using a three dimensional finite element model, and validated their investigation by measuring the strain with strain gauges, bonded to the upper and lower surface of the strip. Another three dimensional finite element prediction of a U-shaped cold roll forming process consisting of three passes was undertaken by Heislitz et al. (1996). They found a continuous rise of longitudinal strain in the strip just ahead of each roll stand and comparison of their numerical work to previous experiments showed an approximate deviation of 10%. Around the same time Panton et al. (1996) also predicted the strain distribution in a cold roll forming process. Experiments using strain gauge rosettes

* Corresponding author. Tel.: +44 01484 47 3917.
E-mail addresses: m.muller@hud.ac.uk, matthias_mueller17@yahoo.de (M. Muller), s.m.barrans@hud.ac.uk (S.M. Barrans), l.a.blunt@hud.ac.uk (L. Blunt).

0924-0136/$ – see front matter © 2010 Elsevier B.V. All rights reserved.
doi:10.1016/j.jmatprotec.2010.11.020

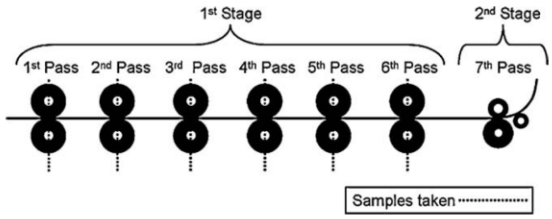

Fig. 1. Two dimensional schematic of rolling process including 1st stage of forming the V-section and 2nd stage of forming circular shape.

showed an increase of longitudinal strain on the strip surface before each roll stand, and a drop after each roll stand, and a continuous increase in shear strain throughout the forming process. From their finite element work, Hong et al. (2001) conclude that the work-hardening exponent has a significant effect on the forming length. The authors claim that a highly work-hardened strip has a shorter forming length, and an annealed strip has a longer. Numerical data for the longitudinal stress was compared to experiments, in which there was good correlation only for the first out of three roll stands.

Lindgren (2005) predicted the longitudinal membrane strain in the flange of a metal strip roll formed in a process consisting of six roll stands. The results correlated very well with those of Heislitz et al. (1996). In their numerical investigation on edge buckling of a roll forming process producing a symmetric channel section, Tehrani et al. (2006) validated their numerical results with strain gauge analysis and agreed with McClure and Li (1995) that the strain is positive/tensile in the flange, and negative/compressive in the web. From the three dimensional finite element simulation of Bui and Ponthot (2008) it can be observed that the product quality of the rolled strip significantly depends on the yield limit and work-hardening exponent, this latter conclusion being close to the findings of Hong et al. (2001). For the first time, Zeng et al. (2009) introduced the response surface method to optimise the design of cold roll formed profiles. Employing a finite element model to predict the maximum edge longitudinal membrane strain, the method enabled the authors to reduce the roll passes from six to four, which, as they concluded, saves money and time. Paralikas et al. (2009) developed a model to predict the effect of major process parameters on the quality characteristics of a V-section profile. The characteristics that they mainly focussed on were elastic, and longitudinal residual strains. This work is particularly interesting, as it discusses the possibility of using a simulation of the whole manufacturing chain of the roll forming process to predict the development and transmission of residual strains. Based on their work, Paralikas et al. (2010) introduced an optimisation procedure to improve the quality of the product and reduce costs. Selecting the optimum major process parameters, they managed to reduce longitudinal strains by up to 20–35%, and shear strains by up to 30–50%. Han et al. (2002) also investigated a multi-stand cold roll forming process, but by using the finite strip rather than the finite element method. They, too, mainly analysed the development of longitudinal strains throughout the process. This model was employed by Han et al. (2005) to investigate the effect of forming parameters on the peak longitudinal edge membrane strain development. Zhang et al. (2010) introduced a finite strip model in which the stiffness and transition matrix have been improved. Proving the accuracy of the method by predicting the longitudinal strain, the authors claim that their results are more applicable. One phenomenon that has been found by all authors mentioned so far is that the peak longitudinal strain occurs just ahead of the roll stand. McClure and Li (1995) showed that the maximum strain is a function of fold angle, whereas Han et al. (2005) proved that increasing the bend angle increment, the strip thickness, the flange length, the distance between roll stands, and the web width increased the peak longitudinal edge membrane strain. Zhu et al. (1996) claim that the peak longitudinal strain increases with a larger material thickness and bend angle. Han et al. (2005) and Lindgren (2007a) agree that increasing the material yield limit decreases the longitudinal membrane strain. Paralikas et al. (2009) identified several other parameters to be influential to the longitudinal strain peak. Bhattacharyya et al. (1984) and based on their work Lindgren (2007b), have mathematically analysed a cold roll forming process. Whilst all of the work discussed so far has helped understanding of forming processes, none of the work has taken into account stress and strain distributions through the thickness of the formed metal sheet. Moreover, the roll forming processes investigated have only focussed on sheets with a very large width to thickness ratio, in which shear stress effects can almost be neglected. The exception is Paralikas et al. (2010), who showed that reducing shear stress by up to 50% can significantly increase the quality of the roll formed product, and Panton et al. (1996) who showed a continuous increase of shear strain throughout the roll forming process.

Residual stresses in cold formed products have been studied by Weng and Pekoz (1990) for channel sections, Weng and White (1990a, 1990b) for thick steel plates, and Kleiner et al. (2004) for sheet metal forming. These authors have all applied either the hole-drilling or sectioning technique using strain gauges to measure residual strains. The latter technique was also used by Cruise and Gardner (2008) who stated that this is the better method when testing stainless steel. Quach et al. (2006) have numerically investigated residual stresses through the thickness of press-baked thin-walled sections, but only validated their finite element model by comparing outer surface and peak compressive stresses. It is very well understood that stainless steel can be work hardened as demonstrated by Hong et al. (2001) and Kain et al. (2004). Kumar et al. (2004) and Milad et al. (2008) state that for austenitic stainless steel unstable austenite partially transforms into martensite, greatly increasing the mechanical strength and hardness. Kim et al. (2007) have studied exactly this relation and their results showed good agreement between numerically predicted plastic strain and experimentally obtained hardness values.

Despite cold roll forming processes being studied so extensively, none of the work presented here has managed to accurately measure the plastic strain distribution through the thickness of a cold formed metal strip and used this information to validate finite element simulations of the process.

In this paper a new technique for validating roll forming simulations is presented. A sample of the initial flat metal strip was subjected to a tensile load and the extension and load reported. After each extension, the sample was taken off the tensile machine and its hardness was measured. From the permanent extension generated the plastic strain was calculated and this was then related to the hardness. A two dimensional finite element model was created to predict the equivalent plastic strain (PEEQ) in the cross section of the V-band after each roll pass. Only the first stage of the forming process was investigated to keep the results independent of the band clamp diameter. At the same positions in the roll forming process samples were cut out and the hardness in the cross section was measured using a hardness tester. The previously established relationship between plastic strain and hardness was then used to compare predicted plastic strain values from the finite element model with measured hardness values from the experiments.

2. Finite element model of plastic deformation

2.1. General set up of model

The Finite Element Analysis package ABAQUS (v6.7) was employed to simulate the cold roll forming process to manufacture

V-band clamps. To make the analysis independent of the clamp diameter only the first stage incorporating six passes were set up, only analysing one half as the process has a symmetry. The strip was modelled using three different mesh densities with 12 × 90, 24 × 180, and 48 × 360 equally spaced 2 dimensional reduced integration linear plane strain elements (CPE4R). The analysis was carried out in an implicit static environment and, as undertaken by Papeleux and Ponthot (2002) for a similar 2 dimensional forming process, a penalty algorithm was used to enforce contact. All tools and contact interactions were removed after every pass to include the effect of springback. Papeleux and Ponthot (2002) state that the results obtained for explicit and implicit solver were only slightly different but CPU costs for the explicit solver were almost 60 times higher than for its implicit counterpart. This analysis was generated in two dimensions because although the rolling process is 3 dimensional, the final state of each rolling pass is achieved on a plane. Linear Elements had to be used since as described by Konter (2000) in ABAQUS second-order quadrilateral elements at the contact surface will transfer the contact-force/pressure non-uniformly, sharing 1/6 on each corner node and 2/3 for each middle node. Moreover, Bui et al. (2004) found linear elements with reduced integration to be very suitable for metal forming processes including large bending and large plastic strains, and compared to their fully integrated counterparts, do not suffer from shear locking.

Within the finite element simulation each pass consisting of a pair of rollers was modelled using analytical rigid bodies representing a surface. The rollers were therefore not meshed. The contact between the rollers and the band was simulated using surface-to-surface interactions. No friction was assumed because this would add extra surface stress and strains as the rigid rollers slide over the surface, whereas in the real process the rollers do not slide over the band surface in the vertical direction. All upper rollers were prevented from moving in any direction by applying a boundary condition at their reference points, whereas the lower rollers where moved upwards pushing the band against their upper counterpart until the distance between the rollers in the simulation matched the clearance in the real rolling process. The clearance between the rollers is the same as the thickness of the initial flat strip.

2.2. Material properties

The material used was AISI 304 stainless steel quarter hard, with experimentally determined values for Young's Modulus of 227 GPa, Poisson's Ratio of 0.29, yield stress of 648 MPa and an ultimate tensile strength of 857 MPa, taken from Shoghi et al. (2004). For the FE-Analysis the material was defined to be elastic-plastic with linear hardening, as also used in the study of Kiuchi (1973) and with a von-Mises yield function as mentioned in Dixit and Dixit (2008). Using Eqs. (1)–(3) all engineering values were transformed into true values for the yield stress σ_{ty} and ultimate tensile strength σ_{tUTS}, and the plastic behaviour could be calculated as described by Tehrani et al. (2006) and Meyers and Chawla (1999).

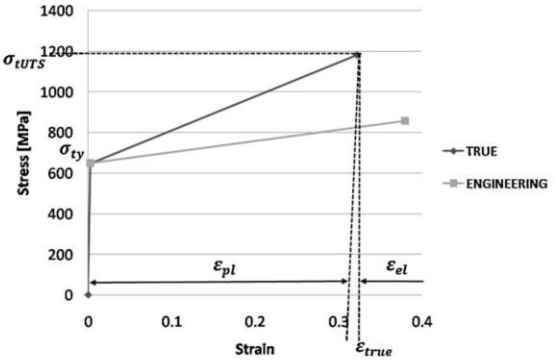

Fig. 2. Material model used for finite element simulation.

$$\sigma_t = \sigma_e(1 + \varepsilon_e) \quad (1)$$

$$\varepsilon_t = \ln(1 + \varepsilon_e) \quad (2)$$

$$\varepsilon_{pl} = \varepsilon - \varepsilon_{el} \quad (3)$$

The complete strain hardening curve and all engineering stress and strain values are shown in Fig. 2.

2.3. Finite element results

2.3.1. Mesh convergence study

The predicted equivalent plastic strain (PEEQ) in each of the six roll passes for a finite element model with a mesh density of 12 × 90 elements can be seen in Fig. 3. The simulation clearly shows a large increase in plastic strain in the bent areas, and first noticeable in the 4th pass, plastic deformation along the neutral line in the straight part of the clamp leg. As the mesh deformation shows, this latter deformation is due to shear stresses acting in this area.

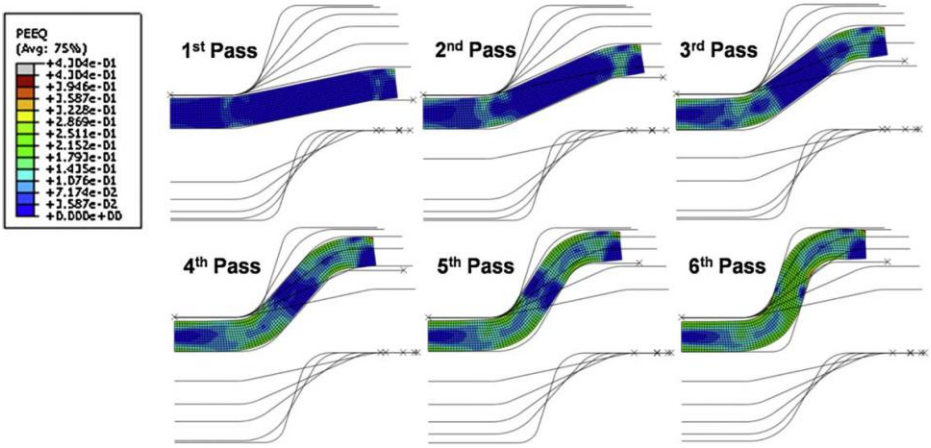

Fig. 3. Equivalent plastic strain (PEEQ) in each roll pass for a 12 × 90 element mesh.

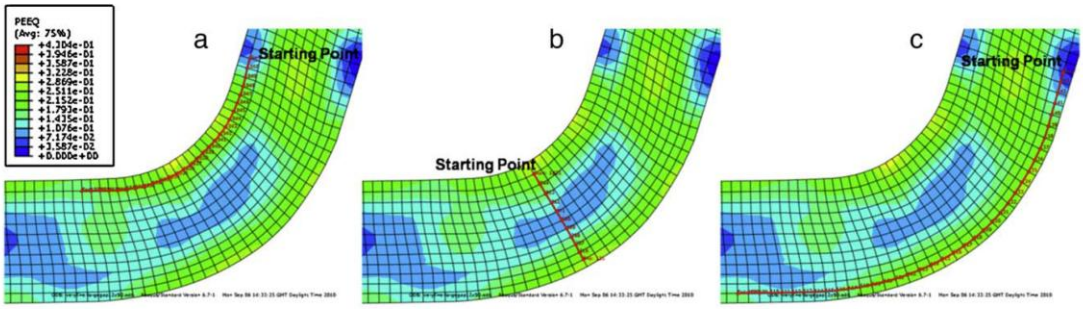

Fig. 4. Line of element corner nodes, where plastic strain was reported after 6th pass, (a) close to inner surface, (b) through the thickness and (c) close to outer surface.

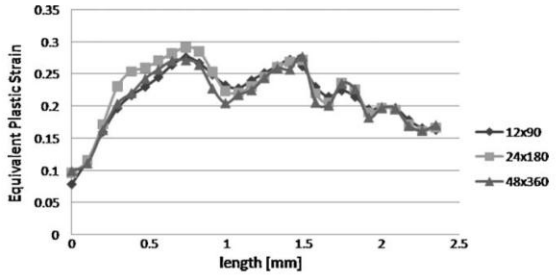

Fig. 5. Equivalent plastic strain distribution close to inner surface of the cross section after the 6th pass.

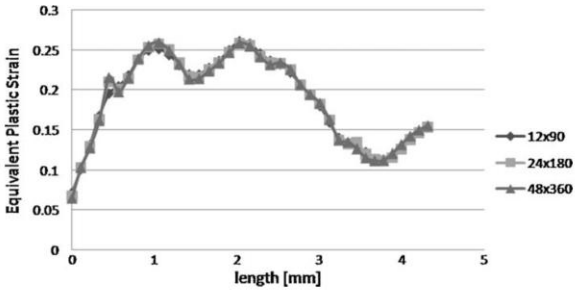

Fig. 6. Equivalent plastic strain distribution close to outer surface of the cross section after the 6th pass.

In order to demonstrate the accuracy and correctness of the initial mesh density with 12 × 90 elements, a convergence study with two more mesh densities of 24 × 180 and 48 × 360 elements was carried out. Three areas in the cross section of the 6th pass were chosen to be compared to each other. These areas were where predicted plastic strain values were compared to measured hardness values to validate the finite element model, as discussed in further detail in Section 4. The areas compared in the convergence study are indicated in Fig. 4 by red lines through the corner nodes of the elements from which the strain values were extracted. In all three meshes nodes existed along the indicated lines making it possible to make a direct comparison between models (for interpretation of the references to color in this sentence, the reader is referred to the web version of the article).

Fig. 5 shows the plastic strain values taken from line a (Fig. 4). These results show very good agreement, and only differ slightly between 0.5 mm and 1.2 mm. As expected, the plastic strain significantly drops at both ends of the red line, as these nodes lie further away from the bent area and either no or very little plastic deformation has taken place. The peaks and valleys visible in the bent area between 0.5 mm and 2 mm along the line will be discussed further in Section 2.3.2.

The next area of interest was at the outside corner (line c in Fig. 4), where mainly tension rather than compression took place. Again reading the plastic strain values taken from the element corner nodes the predicted values are shown in Fig. 6. Very good correlation between the results for all mesh densities can be seen, and as in the results for the inner side, the plastic strain drops further away from the bent area, at 0 mm and 3.8 mm. The two peaks are due to the bending area being slightly shifted to the right of the section (i.e. the left of the graph) as the cold roll forming process progresses, with the peak at 1.1 mm being introduced in the 6th pass.

The increase in plastic strain between 3.8 mm and 4.5 mm lies in the nature of the cold roll forming process, as the band is initially bent at the symmetry line as shown in Fig. 7 shortly before the band gets fully deformed during this first pass. This phenomenon appears throughout all six passes, leading to the plastic strain increasing as well.

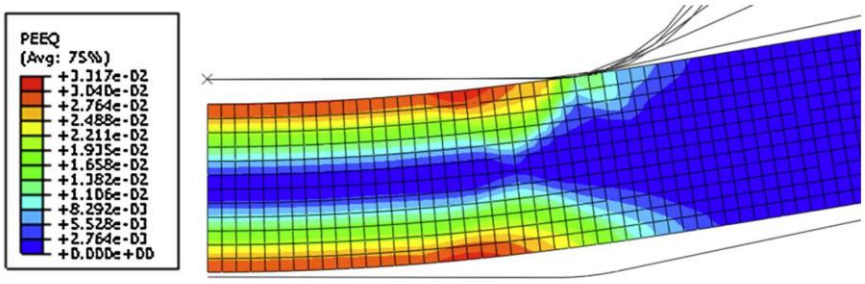

Fig. 7. Plastic strain close to the symmetry plane shortly before entering the first pass.

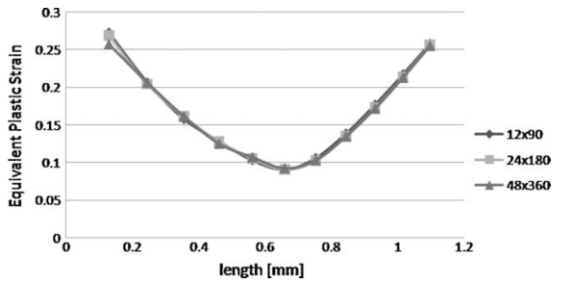

Fig. 8. Equivalent plastic strain distribution through the thickness of the cross section after the 6th pass.

The plastic strain distribution through the thickness of the band in the third area investigated in the convergence study, indicated by the red line in Fig. 4b, can be seen in Fig. 8. The graphs show very good correlation for all mesh densities, and distributions as expected, with very little plastic deformation towards the neutral line halfway through the thickness.

In all three areas the results shown here demonstrate good convergence after the 6th pass.

2.3.2. Influence of hydrostatic stress on plastic strain distribution

As described in the previous sub-section, the non-uniform distribution of the equivalent plastic strain (PEEQ) in Fig. 5 is worth further investigation. This is of particular interest as Muller and Barrans (2009) have discussed the problem of cracks occurring in this particular area of the inner surface of V-band clamps assembled to turbochargers for diesel engines.

In the zone of band strip where it is in contact with the upper rollers, the stress distribution consists of three compressive stress components. The first one σ_1 acting in the plane of the section and parallel to the surface of the strip is largest at the inner surface due to the bending. The second component σ_2 acts out of the plane as 2 dimensional plane strain is assumed and in this area the compressive bending strain would cause material in a short section to expand out of plane. The third compressive stress σ_3 is due to the contact force between upper roller and band strip. Considering the yield surface geometrically representing the von Mises yield criterion (also see Dixit and Dixit, 2008) the first two components σ_1 and σ_2 on their own would pass the yield surface leading to material yielding in this zone and significantly increasing the plastic strain. The stress component σ_3 due to the contact pressure however, acts in the perpendicular direction to the plane represented by σ_1 and σ_2, and brings the material closer towards the yield surface, significantly reducing plastic strain. This phenomenon can be seen several times in this cold roll forming process such as in Fig. 9a. Here two large peaks in plastic strain appear on both sides of the contact zone with the upper roller during pass 1. Fig. 9b shows a peak in the hydrostatic stress (termed "pressure" in ABAQUS), at the contact zone due to the large contact force. For the first pass, this larger hydrostatic stress indicates the correctness of the theory, in which the stress due to contact leads to less plastic deformation.

For the second roll pass, the same tendency can be observed as Fig. 10a shows not only two peaks in plastic strain next to the contact zone, but also another third peak left from pass one. Again the two peaks in plastic strain are next to the high hydrostatic stress zone, shown in Fig. 10b.In Fig. 11a, several peaks in plastic strain can be observed at the inner surface of band cross section. The largest peak in plastic strain of 0.29 is generated from the contact in the first and second passes, and the next slightly smaller peak of 0.1995 is generated from the contact interaction in the second, third and fourth passes. The final strain peak of 0.1711 is the second part due to the contact in pass 4, which is clearer when taking into account the large hydrostatic stress in Fig. 11b.

The two dimensional finite element model clearly showed that in a plane strain case with bending acting, stresses due to the contact force can significantly reduce the plastic deformation this area.

3. Experimental testing

3.1. Methods

A tensile test for austenitic stainless steel AISI 304 was carried out to establish data to validate the finite element simulations described above. Using a tensile test machine a standard test sample of the initial flat band was extended in increments of plastic strain. The sample was taken off the machine to measure the work hardness (HMV) at each increment. All hardness measurements used the Vickers hardness scale and were taken using a Microhard-

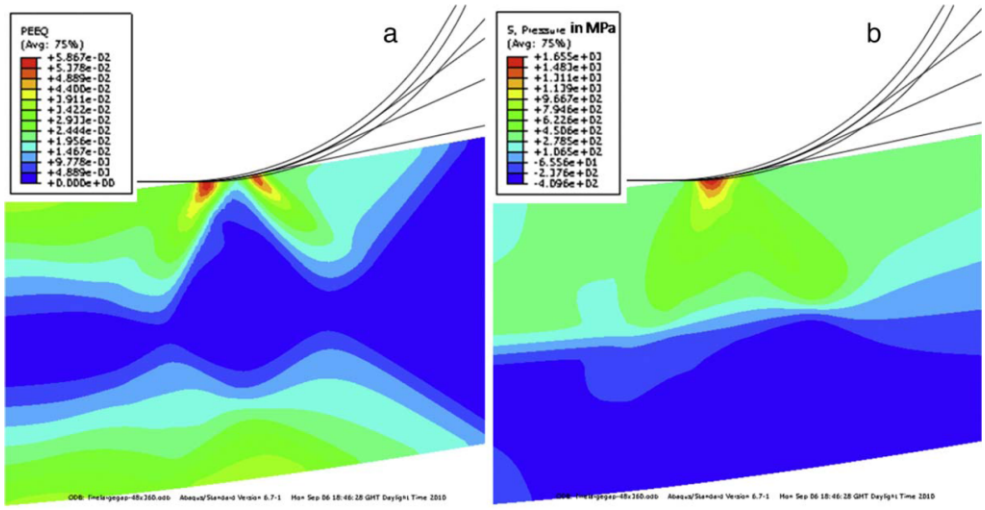

Fig. 9. Band strip in contact with upper roll 1 before being fully deformed, (a) equivalent plastic strain (PEEQ), (b) stress component due to contact force of roller.

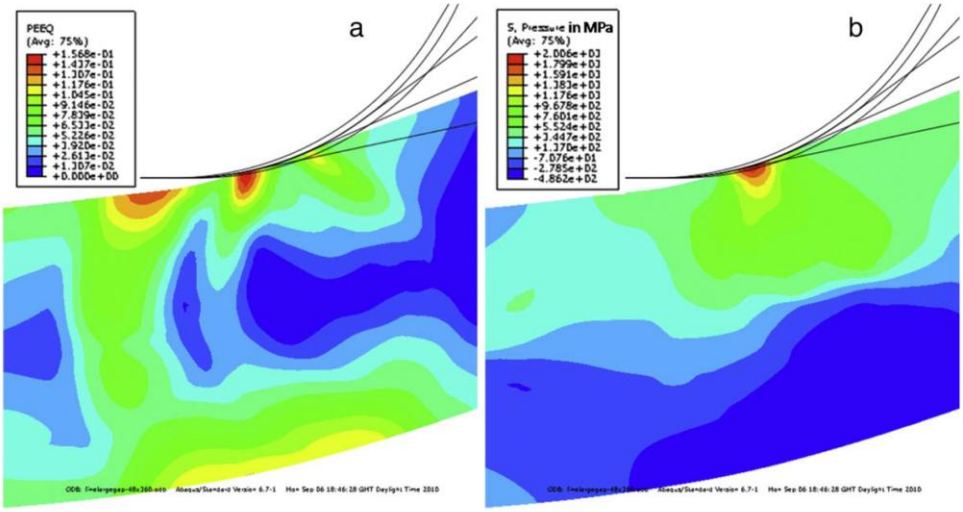

Fig. 10. Band strip in contact with upper roller 2 before being fully deformed, (a) equivalent plastic strain (PEEQ), (b) stress component due to contact force of roller.

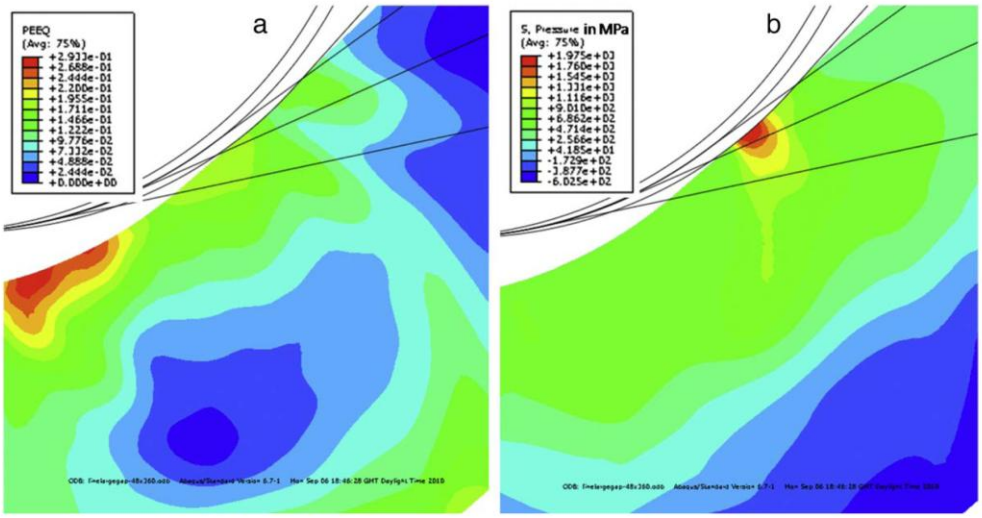

Fig. 11. Band strip in contact with upper roller 4 before being fully deformed, (a) equivalent plastic strain (PEEQ), (b) stress component due to contact force of roller.

ness Tester Buehler 1600-6100. For the tensile tests specimens, care was taken to ensure that the sample had not started to neck before measurements were taken.

The second set of hardness measurements can be sub-divided into two categories. The first showed the increase in work hardness throughout the cold roll forming process starting from the initial flat band to a sample of the sixth roll pass. The second was used to establish a new method to validate the finite element results for the sixth pass. For both categories the hardness was measured at several points through the cross-section of the band perpendicular to the rolling direction. The samples were obtained by taking a strip out of the roll forming machine including all six passes. The position of each pass was marked on the strip and after that small samples were cut off the string close to each marked position. Fig. 1 shows at which positions the samples were taken from. Fig. 12 gives an overview of the measuring points in the cross-section for the final forming stage, pass 6.

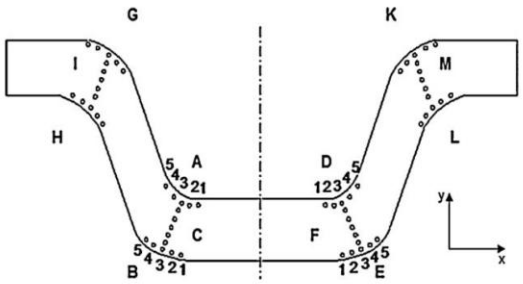

Fig. 12. Work hardness measuring points to show increase throughout roll forming process (6th pass).

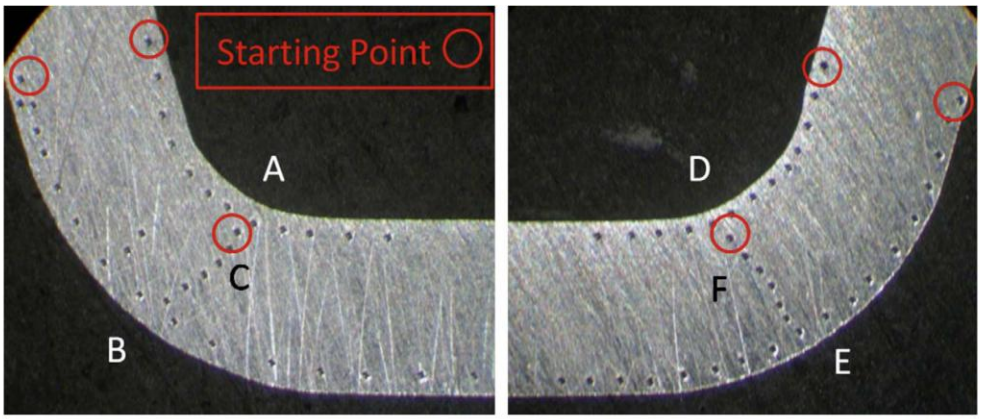

Fig. 13. Work hardness measuring points for validating finite element analyses (6th pass).

The regions measured in the cross-section, A to M were chosen because the finite element results showed large changes in plastic deformation, so these are likely to have the largest change in hardness through the forming process. The points of regions A, B, D, E, G, H, K and L were measured with a distance to the outside surface between 0.08 and 0.15 mm. Using an optical microscope with a micro adjustable *x*–*y* stage on the hardness machine, the position of the right and left hand side of each sample was set. It was then possible to define the plane of symmetry and from there the *x*-distance to each point was defined. A similar process using the upper and lower edges of the samples was used to define the *y*-coordinate for each point. Considering that each machining process has certain tolerances it was not possible to measure the hardness of a specific point at exactly the same position for each pass. This paper focuses especially on regions A, B, C, D, E, and F, as they are expected to have the largest impact on the actual strength of the joint and crack development in the V-band cross section. Five measuring points in each region were assumed to be sufficient to show the work hardness progression, whereas between 6 and 16 points were required to establish an accurate validation for the finite element work, as shown in Fig. 13.

3.2. Results

3.2.1. Tensile and hardness test to establish validation method

Using Eqs. (1)–(3) and undertaking the same procedure as for the finite element model, all engineering values gathered from the tensile test sample were transformed into true values and the plastic behaviour could be calculated. This allowed the relationship between plastic strain and work hardness to be established, as shown in Fig. 14.

The hardness values in Fig. 14 were determined for plastic strain values between 0.009 and 0.0277 and then partially linearised (dashed lines) in three regions, generating Eqs. (4)–(6):

Region 1 $0.009 \leq \varepsilon_{pl} < 0.039$:

$$H_1 = \varepsilon_{pl} \times 1000 + 320 \quad (4)$$

Region 2 $0.039 \leq \varepsilon_{pl} < 0.095$:

$$H_2 = \varepsilon_{pl} \times 643 + 336 \quad (5)$$

Region 3 $0.095 \leq \varepsilon_{pl} < 0.277$:

$$H_3 = \varepsilon_{pl} \times 362 + 360 \quad (6)$$

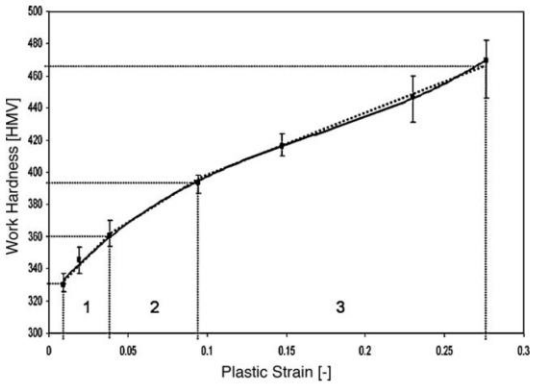

Fig. 14. Correlation between work hardness and plastic strain for AISI 304.

3.2.2. Determination of work hardness throughout cold roll forming process

Figs. 15–17 display the experimental results for the development of work hardness in three regions through the six pass roll forming process. The ordinate shows the Vickers Hardness and the abscissa the number of the sample point. Fig. 15 indicates that for region A the greatest work hardening is in the centre of the fillet. This is the area predicted by the FE analysis as having the largest plastic deformation. The further away the sample points are from

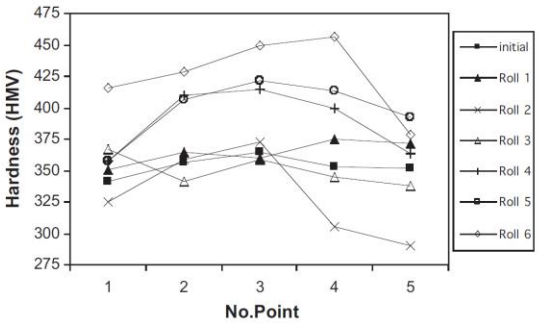

Fig. 15. Hardness measured at region A (all passes).

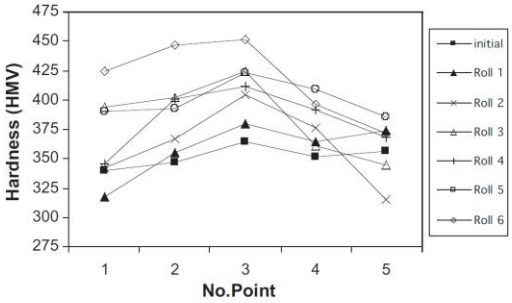

Fig. 16. Hardness measured at region B (all passes).

the centre, the smaller is the work hardness. Only the graph for the initial flat band has a relatively constant value of hardness taking account of measurement uncertainty.

The behaviour observed for region A can also be seen for area B in Fig. 16. The largest magnitude of hardness occurred at the centre of the fillet indicated as number 3. Again, this is where the FE analysis predicts the largest plastic strain.

The graphs in Fig. 17 show the development of work hardening through the thickness of the band in region C. The graph for the initial flat band indicates that the band has already had a range of hardness through the thickness, with the magnitude decreasing towards the neutral plane. This range was due to the preceding flat rolling process. As the graphs for the six pairs of rollers display, this trend develops further as the band undergoes more deformation.

The trends shown by the experimental results obtained in this investigation agreed with the numerical results obtained from FE analysis. In order to get a quantitative comparison a further experimental investigation was undertaken to relate work hardness and plastic strain directly.

4. Experimental validation

Using the relationship established in Section 3.2.1, it was then possible to convert the plastic strain values found by the FE analysis into hardness values. The transformed numerical hardness results taken from pass six were then compared to the measured hardness values at regions A, B, C, D, E, and F.

The Hardness values for areas A and D (see Figs. 4 and 13) determined in the experimental tests compared to their numerical counterparts (48 × 360 element mesh) are shown in Fig. 18. The values for the hardness are shown over the length as the distance between the points was measured, starting at zero with the point at the top of the areas A and D. The same was done for the finite element results, but there the distance between the nodes was taken as the length value. As indicated, these values correlate with each other very well showing the largest magnitude in the centre of the fillet. The overall trend of the measured hardness fits well with the predicted results, especially for the parts between 0 mm and 1 mm. and 2 mm to 2.5 mm. In between 1 mm and 2 mm, it can be noticed that the overall trend, as well as the absolute hardness values seem to deviate and do not show the best correlation. This may be due to uncertainties when measuring the *x*- and *y*-distance of each point. The V-section angle was assumed to be 37° in the sixth pass as specified for the component. However the manufacturing process has an associated tolerance and in the current experiments, the angle of the V-section was not initially measured. An additional difficulty found in this method was accurately controlling the position of the hardness points relative to the surface and hence to specific points on the finite element simulation.

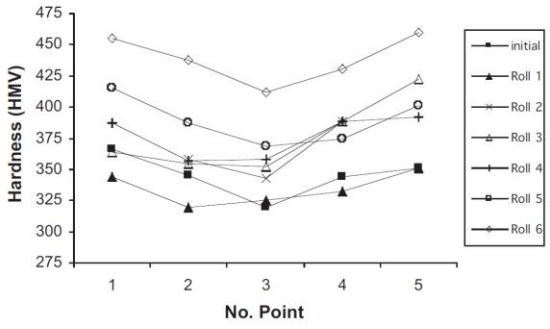

Fig. 17. Hardness measured at region C (all passes).

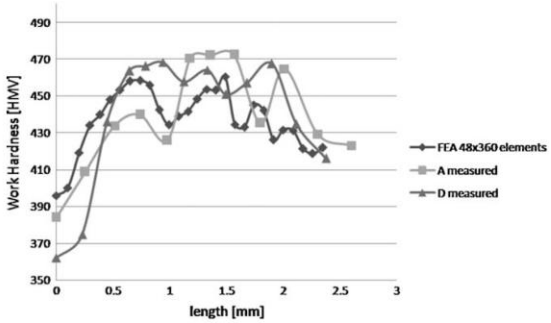

Fig. 18. Comparison of hardness determined for regions A, D and hardness obtained by predicting plastic strain (6th pass).

The same good correlation for the overall trend of measured areas B and E compared to the finite element results can be seen in Fig. 19, with the peaks in the centre of the fillet. As for areas A and D, also here very good correlation can be seen for results between 0 mm and approximately 1.5 mm. From 1.5 mm onwards the results for area F give a better fit to the numerical results than area B. However, the decrease of the hardness further away from the bent area can be seen for both regions. Again, the absolute values for the measured and predicted hardness values differ from 1.5 mm.

Very good correlation in the overall trend as well as the absolute values between predicted and measured hardness for regions C and F can be observed from Fig. 20. All three graphs show the expected distribution through the thickness of the cross section as a parabola, with the hardness values decreasing towards the neutral line.

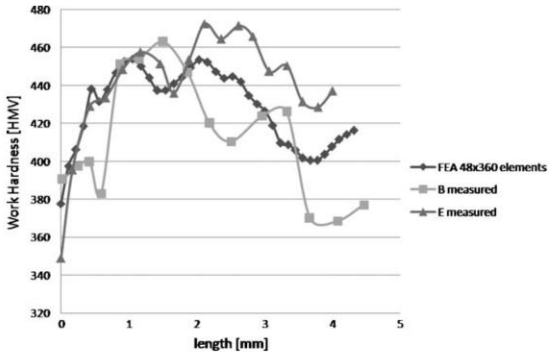

Fig. 19. Comparison of hardness determined for regions B, E and hardness obtained by predicting plastic strain (6th pass).

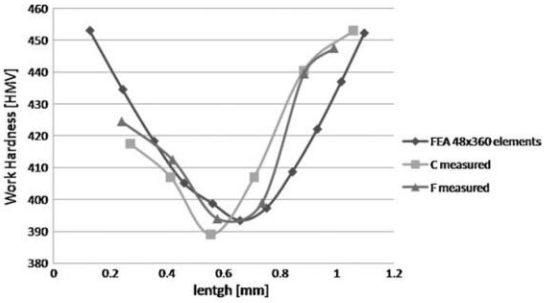

Fig. 20. Comparison of hardness determined for regions C, F and hardness obtained by predicting plastic strain (6th pass).

Although the experiments carried out in the presented work have shown partial deviations between predicted and measured hardness, it is clear that validating predicted plastic strain in finite element analysis by measuring the work hardness is useful technique.

5. Conclusion

In this paper, a new method of validating finite element predictions has been demonstrated. Compared to more classical methods of measuring plastic strain, such as the cutting and hole drilling technique, the method presented in here does not apply strain gauges, but operates by measuring the work hardness with a hardness tester and uses information gathered from a tensile test. Moreover, the classical use of strain gauges only measures the surface strain. Whilst for thin metal sheets this technique provides enough data, it does not deliver enough information about the plastic deformation for thicker cross sections in which shear stresses have greater effects. As crack growth is more severe in thicker metal sheets, the additional, more detailed information gathered by the presented method of measuring the actual hardness may be important for investigating the development of cracks and improving the roll forming process. The finite element work has also shown significant changes in plastic deformation in the bent area and correlates with measurements very well.

In addition to employing a new method of validating finite element results, the development of work hardness throughout the cold roll forming process of manufacturing V-band clamps has been investigated. The results showed good agreement with existing knowledge in the field. The overall trend showed hardness increasing in areas where plastic deformation has taken place.

6. Further work

In future, the knowledge obtained in this paper can be used to investigate the behaviour of V-band clamps when assembled to a pair of flanges and sustaining an axial load. To achieve this, a 3D FE-Analysis of the roll forming process (including the 7th ring forming stage) should be carried out to generate a model of V-band containing the plastic strains generated during manufacturing. This model could then be assembled to a model of a pair of flanges. Simulating an axial load using this combined model would greatly enhance understanding of the failure mode of V-band clamps of different sizes.

Acknowledgement

The authors would like to gratefully thank Ian Brown, Teconnex Ltd. Keighley, UK and Dr Kiumars Shoghi, Borg Warner, Bradford, UK for supporting this research.

References

Barrans, S.M., Muller, M., 2009. Finite element prediction of the ultimate axial load capacity of V-section band clamps. In: 7th International Conference on Modern Practice in Stress and Vibration Analysis, Cambridge, UK.
Bhattacharyya, D., Smith, P.D., Yee, C.H., Collins, I.F., 1984. The prediction of deformation length in cold roll-forming. Journal of Mechanical Working Technology 9, 181–191.
Bui, Q.V., Papelux, L., Ponthot, J.P., 2004. Numerical simulation of springback using enhanced assumed strain elements. Journal of Materials Processing Technology 153–154, 314–318.
Bui, Q.V., Ponthot, J.P., 2008. Numerical simulation of cold roll-forming processes. Journal of Materials Processing Technology 202, 275–282.
Cruise, R.B., Gardner, L., 2008. Residual stress analysis of structural stainless steel sections. Journal of Constructional Steel Research 64, 352–366.
Dixit, P.M., Dixit, U.S., 2008. Modeling of Metal Forming and Machining Processes by Finite Element and Soft Computing Methods. Springer, London, pp.101.
Han, Z.W., Liu, C., Lu, W.P., Ren, L.Q., 2002. Simulation of a multi-stand roll-forming process for thick channel section. Journal of Materials Processing Technology 127, 382–387.
Han, Z.W., Liu, C., Lu, W.P., Ren, L.Q., Tong, J., 2005. Spline finite strip analysis of forming parameters in roll forming a channel section. Journal of Materials Processing Technology 159, 383–388.
Heislitz, F., Livatyali, H., Ahmetoglu, M.A., Kinzel, G.L., Altan, T., 1996. Simulation of roll forming process with the 3-D FEM code PAM-STAMP. Journal of Materials Processing Technology 59, 59–67.
Hong, S., Lee, S., Kim, N., 2001. A parametric study on forming length in roll forming. Journal of Materials Processing Technology 113, 774–778.
Kain, V., Chandra, K., Adhe, K.N., De, P.K., 2004. Effect of cold work on low-temperature sensitization behavior of austenitic stainless steel. Journal of Nuclear Materials 334, 115–132.
Kim, W., Kawai, K., Koyama, H., Miyazaki, D., 2007. Fatigue strength and residual stress of groove-rolled products. Journal of Materials Processing Technology 194, 46–51.
Kiuchi, M., 1973. Analytical study on cold roll forming process. In: Report of Inst. Ind. Sci. University of Tokyo, p. 23.
Kiuchi, M., Koudabashi, T., 1984. Automated design system of optimal roll profiles for cold roll forming. In: Bedford (Ed.), Proceedings of the Third International Conference on Rotary Metalworking Processes. Kyoto, Japan, pp. 423–436.
Kleiner, M., Krux, R., Homberg, W., 2004. Analysis of residual stresses in high-pressure sheet metal forming. CIRP Annals-Manufacturing Technology 53 (1), 211–214.
Konter, A., 2000. How to – Undertake a Contact and Friction Analysis. NAFEMS, Glasgow, pp. 11–13.
Kumar, B.R., Singh, A.K., Das, S., Bhattacharya, D.K., 2004. Cold rolling texture in AISI 304 stainless steel. Materials Science and Engineering A 364 (1–2), 132–139.
Lindgren, M., 2005. Finite element model of roll forming of a U-channel profile. In: International Conference on Tech. of Plasticity, Verona.
Lindgren, M., 2007a. Cold roll forming of a U-channel made of high strength steel. Journal of Materials Processing Technology 186, 77–81.
Lindgren, M., 2007b. An improved model for the longitudinal peak strain in the flange of a roll formed U-channel developed by FE-analysis. Steel Research International 78 (1), 82–87.
McClure, C.K., Li, H., 1995. Roll forming simulation using finite element analysis. Manufacturing Review 8, 114–119.
Meyers, M.A., Chawla, K.K., 1999. Mechanical Behavior of Materials, London, p. 116.
Milad, M., Zreiba, N., Elhalouani, F., Baradai, C., 2008. The effect of cold work on structure and properties of AISI 304 stainless steel. Journal of Materials Processing Technology 203, 80–85.
Mountford, R., 1980. Design of clamp joints. Engineering Designer, 37–39.
Muller, M., Barrans, S.M., 2009. Ultimate axial load capacity of V-band clamp joints. In: University of Huddersfield (Ed.), Proceedings of Computing and Engineering Annual Researchers' Conference. Huddersfield, UK, pp. 14–18.
Muller, M., Barrans, S.M., 2010. Impact of flange geometry on the ultimate axial load capacity of V-band clamps. In: 9th International Conference on Turbochargers and Turbocharging, London, UK.
Panton, S.M., Duncan, J.L., Zhu, S.D., 1996. Longitudinal and shear strain development in cold roll forming. Journal of Materials Processing Technology 60, 219–224.
Papeleux, L., Ponthot, J.-P., 2002. Finite element simulation of springback in sheet metal forming. Journal of Materials Processing Technology, 785–791.
Paralikas, J., Salonitis, K., Chryssolouris, G., 2009. Investigation of the effects of main roll-forming process parameters on quality for a V-section profile from AHSS. International Journal of Advanced Manufacturing Technology 44, 223–237.
Paralikas, J., Salonitis, K., Chryssolouris, G., 2010. Optimization of roll forming process parameters – a semi-empirical approach. International Journal of Advanced Manufacturing Technology 47, 1041–1052.
Quach, W.M., Teng, J.G., Chung, K.F., 2006. Finite element predictions of residual stresses in press-braked thin-walled steel sections. Engineering Structures 28, 1609–1619.
Shoghi, K., 2003. Stress and Strain Analysis of Flat and V-Section Band Clamps. University of Huddersfield, Huddersfield.
Shoghi, K., Barrans, S.M., Rao, H.V., 2004. Stress in V-section band clamps. Journal of Mechanical Engineering Science 218 (part C), 251–261.

Shoghi, K., Barrans, S.M., Rao, H.V., 2003. Classical and finite element analysis of V-band retainers. In: NAFEMS World Congress, Orlando, Florida, USA.
Shoghi, K., Barrans, S.M., Ramasamy, P., 2006. Axial load capacity of V-section band clamp joints. In: 8th International Conference on Turbochargers and Turbocharging, London, UK, pp. 273–285.
Tehrani, M.S., Hartley, P., Naeini, H.M., Khademizadeh, H., 2006. Localised edge buckling in cold roll-forming of symmetric channel section. Thin-Walled structures 44, 184–196.
Weng, C.C., Pekoz, T., 1990. Residual stresses in cold-formed steel members. Journal of Structural Engineering 116 (6), 1611–1625.
Weng, C.C., White, R.N., 1990a. Residual stresses in cold-bent thick steel plates. Journal of Structural Engineering 116 (1), 24–39.
Weng, C.C., White, R.N., 1990b. Cold-bending of thick high-strength steel plates. Journal of Structural Engineering 116 (1), 40–54.
Zeng, G., Li, S.H., Yu, Z.Q., Lai, X.M., 2009. Optimization design of roll profiles for cold roll forming based on response surface method. Materials and Design 30 (6), 1930–1938.
Zhang, L., Tan, N., Liu, C., 2010. A new model for simulation of cold roll-forming of tubes by using spline strip method. Journal of Shanghai Jiaotong University 15 (1), 70–75.
Zhu, S.D., Panton, S.M., Duncan, J.L., 1996. The effects of geometric variables in roll forming a channel section. Proceedings of the Institution of Mechanical Engineers 210, 127–134.